Global stability and feedback control of boundary layer flows

by

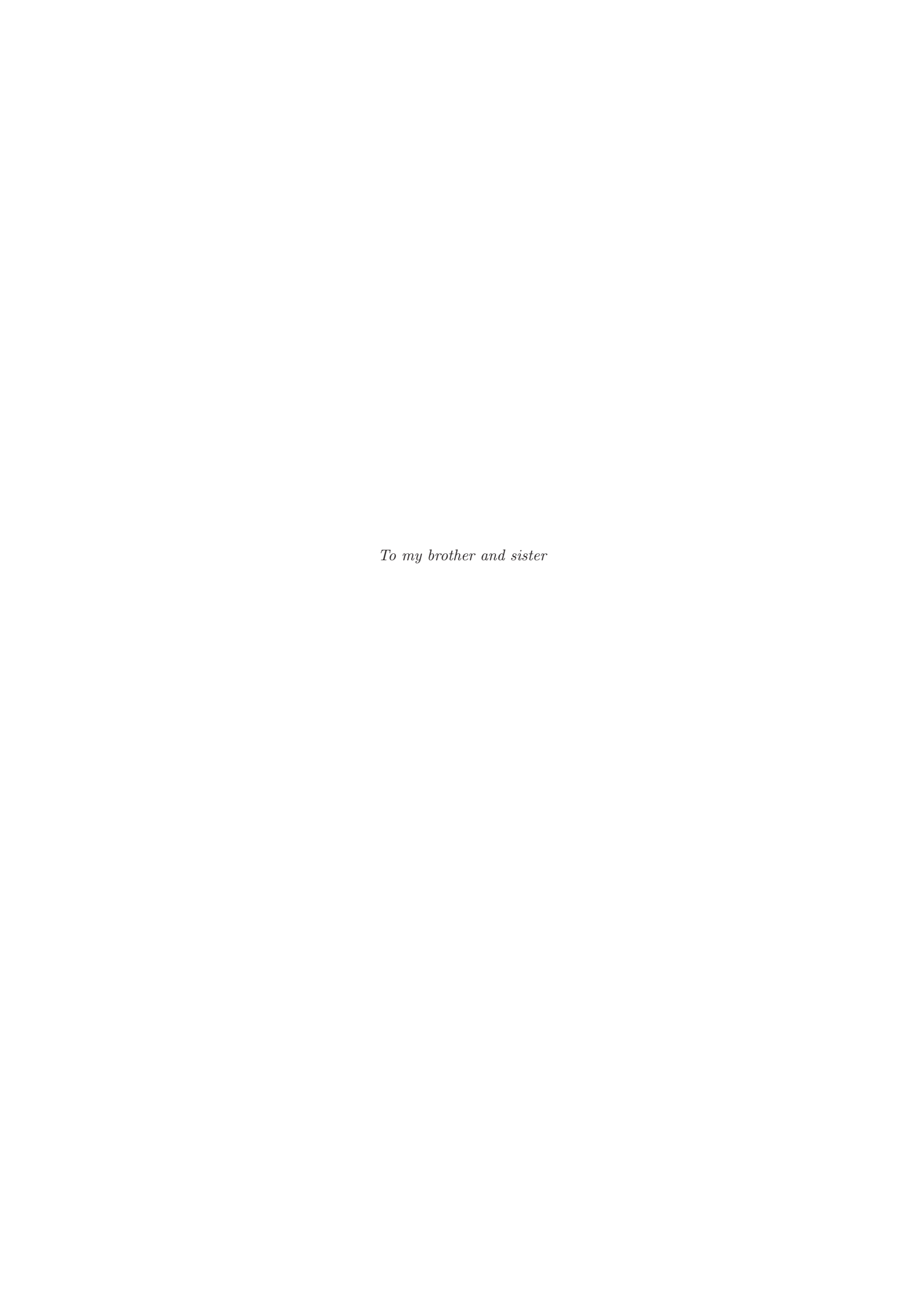
Espen Åkervik

December 2008
Technical Reports from
Linné Flow Centre
KTH Mechanics
Royal Institute of Technology
SE-100 44 Stockholm, Sweden

Typsatt i \mathcal{AMS} - \mathbb{AT}_{EX} .

Akademisk avhandling som med tillstånd av Kungliga Tekniska Högskolan i Stockholm framlägges till offentlig granskning för avläggande av teknologie doktorsexamen fredagen den 5:e december 2008 kl 10.30 i sal E1 vid Kungliga Tekniska Högskolan, Lindstedtsvägen 3, Stockholm.

©Espen Åkervik, 2008 Universitetsservice US–AB, Stockholm 2008



Global stability and feedback control of boundary layer flows

Espen Åkervik

Linné Flow Centre, KTH Mechanics, SE-100 44 Stockholm, Sweden

Abstract

In this thesis the stability of generic boundary layer flows is studied from a global viewpoint using optimization methods. Global eigenmodes of the incompressible linearized Navier-Stokes equations are computed using the Krylov subspace Arnoldi method. These modes serve as a tool both to study asymptotic stability and as a reduced basis to study transient growth. Transient growth is also studied using adjoint iterations. The knowledge obtained from the stability analysis is used to device systematic feedback control in the Linear Quadratic Gaussian framework. The dynamics is assumed to be described by the linearized Navier-Stokes equations. Actuators and sensors are designed and a Kalman filtering technique is used to reconstruct the unknown flow state from noisy measurements. This reconstructed flow state is used to determine the control feedback which is applied to the Navier-Stokes equations through properly designed actuators. Since the control and estimation gains are obtained through an optimization process, and the Navier-Stokes equations typically forms a very high-dimensional system when discretized there is an interest in reducing the complexity of the equations. A standard method to construct a reduced order model is to perform a Galerkin projection of the full equations onto the subspace spanned by a suitable set of vectors, such as global eigenmodes and balanced truncation modes.

 $\begin{tabular}{ll} \textbf{Descriptors:} & \textbf{Global stability, control, estimation, absolute/convective instabilities, model reduction.} \end{tabular}$

Preface

This thesis consists of two parts. In part 1 an introduction to the topic is presented, whereas part 2 contains the papers. A short description of each paper and division of work between authors is given in Chapter 8 of part 1. The papers in part 2 are adjusted to comply with the present thesis format for consistency, but their contents have not been altered compared to published or submitted versions, except for minor corrections. The included papers are:

Paper 1

Global two-dimensional stability measures of the flat plate boundary-layer flow Espen Åkervik, Uwe Ehrenstein, François Gallaire and Dan S. Henningson Eur. J. Mech. B/Fluids, 27 (2008), pages 501–513

Paper 2

Steady solutions of the Navier–Stokes equations by selective frequency damping. Espen Åkervik, Luca Brandt, Dan Henningson, Jérôme Hæpffner, Olaf Marxen, Philip Schlatter. Phys. Fluids 18, 068102 (2006).

Paper 3

Optimal growth, model reduction and control in a separated boundary-layer flow using global eigenmodes Espen Åkervik, Jérôme Hæpffner, Uwe Ehrenstein, Dan S. Henningson. J. Fluid Mech., **579** (2007), pages 305–314.

Paper 4

Matrix-free methods for the stability and control of boundary layers. Shervin Bagheri, Espen Åkervik, Luca Brandt, Dan S. Henningson. $AIAA\ Journal$, submitted.

Paper 5

Linear feedback control and estimation applied to instabilities in spatially developing boundary layers.

MATTIAS CHEVALIER, JÉRÔME HŒPFFNER, ESPEN ÅKERVIK, DAN S. HENNINGSON. J. Fluid Mech., **588** (2007), pages 163–187.

Paper 6

Global optimal disturbances in the Blasius flow using time-steppers. Antonios Monokrousos, Espen Åkervik, Luca Brandt, Dan S. Henningson. Technical report.

Related paper, not included in thesis:

The use of global modes to understand transition and perform flow control. DAN S. HENNINGSON AND ESPEN ÅKERVIK. Phys. Fluids 20, 031302 (2008).

Abstract			
Prefac	ce	iv	
Part 1	. Summary	1	
Chapt	er 1. Introduction	3	
Chapt	er 2. Governing equations	7	
2.1.	The incompressible Navier–Stokes equations	7	
2.2.	The linearized Navier–Stokes equations	8	
2.3.	State space formulation	9	
Chapt	er 3. Numerical Simulations	11	
3.1.	Spectral methods	11	
3.2.	DNS, RANS and LES	12	
3.3.	How to handle the pressure	12	
3.4.	A spectral DNS code	13	
3.5.	A mixed finite-difference Chebyshev DNS code	14	
3.6.	Discretized state space formulation	14	
Chapt	er 4. Computation of eigenvalues	15	
4.1.	The QR method	16	
4.2.	•		
4.3.	Time stepping, a way to avoid building the full matrix	18	
Chapt	er 5. Hydrodynamic stability	20	
5.1.	Flow cases	20	
5.2.	Strategy	22	
5.3.	From eigenvalues to optimal growth	23	
5.4.	Worst case disturbances	24	
5.5.	Global stability of the flat plate boundary layer flow	27	
5.6.	Global stability of the cavity flow	30	
Chapt	er 6. Flow control	33	
6.1.	Feedback control	35	
6.2.	Inputs and outputs	36	
6.3.	Model reduction	37	
6.4.	LQG control of the Navier–Stokes equations	40	
6.5.	Control of the flat plate boundary layer flow	42	

6.6. Control of the cavity flow	43
Chapter 7. Conclusions and outlook	46
Chapter 8. Summary of papers and divison of work	48
Acknowledgements	52
References	53
Part 2. Papers	59
Paper 1. Global two-dimensional stability measures of the fla plate boundary-layer flow	t 63
Paper 2. Steady solutions of the Navier-Stokes equations by selective frequency damping	85
Paper 3. Optimal growth, model reduction and control in a separated boundary-layer flow using global eigenmodes	99
Paper 4. Matrix-free methods for the stability and control of boundary layers	f 115
Paper 5. Linear feedback control and estimation applied to instabilities in spatially developing boundary layers	145
Paper 6. Global optimal disturbances in the Blasius flow usin time-steppers	g 179

Part 1 Summary

CHAPTER 1

Introduction

You find yourself out walking, your head filled with thoughts about work, family, how to get by in the modern society. Suddenly your left foot steps into a pond. At first you swear, then your eyes catch the motion of the water that already has reacted to your invasion by turning the energy into beautiful waves, searching for equilibrium. You feel a wind gust, autumn is coming so the big weather systems from the Atlantic are building up. It is outdoors, so it is okay to light a cigarette (though perhaps not from a health perspective). Upon exhalation the cigarette smoke enters free air peacefully, suddenly to break down into chaotic patterns. You come home and think that a cup of tea would do good. The teapot never pours a straight beam! Some of the tea ends up on the table. You think for yourself that one of these days you should learn how to control this device.

We are constantly surrounded by flowing fluids. In most cases we are only able to observe their behaviour, while in other cases we interact with them to obtain our objectives. Meteorologists track the motion of the big weather systems and strive for perfection in predicting them. On the other hand engineers have constantly modified the behaviour of the air, by tweaking the design of wings, to produce aeroplanes that gradually become more and more fuel efficient. In all aspects of our interaction with flowing fluids a common feature always observed is the presence of turbulence. Turbulence is the regime known to be the counterpart of the laminar regime; a laminar flow is ordered and predictable, whereas a turbulent flow is swirly and chaotic in its motion.

Understanding how fluid flows develop from being laminar, to becoming turbulent, has been the occupation of transition research for over a century. And still it is not fully understood. As early as in 1883 Osborne Reynolds performed what is considered to be the first transition experiment. He studied the flow inside a glass tube where he by injecting ink at the center line could monitor the flow structures. When varying different quantities such as the velocity of the fluid U, the pipe radius r and the viscosity ν he could observe totally different regimes. A non-dimensional number $Re = \frac{Ur}{\nu}$, known as the Reynolds number, was found to govern the transition from laminar to turbulent flow. This number can physically be understood to describe the ratio of inertial

4 1. INTRODUCTION

forces to viscous forces. If the Reynolds number is high, implying that inertia is dominating, transition occurs more rapidly.

The importance of obtaining knowledge and finally of fully understanding the transition process is substantial both from an industrial and an environmental point of view. Examples of the importance of this includes the resistance (or drag) on aeroplanes, cars, trains and boats that are propagating through a fluid. Around such objects a boundary layer forms, where following a frame of reference fixed to the vehicle, the fluid accelerates from zero velocity at the surface to the velocity of the object some distance outwards from the surface. When the velocity and/or the boundary layer thickness increase, or in other words the Reynolds number increases, the boundary layer turns turbulent. It is well known that turbulent boundary layers exert more drag on the surface than a laminar one. It is hence desirable to manipulate the flow in such a way that the transition to turbulence is delayed, thereby reducing the drag. On the other hand turbulence increases the mixing properties of the flow, and this has implications when it comes to for instance combustion processes. These processes rely on efficient mixing of the injected fluids (fuel and air) to maintain a high reaction rate.

The transition process may be divided into three stages; receptivity where disturbances enter the flow; disturbance growth where specific structures that are unstable extract energy from the laminar unperturbed flow. If these structures become sufficiently energetic the third stage, known as the breakdown stage, is entered. At this point many structures interact and redistribute energy to smaller and smaller scales until the flow is finally fully turbulent. A visualisation of the disturbance growth and breakdown phase in the flat plate boundary layer flow is shown in figure 1.1. The picture is based on a so called large-eddy simulation in Schlatter et al. (2006).

This thesis deals with obtaining better knowledge on the second part of this process, thereby placing it into the field of hydrodynamic stability. It also deals with flow control, where the aim is to use the knowledge obtained from the stability analysis in order to suppress disturbances from growing, hopefully delaying transition to turbulence.

Hydrodynamic stability is in principle very simple. One takes a laminar reference base flow. This might be the laminar flow around any object. Then one perturbs the flow in any way one can think of and observes the resulting evolution. In order to find some universal truth in the process however, one has to make sure that one understands what is observed and how the flow has been perturbed. Throughout the years experimental and theoretical studies have been tightly connected. Often instability structures are first observed experimentally, where the evolution of the flow is observed in real time. However in the experimental setting the main challenges are how to extract the relevant

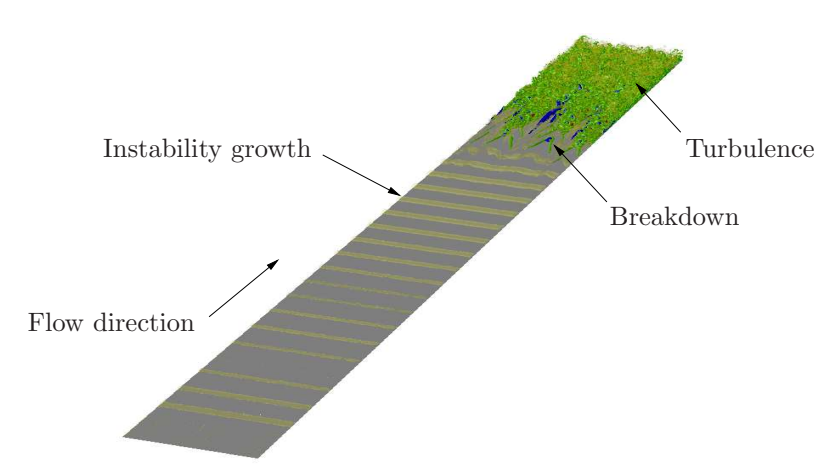


FIGURE 1.1. Transition along a flat plate boundary layer, visualised by the so called λ_2 criterion for vortex identification. The flow is forced at an upstream location by waves at a certain frequency. As the Reynolds number increases downstream due to the thickening of the boundary layer, the flow disturbances extract energy from the basic flow due to linear mechanisms. As their amplitude becomes sufficiently large a phase of nonlinear breakdown renders the flow fully turbulent. (Picture is obtained through private communication with Philipp Schlatter, based on a large-eddy simulation in Schlatter et al. (2006)).

information and how to to obtain a sufficiently clean environment. In theoretical studies one has attempted to single out the important mechanisms of the observed instabilities by studying simplified configurations by mathematical models. These mathematical models have typically been idealised versions of the so called Navier–Stokes equations. In recent years, due to increased computational capacity, numerical solutions to these equations in their full form have become feasible, thereby more closely relating theoretical studies to experimental.

While the subject of hydrodynamic stability is to understand the disturbance growth mechanisms, *i.e.* providing a model of the flow, flow control aims at using this knowledge to correctly interact with it. The objective of the interaction might be to delay transition to turbulence along an aeroplane wing or it might be to promote turbulence in combustion processes. Control of fluid flows can essentially be performed in two ways; either passively or actively. The optimised shape of an aeroplane wing, the rough surface of the golf ball or the evolutionary design of the skin of fish are all examples of passive control. By

6 1. INTRODUCTION

controlling flows in this manner no energy is put into the system, there is only a cooperation with the flow. Using active control on the other hand, energy is put into the system through actuators, hopefully saving more energy than what is spent. Active control can be split into two main categories, namely open-loop and closed-loop control. The former assumes exact knowledge of the system so that the interaction with it is prescribed a priory. However if disturbances that are not accounted for in the model are present, the controller will in general fail. The latter, which is commonly called feedback control, uses information from the system in order to detect the real disturbances present, making it more robust to deviations from the assumed model. Systematic strategies for feedback control rely on solving optimization problems using the equations describing the flow evolution. Hence we are again faced with the problem of the complexity of the equations, and recent advances are also due to the increase in computer power.

CHAPTER 2

Governing equations

The aim of this chapter is to introduce the equations used to describe the behaviour of the flow. First the Navier–Stokes equations for incompressible flows are introduced. The linearization step in order to study the evolution of small disturbances necessary to both stability analysis and control design is given in Section 2.2. Finally a discussion on a more compact way of writing the equations, namely in state space form, is given in Section 2.3.

2.1. The incompressible Navier–Stokes equations

The equations describing the conservation of mass and momentum for Newtonian fluids are well established and have been around for more than 150 years. They were the end result of the work of many of the great mathematicians such as Isaac Newton, Daniel Bernoulli, Leonard Euler and others. The final building bricks were however laid independently by Henry Navier and Sir Gabriel Stokes, hence yielding the name of the Navier–Stokes equations, which for incompressible flows can be written as

$$\partial_t \mathbf{u} + \mathbf{u} \cdot \nabla \mathbf{u} = -\nabla p + Re^{-1} \Delta \mathbf{u},$$
 (2.1)

$$\nabla \cdot \mathbf{u} = 0. \tag{2.2}$$

Here $\mathbf{u}=(u,v,w)^T$ are the velocity components in the three spatial directions $\mathbf{x}=(x,y,z)^T$ and p is the pressure. The term ∂_t denotes the partial time derivative, $\nabla=(\partial_x,\partial_y,\partial_z)^T$ the gradient operator and $\Delta=\nabla\cdot\nabla=\partial_{xx}+\partial_{yy}+\partial_{zz}$ the Laplacian. These equations are on non-dimensional form, where the velocities have been scaled with a characteristic scale U and the spatial differentiation operators with a characteristic length scale L. Typical velocity scales are for instance bulk velocity of a pipe flow or the freestream velocity of a boundary layer. Relevant length scales may for instance be the pipe diameter or the boundary layer thickness. As already mentioned the non-dimensional Reynolds number $Re=\frac{UL}{\nu}$ is a measure of the ratio of inertial forces to viscous forces, with ν being the kinematic viscosity. The above equations constitute a set of nonlinear partial differential equations to be solved in a computational spatial domain Ω from time t=0 to t=T with a set of consistent boundary (spatial edge of computational domain) and initial (starting time) conditions.

Typical boundary conditions are the requirement of zero velocity at walls (noslip condition), sufficiently fast decay of velocity components at infinity or periodic behaviour. In the same manner appropriate initial conditions consist of prescribed velocity components at time t=0. The varying initial and boundary conditions determine the specific behaviour of (2.1)-(2.2) for a given set up. The left hand side of the momentum equation (2.1) describes the inertia of the flow and is composed of a rate of change in time term $\partial_t \mathbf{u}$ and a convection term $\mathbf{u} \cdot \nabla \mathbf{u}$ that describes how a particle momentum is changed due to transport with the flow. The right hand side of (2.1) contains the forces that balance the inertia and consist of the pressure forces ∇p and the viscous forces $Re^{-1}\Delta \mathbf{u}$. Incompressibility is described by (2.2).

Over the years several aspects of understanding fluid flows have been addressed through solutions of the Navier–Stokes equations. However, given the complexity of the equations such as their ability to describe both laminar and turbulent flows, it is still an ongoing field of research to solve them numerically for relevant applications.

2.2. The linearized Navier–Stokes equations

The Navier–Stokes equations are as stated previously non-linear and complex in nature. Important aspects of understanding the transition process can however be captured by studying solutions to the linearized version of the equations. This can be seen by inspection of the Reynolds–Orr equations for the instantaneous energy growth of the disturbances, where non-linear terms are only redistributing energy among different length scales (Schmid & Henningson 2001). Assume that a base flow $\mathbf{U} = (U, V, W)^T$ and P is available. This base flow might in principle be time dependent, but here we focus on the steady state $(\partial_t \mathbf{U} = 0)$ solution to (2.1) and (2.2). We perturb the base flow with small disturbances

$$\mathbf{u} = \mathbf{U} + \epsilon \mathbf{u}', \quad \text{and} \quad p = P + \epsilon p', \quad \epsilon << 1.$$
 (2.3)

By inserting this in the Navier–Stokes equations (2.1) and (2.2) and keeping the terms that are $\mathcal{O}(\epsilon)$ one arrives after dropping the primes at the linearized Navier–Stokes equations

$$\partial_t \mathbf{u} + \mathbf{U} \cdot \nabla \mathbf{u} + \mathbf{u} \cdot \nabla \mathbf{U} = -\nabla p + Re^{-1} \Delta \mathbf{u},$$
 (2.4)

$$\nabla \cdot \mathbf{u} = 0. \tag{2.5}$$

These equations are equipped with suitable boundary conditions and initial condition $\mathbf{u}(\mathbf{x},t=0)=\mathbf{u}_0(\mathbf{x})$. The term ϵ measures how small the perturbations are and hence if the linearization is valid. If the magnitude of the terms $\epsilon \mathbf{u}$ reach an amplitude of a few percent of the base flow magnitude, non-linear terms become important and the linearization around this specific base flow is no longer valid.

2.3. State space formulation

When performing systematic analysis of the linearized Navier–Stokes equations one is interested in the initial condition $\mathbf{u}(0)$ and what type of flow states $\mathbf{u}(t)$ are reached at times t>0. By flow state we mean the entire velocity field throughout the computational domain Ω at time t. It is preferable to put the equations in a more compact form. In order to do so we define the velocities as our state variable, *i.e.* $\mathbf{u} = (u, v, w)^T$. Many of the standard tools from linear systems theory can readily be applied to the so called state space equation

$$\partial_t \mathbf{u} = \mathcal{A}\mathbf{u}, \quad \mathbf{u}(0) = \mathbf{u}_0.$$
 (2.6)

In particular the above system has a formal solution in terms of the evolution operator

$$\mathbf{u}(t) = \mathcal{T}(t)\mathbf{u}_0 = \exp(\mathcal{A}t)\mathbf{u}_0. \tag{2.7}$$

In order to cast the linearized Navier–Stokes equations (2.4) and (2.5) in the form of (2.6) the pressure p has to be removed from the equations. To achieve this, an important observation can be made from equations (2.4) and (2.5); for incompressible flows the pressure only acts as a Lagrange multiplier to maintain divergence free velocity fields. We follow the notation of Kreiss $et\ al.\ (1994)$ and let the linearized Navier–Stokes equations be written as

$$\partial_t \mathbf{u} = A\mathbf{u} = -(\mathbf{U} \cdot \nabla)\mathbf{u} - (\nabla \mathbf{U})\mathbf{u} + Re^{-1}\Delta\mathbf{u} + \nabla p, \tag{2.8}$$

where the pressure is a known function of the divergence free velocity field ${\bf u}$ and the base flow ${\bf U}$

$$\Delta p = \nabla \cdot (-(\mathbf{U} \cdot \nabla)\mathbf{u} - (\nabla \mathbf{U})\mathbf{u}). \tag{2.9}$$

Inversion of the Laplacian requires boundary conditions, and formally we may obtain these by projecting (2.8) on the outwards pointing normal of the domain ${\bf n}$ to obtain

$$\frac{\partial p}{\partial \mathbf{n}} = \mathbf{n} \cdot \left(-\partial_t \mathbf{u} - (\mathbf{U} \cdot \nabla) \mathbf{u} - (\nabla \mathbf{U}) \mathbf{u} + Re^{-1} \Delta \mathbf{u} \right). \tag{2.10}$$

At solid walls it expected that all the velocity components are zero. This so called no-slip condition reduces the above relation to

$$\frac{\partial p}{\partial \mathbf{n}} = \mathbf{n} \cdot \left(Re^{-1} \Delta \mathbf{u} \right). \tag{2.11}$$

If we let the solution of (2.10) be denoted as $p = \mathcal{K}\mathbf{u}$ we end up with the state space system with \mathcal{A} given by

$$A = -(\mathbf{U} \cdot \nabla) - (\nabla \mathbf{U}) + Re^{-1}\Delta + \nabla \mathcal{K}. \tag{2.12}$$

The operator \mathcal{A} may also be defined using semi-group theory, where it is referred to as an infinitesimal generator defined through the evolution operator $\mathcal{T}(t)$. For an explanation of this way of defining \mathcal{A} see e.g. Bagheri *et al.* (2008) or Trefethen & Embree (2005).

10 2. GOVERNING EQUATIONS

Note that it is possible to define the state variable to include both velocities and pressure, but this leads to a generalized state space or descriptor system form, where the left hand side is singular, rendering the system more difficult to analyze. In Paper 1 and Paper 3 we have used the descriptor system form, whereas in Paper 2, Paper 4 and Paper 6 the standard state space form (2.8)-(2.10) is used. Throughout the rest of this introduction we will use the latter form for simplicity. It is important to note though that regardless of the form chosen the evolution operator $\mathcal{T}(t)$ defines the same solution $\mathbf{u}(t)$ at time t given the same initial condition \mathbf{u}_0 at time t = 0.

CHAPTER 3

Numerical Simulations

In order to perform stability analysis and control design of the flows studied in this thesis we need to access solutions of the Navier–Stokes equations. The time evolution of the velocities for both the non-linear and linear Navier–Stokes equations is obtained through numerical simulations. When numerically solving partial differential equations a discretization of the variables is performed in both time and space. The continuous spatial domain Ω is divided into discrete grid points upon which the variables of interest, *i.e.* the velocities $(u, v, w)^T$ and the pressure p, are required to approximately satisfy the governing equations. Likewise the continuous time domain $t \in [0, T]$ is divided into discrete instances of time.

3.1. Spectral methods

Methods for solving partial differential equations are mainly distinguished by the way the continuous functions and their derivatives are discretized (or approximated). We focus here on the spatial approximation. On one hand there are local methods, such as the finite difference, finite volume and finite element methods, where the main idea is to use near neighbour information in order to approximate the functions and their derivatives. For instance in the finite-difference method continuous functions are interpolated on the grid by means of a sequence of overlapping local low order polynomials. Consider a one-dimensional function f(x) depending only on x. The derivative of the local interpolant is used to approximate the derivative of f(x). A standard quadratic interpolation gives a centered finite difference approximation $f_x(x_i) = (f(x_i + h) - f(x_i - h))/(2h) + \mathcal{O}(h^2)$, with h being the grid spacing and $\mathcal{O}(h^2)$ stating that the error goes as h^2 . There is in other words a quadratic convergence upon grid refinement. In contrast global methods (or spectral methods) approximate f(x) by global functions $\phi(x)$ living in the entire domain. Typical functions are the sines and cosines leading to the Fourier method or transformed cosines leading to the Chebyshev method. With these global approximations the derivatives at each grid point depend on all the other grid points, i.e. $f_x(x_i) = \sum_{j=1}^{N_x} f(x_j) \partial_x \phi_j(x_i) + \mathcal{O}(h^{1/h})$, with exponential convergence upon grid refinement. The convergence properties of the global methods are hence far superior to local methods, but are not easily applied to complex geometries. However the essence is that with the superior convergence property fewer grid points are needed to approximate the continuous problem with a sufficient accuracy. The result is a lower computational cost. It should be noted that is possible to gain the best of both worlds by combining spectral and finite element methods to obtain the Spectral Element Method (c.f. Deville et al. 2002). For an in depth explanation of the convergence properties of local and global methods see for instance Boyd (2000) and for the application of spectral methods in fluid dynamics see either Canuto et al. (1993) or Peyret (2002).

3.2. DNS, RANS and LES

The term Direct Numerical Simulation (DNS) reflects the manner in which a certain class of numerical methods solve the Navier-Stokes equations. In this framework no approximations as to the behaviour of the turbulence are made. Instead one solves the equations for a domain Ω large enough to capture the large scales of the physical problem and sufficiently small grid point distance to capture the smallest scale of the turbulence. The discretized solution has to resolve scales that are only slightly larger than the Kolmogorov scale, i.e. the length scale at which the majority of the energy is dissipated by viscosity (for a review of the DNS method see e.g. Moin & Mahesh 1998). It is with the computer power available today however only possible to perform full DNS for idealised situations and small domains. Understanding the flow of general configurations such as the flow around a car, train or aeroplane is still out of reach for DNS. For these applications the method to obtain knowledge about mean quantities of the flow is through solving the so called Reynolds Averaged Navier-Stokes equations (RANS) (see e.g. Wilcox 1998). In the RANS approach, the mean flow field is solved for whereas the effect of the turbulence is modelled by the mean flow gradients. In between these two outer boundaries, a new approach has started to gain popularity. In the Large Eddy Simulation (LES) approach the large fluctuating scales are solved for but the small scales are modelled through a sub-grid stress model (SGS) (Sagaut 2002).

3.3. How to handle the pressure

For all of the above approaches an important subject is how the pressure p is handled. By inspection of (2.1)-(2.2) or (2.4)-(2.5) it becomes apparent that the pressure does not have a separate time evolution equation. As stated in Section 2.3; an interpretation of this is that in the incompressible Navier–Stokes equations (both linear and non-linear) the pressure acts only as a Lagrange multiplier completely determined by the velocities, its role being to enforce divergence-free velocity fields $\nabla \cdot \mathbf{u} = 0$. One standard way of handling this is to perform a Fractional Step procedure (c.f. Kim & Moin 1985). In this procedure intermediate velocities are updated with the pressure forces omitted, in general not satisfying continuity. A projector, in the form of a Poisson

type of equation, is introduced to update the corrected divergence free velocities. Another possibility is to take the divergence of the momentum equation (2.1) to explicitly obtain the pressure Poisson equation. A complication with both methods is related to the choice of boundary conditions for the pressure (Rempfer 2006). A solution to this is provided by the Influence Matrix Technique of Kleiser & Schumann (1980). The pressure can however be removed from the equations altogether by taking the curl of the momentum equations, i.e. $\nabla \times$ (2.1) and explicitly enforce divergence free solutions. This leads to the vorticity formulation of the equations. However, also in this approach there are some subtleties involved in defining proper boundary conditions.

Two DNS codes have been used in this thesis to solve both the non-linear and linear Navier–Stokes equations. For the relatively simple flat plate boundary-layer flows a highly accurate spectral DNS code was used. The drawback of this spectral code is that it only handles simple geometries. Hence to do more complex geometries a combined finite difference–Chebyshev code was applied.

3.4. A spectral DNS code

The Navier-Stokes equations are recast in wall-normal velocity-vorticity form, thereby eliminating the pressure. In the streamwise x and spanwise z-direction a Fourier transform is performed, whereas in the wall normal direction a Chebyshev-tau technique is used. The method is hence spectral (or global) in all three space directions. The time integration is carried out by a low storage four step third order explicit Runge-Kutta scheme for the explicit terms arising from the non-linear part of the equations, combined with a semi-implicit Crank-Nicholson scheme for the terms stemming from the linear part of the equations. By applying a pure spectral scheme the explicit nonlinear part arising from the terms $\mathbf{u} \cdot \nabla \mathbf{u}$ gives rise to convolution terms which are typically too heavy from a computational perspective. In order to remedy this the non-linear terms are computed instead by multiplication in physical space. The efficiency on the procedure then relies heavily on the performance of the Fourier transform needed to go back and forth between physical and spectral space. Fortunately Fast Fourier Transforms (FFT) are now standard library operations that have become very efficient. Once the non-linear terms are obtained the implicit linear terms in the equations are solved efficiently in spectral space.

The Fourier transform is only valid for periodic domains. However in order to apply the method to non-periodic domains a fringe region technique is applied. This amounts to applying a forcing term on the Navier–Stokes equations in a region close to the outflow to map the equations back to its inflow form. A full description of the code can be found in Chevalier *et al.* (2007).

3.5. A mixed finite-difference Chebyshev DNS code

In order to handle more complex geometries we use a mixed finite difference— Chebyshev collocation discretization. The Navier–Stokes equations are solved in primitive variables $\mathbf{u} = (u, v)^T$ and p on a two-dimensional domain $\Omega =$ $(0, L_x) \times (\eta(x), L_y)$, with $\eta(x)$ being a smooth function describing the lower wall curvature. Instead of meshing the curved geometry a variable transformation of the wall normal variable $\bar{y} = y - \eta(x)$ is performed, thereby redefining the differentiation operators ∇ and Δ . The full details of this transformation is given in Marquillie & Ehrenstein (2001). Once transformed the resulting equations are solved on a rectangular domain with extra stiffness terms arising due to the variable transformation. For space discretization fourth-order central finite differences are used for the second derivatives in the streamwise x-direction, whereas the first derivatives in the same direction are handled with eighth-order finite differences. In the wall normal direction a Chebyshev collocation technique is applied. The time integration is carried out by an implicit second-order backward Euler scheme for the Laplacian $\Delta \mathbf{u}$ part of the equations whereas the nonlinear convective terms $\mathbf{u} \cdot \nabla \mathbf{u}$ and the stiffness terms due to the wall curvature are handled by an explicit second-order Adams Bashforth scheme. This is the well known BDF-2 scheme. In order to ensure divergence—free velocity fields a Fractional Step technique is employed.

3.6. Discretized state space formulation

For practical numerical calculations the equations (2.4)-(2.5) are discretized in space on $n_x \times n_y \times n_z$ grid points, and as a consequence we write the collection of discretized velocities as the *n*-dimensional vector u with n being $n = 3n_x \times n_y \times n_z$. In this formulation it is assumed that the operator \mathcal{A} is explicitly built by differentiation matrices to form the matrix \mathcal{A} so that

$$\partial_t u = Au, \quad A \in \mathbb{R}^{n \times n},$$
 (3.13)

with the initial condition u_0 . For details on how to obtain discrete differentiation matrices from differentiation operators it is referred to Weideman & Reddy (2000). Whenever a solution at time t is needed the discretized form of (2.7) is used, which simply represents marching a DNS forward in time with a sufficiently high accuracy in both time and space. This is written as

$$u(t) = \exp(At)u_0. \tag{3.14}$$

In this thesis the continuous form of the equations will be used for most parts, but it should be noted that when performing numerical simulations of the system it is in a discrete setting.

CHAPTER 4

Computation of eigenvalues

In the remaining part of this thesis we will need the concept of eigenvalues, which classically in hydrodynamic stability analysis are used as a tool to understand the asymptotic behaviour of the linearized Navier–Stokes equations (3.13). Later we will also see that eigenvalues are of interest for solving optimization problems. The discretized linearized Navier–Stokes equations can be cast to a standard eigenvalue problem by assuming exponential time dependence of the solutions, i.e. $u = \hat{u} \exp(\lambda t)$. Inserting this in the linearized Navier–Stokes equations we arrive at

$$A\hat{u} = \lambda \hat{u}, \quad A \in \mathbb{R}^{n \times n}, \quad \lambda \in \mathbb{C}, \quad \hat{u} \in \mathbb{C}^n$$
 (4.15)

where \mathbb{C} denotes a complex number, \mathbb{C}^n a n-dimensional complex vector and $\mathbb{R}^{n\times n}$ a real valued matrix of size $n\times n$. We say that the pair (λ_j,\hat{u}_j) is a right eigenpair of A. Similarly we may formulate a left (or adjoint) eigenvalue problem by $\hat{u}_l^H A = \hat{u}_l^H \lambda$, where the pair (λ_j^H,\hat{u}_l) is a left eigenpair of A. The superscript H denotes the complex conjugate transpose operation that reduces to the ordinary transpose T for real vectors and matrices. An important observation can be done from the expression (4.15). Given an eigenpair (λ_j,\hat{u}_j) , the action of A on \hat{u}_j only scales the vector with a factor λ_j , hence the evolution of \hat{u}_j is independent of all other eigenpairs. Further, if the real part of λ_j is positive, then the solution \hat{u}_j grows exponentially, and the system is said to be linearly unstable.

Although we here for simplicity focus on the solution of the standard eigenvalue problem (4.15) stemming from the state space form (2.8), a formulation of the so called generalized eigenvalue problem stemming from the discretized generalized state space form briefly discussed in Section 2.3 is readily obtained. For details it is referred to Henningson & Åkervik (2008) where that eigenvalue problem is solved using the shift and invert strategy.

The eigenvalues of A are the n roots of the characteristic polynomial $p_A(\lambda) = \det(A - \lambda I)$. However it is known that no direct solution can be found for a polynomial of degree more than four. This essentially means that all eigenvalue solvers are iterative. The first eigenvalue solver around was the so called power iteration scheme, where starting from a first guess v^0 the action

of the matrix A is applied repeatedly

$$v^0, Av^0, A^2v^0, \dots, A^mv^0 \tag{4.16}$$

until convergence towards the eigenvector $\hat{u}_1 = A^m v^0$ with the largest magnitude eigenvalue λ_1 is obtained. The convergence of this method is λ_1/λ_2 , where λ_2 is the second largest in magnitude eigenvalue. Faster convergence to any single eigenvalue close to the complex value μ can be achieved by the inverse iteration scheme $A^{-1}\hat{u} = 1/(\lambda_1 - \mu)\hat{u}$, but a main difficulty is how to choose the shift μ . A drawback of both these methods is that they are able to compute only one eigenpair at the time.

4.1. The QR method

The quest for a method that could compute all the eigenvalues of A and do it fast lead to the implicitly shifted QR method (Francis 1961). A crucial step in the design of the QR method was the understanding gained from the Schur decomposition which states that for a unitary matrix (spans an orthonormal basis) Q, there exist an upper triangular matrix U such that

$$AQ = QU, \quad Q, U \in \mathbb{R}^{n \times n}$$
 (4.17)

where the diagonal of U contains the eigenvalues of A. The aim of the QR method is to compute a unitary basis for A such that (4.17) is fulfilled. To this end the first step is to bring A to upper Hessenberg form

$$AV = VH, \quad V, H \in \mathbb{R}^{n \times n}$$
 (4.18)

The matrix H is upper Hessenberg (almost upper triangular except for a subdiagonal) and V is unitary. This step is achieved either by Householder reduction or by the numerically less stable modified Gram–Schmidt (MGS) procedure. After the Hessenberg form is obtained an iteration scheme using a QR decomposition on the shifted H_i at step i is carried out as follows:

$$H_{i-1} - \mu_{i-1}I = QR \tag{4.19}$$

where Q is unitary and R is upper triangular. Then H_i and V_i are updated according to

$$H_i = Q^H H_{i-1} Q$$
, and $V_i = V_{i-1} Q$. (4.20)

As the iteration scheme proceeds different elements on the subdiagonal of H_i converge to zero at different rates and after a sufficient number of iterations H_i is upper triangular, thereby defining a Schur decomposition of A. Hence all the eigenvalues of A can be picked from the diagonal of H_i .

4.2. The Arnoldi method

Unfortunately the cost of the QR method is too high to be applied to many problems such as those arising from the discretization of the Navier–Stokes

equations in more than one spatial dimension. The power iteration and inverse iteration schemes are still possible to use, but they only produce single eigenpairs. Nowadays the standard approach to deal with large problems is through Krylov subspace projections together with the Arnoldi factorisation (or Lanczos factorisation for Hermitian problems $A = A^H$). A Krylov subspace of size m is defined as follows

$$\mathcal{K}^m = \{ \mathbf{v}_0, A\mathbf{v}_0, A^2\mathbf{v}_0, \dots, A^{m-1}\mathbf{v}_0 \}. \tag{4.21}$$

Note the similarity to the power method. The main difference is that while the the power method throws away all but the last term, the Krylov subspace contains all the generated information from the power sequence. While the aim of the QR method is to compute all eigenpairs of A the Arnoldi method aims at computing only a fraction of the eigenpairs. To this end the idea of the Arnoldi method is to build a reduced Hessenberg matrix of size $m \times m$, with m << n. In other words the first step in the Arnoldi method is to build

$$AW = WH + f_{m+1}e_m^T, \quad W \in \mathbb{R}^{n \times m}, H \in \mathbb{R}^{m \times m}, \tag{4.22}$$

where $W = \operatorname{col}\{w_1, w_2, \dots, w_m\}$ are the unitary Arnoldi vectors, f_{m+1} is an error term orthogonal to W and e_m is the unit vector in the direction m. This term measures to which extent the Krylov subspace fails to represent the action of A. The need for a reduced size Hessenberg form rules out using Householder reduction, so we are left with the modified Gram-Schmidt (MGS) procedure. The MGS procedure can be stated as follows: Starting with a random initial vector w_0 a Krylov sequence is built. At the j-th step a new vector is added by means of the matrix vector product

$$w_j = Aw_{j-1}. (4.23)$$

The entries of the upper Hessenberg matrix H is created from the inner products between the present vector w_j and the previously added ones. The elements at the j-th step are

$$H_{i,j} = \mathbf{w}_i^H \mathbf{w}_{j-1}, \qquad i = 1, \dots, j.$$
 (4.24)

A new Arnoldi vector is obtained by projecting w_j on the space orthogonal to all the previous vectors

$$w_{j} = w_{j} - (H_{1,j}w_{0} + \dots + H_{j,j}w_{j-1}). \tag{4.25}$$

The norm of w_j forms the sub-diagonal element of the Hessenberg $H_{j+1,j}$ and w_j is normalized accordingly. The Arnoldi vectors are after m steps $W = \text{col}\{w_0, w_1, \ldots, w_{m-1}\}.$

The Arnoldi method then proceeds by iteratively performing QR decomposition of the small H converging to a few of the eigenpairs of A. The eigenvalues θ_j obtained are called Ritz approximate eigenvalues $\lambda_j \approx \theta_j$ and the eigenvectors y_j obtained are called Ritz eigenvectors, related to the eigenvectors \hat{u}_j of A

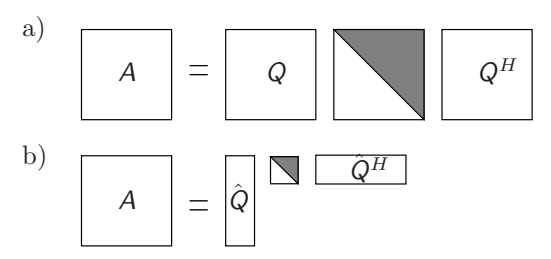


FIGURE 4.1. Figure showing the difference in Schur factorisation of A. a) The QR method. b) The Arnoldi method leading to an approximate Schur factorisation

by $\hat{u}_j = W y_j$ and satisfy the following error criteria due to the orthonormality of the Arnoldi vectors

$$||A\hat{u}_j - \theta_j \hat{u}_j|| = |\beta_m \mathbf{e}_m^T \mathbf{y}_j|, \tag{4.26}$$

with $\beta_m = ||f_m||$. A schematical difference in the way the Schur factorisation to obtain eigenvalues is performed in the QR method and the Arnoldi method is shown in figure 4.2.

There are two main problems with the Arnoldi process: The first is that one does not know beforehand how big m has to be in order to converge to the desired number of eigenvalues, but in general m has to be much larger than the number of desired eigenvalues. A way to keep the Krylov subspace fairly small is to use either explicit or implicit restart of the Arnoldi method. This essentially amounts to producing a Hessenberg of size $m \times m$ and compute the eigenvalues. If there are p unwanted eigenvalues, then the part of the Hessenberg containing the m-p wanted eigenvalues are kept, but the rest is thrown away. Subsequently a new round of a p-step Arnoldi factorisation is performed, and p new eigenvalues, hopefully belonging to the wanted set, are computed. The second problem with the Arnoldi method is that as the Krylov subspace becomes fairly large, the MGS produces Arnoldi vectors that are not orthogonal to machine precision, leading to spurious eigenvalues. In this case it is preferable to explicitly re-orthogonalize the basis. A common way to do this is provided by the DKGS method (Daniel $et\ al.\ 1976$).

For a more thorough description of the Arnoldi method we refer to the user guide of the ARPACK package (Lehoucq et al. 1997). Note that in principle it is simple to implement your own Arnoldi solver, but this package provides an easy to use interface to solving eigenvalue problems using the Arnoldi method, with both implicit restarting and DKGS stabilization.

4.3. Time stepping, a way to avoid building the full matrix

In contrast to the QR method the Arnoldi method does not depend on the explicit manipulation of the matrix A. This can be seen by inspection of the

power sequence defining the Krylov subspace (4.21), where only the repeated action of A on w_0 is needed. This is extremely important for large problems. As an example a matrix stemming from the discretization of the three-dimensional Navier–Stokes with 100 grid points in all directions leads to a system matrix A with a storage requirement of $\mathcal{O}(100TB)$, which is clearly infeasible to keep in RAM on any computer architecture available today. However the storage of each vector only needs $\mathcal{O}(50MB)$. Another observation to be made from the Krylov subspace definition is that it defines an eigenvalue problem for whatever matrix used to generate it. To this end note that snapshots at times $\{T, 2T, \ldots, (m-1)T\}$ from a DNS time integration (see equation (3.14)) yield the Krylov subspace

$$\mathcal{K}^{m} = \{ w_{0}, \exp(AT)w_{0}, \exp(2AT)w_{0}, \dots, \exp((m-1)AT)w_{0} \}, \tag{4.27}$$

which defines an eigenvalue problem

$$\sigma \hat{u} = \exp(AT)\hat{u}. \tag{4.28}$$

Due to the spectral transformation theorem one can conclude that the eigenvectors \hat{u} are also eigenvectors of A and the eigenvalues λ of A can be found from the relation

$$\lambda = \frac{\log(\sigma)}{T}.\tag{4.29}$$

A conclusion that can be drawn from this is that for very large problems it is preferable to use a time stepper technique (Tuckerman & Barkley 2000) in order to compute eigenpairs of the system.

CHAPTER 5

Hydrodynamic stability

In the introductory chapter it was mentioned that stability enters as one of the three components in understanding why a flow undergoes transition from the laminar to the turbulent regime. In this chapter the aim is to introduce the steps necessary to take in order to establish whether a flow is stable or not.

5.1. Flow cases

This thesis deals with a certain class of flows, namely those arising from the flow over a wall. Due to the presence of the wall a boundary layer forms, starting at the leading edge, where the velocity is decelerated from uniform free stream velocity U_{∞} to zero velocity at the surface. The boundary layers are hence viscous in their nature. Another characteristics is that they are very thin compared to their length, i.e. the streamwise length scale L is much larger than the wall normal length scale δ^* , or in other words, the most drastic changes occur when moving outwards from the wall. In this manner one can conclude that the important length scale is $\delta^* = \sqrt{x\nu/U_{\infty}}$, known as the displacement thickness, and hence the Reynolds number should be defined as $Re = \frac{U_{\infty} \delta^*}{\nu}$. To quantify how thin a boundary layer is for real applications one might consider the boundary layer forming on the wings of an aeroplane cruising at 800 km/h. Given a kinematic viscosity of $\nu \approx 1.3 \, 10^{-5} \, \mathrm{m}^2/\mathrm{s}$ one arrives at a displacement thickness of $\delta^* \approx 0.4$ mm one meter from the leading edge, if the flow stays laminar. Ten meters downstream the thickness has developed to no more than $\delta^* \approx 1.3$ mm. The boundary layer is hence both thin and increases very slowly downstream.

Two prototype boundary layer flows are studied here. The first one is the classical flat plate boundary layer, also known as the Blasius boundary layer or zero pressure gradient boundary layer, serving as a simple model of an unswept aeroplane wing (see figure 5.1(a)). The computational inflow boundary is set some distance downstream of the leading edge with corresponding Reynolds number $Re_{\delta_0^*} = U_\infty \delta_0^* / \nu$, with δ_0^* being the local displacement thickness of the boundary layer. The second case studied is the flow over a smooth cavity mounted on a flat plate as seen in figure 5.1(b). The length to depth ratio is $L/D \approx 25$ and the two-dimensional Navier–Stokes equations is solved in a physical domain $0 \le x \le 400$, $\eta(x) \le y \le 80$, where x and y are the streamwise

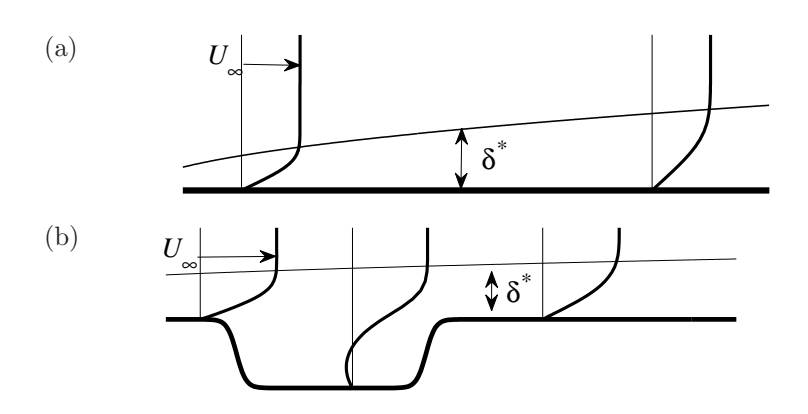


FIGURE 5.1. Sketches of boundary layer flows with inflow from the left. (a) Flat plate boundary layer flow; the flow is slowly evolving with the boundary layer thickness δ increasing downstream. (b) The cavity flow; upstream and downstream of the cavity there is a boundary layer flow, whereas in the cavity there is a separated shear-layer flow.

and wall-normal coordinates. The lower wall is curved and described by the function $\eta(x)$. The smooth cavity is symmetric with respect to its center at $x_c = 89$, and its upstream part is given by

$$\eta(x) = -2.25 \left(\tanh(a(x-b)) + 1 \right), \quad 0 \le x \le x_c,$$
(5.30)

with a=0.2 and b=39 matching smoothly the flat plate upstream and downstream. At inflow the Blasius profile is introduced. The mean flow profile develops downstream as a flat plate boundary layer flow, however at $x\approx 30$ there is a smooth expansion of the geometry generating a shear layer unstable to Kelvin–Helmholtz instability. As the shear-layer develops downstream it encounters a smooth contraction of the geometry at $x\approx 150$ so that the flow again forms a developing boundary layer flow.

Boundary layer flows display the particular feature that the instability characteristics may change throughout the domain. There can be regions where the flow is stable, convectively unstable or absolutely unstable (Huerre & Monkewitz 1990; Chomaz 2005). In a convectively unstable region the disturbances are swept downstream with the flow while growing in size and amplitude. In this case the disturbances disappear in absence of external forcing so that the flow might be seen as a noise amplifier. The flat plate boundary layer flow is a typical example of a convectively unstable configuration. Whenever the base flow satisfies certain conditions, for example if there is a sufficiently large

reverse flow in a separation bubble, the flow may become absolutely unstable, characterized by disturbances growing both upstream and downstream of the origin of generation, so that the flow itself will sustain the instability growth. The cavity flow is an example of such a configuration.

5.2. Strategy

The stability characteristics of a base flow U to small perturbations u is determined by monitoring (measuring) the perturbation evolution as described by the linearized Navier–Stokes equations introduced in Section 2.2. For clarity the equations are repeated here in state space form

$$\partial_t \mathbf{u} = \mathcal{A}\mathbf{u},\tag{5.31}$$

given an initial condition $\mathbf{u}(0) = \mathbf{u}_0$. The operator \mathcal{A} is completely determined by the base flow \mathbf{U} and the boundary conditions. In order to measure the departure from the base flow we introduce the norm based on the kinetic energy of the flow

$$E(t) = \|\mathbf{u}(t)\|^2 = (\mathbf{u}(t), \mathbf{u}(t)) = \int_{\Omega} \mathbf{u} \cdot \mathbf{u} \, d\Omega.$$
 (5.32)

If the perturbation kinetic energy goes to zero as $t \to \infty$, implying that the flow returns to its basic state, the flow is considered stable. Otherwise it is unstable. Even if the kinetic energy vanishes asymptotically there might however exist initial conditions of amplitude $a_0 = \|\mathbf{u}_0\|$ such that the flow at a finite time triggers non-linear effects. Hydrodynamic stability deals with the task of finding critical parameters such as critical Reynolds number, that renders the flow to depart from the base flow either permanently or transiently.

The central element to inquiring asymptotic stability of \mathcal{A} is to compute its eigenvalues. This approach is often called modal instability analysis or normal mode analysis. As described in Chapter 4 we may require that the system (5.31) has a harmonic/exponential time dependence, *i.e.*

$$\mathbf{u} = \hat{\mathbf{u}} \exp(\lambda t), \quad \lambda \in \mathbb{C}.$$
 (5.33)

By putting ansatz (5.33) into (5.31) an eigenvalue problem is obtained

$$\lambda \hat{\mathbf{u}} = \mathcal{A}\hat{\mathbf{u}},\tag{5.34}$$

If λ_j is an eigenvalue of (5.31) with an associated eigenvector $\hat{\mathbf{u}}_j$, then the action of \mathcal{A} on $\hat{\mathbf{u}}_j$ is a rescaling of $\hat{\mathbf{u}}_j$ with the factor λ_j . This implies that the evolution of different eigenpairs $(\lambda_j, \hat{\mathbf{u}}_j)$ is independent of all the others $(\lambda_{k\neq j}, \hat{\mathbf{u}}_{k\neq j})$. Further, if the complex eigenvalue $\lambda_j = \lambda_j^r + i\lambda_j^i$ has a positive real part $\lambda_j^r > 0$ the solution (5.33) will grow exponentially.

Note that in addition to considering the response to initial conditions it is also of interest to examine the response to forcing, where the equations are equipped with a harmonic forcing term $\{\mathbf{f} \exp(i\omega t)\}_{\text{real}}$ such that

$$\partial_t \mathbf{u} = A\mathbf{u} + \{\mathbf{f} \exp(i\omega t)\}_{\text{real}}, \quad \mathbf{u}_0 = 0.$$
 (5.35)

In Paper 1 and Paper 6 we study the response of the flat plate boundary layer flow to harmonic forcing. In this introductory part the subject of response to forcing will be omitted, and it is referred to Schmid & Henningson (2001) or Trefethen & Embree (2005) for details.

5.3. From eigenvalues to optimal growth

It is only recently due to increased computer power that the research community has been able to perform systematic stability studies of the full equations (2.4). A number of flows previously inaccessible to stability analysis are now being investigated. These flows include cavities (Åkervik et al. 2007; Sipp & Lebedev 2007), cylinders (Giannetti & Luchini 2007), jets (Nichols et al. 2007), backward facing steps (Blackburn et al. 2008) and separation bubbles (Gallaire & Ehrenstein 2008; Marquet et al. 2008).

A method to deal with the problem of the high dimensionality of the equations has been to assume that the streamwise x and spanwise z directions are periodic, hence allowing for Fourier decomposition. In this locally parallel assumption the base flow is assumed to vary slowly in x and z directions such that the perturbation variables can be written as the real part of

$$\mathbf{u} = \hat{\mathbf{u}}(y,t) \exp(i(\alpha x + \beta z)), \quad p = \hat{p}(y,t) \exp(i(\alpha x + \beta z)), \tag{5.36}$$

for the streamwise wavenumber α and spanwise wavenumber β . Insertion into (5.31) yields the famous Orr-Sommerfeld-Squire equations (Orr 1907; Sommerfeld 1908; Squire 1933). From a practical point of view what is gained by the Fourier transformation of system (5.31) is that instead of treating the problem as one large problem, the equations for different wave numbers α and β are decoupled. In practice this means that the stability characteristics of a given parallel mean flow $\mathbf{U}=(U(y),0,0)^T$ can be determined by looping over all the relevant wave numbers. It is important to note that for some flows like for instance pressure driven Poiseuille channel flow or the shear driven Couette flow the Orr–Sommerfeld/Squire equations provide a fully valid set of equations. For spatially inhomogeneous flows like the boundary layers studied in this thesis the Orr–Sommerfeld/Squire equations provide only an approximation that can be justified based on dimensional arguments.

Preceding the Orr–Sommerfeld framework by almost thirty years, Rayleigh formulated the necessary condition for inviscid modal instability. He found that the base flow needed to have an inflectional profile in order for unstable eigenvalues to appear. For the Orr–Sommerfeld equation a viscous instability mechanism in the form of Tollmien–Schlichting (TS) waves was found as eigensolutions of the governing equations by Tollmien (1929); Schlichting (1933). The existence of such solutions was experimentally shown to exist by Schubauer & Skramstad (1947). In experiments however the TS waves were seen as waves propagating downstream while spatially growing. This apparent discrepancy

was addressed and removed by Gaster (1965) who showed that it was possible to connect the two perspectives through the so called Gaster transformation.

Although successful to explain the exponentially growing features of many flow systems, the combination of the Orr–Sommerfeld/Squire equations and the eigenvalue decomposition had its drawbacks. An apparent flaw was that linear stability theory predicted both pipe and Couette flow to be linearly stable for all Reynolds numbers, whereas in experiments and DNS both of these flows turned turbulent. Also in the boundary layer flow discrepancies between linear stability theory and experiments where discovered. The determination of the critical Reynolds number for the Tollmien–Schlichting instability, i.e. the neutral curve, could not be accurately captured using the Orr–Sommerfeld/Squire equations. An extension of the locally parallel theory was provided by the Parabolized Stability Equations (Bertolotti et al. 1992), where the slow streamwise variation of the base flow is incorporated in better agreement with experiments and DNS.

In addition experiments revealed that it was possible to also for boundary layer flows obtain transition well below the critical Reynolds number predicted by linear stability theory, thereby sharing features with the pipe and Couette flow. A first convincing mathematical description of the possibility for such a situation to occur in the linear inviscid framework was given by Ellingsen & Palm (1975) who introduced the concept of algebraic growth. A physical explanation to this process was given by Landahl (1980), who explained the algebraic growth to be governed by a so called "lift-up" mechanism, where a wall normal displacement of a fluid particle in a shear layer will lead to a perturbation in the streamwise velocity perturbation. A mathematical framework able to predict the lift-up mechanism was presented in Butler & Farrell (1992); Reddy & Henningson (1993); Trefethen et al. (1993), showing that the Orr-Sommerfeld/Squire equations supported transient growth, related to the non-normal nature of the underlying operators. This modern approach to stability has converged to the formulation of the stability problem as an optimization problem, which may be solved either by singular value decomposition of the evolution operator $\exp(At)$, or by time-marching methods involving the adjoint system (Schmid 2007).

5.4. Worst case disturbances

In the quest for stability of (5.31) we saw that the asymptotic limit as given by eigenvalues λ with real part greater than zero did not provide the full answer to understanding why flows are unstable. In this section a framework for computing the worst possible disturbances is given. By worst possible disturbances we mean the disturbances that gives the largest growth at any time t > 0. The central element in determining these disturbances is to systematically utilise the kinetic energy measure E, with the associated norm $\|\mathbf{u}\|$. Using the above measure a natural definition of worst possible initial disturbance becomes: Find

an initial condition \mathbf{u}_0 of energy one such that the energy $\|\mathbf{u}\|^2 = (\mathbf{u}(t), \mathbf{u}(t))$ at time t is as large as possible. Mathematically this can be written

$$G(t) = \max_{\mathbf{u}_0 \neq 0} \frac{\|\mathbf{u}(t)\|^2}{\|\mathbf{u}_0\|^2} = \max_{\mathbf{u}_0 \neq 0} \frac{\|\exp(\mathcal{A}t)\mathbf{u}_0\|^2}{\|\mathbf{u}_0\|^2} = \|\exp(\mathcal{A}t)\|^2.$$
 (5.37)

In order to calculate the optimal growth we are faced with the problem of evaluating the matrix norm of $\exp(\mathcal{A}t)$. Computationally this amounts to performing a Singular Value Decomposition (SVD). There are however some problems with this definition from a computational point of view. Firstly; the evaluation of the exponential matrix for a large dense matrix is ill conditioned (Molder & Van Loan 2003). Secondly; performing SVD of large matrices is computationally very heavy. There are however ways to deal with this and below two such approaches are given.

5.4.1. Projecting on the basis of eigenmodes

The eigenmodes of (5.31) constitutes a divergence free basis onto which the system may be projected. By assuming that a small number of eigenmodes are able to describe the relevant dynamics of the flow we write

$$\mathbf{u} = \sum_{l=1}^{m} \kappa_l(t) \hat{\mathbf{u}}_l. \tag{5.38}$$

Inserting this assumption into (5.31) we see that the flow dynamics is described by

$$\frac{\mathrm{d}k}{\mathrm{d}t} = \Lambda k, \quad k(0) = k_0, \tag{5.39}$$

where $k = [\kappa_1, \kappa_2, \dots, \kappa_N]$ is the vector of expansion coefficients and Λ is a diagonal matrix whose elements are given by $\Lambda_{ll} = \lambda_l$. The flow perturbation energy in this basis is $\|\mathbf{u}\|^2 = \|F \exp(\Lambda t) k_0\|^2$, where F is the Cholesky factor of the Hermitian energy measure matrix M with entries $M_{ij} = \int \hat{\mathbf{u}}_i^H \hat{\mathbf{u}}_j d\Omega$. Hence, the maximum growth expressed in the basis of eigenmodes reads

$$G(t) = \|F \exp(\Lambda t)F^{-1}\|^2.$$
 (5.40)

The largest growth at time t is given by the largest singular value of $F \exp(\Lambda t)F^{-1}$ and the optimal initial condition is $k_0 = F^{-1}z$, where z is the right singular vector.

With this formulation of the problem the evaluation of the matrix exponential is simple because Λ is diagonal. Also the computation of the SVD of this matrix is computationally cheap if the number of modes m is small. From (5.40) it can also be seen that the asymptotic growth of unstable eigenmodes is captured, implying that one can view the optimal growth framework as a more complete way of studying stability.

5.4.2. Using the adjoint evolution operator

It is possible to avoid building the matrices involved in (5.37) altogether. The central element in doing so is to make use of the adjoint evolution operator $\mathcal{T}^{\dagger}(t) = \exp(\mathcal{A}^{\dagger}t)$ which given two test vectors \mathbf{p} and \mathbf{q} satisfies

$$(\mathbf{p}, \mathcal{T}\mathbf{q}) = (\mathcal{T}^{\dagger}\mathbf{p}, \mathbf{q}). \tag{5.41}$$

The choice of inner product inner product dictates the form of \mathcal{T}^{\dagger} . In defining the adjoint evolution operator the inner product in the time space domain $\Sigma = [0,T] \times \Omega$

$$(\mathbf{u}, \mathbf{u})_{\Sigma} = \int_{0}^{T} (\mathbf{u}, \mathbf{u}) dt = \int_{0}^{T} \int_{\Omega} \mathbf{u}^{T} \mathbf{u} d\Omega dt$$
 (5.42)

is used. By noting that the linearized Navier–Stokes equations can be written as $(\partial_t - \mathcal{A})\mathbf{u} = 0$ we will recognise that the adjoint should satisfy the following property

$$(\mathbf{u}^{\dagger}, (\partial_t - \mathcal{A})\mathbf{u})_{\Sigma} = ((-\partial_t - \mathcal{A}^{\dagger})\mathbf{u}^{\dagger}, \mathbf{u})_{\Sigma} = 0$$
 (5.43)

In order to move the action of the operators ∂_t and \mathcal{A} from \mathbf{u} to \mathbf{u}^{\dagger} we will need to perform integration by parts on the leftmost part of the above expression. To arrive at the adjoint operator \mathcal{A}^{\dagger} there are two possible strategies; either to discretize the system in space including the boundary conditions and use the discretized inner product, or to use the continuous variables and operators in (5.43) to arrive at the the adjoint system (Giles & Pierce 2000). Once obtained in its continuous form the system is discretized for numerical implementation. We here outline the latter strategy. We utilise the Navier–Stokes equations and the time space inner product to perform integration by parts

$$0 = (\mathbf{u}^{\dagger}, (\partial_{t} - \mathcal{A})\mathbf{u})_{\Sigma}$$

$$= \int_{0}^{T} \int_{\Omega} (\mathbf{u}^{\dagger})^{T} (\partial_{t}\mathbf{u} - (\mathbf{U} \cdot \nabla)\mathbf{u} - (\nabla \mathbf{U})\mathbf{u} + Re^{-1}\Delta\mathbf{u} + \nabla p) d\Omega dt$$

$$= \int_{0}^{T} \int_{\Omega} \mathbf{u}^{T} (-\partial_{t}\mathbf{u}^{\dagger} + (\mathbf{U} \cdot \nabla)\mathbf{u}^{\dagger} - (\nabla \mathbf{U})^{T}\mathbf{u}^{\dagger} + Re^{-1}\Delta\mathbf{u}^{\dagger} + \nabla \sigma) d\Omega dt$$

$$+ \int_{0}^{T} B.C. dt + \int_{\Omega} (\mathbf{u}^{\dagger}(T))^{T}\mathbf{u}(T) d\Omega - \int_{\Omega} (\mathbf{u}^{\dagger}(0))^{T}\mathbf{u}(0) d\Omega$$

$$= ((-\partial_{t} - \mathcal{A}^{\dagger})\mathbf{u}^{\dagger}, \mathbf{u})_{\Sigma} + \int_{0}^{T} B.C. dt + (\mathbf{u}^{\dagger}(T), \mathbf{u}(T)) - (\mathbf{u}^{\dagger}(0), \mathbf{u}(0)).$$
(5.44)

The pressure for the adjoint equations σ can similarly to the regular equations be obtained through a Poisson equation, *i.e.* $\sigma = \mathcal{K}^{\dagger} \mathbf{u}^{\dagger}$. The B.C term contains the inner product between boundary terms in the direct and adjoint solution.

The above expression defines the adjoint linearized Navier–Stokes equations

$$-\partial_t \mathbf{u}^{\dagger} = \mathcal{A}^{\dagger} \mathbf{u}^{\dagger} = (\mathbf{U} \cdot \nabla) \mathbf{u}^{\dagger} - (\nabla \mathbf{U})^T \mathbf{u}^{\dagger} + Re^{-1} \Delta \mathbf{u}^{\dagger} + \nabla \mathcal{K}^{\dagger} \mathbf{u}^{\dagger}, \quad \mathbf{u}^{\dagger}(T) = \mathbf{u}_T^{\dagger}$$
(5.45)

if the boundary conditions of the adjoint system is set so that the integral containing B.C. vanishes and the initial and end time inner products equals, i.e.

$$(\mathbf{u}^{\dagger}(T), \mathbf{u}(T)) = (\mathbf{u}^{\dagger}(T), \mathcal{T}(T)\mathbf{u}(0)) = (\mathcal{T}^{\dagger}(T)\mathbf{u}^{\dagger}(T), \mathbf{u}(0)) = (\mathbf{u}^{\dagger}(0), \mathbf{u}(0)).$$
(5.46)

This leads to the conclusion that the adjoint evolution operator

$$\mathbf{u}^{\dagger}(T-t) = \exp(\mathcal{A}^{\dagger}t)\mathbf{u}^{\dagger}(T), \tag{5.47}$$

is the operator that solves the Navier–Stokes equations backwards in time to fulfil the inner product relation (5.43).

Having defined the adjoint evolution operator we may use it on (5.37) to obtain the largest growth as

$$G(t) = \max_{\mathbf{u}_0 \neq 0} \frac{(\exp(\mathcal{A}t)\mathbf{u}_0, \exp(\mathcal{A}t)\mathbf{u}_0)}{(\mathbf{u}_0, \mathbf{u}_0)} = \max_{\mathbf{u}_0 \neq 0} \frac{(\mathbf{u}_0, \exp(\mathcal{A}^{\dagger}t) \exp(\mathcal{A}t)\mathbf{u}_0)}{(\mathbf{u}_0, \mathbf{u}_0)}. \quad (5.48)$$

The above expression is a Rayleigh quotient and therefore by definition an eigenvalue problem. We can now write the optimization problem as

$$\sigma(t)\mathbf{u}_0 = \exp(\mathcal{A}^{\dagger}t)\exp(\mathcal{A}t)\mathbf{u}_0. \tag{5.49}$$

The largest eigenvalue of this Hermitian matrix is the maximum possible growth and the corresponding eigenvector is the structure in the flow that leads to the largest growth. Note the similarity with the standard eigenvalue problem. Whereas the eigenvalues of \mathcal{A} or equivalently $\exp(\mathcal{A}T)$ give the asymptotic growth of the system, the eigenvalues of the above system yield the potential for growth. Of course, to build the matrix $\exp(\mathcal{A}^{\dagger}t)\exp(\mathcal{A}t)$ is in most cases infeasible. Instead one can see this as the application of two DNS simulations; one for the normal Navier–Stokes system and one for the adjoint Navier–Stokes system, thereby making it suitable for solution by the Arnoldi method as described in Section 4.3.

5.5. Global stability of the flat plate boundary layer flow

The stability of the flat plate boundary layer flow was possible to explain using the Orr–Sommerfeld/Squire equations, but it is of interest to interpret the stability characteristics of this flow from a global perspective. In essence Paper 1 deals with the use of the two-dimensional temporal eigenmodes (we assume two-dimensional disturbances and harmonic time dependence) to characterise the growth due to two-dimensional structures. Figure 5.2(a) shows a subset of the 1205 converged eigenvalues obtained by choosing a Krylov subspace of dimension 2000. The branch of the spectrum associated with TS-instability is seen here marked with circles. These modes can be selected by identifying the

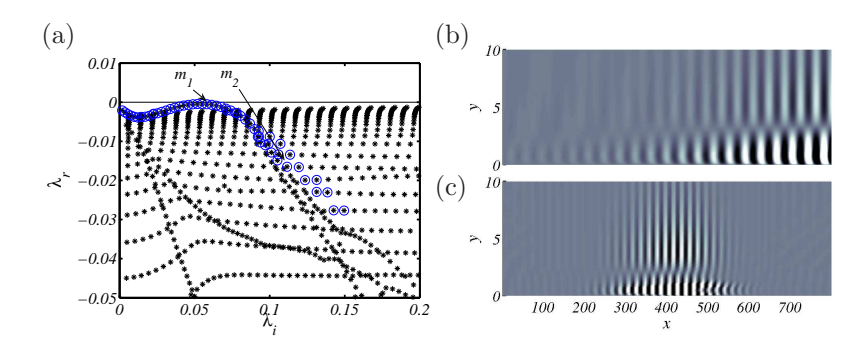


FIGURE 5.2. (a) Eigenvalues of the linearized two-dimensional Navier–Stokes system as obtained by the Arnoldi method. The eigenvalues enclosed by circles belong to the TS branch. (b) Streamwise velocity component of the eigenfunction related to an almost neutrally stable eigenvalue m_1 at the frequency $\lambda_i = 0.055$. (c) Eigenfunction corresponding to a high frequency highly damped eigenvalue m_2 .

slightly damped eigenvalues with the corresponding eigenfunctions obtaining their maximum values inside the boundary layer while decaying exponentially in the free stream. Figure 5.2(b)-(c) shows examples of eigenfunctions associated with eigenvalues m_1 and m_2 in figure 5.2(a). The streamwise wavelength of the eigenfunctions increases as we go towards lower frequencies. The wall normal structures of these are very similar to those obtained by local temporal analysis. Apart from the TS branch, figure 5.2(a) also reveals that the global spectrum give both the wall normal continuous spectrum (the slightly damped eigenvalues) and the damped discrete Orr modes, which both can be linked to the local temporal spectrum, however modified by non-parallel effects (see Paper 1).

A first observation to be made is that all eigenvalues are stable, hence we do not expect to see any single eigenmode dominating the flow. Tentatively we examine the possibility of transient growth by projecting the system on m two-dimensional eigenmodes as described in Section 5.4.1.

Figure 5.3(a) shows the envelope G as a function of time. The envelope reveals at each instance of time the maximum possible amplification due to a specific initial condition, *i.e.* there is a different initial condition leading to the specific maximum growth at each instance of time. The solid thick line shows the envelope using a sufficient amount of eigenmodes, leading to the combined Orr mechanism and the TS wave growth. The thin solid line shows the envelope obtained when using only the TS type of modes in the optimization, revealing that there is a gain with a factor of 20 in energy growth by initializing the TS wavepacket with the Orr mechanism.

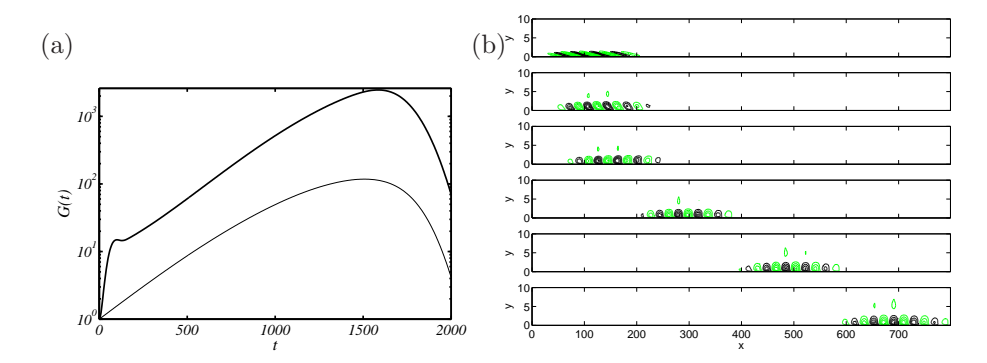


FIGURE 5.3. (a) Envelope of growth due to worst case initial conditions. Solid thick line shows the envelope using a sufficient amount of eigenmodes, leading to the combined Orr mechanism and the TS wave growth. The thin solid shows the envelope obtained when using only the TS type of modes in the optimization. (b) Time evolution for streamwise velocity with the combined Orr and TS mechanism. Note that the maximum amplitude A is growing from frame to frame.

In figure 5.3(b) we see snapshots of the optimal disturbance at different times of its evolution. At the initial time it is leaning backwards against the shear. During the initial phase of development the disturbance is raised up, exploiting the Orr mechanism, forming a wavepacket consisting of TS-waves. The wavepacket then grows as it propagates downstream and finally decays as it leaves the window of observation. In several recent investigations it has been found that the concept of transient growth in the form of wavepacket propagation can be important in non-parallel flows analysed from a global perspective. Using the Ginzburg-Landau equation Cossu & Chomaz (1997) showed that the transient growth associated with a sum of damped global modes can describe a spatially growing disturbance associated with a local convective instability. The recent review of Chomaz (2005) further elaborates on these ideas. Schmid & Henningson (2002) applied this concept to a falling liquid curtain and found that in contrast to the evolution of single modes, the sum of modes, i.e. the cooperation of modes that produces the largest growth, was in fact able to bring out a physical mechanism of growth and regeneration of the wavepacket, namely the triggering of a new wavepacket by the pressure feedback of the disturbance created by the previous packet as it hits the downstream end of the domain.

It is interesting to note that, as in the falling liquid sheet problem of Schmid & Henningson (2002), the optimal sum of the global eigenmodes brings out the

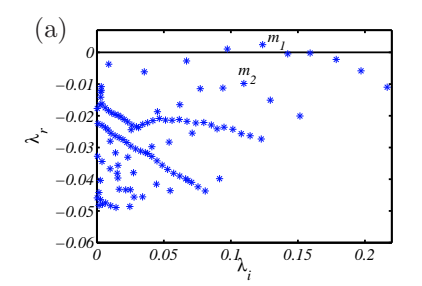
physical mechanism that optimally triggers wave packets also for boundary layers. From the global approach we see that both TS waves and streaks scenario can be seen as transient growth, i.e. neither of the mechanisms can be seen to stem from single eigenmodes. The TS waves can be interpreted in terms of streamwise non-normality, where the perturbations are growing while being convected with the flow. Likewise the Orr mechanism which is present also in the Orr-Sommerfeld equation can be seen as a wall normal non-normality, where it is the propagation of the mean flow by the disturbances that creates the instability. The famous lift up mechanism may be seen as a component-wise non-normality, where there is a transfer of momentum from the wall normal and spanwise velocities to the streamwise velocities (Marquet et al. 2008). Note that using a sum of eigenmodes yields a low dimensional description of the system. The direct computation of the optimal growth using the direct and adjoint evolution operator may in many cases be the best choice of method. Blackburn et al. (2008) studied a backward-facing step flow using a direct approach and found that also for that geometry wavepackets originating at the upstream end of the domain propagates downstream as they grow spatially. In Paper 6 we study both the optimal initial condition and the optimal forcing in the Blasius boundary subject to three-dimensional disturbances using this approach, comparing the growth due to wave-packet propagation and the liftup mechanism.

5.6. Global stability of the cavity flow

Due to its rapid change in geometry, the cavity flow is not possible to analyse using the Orr–Sommerfeld/Squire equations. In the previous section we observed that for the high Reynolds number flat-plate boundary layer flow the optimal sum of eigenmodes yielded upstream tilted structures that efficiently initialised Tollmien-Schlichting type of wave packets. With this knowledge in hand we are ready to attack a strongly non-parallel problem, to see the interaction of convective and absolute instability.

In absolutely unstable flows any noise present in the high order numerical discretization will grow exponentially, making it impossible to numerically compute a steady-state base flow for linearization by standard time-marching methods. Therefore the Selective Frequency Damping technique proposed in Paper 2 is used to recover the steady state at this Reynolds number. The Navier–Stokes equations are forced by adding a term proportional to the difference between the flow state and a filtered solution. In order to examine the stability of the flow we again compute the eigenvalues of the two-dimensional linearized Navier–Stokes operator linearized about the unstable base flow.

As in Section 5.5 we use the Arnoldi procedure to obtain global eigenmodes of the flow. For this highly non-parallel flow we find, as seen in figure 5.4(a), about 150 converged complex conjugate pairs of eigenmodes when using a Krylov subspace of size m=800. Two of the eigenvalues are found in the



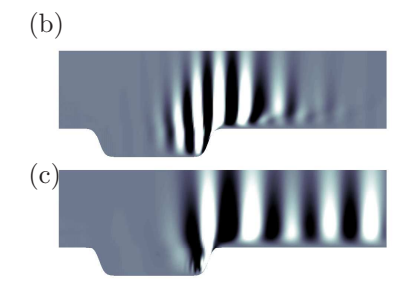


FIGURE 5.4. (a) Eigenvalues of the cavity flow at Re = 350. There are two unstable modes labelled (the most unstable being labelled m_1), the distance in frequency of which is related to the length of the cavity. (b) Vertical velocity component of mode m_1 . (c) Vertical velocity component of mode m_2 .

unstable half plane, i.e. they have positive real part. An unstable eigenvalue indicates that the flow is globally unstable, supporting self-sustained oscillations. Figure 5.4(b) shows the vertical velocity of the eigenfunction associated with the eigenvalue labelled m_1 . All the slightly damped modes are quite similar, they display Kelvin–Helmholtz type structures, all growing exponentially throughout the shear-layer. Note that the distance in frequency λ_i of these modes are set by the length of the cavity and the propagation speed of disturbances in the shear layer, similar to the waterfall problem of Schmid & Henningson (2002). Slightly more damped modes labelled m_2 in figure 5.4(a) with corresponding eigenfunctions displayed in figure 5.4(c) are also present. These eigenfunctions are reminiscent of the TS modes obtained in section 5.5.

The non-normality of the operator we investigate allow the possibility of transient growth also in this globally unstable flow configuration. Using an eigenfunction expansion in a number of selected modes we optimize the energy output in the same way as for the waterfall and Blasius problems. Figure 5.5(a) shows the optimal energy growth using different numbers of global modes in the eigenfunction expansion. Using one mode we observe the exponential growth of the most unstable mode. Transient energy growth, due to non-normality of the eigenmodes, results in a much faster growth up to t = 200, followed by a global cycle of approximately 300 time units. This cycle is associated with the least stable eigenvalues in figure 5.4(a). Since the spacing in λ_i between adjacent modes is $\Delta \lambda_i \approx 0.02$, and the corresponding eigenfunctions have a very similar structure, they have the ability to cancel each other, giving rise to a cycle with a period of $2\pi/\Delta\lambda_i$ (Schmid & Henningson 2002). In order to get a more physical feeling with the oscillating cycle we consider spatio-temporal diagrams of the pressure field obtained from the eigenfunction expansion at a height of y = 10 above the plate, tracing the development of the wavepacket.



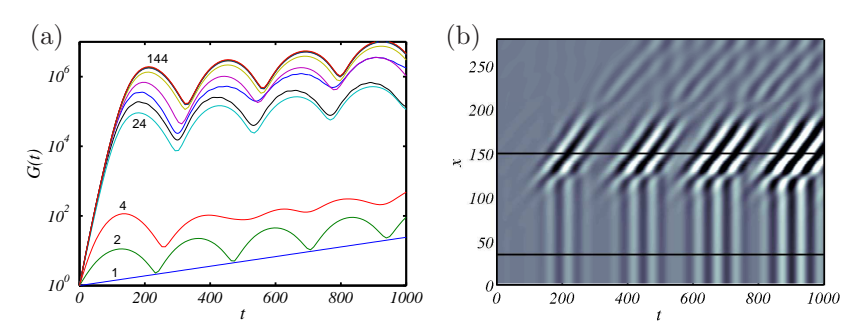


FIGURE 5.5. Optimal growth for the cavity flow. (a) Envelope as obtained from the global mode expansion. Different lines correspond to increasing number of eigenmodes included in the optimization, $1, 2, 4, 24, \ldots, 124, 144$ from bottom to top. Using one eigenmode in the expansion results in the exponential growth of the least stable eigenmode. When including two modes in the optimization there is a cancellation effect leading to an oscillating cycle. (b) Spatio-temporal diagram for the pressure at y=10, for the time evolution in the eigenmode system due to the worst case initial disturbance. The horizontal lines show the location of the cavity lips. As the wave packet reaches the downstream lip there is a significant pressure reflection regenerating the wave packet.

The bottom horizontal line in figure 5.5(b) signifies the upstream lip and the top horizontal line the downstream lip. We first see the wavepacket as it hits the downstream end, then it appears again and again as the global cycle continues. We also see vertical (instantaneous) pressure pulses when the waves hit the trailing lip. If we trace back a wavepacket to the downstream lip of the cavity we see that it is triggered by the pressure pulse of the previous wavepacket. This instability mechanism may be seen as a destabilization of the global mode by the pressure field, where the pressure constitutes an immediate feedback mechanism and the strong streamwise non-normality causes a large growth of the disturbances along the shear layer.

CHAPTER 6

Flow control

The interest in devising efficient controllers for real applications such as the flow around vehicles is substantial both from an economic and environmental point of view. A large portion of the drag on boats, aeroplanes and trains stems from the turbulent boundary layer surrounding these, hence an important aspect of flow control is to delay the transition to turbulence. Flow control in its widest sense refers to any mechanism that modifies the behaviour of the flow. During the last decade several strategies such as active, passive, open-loop, closed-loop control have been implemented both numerically and experimentally with various degrees of success. Passive control methods rely on modifying the mean flow by means of disturbance generators, such as ribblets, roughness elements or compliant walls, or by altering the shape of for instance an aeroplane wing. As an example Fransson et al. (2006) showed experimentally that streaks induced by roughness elements mounted on a flat plate could delay transition due to Tollmien-Schlichting waves in the Blasius boundary layer flow.

This thesis deals with active feedback (closed loop) control, where the aim is to control the flow at a disturbance level by minute perturbations of the flow. Important reviews in the field of active feedback control include Gunzberger (1996); Bewley (2001); Kim (2003); Kim & Bewley (2007). All results presented are obtained in the numerical framework, but it should be kept in mind that the goal is to approach the possibility of experimental implementation of feedback controllers. The justification of applying linear feedback control to inherently non-linear processes such as the evolution of fluid flows is threefold; first of all the transition process consists of a linear stage, where small disturbances grow until non-linear breakdown occurs (Schmid & Henningson 2001), secondly linear processes are important to sustain turbulence in wall-bounded turbulent flows (Kim & Lim 2000), thirdly stochastic disturbance models can be introduced in the linearized Navier–Stokes equations mimicking flow statistics of full DNS (Jovanovič & Bamieh 2001).

Over the years several important steps have been taken in the field of numerical linear feedback control. Early studies focused on the parallel channel flow (Joshi *et al.* 1997; Bewley & Liu 1998; Keun *et al.* 2001; Högberg *et al.* 2003; Hoepffner *et al.* 2005; Chevalier *et al.* 2005), where the Orr–Sommerfeld/Squire

equations were sufficient to describe the linear mechanisms of the flow. Linear feedback control in the Orr–Sommerfeld/Squire framework has also been applied to spatially developing flows in Högberg & Henningson (2002); Cathalifaud & Bewley (2004a,b). In Paper 5 we perform control in boundary layer flows such as the Blasius and Falkner–Skan–Cooke flows following this strategy. A substantial drawback with the assumption of locally parallel flow is that distributed sensors and actuators along the wall are assumed, which is clearly infeasible for experimental implementations, where only localized sensors and actuators are possible.

In order to capture localized sensors and actuators controllers have to be constructed using a global approach. This new approach is developed in Paper 3 and Paper 4. Since the linearized Navier-Stokes equations once discretized constitute a very high dimensional system, the systematic manipulation of the full equations becomes too demanding. Reduced representations of the equations by Galerkin projection onto global basis functions have received substantial attention during the last years. Specifically various models based on proper orthogonal decomposition (POD) modes able to capture the non-linear dynamics of the Navier-Stokes equations can be found in Gillies (1998); Noack et al. (2003, 2004); Tadmor et al. (2004); Rowley et al. (2004). A problem with using POD modes is that although they are optimal at capturing the energy of the flow they do not in general capture the dynamically important low energy structures created by the actuator. Different strategies to overcome this problem have been introduced in Gillies (1998) and in Tadmor et al. (2004). For linear systems balanced truncation provides an attractive basis for model reduction (Moore 1981), and examples of successful applications are channel flow (Ilak & Rowley 2008), the flow around a pitching air foil (Ahuja & Rowley 2008) and the Blasius boundary layer flow (Bagheri et al. 2008).

Reduced order modelling provides the natural bridge to experimental implementations of optimal controllers. Until recently the experimental community has restricted their studies to the performance of the actuators their selves and not the specific performance of different control laws. In experiments typical sensors are wall wires and hot films measuring wall shear stress (Alfredsson et al. 1988), whereas actuators are provided by suction/blowing through holes (Lundell 2007). An example of active feedback control for the Blasius boundary layer is found in for instance Lundell (2007) who showed that arrays of wall wires extracting wall shear stress connected to wall suction actuators could by utilising simple control laws reduce the disturbance growth due to streaks. Successful experimental implementations of optimal linear feedback control are scarce, but an exception is Caraballo et al. (2008), who attenuate the peak in the frequency response of the globally unstable square cavity flow. In that work POD modes obtained from particle image velocimetry snapshots are used to construct a reduced order model from which a Linear Quadratic Gaussian controller is computed.

6.1. Feedback control

In this thesis we deal with active control in the framework of closed loop feedback control. The essence of a closed loop controller is illustrated in figure 6.1. The flow system may be seen as a plant onto which we have disturbances ψ . The plant may be the flow in a wind tunnel or as described by the Navier-Stokes equations. From the plant we have measurements r available. These measurements are fed into a controller which in real time (on line) computes control signals ϕ that are fed back into the plant. A second set of measurements s monitor how well the controller has been performing. An alternative set up is an open loop controller where the outputs r are discarded in the computation of the control signals, thereby enabling off line computation of the control law. The latter control strategy is only reasonable if exact knowledge of the plant dynamics is available, whereas the former is able to account for uncertainties in the plant. The outputs r and s are obtained through sensors, which for flow systems typically are located at the wall. Similarly the inputs ϕ are driving actuators that allows for manipulation of the flow behaviour. The mapping of the disturbances ψ onto the state needs in general to be modelled. For flow systems this essentially amounts to describing the shape and location of typical instability structures.

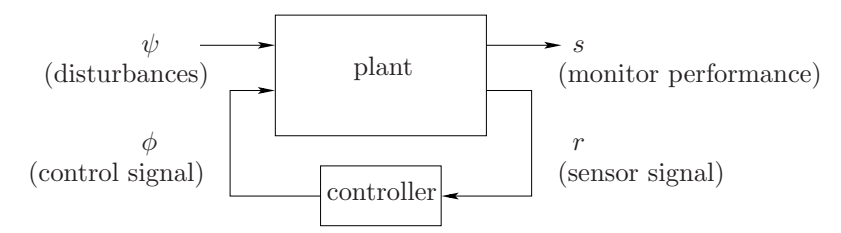


FIGURE 6.1. Schematic view of a control setting. The flow is seen as a plant driven by disturbance signals ψ . From the plant measurement signals r are into a controller which calculates a control signal ϕ that is fed back into the plant. A second set of measurements s monitors the performance of the controlled system.

The most essential question for control is what to put in the "controller" box, or in other words how to connect the sensors to the actuators in order to obtain the desired goal. Simple controllers do exist, and the most popular in industrial applications (control of robot arms, cd players, car steering systems etc.) is the so called Proportional Integral Derivate (PID) controller. This controller takes output signals r and calculates the control signal through the relation

$$\phi(t) = Pr(t) + D\frac{\mathrm{d}r}{\mathrm{d}t} + I\int_0^t r(\tau)\mathrm{d}\tau, \tag{6.50}$$

where P, D and I are tunable constants. The tuning of the constants can be done by a lead-lag technique working in the frequency domain, with a frequency domain model of the plant available. This can also be seen as a pole placement (moving eigenvalues) technique. For a general fluid dynamical system, which has quite intricate dynamics (such as non-normality of the underlying operator) the task of tuning the constants may become difficult (Glad & Ljung 1994). There are other more systematic (and complicated) ways of constructing controllers, namely controllers that stem from optimization of quadratic criteria. The famous Linear-Quadratic-Gaussian (LQG) controller is an example of this class of controllers. The essence of the LQG controller is that a Kalman filter (state space filter) is running on the side of the plant continuously estimating the state based on measurements. Based on the estimated state an optimal controller computes control signals. There are of course drawbacks to using this technique, the most obvious being that large scale optimization problems have to be solved if the full state space equations are used as a basis for control. In addition the Kalman filter has to be run on-line in order to yield the control signals, typically at the cost of a DNS time integration. There are however methods to cope with the high dimensionality of the system.

6.2. Inputs and outputs

In order to perform systematic manipulation of the linearized Navier–Stokes equations we equip them with inputs that allow us to manipulate the flow

$$\partial_t \mathbf{u} = \mathcal{A}\mathbf{u} + \mathcal{B}_1 \phi + \mathcal{B}_2 \psi = \mathcal{A}\mathbf{u} + \mathcal{B}\mathbf{f} \tag{6.51}$$

and outputs

$$\begin{cases}
s = \mathcal{C}_1 \mathbf{u} \\
r = \mathcal{C}_2 \mathbf{u},
\end{cases} \Rightarrow \mathbf{r} = \mathcal{C} \mathbf{u}, \tag{6.52}$$

that enable us to extract information. Here \mathbf{u} is the state consisting of the velocities and \mathcal{A} is the discretized linearized Navier–Stokes operator. Without loss of generality only single input and output signals are considered here. The input operator \mathcal{B}_2 allows for the manipulation of the flow through the scalar control signal ϕ . The scalar measurement r is obtained through the operator \mathcal{C}_1 . Disturbances to the state equation are modelled by the input \mathcal{B}_1 driven by the scalar signal ψ . We are able to monitor the behaviour of the controlled system via the scalar signal s generated from the state via the output operator \mathcal{C}_1 . It is convenient to group the inputs to obtain an input signal vector $\mathbf{f} = [\psi, \phi]^T$ with the corresponding input operator $\mathcal{B} = [\mathcal{B}_1 \mathcal{B}_2]$ and likewise the outputs to an output signal vector $\mathbf{r} = [s, r]^T$ with the corresponding output operator $\mathcal{C} = [\mathcal{C}_1, \mathcal{C}_2]^T$. The state space formulation requires the inputs to be volume forcing operators and the outputs to operate on the state \mathbf{u} . If applying control via boundary conditions for instance by means of blowing and suction it is convenient to perform a lifting procedure (Curtain & Zwart 1995). A derivation of this procedure for the one dimensional Orr–Sommerfeld/Squire equations with

distributed actuators is found in Högberg et al. (2003), and similarly for the two-dimensional Navier–Stokes equations with localized actuators the reader is referred to Paper 4 for an explanation. The basic idea of that procedure is to divide the solution into a particular part satisfying the boundary conditions and homogeneous part with homogeneous boundary conditions. Then the control problem of the total solution is written in terms of the homogeneous solution forced by a steady state solution of the particular system.

Figure 6.2 shows the inputs and outputs for the two flow cases studied in this thesis. For the convectively unstable Blasius case we model the disturbance input \mathcal{B}_1 to the system by an upstream located volume forcing as seen in figure 6.2(a). Remember from Section 5.5 that the dominating instabilities in the flow were upstream located structures that are propagated downstream in the form of wavepackets while being amplified. Downstream of the disturbance the sensor C_2 senses the incoming disturbances extracting the wall-shear stress $(\partial_y u)$ with the shape shown in figure 6.2(a). The actuator is a zero mass flux wall blowing and suction device that is lifted to a state space forcing term as described in Paper 4. In total the flow is now subject to input from both disturbances and actuation, the effect of which is convected downstream. To this end there is a sensor \mathcal{C}_1 located downstream monitoring the performance of the controller by extracting the wall-shear stress. In Figure 6.2(b) the control setup for the globally unstable cavity flow is shown. In Section 5.6 it was shown that the destabilising mechanism was wave packet propagation across the cavity shear layer that triggered a pressure wave when hitting the downstream end of the cavity. This makes it natural to assume that the disturbance \mathcal{B}_1 should be modelled by a volume forcing in the cavity shear layer and likewise that the best location for sensor C_2 is at the downstream cavity lip. Once the disturbances hit the downstream lip the pressure wave immediately hits the upstream lip of the cavity recreating vortical disturbances that again propagate across the shear layer. It is hence at the upstream lip a suitable location for the actuator \mathcal{B}_2 is found. In order to access the performance the full domain perturbation kinetic energy is monitored. From the above it is evident that while finding the best control law may be solved by optimization problems the placing of actuators and sensors is an engineering judgement based on the knowledge of the flow instability.

6.3. Model reduction

The linearized Navier—Stokes equations subject to control constitute a very high dimensional system once discretized. Systematic control strategies involve solving optimization problems that rely on direct manipulation of the system matrices involved. In general this becomes computationally too demanding. A way to avoid the problem of high dimensionality is by model reduction, for which the aim is to construct a reduced order state space realization with input-output characteristics that are similar to the original state space model.



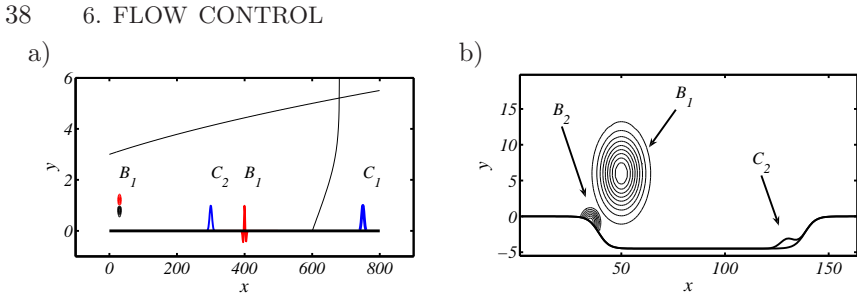


FIGURE 6.2. Set up of inputs and outputs for a) The flat plate boundary layer flow. The input B_1 models the upstream initial receptivity phase. The wall blowing and suction actuator \mathcal{B}_2 is located after the first sensor C_1 which measures the wall-shear stress. The second sensor C_2 quantifies the effect of the control. b) The shallow cavity flow. The actuator \mathcal{B}_2 is placed in the vicinity of the upstream lip of the cavity and the sensor C_2 measuring the skin friction is placed at the downstream lip of the cavity The unknown stochastic disturbances \mathcal{B}_1 is assumed to be located upstream in the shear layer. The output C_1 is not shown because it measure kinetic energy in the whole domain.

The standard procedure to obtain a reduced state space model is by Galerkin projection on a set of suitable vectors. In this thesis we have used two different sets of vectors, namely the eigenmodes of the linearized equations and the balanced truncation modes (Moore 1981).

Given a set of input operators \mathcal{B}_1 and \mathcal{B}_2 a crucial element for control design is to quantify their effect on the state. The systematic approach to quantifying this effect is commonly given by the controllability Gramian, which measures the energy of the states u that can be reached by the inputs

$$\mathcal{J}_c = \int_0^\infty \exp(\mathcal{A}\tau) \mathcal{B}\mathcal{B}^\dagger \exp(\mathcal{A}^\dagger \tau) d\tau, \qquad (6.53)$$

for the input $\mathcal{B} = [\mathcal{B}_1 \, \mathcal{B}_2]$. The controllability Gramian once diagonalized provides a way to rank different states according to how they can be influenced by the inputs \mathcal{B} . In the same manner, given output operators \mathcal{C}_1 and \mathcal{C}_2 the most easily observed states are quantified by the observability Gramian

$$\mathcal{J}_o = \int_0^\infty \exp(\mathcal{A}^{\dagger} \tau) \mathcal{C}^{\dagger} \mathcal{C} \exp(\mathcal{A} \tau) d\tau, \qquad (6.54)$$

for the outputs $\mathcal{C} = [\mathcal{C}_1 \mathcal{C}_2]^T$. The observability Gramian provides upon diagonalization a way to rank the states according to how easily they are detected by the outputs. Both measures (6.53) and (6.54) are obtained as solutions of Lyapunov equations, which in their direct form are computationally too heavy. Most methods to deal with this issue are based on subspace projections (Saad & Gv 1990), and the snapshot method (c.f. Sirovich 1987; Rowley 2005) falls under this category. The key elements in the snapshot method are; to replace the upper integration limit in (6.53) and (6.54) with a sufficiently large finite time; to introduce a numerical quadrature to obtain discrete approximations to the integrals; and finally to project the solutions on the snapshots. A set of snapshots for the controllability Gramian is obtained by doing two forward simulations (DNS) subject to initial conditions \mathcal{B}_1 and \mathcal{B}_2 to obtain the collection of snapshots X of size $n \times 2m$ for the discretized state. In addition a set of adjoint snapshots for the observability Gramian is obtained through two adjoint simulations subject to end conditions C_1 and C_2 to end up with Y of size $n \times 2m$. The discretized gramians are formally given by $J_c = XX^T$ and $J_o = YY^T$. The balanced modes are the modes that mutually diagonalize J_c and J_o , i.e. they are the eigenmodes of J_cJ_o . To this end it can be seen that the singular value decomposition of the small $2m \times 2m$ sized matrix Y^TX is sufficient to obtain these modes. For a more in depth explanation to the snapshot method for computing balanced modes it is referred to Rowley (2005). For stable systems the balanced truncation modes provides the preferable basis for model reduction due to their inherent quantification on how well the input-output behaviour is captured.

Although in its original form balanced truncation applies to stable systems only, it is possible to extend it to unstable systems by projecting out the unstable eigenmodes of the system and creating an augmented system of balanced modes and eigenmodes (Ahuja & Rowley 2008). If the aim is to stabilise an absolutely unstable flow it is possible to use only the eigenmodes as a total basis for projection (Åkervik *et al.* 2007).

Whether we use the eigenmodes or the balanced modes we denote the basis as $\mathcal{V} = [\mathbf{v}_1, \mathbf{v}_2, \dots, \mathbf{v}_m]$ and the corresponding adjoint basis as $\mathcal{V}^\dagger = [\mathbf{v}_1^\dagger, \mathbf{v}_2^\dagger, \dots, \mathbf{v}_m^\dagger]$, where m is the number of modes kept in the reduced order representation of the system. Typically m should be chosen as small as possible. The direct and adjoint modes satisfy the bi-orthogonality condition

$$(\mathbf{v}_i^{\dagger}, \mathbf{v}_j) = \delta_{ij}. \tag{6.55}$$

The flow state \mathbf{u} is expanded in the basis as in Section 5.4

$$\mathbf{u} = \sum_{j=1}^{m} \kappa_j(t) \mathbf{v}_j = \mathcal{V} k(t), \tag{6.56}$$

for the flow state $k = [\kappa_1, \kappa_2, \dots, \kappa_m]^T$. The above relations enable us to perform a Galerkin projection of the linearized Navier–Stokes equations via

the inner products

$$\begin{aligned}
A_{ij} &= (\mathbf{v}_i^{\dagger}, A\mathbf{v}_j) \\
B_{1,i} &= (\mathbf{v}_i^{\dagger}, B_1) \quad B_{2,i} &= (\mathbf{v}_i^{\dagger}, B_2).
\end{aligned} (6.57)$$

The reduced matrix A is of size $m \times m$ and the input matrices B_i are of sizes $m \times 1$. If the eigenmodes are used as a basis for reduction, the matrix A is diagonal with the eigenvalues on the diagonal, but for the balanced modes the matrix is in general full. The reduced order representation of the output operators is obtained via the expansion (6.56)

$$C_{1,i} = C_1 \mathbf{v}_i, \qquad C_{2,i} = C_2 \mathbf{v}_i. \tag{6.58}$$

Finally we end up with the reduced system

$$\dot{k} = Ak + B_1 \phi + B_2 \psi,
s = C_1 k
r, = C_2 k,$$
(6.59)

to be used for systematic control design in the LQG framework.

6.4. LQG control of the Navier-Stokes equations

In the design of an LQG controller our concern is to find an optimal mapping from the output r to the input ϕ so that a quadratic measure of the disturbances are minimized. An example of such a measure is the total kinetic energy in the domain, but it might also be based on a measurement at a specific location. A direct formulation of the optimization problem results in a sequence of coupled non-linear equations, and there are no robustness guaranties to the resulting controller (see e.g. Lewis & Syrmos 1995). On the other hand by splitting the problem in two, where an optimal controller is built using full knowledge of the state (Linear Quadratic Regulator), but replacing that state with an estimated state reconstructed from the measurement based on a Kalman filter, results in a controller with certain desirable properties. For instance if the full information controller and the Kalman filter are both stable, then the resulting controller is also stable, as guaranteed by the separation principle (Zhou et al. 2002).

Let the first step in the LQG design be to reconstruct the state from the measurements r discarding the output s. The state equations can be written as

$$\begin{cases} \dot{k} = Ak + B_1 \psi + B_2 \phi, & k(0) = k_0 \\ r = C_2 k + g, \end{cases}$$
 (6.60)

where we have added measurement noise g. To explicitly state that there are uncertainties in the system, both ψ and g are considered to be stochastic

uncorrelated white noise processes, only known through their covariances. The detailed form of the initial condition k_0 is assumed to be unknown, and only covariance data is available. The stochastic nature of the uncorrelated inputs ψ , g and k_0 renders also the state k stochastic. The time evolution of the state covariance $P = \mathbb{E}\{k^*k\}$ is governed by a Lyapunov equation (Kailath *et al.* 1999).

The process of estimating a linear system with noisy and a limited amount of information is an optimal filtering problem (Kailath $et\ al.\ 1999$). Now let the state equation itself serve as a time-domain filter

$$\begin{cases} \dot{\hat{k}} = A\hat{k} + B_2\phi + L(r - \hat{r}), & k(0) = 0\\ \hat{r} = C_2\hat{k}, \end{cases}$$
(6.61)

for the estimated state \hat{k} . The above equation is the famous Kalman filter, where neither state disturbances nor measurement noise is present. A forcing term $L(r-\hat{r})$ is introduced to force the estimated state towards the noisy unknown state based on the measurement differences in the two systems. This forcing vanishes when the difference in the measurements is zero. The error $\tilde{k}=k-\hat{k}$ involved in this process has the evolution equation

$$\dot{\tilde{k}} = (A + LC_2)\tilde{k} - Lg,\tag{6.62}$$

with corresponding covariance \tilde{P} . The task is now to find the optimal forcing gain L that minimises the quadratic measure trace(\tilde{P}) in the infinite horizon. The resulting optimization problem can be solved by a Lagrange multiplier technique where the objective function is subject to the constraints of satisfying the Lyapunov equation for the estimation error covariance \tilde{P} . It can be seen that the solution is given by an algebraic Riccati equation for \tilde{P} , and the optimal gain L can be extracted from

$$L = -\tilde{P}C_2^H G^{-1}. (6.63)$$

Here G is the variance of the measurement noise. The optimal gain L is now designed such as to drive the estimated state \hat{k} towards the unknown state k based on the measurement difference $r - \hat{r}$. For a detailed derivation of the estimation process the reader is referred to Kailath $et\ al.\ (1999)$, and for a discussion on how to model the stochastic disturbances for fluid flows it is referred to Hoepffner $et\ al.\ (2005)$; Chevalier $et\ al.\ (2005)$.

6.4.2. The Linear Quadratic Regulator

When designing an optimal full information controller we take a deterministic approach, where we assume that full state information is available and that the

measurement s is used as an objective function

$$\dot{k} = Ak + B_2 \phi,
s = C_1 k + \ell \phi.$$
(6.64)

The measurement s is equipped with a term $\ell\phi$ that allows us to add the control signal strength to the objective function

$$||s||^2 = \int_0^\infty ||C_1 k||^2 + \ell^2 \phi^H \phi \, dt.$$
 (6.65)

Minimisation of this expression can also be achieved through a Lagrange multiplier technique where the constraint is the state equation $\dot{k}=(A-B_2K)k$. The optimal control gain K is obtained as the solution of an algebraic Riccati equation. As stated earlier the separation principle guarantees that the optimal measurement feedback control is given by

$$\phi(t) = K\hat{k}(t), \tag{6.66}$$

where \hat{k} is indeed the state estimate provided by the Kalman filter. Note that in general the cost functions for both control and estimation can be time varying functions and in this case the gains K and L become time dependent and their solution is governed by differential Riccati equations (see e.g. Lewis & Syrmos 1995).

6.4.3. Application to the Navier-Stokes

Applying the optimal controller to the Navier–Stokes equations amounts to solving the system

$$\partial_t \mathbf{u} = NS(\mathbf{u}) + \mathcal{B}_2 \phi, \qquad r = \mathcal{C}_2 \mathbf{u},
\dot{\hat{k}} = (A + B_2 K + L C_2) \hat{k} - L r, \quad \phi = K \hat{k}.$$
(6.67)

The evolution of the flow state \mathbf{u} is updated for example by means of a DNS time-stepper technique. At every time step measurements r are extracted, driving the small estimated state \hat{k} . The estimated state is updated on-line by any suitable time-integration procedure, feeding back at every time step control signals ϕ to the DNS. It is important to note that if we were using the full equations for the control design, it would have been necessary to solve a full DNS on-line in order to obtain the estimated state. Hence it can be seen that model reduction is essential both to solve the optimization problems and to construct realizable controllers for on-line use.

6.5. Control of the flat plate boundary layer flow

For the flat plate boundary layer flow discussed in Section 5.5 we use the 70 most dynamically important balanced truncation modes as a projection basis for model reduction. The performance of the controller is tested using the propagating wavepacket stemming from the optimal initial condition. This case is

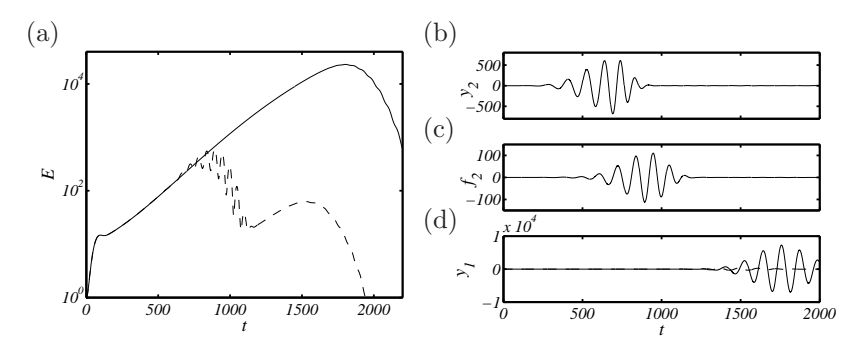


FIGURE 6.3. Control of the wavepacket due to the worst case initial condition. (a) Solid black line shows uncontrolled energy evolution and dashed black line shows the controlled energy. (b) Output signal as measured by the sensor C_2 driving the controller. (c) Control signal fed into the wall actuator. (d) Signals from the sensor C_1 measuring the objective function. Solid black line shows uncontrolled case whereas dashed black line shows the controlled case.

interesting because the controller is not designed specifically for this configuration and it has only a limited window in time to counteract the disturbances that are propagating through the domain in the form of a localized wavepacket. In figure 6.3(a) the full domain kinetic energy as a function of time is shown as a solid black line for the uncontrolled evolution and as a dashed line for the controlled case. The effect of the controller is evident. The measurement signal detected by the sensor C_2 is shown in figure 6.3(b) revealing that the sensor picks up the front of the wavepacket arriving at $t \approx 350$. A time lag of ≈ 300 consistent with the speed of the propagating wavepacket (c=0.3) is observed until the controller starts acting on the information (see figure 6.3(c)). The downstream measurement, *i.e.* the objective function to be minimized, is shown in figure 6.3(d) as a black solid line for the uncontrolled case and as a dashed black line for the controlled case. It can be seen that also this measure shows a satisfactory performance of the controller.

6.6. Control of the cavity flow

For the absolutely unstable cavity flow studied in Section 5.6 we use the eigenmodes of the two-dimensional linearized Navier–Stokes equations as our projection basis for model reduction.

The control and estimation gains are computed using the LQG framework presented in Section 6.4. In order to assess the performance of the computed control and estimation gains the linear reduced order controller is coupled to the full non-linear DNS and applied to the same configuration that led to

44 6. FLOW CONTROL

the evolution shown in figure 5.5. A reduced model consisting of the four least stable eigenmodes is considered, sufficient to at least move the unstable eigenmodes to the stable half plane. Note that this small model cannot fully capture the transient growth associated with the initial propagation of the wave packet (see third line from bottom in figure 5.5(a)), however as already stated, for control purposes it is the actuator to sensor dynamics that is crucial to capture. The shear layer acts as a filter to retain only the leading eigenmodes once the wavepacket has propagated across the cavity. Indeed figure 6.4(a) shows that when control is applied to the full Navier–Stokes equations in terms of DNS, the exponential energy growth is turned into exponential decay after the first peak. It is not possible to control the initial energy growth as the first wavepacket has to propagate down once before the controller knows that it exists.

The sensor signals for the controlled and uncontrolled case are shown in the inset of figure 6.4(a). The sensor signal from the controlled case decays after the first reflections of the wavepacket at $t \approx 125$. The spatio-temporal diagram for the controlled flow in figure 6.4(b) is to be compared with figure 5.5(b). When the control is applied one still observes the vertical rays of the global pressure oscillations but the wavepacket regeneration is reduced, leading to a decrease in the levels of fluctuations at each cycle, *i.e.* flow stabilization.

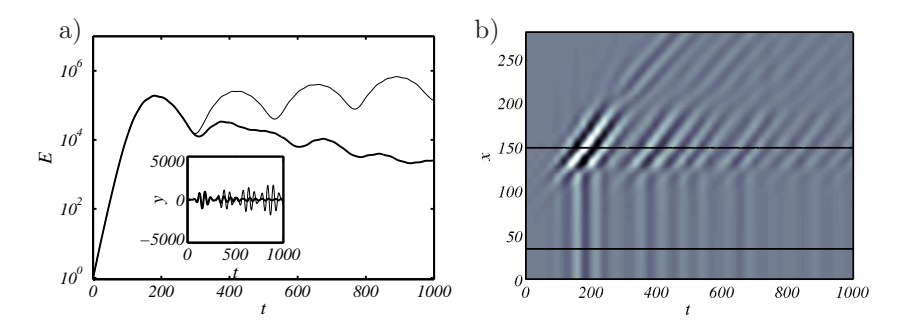


FIGURE 6.4. a) Energy obtained from DNS of the uncontrolled flow (thin solid line) and controlled flow using model with four modes (thick solid). After the first reflection has taken place the controller counteracts regeneration at the upstream cavity lip and thereby turns exponential growth into exponential decay. Inset shows the sensor signal in the uncontrolled case as thin solid line and controlled using four modes as thick solid line. b) DNS of controlled flow using an estimator constructed from reduced model formed by the four least stable eigenmodes. As can be observed by comparison with the uncontrolled case displayed in figure 5.5 the regeneration of the disturbances at the upstream cavity lip is diminished.

CHAPTER 7

Conclusions and outlook

Modern hydrodynamic stability theory has converged towards the formulation of the stability problem as an optimization problem, thereby sharing the strategy with systematic control theory. There is in other words little difference from a toolbox point of view in determining the stability characteristics of a flow and constructing a controller for it. This thesis has explored the use of global eigenmodes of generic boundary layer flows in order to perform stability analysis and also as a basis for model reduction. It has been possible to describe the main destabilising mechanisms by using a sum of eigenmodes. However the complexity of the systems to be studied in the coming years makes the route of going through the reduced basis of eigenmodes seem intractable. First of all creating the full discretized matrix of the Navier-Stokes equations is not an option for three-dimensional flows due to the vast memory requirements. Secondly, by using a time-stepper technique it is difficult to obtain a large number of eigenmodes needed for solving the optimization problem. Furthermore our computations have shown that the summing of eigenmodes becomes ill-conditioned when the system is very non-normal. Thus it seems more natural to use eigenmodes to describe global instability of the flow and as an initial step towards understanding the optimal growth features of the flow. To obtain fully reliable results on optimal growth one needs in general to solve the optimization problem using direct and adjoint DNS.

Model reduction provides a natural bridge from systematic feedback control in the numerical framework to experimental implementations. There are however still a few steps necessary to take in order to get there. The most important seems to be the detailed modelling of real actuators in the numerics. As it is at the present stage, the wall blowing and suction actuators are modelled by wall functions prescribing an analytic injection profile through a slot. In reality the actuators are small pipes with their own inherent flow dynamics. By using balanced truncation as a model reduction basis it is possible to get a small model that captures well the input output behaviour, but in order to do so the actuator has to be well described. Efforts should be put into creating reasonable actuators in the numerics that match the real ones. This consideration also applies to the numerical modelling of sensors. In other words the main steps towards realisability is to capture the input output behaviour in an

experiment by DNS. Once that is achieved it is envisioned that Direct Numerical Simulation will be used as a tool to construct controllers that optimally couple sensors to actuators such that systematic flow control can be used in real applications.

The teapot will perhaps in the end pour a straight beam.

CHAPTER 8

Summary of papers and division of work

Paper 1

Global two-dimensional stability measures of the flat plate boundary-layer flow Espen Åkervik, Uwe Ehrenstein, François Gallaire and Dan S. Henningson

Eur. J. Mech. B/Fluids, 27 (2008), pages 501-513

This paper deals with the use of global eigenmodes to compute optimal growth and optimal forcing in the flat plate boundary layer flow. A convergence in the number of eigenmodes needed in describing the optimal initial condition is obtained. The Orr mechanism is revisited and it is shown that this mechanism is not separated from the Tollmien–Schlichting mechanism, in fact they cooperate. The optimal forcing structures are similar to the optimal initial condition.

The writing of the paper was done by EÅ in collaboration with UE with feedback from FG and DH. The computation of the eigenmodes were done by EÅ and UE. The computation of the optimal initial condition was done by EÅ and the optimal forcing by EÅ and UE. Direct numerical simulations were performed by UE using a code developed by Matthieu Marquillie and UE.

Paper 2

Steady solutions of the Navier–Stokes equations by selective frequency damping. Espen Åkervik, Luca Brandt, Dan Henningson, Jérôme Hæpffner, Olaf Marxen, Philipp Schlatter.

Phys. Fluids 18, 068102 (2006).

A highly accurate numerical description of the base flow is necessary for stability analysis. Previously, for cases without symmetries, the Newton method was used to solve for steady solutions of the Navier–Stokes equations. We propose a method based on selective frequency damping, easy to implement in existing direct numerical simulation codes to stabilise steady state solutions, and thus reach them by time marching. The method was used in Paper 3 for the computation of the globally unstable base flow in the separated boundary layer flow.

The writing of the paper was done by LB and PS, with feedback from all authors. The computations of the cavity flow was done by EÅ, and by OM

for the recirculation bubble. The analysis of the stabilization and choice of the design parameters was done by JH.

Paper 3

Optimal growth, model reduction and control in a separated boundary-layer flow using global eigenmodes.

ESPEN ÅKERVIK, JÉRÔME HŒPFFNER, UWE EHRENSTEIN, DAN HENNINGSON

J. Fluid Mech., **579** (2007), pages 305–314.

This paper deals with optimal growth and control of a globally unstable cavity flow. Optimal growth analysis yields an upstream located initial wavepacket. This wavepacket propagates through the shear layer in the cavity and pressure reflections regenerate the disturbances upstream. A reduced order model for control based on as few as 4 eigenmodes is built, and the LQG controller is run in parallel to the DNS at a low computational cost. The satisfactory performance of the controller, combined with the low on-line computational effort provides promising perspectives of using reduced order models based on global eigenmodes for fluid flows.

The writing of the paper was done in collaboration by EÅ, JH and UE, with feedback from DH. The controller optimisations were done by JH and EÅ with a code developed by JH. The eigenmode computations were performed by EÅ with a code developed by UE. Implementations and computations of the steady base flow and the controller was done by EÅ with a direct numerical simulation code developed by Matthieu Marquillie and UE.

Paper 4

Matrix-free methods for the stability and control of boundary layers. Shervin Bagheri, Espen Åkervik, Luca Brandt, Dan S. Henningson. $AIAA\ Journal,\ submitted.$

This paper deals with matrix-free methods for the stability analysis and control design of the two-dimensional spatially developing Blasius boundary-layer. Both stability analysis and control design relies on solving very large eigenvalue problems. Iterative and adjoint-based techniques are employed to compute both asymptotic and short time growth. For control design the input-output behavior of the system is of interest and the snapshot-method is employed to compute a system consisting of a few balanced modes that correctly capture this behavior. The inputs are external disturbances and wall actuation and the outputs are sensors that extract wall shear stress.

The writing of the paper was done by SB, EÅ and LB with feedback from DH. Stability calculations using both the matrix and time stepper techniques were performed by EÅ. Implementation of the matrix solver was performed by EÅ, whereas the matrix-free method was implemented in collaboration between EÅ and Antonios Monokrousos. The input-output formulation was developed

by SB, who also implemented corresponding controller codes. Extensions to wall actuation/sensing were implemented by EÅ. Numerical computations for control were performed by EÅ.

Paper 5

Linear feedback control and estimation applied to instabilities in spatially developing boundary layers.

MATTIAS CHEVALIER, JÉRÔME HŒPFFNER, ESPEN ÅKERVIK, DAN HENNINGSON.

J. Fluid Mech., 588 (2007), pages 163-187.

The method to build covariance of the stochastic sources of excitation is applied to control and estimation in spatially developing boundary layer flow. Several cases of fundamental interest are considered: unstable Tollmien–Schlichting waves, unstable cross-flow vortices, transient growth and streaks. This paper is the follow up of Högberg & Henningson (2002) that focused on the control part.

The writing of the paper was done by MC, with feedback from JH, EÅ and DH. The computation of the control and estimation gains were performed by MC and EÅ with a computer program developed by JH and Marcus Högberg. The direct numerical simulation was performed by MC and EÅ using a code originally developed at the Department of Mechanics.

Paper 6

Global optimal disturbances in the Blasius flow using time-steppers. Antonios Monokrousos, Espen Åkervik, Luca Brandt, Dan S. Henningson.

Technical report.

The stability of a high Reynolds number flat plate boundary-layer Blasius flow to three-dimensional disturbances is studied using a time-stepper technique. Both the optimal initial condition leading to the largest growth at finite times and optimal forcing leading to the largest regime response at given frequencies are studied. A Lagrange multiplier technique is used to formulate the optimization problems. Both the optimal initial condition and the optimal forcing is for large spanwise wavenumbers governed by the lift-up mechanism. For small spanwise wavenumbers it is the Orr mechanism combined with oblique wave packet propagation that dominates.

The writing of the paper was done by EÅ, AM and LB with feedback DH. The computation of the optimal initial conditions was performed by EÅ, whereas the optimal forcing results were obtained by AM. The implementation of the adjoint DNS and the optimal forcing power iteration scheme was performed by AM, whereas the Arnoldi iteration scheme using ARPACK method was implemented by EÅ.

Related paper, not included in thesis:

The use of global modes to understand transition and perform flow control. Dan Henningson and Espen Åkervik. Phys. Fluids **20**, 031302 (2008).

This paper is a review of the use of global eigenmodes as a tool for understanding stability, building on the papers Schmid & Henningson (2002), Paper 1 and Paper 3. As such we felt that including this paper would lead to repetition of material. For readers who are new to the field of stability using global eigenmodes, this would however be most suitable paper to read first. Three flow cases are studied, starting with the simple waterfall problem of Schmid & Henningson (2002), through the more realistic Blasius flow (Paper 1) to finally end up with the more complicated Cavity flow (Paper 3). The details, such as the importance of summing eigenmodes, how to compute an Arnoldi factorisation and how to obtain a Riccati equation for control using a reduced order model, are treated more thoroughly than in Paper 1 and Paper 3.

The writing of the paper was done in collaboration by DH and EÅ. Most of the material from the waterfall problem were taken from Schmid & Henningson (2002), whereas the remaining results were produced by EÅ.

Acknowledgements

I would like to thank my main supervisor Dan Henningson for his great dedication to being a supervisor. My co-supervisor Luca Brandt is greatly acknowledged for sharing his bottomless inspiration. Uwe Ehrenstein is much obliged for the hospitality during my stays in Nice and Marseille and for Friday afternoon phone calls.

To my collaborators Mattias Chevalier, Jérôme Hœpffner, Shervin "Bang-Bang" Bagheri and Antonios Monokrousos: You have all taught me a lot. I am grateful to Philipp Schlatter for sharing his knowledge with me. François Gallaire is thanked for the work on the Orr mechanism.

My office mates at Plan 6 Johan "Nekton" Ohlsson, Qiang "Flexible" Li and Antonios deserves a big hug for being such nice guys. The other group members during these years have been Ardeshir Hanifi, Ori Levin, Erik Stålberg, Astrid Herbst, Stefan Ivanell, Carl-Gustav Unckel, Martin Byström, Lars-Uve "LU decomposition" Schrader¹, David Tempelmann (who I almost forgot to include), Olaf Marxen and Yohann Duguet. I thank you all for providing a pleasant work athmosphere.

Pär Ekstrand and Arne Nordmark have done a remarkable job maintaining my Linux machine, dhaulagiri.mech.kth.se, which has such a difficult name it is almost impossible to login into via ssh.

Thanks to Daniel Ahlman¹, Hanno Essén, Gunnar Tibert, Hans Silverhag, Andreas Carlson, Andreas Vallgren, Erik Lindborg, Carl-Ola Danielsson, Geert Brethouwer, Fredrik Lundell¹, Outi Tammisola, Jens Fransson, Bengt Fallenius, Gabrielle Bellani, Linus Marstorp, Tobias Strömgren, Olof Grundestam, Gustaf Mårtenson and all the others at Mechanics for all the chats in the "fikarum".

Takk kjære familie og vennar for all støtte.

I tilfelle du ikkje allereie visste det Ragna: Du er fantastisk! No står det skrive svart på kvitt, slik at du kan sitere meg på det.

¹I also thank you for proof reading

References

- AHUJA, S. & ROWLEY 2008 Low-dimensional models for feedback stabilization of unstable steady states. AIAA Paper 2008-553, 46th AIAA Aerospace Sciences Meeting and Exhibit.
- ÅKERVIK, E., HŒPFFNER, J., EHRENSTEIN, U. & HENNINGSON, D. S. 2007 Optimal growth, model reduction and control in a separated boundary-layer flow using global eigenmodes. *J. Fluid Mech.* **579**, 305–314.
- Alfredsson, P. H., Johansson, A., Haritonidis, J. H. & Eckelmann, H. 1988 The fluctuating wall-shear stress and the velocity field in the viscous sublayer. *Phys. Fluids* **31**, 1026–1033.
- Bagheri, S., Brandt, L. & Henningson, D. S. 2008 Input-output analysis, model reduction and control of the flat-plate boundary layer. *J. Fluid Mech.* Accepted for publication.
- Bertolotti, F. P., Herbert, T. & Spalart, P. R. 1992 Linear and nonlinear stability of the Blasius boundary layer. J. Fluid Mech. 242, 441–474.
- Bewley, T. R. 2001 Flow control: new challenges for a new renaissance. *Progress in Aerospace Sciences* 37, 21–58.
- Bewley, T. R. & Liu, S. 1998 Optimal and robust control and estimation of linear paths to transition. *J. Fluid Mech.* **365**, 305.
- BLACKBURN, H., BARKLEY, D. & SHERWIN, S. 2008 Convective instability and transient growth in flow over a backward-facing step. *J. Fluid Mech.* **608**, 271–304.
- BOYD, J. P. 2000 Chebyshev and Fourier Spectral Methods, 2nd edn. Dover Publications Inc, New York.
- Butler, K. M. & Farrell, B. F. 1992 Three-dimensional optimal perturbations in viscous shear flow. *Phys. Fluids A* 4, 1637–1650.
- CANUTO, C., HUSSAINI, M. Y., QUARTERONI, A. & ZANG, T. A. J. 1993 Spectral Methods in Fluid Dynamics. Springer, New York.
- Caraballo, E., Kasnakoglu, C., Serrani, A. & Samimy, M. 2008 Control input separation methods for reduced-order model-based feedback control. *AIAA Journal* **46** (9).
- Cathalifaud, P. & Bewley, T. 2004a A noncausal framework for model-based feedback control of spatially-developing perturbations in boundary-layer flow systems. part 1: Formulation. Systems and Control Letters 51, 1–13.

- Cathalifaud, P. & Bewley, T. 2004b A noncausal framework for model-based feedback control of spatially-developing perturbations in boundary-layer flow systems. part 2: Numerical simulations using state feedback. Systems and Control Letters 51, 15–22.
- Chevalier, M., Hæpffner, J., Bewley, T. R. & Henningson, D. S. 2005 State estimation in wall-bounded flow systems. Part II: Turbulent flows. *J. Fluid Mech.* **552**, 167 187.
- Chevalier, M., Schlatter, P., Lundbladh, A. & D.S., H. 2007 A pseudo spectral solver for incompressible boundary layer flows. *Technical Report, Trita-Mek* 2007-7
- Chomaz, J. M. 2005 Global instabilities in spatially developing flows: non-normality and nonlinearity. *Annu. Rev. Fluid Mech.* **37**, 357–392.
- Cossu, C. & Chomaz, J. 1997 Global measures of local convective instability. *Phys. Rev. Lett.* **77**, 4387–90.
- Curtain, R. & Zwart, H. 1995 An introduction to infinite-dimensional linear systems theory. New York: Springer Verlag.
- Daniel, J., Gragg, W. B., Kaufman, L. & Stewart, G. W. 1976 Reorthogonalization and stable algorithms for updating the gram-schmidt qr factorization. *Math. Comp.* **30**, 772–795.
- DEVILLE, M. O., FISCHER, P. F. & MUND, E. H. 2002 High-Order Methods for Incompressible Fluid Flow. Cambridge University Press.
- Ellingsen, T. & Palm, E. 1975 Stability of linear flow. Phys. Fluids 18, 487-488.
- Francis, J. G. F. 1961 The qr transformation: A unitary analogue to the lr transformation, parts i and ii. *Comp.J* 4, 265–272,332–345.
- Fransson, J., Talamelli, A., Brandt, L. & Cossu, C. 2006 Delaying transition to turbulence by a passive mechanism. *Phys. Lett. Rev.* **96** (064501).
- Gallaire, F. & Ehrenstein, U. 2008 Two-dimensional global low-frequency oscillations in a separating boundary-layer flow. *J. Fluid Mech.* **614**, 315–327.
- GASTER, M. 1965 On the generation of spatially growing waves in a boundary layer. J. Fluid Mech. 22, 433–441.
- Giannetti, F. & Luchini, P. 2007 Structural sensitivity of the cylinder wake's first instability. *J. Fluid Mech.* **581**, 167–197.
- Giles, M. B. & Pierce, N. A. 2000 An introduction to the adjoint approach design. Flow, Turbulence and Combustion 65 (3-4), 393–415.
- GILLIES, E. A. 1998 Low-dimensional control of the circular cylinder wake. J. Fluid Mech. 371, 157–178.
- GLAD, L. & LJUNG, T. 1994 Modeling of Dynamic Systems. Prentice Hall Information and System Sciences Series.
- Gunzberger, M. D. 1996 Perspectives in flow control and optimization. SIAM.
- Henningson, D. S. & Åkervik, E. 2008 The use of global modes to understand transition and perform flow control. *Phys. Fluids* **20** (031302).
- Hœpffner, J., Chevalier, M., Bewley, T. R. & Henningson, D. S. 2005 State estimation in wall-bounded flow systems. part I: Laminar flows. *J. Fluid Mech.* **543**, 263–294.

- HÖGBERG, M., BEWLEY, T. R. & HENNINGSON, D. S. 2003 Linear feedback control and estimation of transition in plane channel flow. J. Fluid Mech. 481, 149–175.
- HÖGBERG, M. & HENNINGSON, D. S. 2002 Linear optimal control applied to instabilities in spatially developing boundary layers. *J. Fluid Mech.* 470, 151–179.
- HUERRE, P. & MONKEWITZ, P. 1990 Local and global instabilities in spatially developing flows. Annu. Rev. Fluid Mech. 22, 473–537.
- ILAK, M. & ROWLEY, C. W. 2008 Modeling of transitional channel flow using balanced proper orthogonal decomposition. *Phys. Fluids* **20**, 034103.
- JOSHI, S. S., SPEYER, J. L. & KIM, J. 1997 A systems theory approach to the feedback stabilization of infinitesimal and finite-amplitude disturbances in plane poiseuille flow. J. Fluid Mech. 332, 157–184.
- Jovanovič, M. & Bamieh, B. 2001 Modeling flow statistics using the linearized Navier–Stokes equations. *Proc.* 40'th IEEE Conference on decision and control, FL.
- KAILATH, T., SAYED, A. H. & HASSIBI, B. 1999 Linear Estimation. Prentice-Hall, Inc.
- KEUN, L. H., CORTELEZZI, L., SPEYER, J. L. & KIM, J. 2001 Application of reducedorder controller to turbulent flows for drag reduction. *Phys. Fluids* 13 (5), 1321– 1330.
- Kim, J. 2003 Control of turbulent boundary layers. Phys. Fluids 15, 1093–1105.
- KIM, J. & BEWLEY, T. R. 2007 A linear systems approach to flow control. Annu. Rev. Fluid Mech. 39, 383–417.
- Kim, J. & Lim, J. 2000 A linear process in wall-bounded turbulent shear flows. *Phys. Fluids* **12** (8), 1885–1888.
- Kim, J. & Moin, P. 1985 Application of a fractional-step method to incompressible navier–stokes equations. *J. Comp. Phys.* **59**, 308–323.
- KLEISER, L. & SCHUMANN, U. 1980 Treatment of incompressibility and boundary conditions in 3-D numerical spectral simulations of plane channel flow. In *Proc. 3rd GAMM Conf. on Numerical Methods in Fluid Mechanics*, pp. 165–173. Vieweg, Braunschweig, Germany.
- Kreiss, G., Lundbladh, A. & Henningson, D. S. 1994 Bounds for treshold amplitudes in subcritical shear flows. *J. Fluid Mech.* **270**, 175–198.
- Landahl, M. T. 1980 A note on an algebraic instability of inviscid parallel shear flows. *J. Fluid Mech.* **98**, 1–34.
- Lehoucq, R. B., Sorensen, D. & Yang, C. 1997 Arpack users' guide: Solution of large scale eigenvalue problems with implicitly restarted arnoldi methods.
- LEWIS, F. & SYRMOS, V. 1995 Optimal control. John Wiley and Sons, New York.
- LUNDELL, F. 2007 Reactive control of transition induced by free-stream turbulence: an experimental demonstration. *J. Fluid Mech.* **585**, 41–71.
- Marquet, O., Sipp, D., Chomaz, J. M. & Jacquin, L. 2008 Amplifier and resonator dynamics of a low-reynolds-number recirculation bubble in a global framework. *J. Fluid Mech.* **605**, 429–443.
- Marquillie, M. & Ehrenstein, U. 2001 Numerical simulations of separating boundary-layer flow. $Computers\ and\ Fluids$.

- Moin, P. & Mahesh, K. 1998 Direct numerical simulation: A tool in turbulence reshearch. *Annu. Rev. Fluid Mech.* **30**, 539–578.
- MOLDER, C. & VAN LOAN, C. 2003 Nineteen dubios ways to compute the exponential of a matrix, twenty-five years later. Siam Review 45, 3–000.
- Moore, B. C. 1981 Principal component analysis in linear systems: controllability, observability and model reduction. *IEEE trans. on automatic control* **AC-26**, 17.
- NICHOLS, J. W., SCHMID, P. J. & RILEY, J. J. 2007 Self-sustained oscillations in variable-density round jets. *J. Fluid Mech.* **582**, 341–376.
- Noack, B., Afanasiev, K., Morzynski, M., Tadmor, G. & Thiele, F. 2003 A hierarchy of low-dimensional models for the transient and post-transient cylinder wake. *J. Fluid Mech.* 497, 335–363.
- NOACK, B., TADMOR, G. & MORZYŃSKI, M. 2004 Low-dimensional models for feedback flow control. Part I: Empirical galerkin models. In 2nd AIAA Flow Control Conference. Portland, Oregon, U.S.A., June 28 July 1, 2004, AIAA-Paper 2004-2408 (invited contribution).
- ORR, W. M. F. 1907 The stability or instability of the steady motions of a perfect liquid and of a viscous liquid. Part I: A perfect liquid. Part II: A viscous liquid. Proc. R. Irish Acad. A 27, 9–138.
- Peyret, R. 2002 Spectral Methods for Incompressible Viscous Flow. Springer, New York.
- REDDY, S. C. & HENNINGSON, D. S. 1993 Energy growth in viscous channel flows. J. Fluid Mech. 252, 209–238.
- Rempfer, D. 2006 On boundary conditions for incompressible navier–stokes problems. App. Mech. Rev. 59, 107–125.
- ROWLEY, C. R. 2005 Model reduction for fluids, using balanced proper orthogonal decomposition. *Int. J. Bifurcation and Chaos* **15**, 997–1013.
- ROWLEY, C. W., COLONIUS, T. & MURRAY, R. M. 2004 Model reduction for compressible flows using POD and Galerkin projection. *Physica D. Nonlinear Phenomena* **2004**, 115–129.
- SAAD, Y. & Gv, X. V. 1990 Numerical solution of large lyapunov equations. In Signal Processing, Scattering and Operator Theory, and Numerical Methods.
- SAGAUT, P. 2002 Large Eddy Simulation for incompressible flows, 2nd edn. Springer, Berlin, Germany.
- Schlatter, P., Stolz, S. & Kleiser, L. 2006 LES of spatial transition in plane channel flow. *J. Turbulence* 7 (33), 1–24.
- SCHLICHTING, H. 1933 Berechnung der Anfachung kleiner Störungen bei der Plattenströmung. ZAMM 13, 171–174.
- SCHMID, P. J. 2007 Nonmodal stability theory. Annu. Rev. Fluid Mech. 39, 129-162.
- Schmid, P. J. & Henningson, D. S. 2001 Stability and transition in shear flows. Springer.
- SCHMID, P. J. & HENNINGSON, D. S. 2002 On the stability of a falling liquid curtain. $J.\ Fluid\ Mech.\ 463,\ 163-171.$
- Schubauer, G. B. & Skramstad, H. F. 1947 Laminar boundary layer oscillations and the stability of laminar flow. *J. Aero. Sci.* 14, 69–78.

- SIPP, D. & LEBEDEV, A. 2007 Global stability of base and mean flows: a general approach and its applications to cylinder and open cavity flows. *J. Fluid Mech.* **593**, 333–358.
- SIROVICH, L. 1987 Turbulence and the dynamics of coherent structures. I Coherent structures. II Symmetries and transformations. III Dynamics and scaling. *Quarterly of Applied Mathematics* 45, 561–571.
- Sommerfeld, A. 1908 Ein beitrag zur hydrodynamischen erklärung der turbulenten flüssigkeitbewegungen. In Atti del 4 Congr. Internat. dei Mat. III, pp. 116–124. Roma.
- Squire, H. B. 1933 On the stability for three-dimensional disturbances of viscous fluid flow between parallel walls. *Proc. Roy. Soc. Lond. Ser. A* 142, 621–628.
- Tadmor, G., Noack, B., Morzyński, M. & Siegel, S. 2004 Low-dimensional models for feedback flow control. Part II: Controller design and dynamic estimation. In *2nd AIAA Flow Control Conference*, pp. 1–12. Portland, Oregon, U.S.A., June 28 July 1, 2004, AIAA Paper 2004-2409 (invited contribution).
- TOLLMIEN, W. 1929 Über die Entstehung der Turbulenz. Nachr. Ges. Wiss Göttingen, 21–44: Nachr. Ges. Wiss. Göttingen, (English translation NACA TM 609, 1931).
- Trefethen, L. N., Trefethen, A. E., Reddy, S. C. & Driscill, T. A. 1993 Hydrodynamic stability without eigenvalues. *Science* **261**, 578–584.
- TREFETHEN, N. & EMBREE, M. 2005 Spectra and Pseudospectra; The Behaviour of nonnormal matrices and operators. Princeton University Press,.
- Tuckerman, L. & Barkley, D. 2000 Bifurcation Analysis For Timesteppers, pp. 453–566. Numerical Methods for Bifurcation Problems and Large-Scale Dynamical Systems . Springer, New York.
- Weideman, J. A. C. & Reddy, S. C. 2000 A matlab differentiation matrix suite. ACM Transaction of Mathematical Software **26** (4), 465–519.
- WILCOX, D. C. 1998 Turbulence modelling for CFD, 2nd edn. DCW Industries, La Canada, USA.
- Zhou, K., Doyle, J. & Glover, K. 2002 Robust and Optimal Control. New Jersey: Prentice Hall.

Part 2

Papers

Paper 1

Global two-dimensional stability measures of the flat plate boundary-layer flow

By Espen Åkervik¹, Uwe Ehrenstein², François Gallaire³, Dan S. Henningson¹

¹ Linné Flow Centre, KTH Mechanics, SE-100 44 Stockholm, Sweden

Eur. J. Mech. B/Fluids, 27 (2008), pages 501-513

The stability of the two-dimensional flat plate boundary-layer is studied by means of global eigenmodes. These eigenmodes depend both on the streamwise and wall-normal coordinate, hence there are no assumptions on the streamwise length scales of the disturbances. Expanding the perturbation velocity field in the basis of eigenmodes yields a reduced order model from which the stability characteristics of the flow, i.e. the initial condition and forcing function leading to the largest energy growth, are extracted by means of non-modal analysis. In this paper we show that, even when performing stability analysis using global eigenmodes, it is not sufficient to consider only a few of the least damped seemingly relevant eigenmodes. Instead it is the task of the optimization procedure, inherent in the non-modal analysis, to decide which eigenmodes are relevant. We show that both the optimal initial condition and the optimal forcing structure have the form of upstream tilted structures. Time integration reveals that these structures gain energy through the so called Orr mechanism, where the instabilities extract energy from the mean shear. This provides the optimal way of initiating Tollmien-Schlichting waves in the boundary layer. The optimal initial condition results in a localized Tollmien-Schlichting wavepacket that propagates downstream, whereas the optimal forcing results in a persistent Tollmien-Schlichting wave train.

1. Introduction

Boundary layers, jets and mixing layers are examples of convectively unstable flows, where disturbances are amplified while being advected downstream. In these configurations, the flow relaxes in the absence of external disturbances. For certain parameter ranges, for example if the reversed flow in separated boundary layers becomes large, the flow might become absolutely unstable. Instead of constantly requiring external input to maintain the flow disturbances,

 $^{^2}$ IRPHÉ, Université de Provence, F-13384 Marseille Cedex 13, France

³ Laboratoire J.A. Dieudonné, Parc Valrose, F-06108 Nice Cedex 02, France

pockets of absolutely unstable regions support self-sustained oscillations. Following a phase of linear growth of the global mode, there is a saturation into a non linear limit cycle with the absolutely unstable flow domain acting as a wave maker shedding vorticity into the convectively unstable region. When the flow under consideration is slightly non-parallel it is possible to determine criteria for transition from globally stable, to convectively unstable and finally to absolutely unstable based on classical local analysis (Huerre & Monkewitz 1990). In local analyses the streamwise and spanwise directions of the flow are taken to be homogeneous, yielding eigenvalue problems depending only on the wall normal direction. When the length scales of the disturbances becomes comparable to those of the base flow, which is the case for highly non-parallel flows, it is clear that one has to resort to a global formulation of the stability problem, treating also the streamwise direction as inhomogeneous. The resulting matrix eigenvalue problem is typically very large, but owing to increased computer capabilities and efficient large scale eigenvalue solving strategies based on Krylov methods, it is nowadays tractable to compute global eigenmodes for many flow cases.

As the relevance of global analysis is well established for highly non-parallel flows (Åkervik et al. 2007), there are still some important issues to be dealt with when it comes to applying this methodology to slightly non-parallel situations. Considering the model problem provided by the Ginzburg-Landau equation with spatially varying coefficients, Cossu & Chomaz (1997) demonstrated that the non-normality of the streamwise eigenmodes leads to transient growth. This non-normality is considered to be associated with the streamwise separation of the direct and adjoint global modes due to the basic advection (Chomaz 2005). Schmid & Henningson (2002) advocated the robustness of optimally summing the streamwise eigenmodes when studying a model problem for a falling liquid curtain. They showed that the sum of modes, in contrast to single modes, yielded results in agreement with experiments. The use of global modes as a tool for studying the stability characteristics of the slightly non-parallel boundary-layer flow was addressed in Ehrenstein & Gallaire (2005). They found that a superposition of the damped global eigenmodes associated with Tollmien-Schlichting (TS) type of structures gave rise to a localized wavepacket at the inflow boundary. The wavepacket would grow while being advected downstream, in close agreement with direct numerical simulation results.

It is now well accepted that when incoming disturbances exceed a certain amplitude threshold the flat-plate boundary layer is likely to undergo transition due to three-dimensional instabilities through the lift-up effect (Ellingsen & Palm 1975; Landahl 1980). This transient growth scenario, where streamwise vortices form into streamwise streaks by the action of the mean flow, was studied for a variety of shear flows in the locally parallel assumption (cf. Butler & Farrell 1992; Reddy & Henningson 1993; Trefethen et al. 1993). The extension to the non-parallel flat plate boundary layer was performed at the same time

by Luchini (2000); Andersson $et\ al.$ (1999) marching the parabolized stability equations in the streamwise direction.

While emphasizing the strength of three-dimensional disturbances in general shear flows, Butler & Farrell (1992) found a two-dimensional instability mechanism not related to the TS-waves. This instability could extract energy from the mean shear by transporting momentum down the mean momentum gradient through the action of the perturbation Reynolds stress. This means that structures that are tilted against the shear, will first rise to an upright position while borrowing energy from the mean flow, after which the energy is returned to the mean flow and the disturbances decay. They referred to this as the Reynolds stress mechanism, commonly also known as the Orr mechanism.

In this paper we re-address two-dimensional stability mechanisms in the flat-plate boundary-layer flow, by considering the cooperation or competition of the wall-normal non-normal effects responsible for the Orr mechanism and the streamwise non-normal effects triggering the TS-waves, bearing in mind that the latter are the building blocks for the onset of the so-called classical transition in a low-level noise environment (Herbert 1988). The analysis is based on the computation of temporal two-dimensional modes and is hence free from any assumption concerning spatial length-scales. The non-normality of these eigenmodes of the linearized Navier-Stokes operator is shown to lead to large energy gain due to combination of the Orr and TS mechanisms.

The paper is organized as follows. Section 2 is devoted to the description of the numerical tools. Convergence results of the global eigenvalue spectrum are provided in Section 3. The optimal initial condition leading to the maximum energy gain is computed and discussed in Section 4. The signalling problem, that is the determination of the optimal harmonic forcing distribution of the Navier-Stokes system in a Direct Numerical Simulation sense (DNS), is addressed in Section 5. In particular, the disturbance flow evolution obtained through projection on the set of global eigenmodes is compared to the forced Navier-Stokes dynamics. Some conclusions are provided in Section 6.

2. Numerical tools

2.1. Basic state

The Navier–Stokes equations are solved by means of direct numerical simulation (DNS), both in order to obtain a steady state base flow for linearization and to compute the evolution of disturbances on top of this base flow. The Reynolds number $Re = U_{\infty} \delta^* / \nu = 1000$ is based on the freestream velocity U_{∞} , the displacement thickness δ^* at inflow x=0 and the kinematic viscosity ν . All variables are made dimensionless with U_{∞} and δ^* . The computational domain is $0 \le x \le 1000$, $0 \le y \le 80$. At inflow a Blasius profile is prescribed and at outflow a classical advection condition is imposed. No slip condition is enforced at the wall y=0 whereas at the top y=80 the flow is freestream

uniform, i.e. the streamwise velocity component is $u=U_{\infty}$ and the wall normal component is v=0. The DNS procedure has previously been used in Ehrenstein & Gallaire (2005). The flow variables are discretized using fourth-order finite differences in streamwise direction (with 5120 grid points) and Chebyshev-collocation in the vertical direction (with 97 collocation points). The steady state $\mathbf{U}=(U(x,y),V(x,y))$ and P(x,y) is obtained by integrating the Navier–Stokes in time by means of the DNS.

2.2. Two-dimensional temporal modes

By splitting the total flow field into a mean and a perturbation/fluctuating part $\mathbf{U} + \mathbf{u}$ and P + p and by linearizing the Navier-Stokes equations about the base flow one can easily recognize that the disturbance flow field with velocity components $\mathbf{u}(x,y,t)$ and pressure field p(x,y,t) satisfy the partial differential equations

$$\frac{\partial \mathbf{u}}{\partial t} = -(\mathbf{U} \cdot \nabla)\mathbf{u} - (\mathbf{u} \cdot \nabla)\mathbf{U} - \nabla p + \frac{1}{Re}\nabla^2 \mathbf{u},$$

$$0 = \nabla \cdot \mathbf{u}.$$
(1)

After discretization in the space variables this system can be written

$$\frac{d}{dt}\mathbf{B}\mathbf{q} = \mathbf{A}\mathbf{q},\tag{2}$$

where $\mathbf{q} = [\mathbf{u}, p]^T$ and \mathbf{B} is the projection of the total disturbance field \mathbf{q} on its velocity components, i.e. $\mathbf{B}\mathbf{q} = [\mathbf{u}, 0]$. Note that in (2) a divergence-free velocity field trivially satisfies $\mathbf{B}\mathbf{A}\mathbf{q} = \mathbf{A}\mathbf{q}$. Taking the exponential Ansatz for the time dependence $\mathbf{q}(x, y, t) = \tilde{\mathbf{q}}(x, y)e^{-i\omega t}$ yields the generalized eigenvalue problem

$$-i\omega_l \mathbf{B}\tilde{\mathbf{q}}_l = \mathbf{A}\tilde{\mathbf{q}}_l \tag{3}$$

with a divergence free velocity field $\tilde{\mathbf{u}}_l$ associated to each eigenmode $\tilde{\mathbf{q}}_l$. The computational domain used for the eigenmode calculations is $0 \le x \le L_x$, $0 \le y \le L_y$. In the wall normal y-direction a height of $L_y = 40$ was found sufficient to also resolve the eigenvectors associated with the low frequency part of the spectra. In the streamwise x-direction different lengths L_x have been considered, but the main parts of the results are presented for $L_x = 800$. Indeed the flat-plate boundary layer flow is convectively unstable and the box length will set a bound on the timescale at which the spatially growing disturbance wavepacket leaves the domain. Accordingly, the eigenmodes and the instability mechanisms will also be function of the box length. At the wall and at free-stream homogeneous Dirichlet conditions are imposed and at inflow and outflow the non-homogeneous Robin conditions proposed in Ehrenstein & Gallaire (2005) have been used. These boundary conditions essentially amount to matching the streamwise derivative of the global mode with spatial local analysis so that $\partial \mathbf{u}/\partial x = i\alpha \mathbf{u}$. The local dispersion relation connecting the

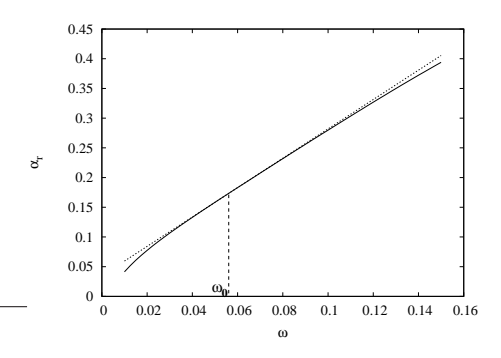


FIGURE 1. Real part of the wavenumber α_r . Solid line shows the α_r as provided by the local dispersion relation for the Blasius profile at inflow Re=1000, and the dotted line shows the linear approximation as given by the Gaster-type of approximation (4).

wave number α to the frequency ω is nonlinear, but performing a Gaster-type of transformation

$$\alpha \approx \alpha_{0,r} + \frac{\partial \alpha_r}{\partial \omega_r}(\omega_0)(\omega - \omega_0) \cdots$$
 (4)

yields a good linear approximation, as long as the imaginary parts of the complex frequency and wavenumber are small. Here the real frequency ω_0 is chosen such that $\alpha_0 = \alpha_{0,r}$ at the inflow boundary, that is at a frequency of neutral instability for the Blasius profile at inflow. Figure 1 shows the real part of the complex wavenumber α_r as function of the real frequency, as provided by the local dispersion relation for the Blasius profile at inflow Re = 1000, which is indeed close to its linear approximation (4) depicted as the dotted line. The domain is mapped into $[-1,1] \times [-1,1]$ and a Chebyshev-Chebyshev collocation discretization is used for the stability system. Chebyshev-collocation provides the most efficient discretization in terms of grid size, which puts a reasonable bound on the dimension of the resulting generalized matrix eigenvalue problem. Consequently, the basic steady flow computed by means of DNS is interpolated on the new grid (cf. Ehrenstein & Gallaire (2005) for details). We have chosen to consider the steady state for the Navier-Stokes system, rather than the self-similar solution of the flat-plate boundary-layer equations. One goal of the present analysis is to compare the Navier-Stokes dynamics with the time evolution of the eigenmodes system. It will be shown in Section 4 that a collocation grid with 250×45 collocation points yields converged stability results. The resulting eigenvalue problem is still far too large to be solved by standard QZ algorithms. Large-scale Krylov subspace projections with dimension m = 2000 together with the Arnoldi algorithm (Nayar & Ortega 1993) proved suitable to provide a complete, with respect to the disturbance dynamics, set of eigenvalues and corresponding eigenmodes.

2.3. Mode superposition

When determining the possibility of growth in a flow system the notions of optimal initial condition and optimal forcing are essential. These features are both closely related to the non-normality of the underlying operators (Schmid & Henningson 2001). We will here give a brief summary on how these optima are computed. The dynamical system (2) obtained after discretization defines an initial value problem by adding the initial condition

$$\mathbf{u}(0) = \mathbf{u}_0 \tag{5}$$

for a divergence-free velocity field \mathbf{u}_0 . We are looking for initial disturbances that maximize the energy at time t

$$G(t) = \max_{\mathbf{u}_0 \neq 0} \frac{||\mathbf{u}(t)||_E^2}{||\mathbf{u}_0||_E^2}$$

and a convenient form of this expression can be obtained by expanding the solution in terms of the generalized eigenmodes $\mathbf{u}(t) = \sum_{l=1}^{N} \kappa_l(t) \tilde{\mathbf{u}}_l$. Recall that the eigenmodes are the solutions to the generalized eigenvalue problem (3). Keeping in mind that the pressure acts as Lagrange multiplier in order to maintain divergence free velocity fields, the flow dynamics is then determined purely by the velocity components of the eigenmodes. Hence the flow dynamics is described by

$$\frac{\mathrm{d}\mathbf{k}}{\mathrm{d}t} = \mathbf{\Lambda}\mathbf{k}, \quad \mathbf{k}(0) = \mathbf{k}_0, \tag{6}$$

where $\mathbf{k} = [\kappa_1, \kappa_2, \dots, \kappa_N]$ is the vector of expansion coefficients and $\mathbf{\Lambda}$ is a diagonal matrix whose elements are given by $\Lambda_{ll} = -i\omega_l$. The flow perturbation energy in this basis is $||\mathbf{u}||_E^2 = ||\mathbf{F} \exp(\mathbf{\Lambda}t)\mathbf{k}_0||_2^2$, where F is the Cholesky factor of the Hermitian energy measure matrix \mathbf{M} with entries $M_{ij} = \int \tilde{\mathbf{u}}_i^H \tilde{\mathbf{u}}_j dx dy$. Hence, the maximum growth expressed in the basis of eigenmodes reads

$$G(t) = ||\mathbf{F} \exp(\mathbf{\Lambda}t)\mathbf{F}^{-1}||_{2}^{2}. \tag{7}$$

The largest growth at time t is given by the largest singular value of $\mathbf{F} \exp(\mathbf{\Lambda} t) \mathbf{F}^{-1}$ and the optimal initial condition is $\mathbf{k}_0 = \mathbf{F}^{-1} \mathbf{z}$, where \mathbf{z} is the right singular vector. Alternative ways of computing the optimal initial condition are by calculus of variations (Butler & Farrell 1992) or by time-marching/space-marching algorithms involving the adjoint operator (Luchini 2000; Andersson *et al.* 1999).

Let us now formulate the optimal forcing frequency and the corresponding forcing function. Consider the harmonically forced system

$$\frac{\partial}{\partial t} \mathbf{B} \mathbf{q} = \mathbf{A} \mathbf{q} + \{ \mathbf{q}_f \exp(-i\Omega t) \}, \quad \Omega \text{ real.}$$
 (8)

The asymptotic long time response for the stable system reads

$$\mathbf{q}_r(t) = -(\mathbf{A} + i\Omega \mathbf{B})^{-1} \mathbf{q}_f \exp(-i\Omega t). \tag{9}$$

Expressing the state in the basis of eigenmodes yields

$$\mathbf{k}_r(t) = -(\mathbf{\Lambda} + i\Omega \mathbf{I})^{-1} \mathbf{k}_f \exp(-i\Omega t). \tag{10}$$

The maximum response to the harmonic forcing at a frequency Ω expressed in this basis is

$$R(\Omega) = \max_{\mathbf{q}_f} \frac{||\mathbf{q}_r||_E}{||\mathbf{q}_f||_E} = ||\mathbf{F}(\mathbf{\Lambda} + i\Omega \mathbf{I})^{-1} \mathbf{F}^{-1}||_2.$$
 (11)

The norm of the the resolvent is readily obtained as the largest singular value of $\mathbf{F}(\mathbf{\Lambda} + i\Omega \mathbf{I})^{-1}\mathbf{F}^{-1}$ and the optimal forcing \mathbf{k}_f is retrieved from the right singular vector \mathbf{z} through the expression $\mathbf{k}_f = \mathbf{F}^{-1}\mathbf{z}$. In a similar manner the asymptotic response can be obtained from the left singular vector.

Two different contributions to large resolvent norms may be identified: resonances are triggered whenever the forcing frequency is chosen close to an eigenvalue of the system. On the other hand, the optimal forcing may exploit the large condition number of \mathbf{F} , related to the non-orthogonality of the eigenvectors.

3. The spectra and convergence of optima

3.1. Global Spectra and mode structures

Figure 2 shows the spectra obtained for the inflow Reynolds number Re=1000 displayed as stars. The box size of $L_x=800$, $L_y=40$ required $N_x=250$ and $N_y=45$ in order to yield converged results. The largest Krylov subspace size considered is m=2000. We found that increasing the number of points in both the streamwise and wall-normal direction only moved the most damped eigenvalues, associated with areas of a resolvent norm of the order of 10^6 (Trefethen & Embree 2005). As can be observed from the figure, there are many eigenmodes obtained by the eigenvalue calculation. We can identify several branches which all can be related to the spectrum of a parallel Blasius boundary layer, as found by solving the Orr-Sommerfeld equations, though modified by non-parallelism and boundary conditions.

From figure 2 one can observe that there is a branch of the global spectra which is identifiable as TS waves. This branch is marked with squares. The mode labelled m_1 is the least stable eigenmode for this specific box. In figure 3 a) the spatial structure of the streamwise velocity component of this eigenfunction is shown. The TS type of eigenfunctions have wall normal profiles that match the ones obtained from the OS equation, however with the difference that the global eigenfunctions are spatially evolving downstream. As shown in Ehrenstein & Gallaire (2005), the global eigenfunctions exhibit a spatial growth that locally match weakly non parallel TS waves at the corresponding global eigenfrequency.

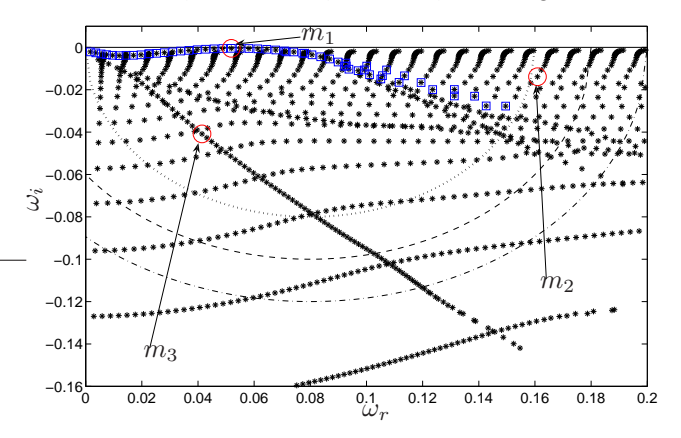


FIGURE 2. Stars show spectra at Re=1000. Included are also contours in the complex plane indicating size of Krylov subspace according to $|\omega-\sigma_0| < R$. (...) shows R=0.08, (...) shows R=0.1 and (...) shows R=0.12. Eigenvectors corresponding to labels m_1 , m_2 and m_3 are depicted in figure 3. Note especially that m_1 represents the TS type of eigenmodes, whereof the others are enclosed by squares.

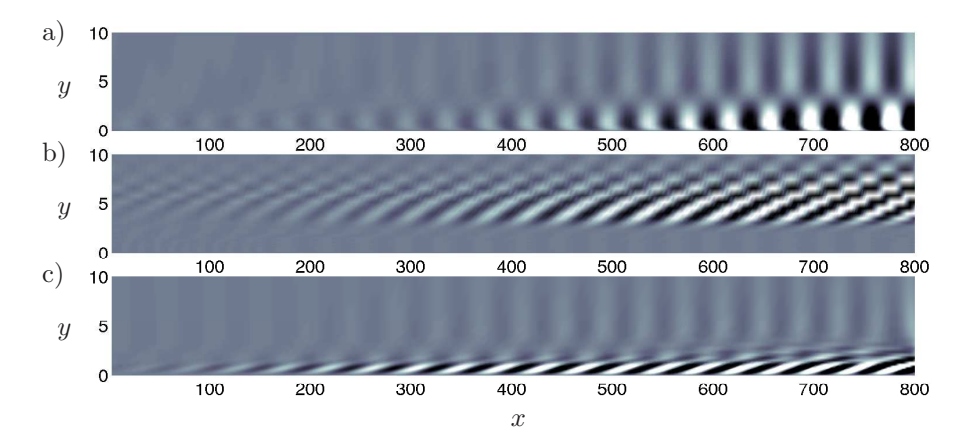


FIGURE 3. Streamwise component of eigenvectors corresponding to the eigenvalues labelled m_1 to m_3 in figure 2. a) (m_1) Least stable TS type of mode. b) (m_2) Mode associated with the wall normal continuous branch. c) (m_3) Orr type of mode. The last two are typical modes that due to cancelling with other non-orthogonal modes contribute to the Orr mechanism. Note that the domain is truncated at y=10 for visualization purposes.

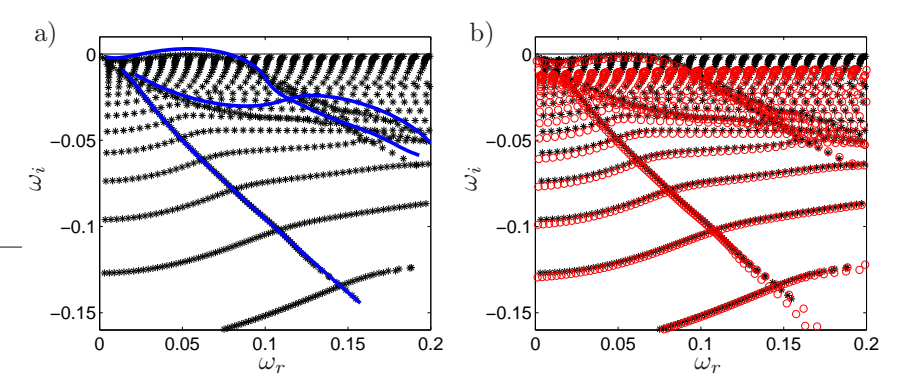


FIGURE 4. a) Solid lines trace three branches (the TS branch and two damped branches) of the spectra computed from the Orr-Sommerfeld equation when the wavenumber is varied continuously at Re=1374. Stars show the spectra already depicted in figure 2. Notice that for the Orr-Sommerfeld equation the TS branch crosses over to the unstable half plane, whereas in the global setting, the non-parallel baseflow renders the global spectrum stable. b) Comparison of spectra computed using the Robin boundary conditions (stars) and Dirichlet-Neumann (circles). One can see that the TS branch is slightly more damped using Dirichlet-Neumann. The continuous spectra is also more damped. Note that the discrete damped branches traced in a) are not significantly affected by the change of boundary conditions.

The modes labelled m_2 in figure 2 reach their maximum in the free stream and are reminiscent of the continuous spectrum of the local Orr-Sommerfeld analysis of a Blasius boundary layer flow. In the latter case the phase speed ω_r/α_r is close to the free stream velocity. In our non parallel framework, since α_r is not prescribed, the modes are aligned on a series of equidistant distorted S shapes.

The eigenmode labelled m_3 is representative of a wall normal discrete damped branch. From figure 3 c) it can be seen that the eigenfunction displays downstream tilted structures with an amplitude maximum inside the boundary layer. One might call these eigenmodes Orr modes, given their tilted structure, reminiscent of late stages of the Orr mechanism.

Let us further compare our global non parallel analysis to the well-known stability analysis of the parallel Blasius flow studied by means of the Orr-Sommerfeld equation. Such a comparison is not straightforward, since for each local position, and for each axial wavenumber, a full discrete and continuous spectrum is retrieved from the Orr-Sommerfeld equation. We found that the

best comparison could be done at the position x = 300, corresponding to a local Reynolds number of Re = 1374. In figure 4 a) we have represented some temporal stability branches of the discrete Orr-Sommerfeld spectrum, as they evolve when the axial wavenumber is continuously varied. More precisely, we depict as continuous lines in figure 4 a) the trace of the TS branch and two damped branches of the Orr-Sommerfeld equations as the wave number is varied. One can clearly see that global and local analysis yield quite similar results. Noticeable though is that under the locally parallel assumption the TS branch does cross over to the unstable half plane with an unstable range of axial wavenumbers, whereas, in the global setting the locally non parallel base flow renders the global spectrum stable. As discussed in Ehrenstein & Gallaire (2005), this is linked to the convective nature of the boundary layer flow. The damped branches are even more similar in the global and local settings, especially concerning the most damped branch which the mode m_3 is part of. Note that the wall normal shapes of the eigenfunctions are very similar in the global and local setting, but the global eigenfunctions are spatially evolving, growing as we move downstream.

Figure 4 b) compares the global spectra obtained with the Robin boundary conditions and the spectra obtained using homogeneous Dirichlet at inflow and homogeneous Neumann conditions at outflow. Clearly the different boundary conditions gives different damping rates for the TS type of eigenmodes, but the frequency of the least stable TS eigenmode is the same. Later we will explain that the different damping rates do not affect how the different set of modes describe the dynamics of the flow in the interior of the domain. It can also be seen that the boundary conditions strongly influence the location of the eigenvalues in the complex plane as the Dirichlet-Neumann boundary conditions yield a more damped continuous branch. However, m_3 types of modes, associated with tilted damped modes of Blasius flow are not especially sensitive to the choice of boundary conditions.

3.2. Convergence of optima

The number of global two-dimensional temporal modes obtained depends strongly on the size of the Krylov subspace, and it may even depend on the value of the shift used in the shift and invert procedure. Further, the location of the eigenvalues in the complex plane seem to be somewhat sensitive to the boundary conditions used. However, we will now show that the optimal transient growth that may be retrieved from them are far more robust. By selecting only the TS type of modes, Ehrenstein & Gallaire (2005) could obtain a growth in energy of one order of magnitude for Re=780 and a box length of 500 for the propagating wavepacket. In this paper we will show that by adding the other types of modes, one obtains a much larger growth which is associated with the combination of the Orr mechanism (Butler & Farrell 1992) and the spatiotemporal growth of the wavepacket formed by TS wave type of structures. An

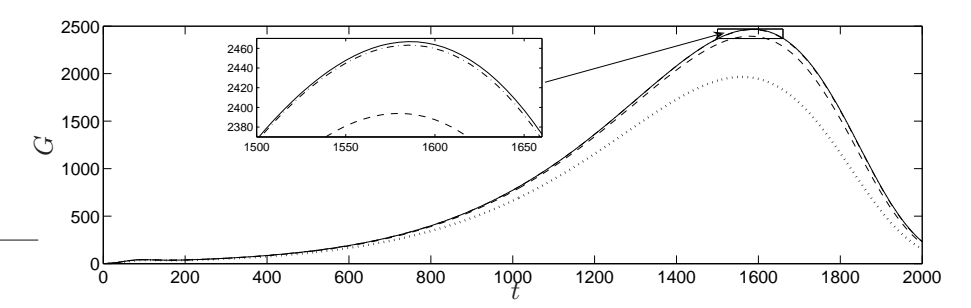


FIGURE 5. Envelope of optimal growth for different Krylov subspace sizes. (...) corresponds to R=0.08, (___) to R=0.1 and (_.._) to R=0.12. The solid line shows the envelope including all modes obtained (R=0.16). The inset shows a zoom at the maximum, indicating that the optimal growth is converged at R=0.12. The kink in energy at time $t\approx 100$ will be explained together with figure 6.

important issue that is discussed is the convergence of the optimal growth results in terms of number of modes included in the expansion. We here take the tentative approach, gradually increasing the number of modes used to describe our flow state, searching for convergence. To our knowledge no analysis similar to that performed by Gustavsson (1979) for the Orr-Sommerfeld equation has been published on the two dimensional problem.

The total number of eigenvalues obtained by the Arnoldi method when using a Krylov subspace of size m=2000 was 1205. For a given dimension of a Krylov subspace the Arnoldi method recovers converged eigenvalues contained within a circle of radius R around the shift value σ_0 . Note that for this case the suitable shift value of $\sigma_0=0.08$ could be taken a priori from local theory, but within reasonable limits the choice of σ_0 is not crucial when working with such large Krylov subspaces. Increasing the Krylov subspace dimension is equivalent to drawing a larger circle in the complex space, where eigenvalues are obtained. The resulting eigenvalues hence satisfy

$$|\omega - \sigma_0| \le R,\tag{12}$$

where the radius R depends on how large the Krylov subspace is. Figure 2 shows the radius resulting from three different Krylov subspace sizes on top of the spectra. The optimal growth envelope G(t), as computed according to equation (7), obtained using different truncations is shown in figure 5. We stress that the envelope reveals at each instance of time the maximum possible amplification due to a specific initial condition, i.e. there are possibly different initial conditions leading to the specific growth at each instance of time. It is seen that a radius of R = 0.08, corresponding to 715 eigenmodes, is not

sufficient to obtain converged results. A converging trend is seen for a radius of R=0.1, corresponding to 854 modes, whereas for R=0.12 (1014 modes) one may neglect the modification of the optimal growth envelope induced by a further increase of modes included in the optimization procedure. As mentioned earlier the spectra obtained when using Robin boundary conditions at inflow and outflow differed substantially in terms of damping rate ω_i from the spectra obtained using the Dirichlet-Neumann boundary conditions. In order to examine the influence of the different localization of eigenvalues in the complex plane we performed the optimal growth analysis using modes from both type of boundary conditions, truncating the basis at R=0.12. Indeed we did find that the optimal initial condition obtained using both sets are identical and the subsequent time evolution remains exactly the same.

Cossu & Chomaz (1997) was working on the model problem of Ginzburg-Landau mimicking convective growth. They conjectured that the more parallel the base flow becomes, the more non-normal the operator becomes and that consequently more modes are needed in order to locate optimal perturbations upstream. The flat plate boundary layer becomes more parallel with increasing Reynolds numbers. Indeed by performing the same convergence study for the lower Reynolds number of Re=500 we observed convergence could be obtained already at a radius of R=0.08, i.e. a small number of modes are needed.

4. Optimal initial condition

In the previous section we mentioned that it was possible to get a larger growth than that obtained when considering only the propagation of the TS type of wavepacket, and that this was due to the Orr mechanism. The thick solid line in figure 6 shows the envelope using an eigenmode expansion corresponding to a radius of R = 0.12 in a log scaling in order to emphasize the quick growth due to the Orr mechanism. Plotted as a thick dashed line in figure 6 is the envelope obtained when using only modes related to the TS instabilities, however multiplied by a factor of ≈ 20 . This effectively means that one through the Orr mechanism has gained a factor of ≈ 20 compared to using only TS type of eigenfunctions. As earlier mentioned the envelope of the growth yields the maximum possible growth at each instance of time, with possibly different initial conditions leading to the optimal growth at different times. The thin solid line in figure 6 shows the actual energy evolution obtained by initializing the flow system with the structures leading to the global maximum growth at time t = 1594. The thin dash-dotted line shows the actual energy evolution of the disturbance leading to maximum energy growth at time t = 98. One can see that the optimal growth due to this pure Orr mechanism is a fast growing fast decaying disturbance. Note that the growth-factor as well as the corresponding optimal time (t = 98 and E = 41.6) are approximately twice as high as those provided by the local analysis of Butler & Farrell (1992) for a parallel Blasius boundary layer at Re = 1000 (t = 45 and E = 28). However,

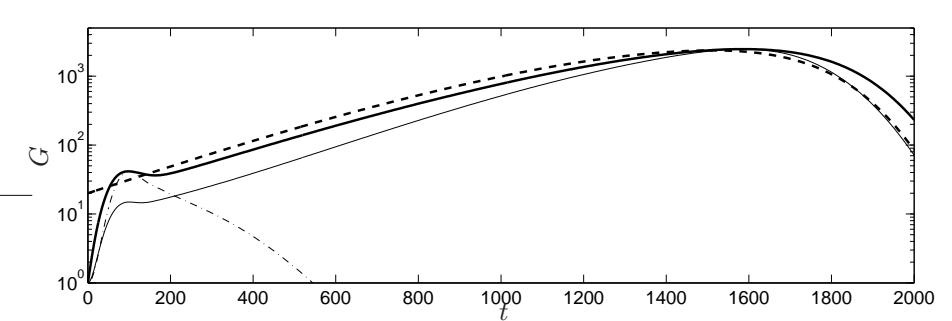


FIGURE 6. Thick lines show envelopes of energy growth due to initial conditions. The thick solid line shows the envelope when using a Krylov subspace corresponding to R=0.12 and the thick dashed line shows the envelope obtained when using only the TS type of modes in the optimization, magnified by a factor of 20, i.e. there is a gain of ≈ 20 in combining the Orr and TS mechanism. The thin lines shows actual energy evolution when initializing the flow system with the structures that leads to the maximum growth at time t=98 (thin dash-dotted) and t=1594 (thin solid).

according to the time evolution of the streamwise velocity during the growth interval displayed in figure 7, it becomes clear, that comparison with the local theory should not be attempted using the inlet Reynolds number Re = 1000but rather with a local Reynolds number representative of the location of the initial condition (using for instance the midpoint of the support of the initial perturbation, located at x = 610, this yields Re = 1700). We have therefore performed local optimal growth calculations based on a parallel Blasius boundary layers of displacement thickness 1.7 (corresponding to the local Reynolds number Re = 1700), yielding an optimal time t = 120 with corresponding optimal growth 34.8, closer to the result provides by the global optima. Note that there is no reason that the local results based on the parallel flow assumption should perfectly match with the global non parallel computations. The corresponding optimal wavelength from local theory equals 25 and is depicted by an double arrow in figure 7 a), comparing favourably with the underlying wavelength in the wavepacket. Our local computations have further shown a tendency for the Orr mechanism of increasing optimal growth, increasing optimal time and increasing optimal wavenumber, when the boundary layer thickness and thereby the Reynolds number both increase. This tendency is clearly illustrated by figure 8 which shows for various box lengths, $L_x = 800,600,400$ for the different frames from top to the bottom, that the optimal initial condition for this pure Orr mechanism is always located as far downstream as possible within the box. In contrast to the downstream located structures that yield

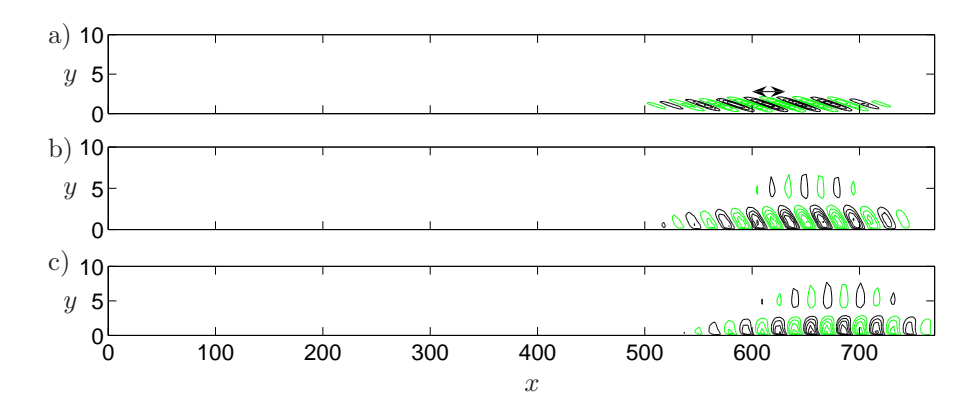


FIGURE 7. Time evolution of streamwise velocity with the Orr mechanism at Re = 1000 leading to the energy evolution depicted as the thin dash-dotted line in figure 6. a) Initial condition. b) t = 50. c) The maximum is located at t = T = 98 for which $E_T/E_0 = 41.6$. The double arrow in a) shows the wave length of 25 as predicted by local theory.

the maximum growth for short times (see thin dash-dotted line in figure 6), the structures that leads to a large growth at larger times (see the thick line) are located far upstream as depicted in figure 9 a). The energy gain due to the upstream Orr mechanism is only half of that of the downstream located one (compare thin-solid and thin dash-dotted lines in figure 6, however as can be seen from figure 9 the disturbances gain energy through the Orr mechanism, after which they have the form of a TS type of wavepacket that propagates throughout the domain. The above results demonstrate that while the long-time behaviour of the disturbance is governed by the travelling wavepacket, its starting amplitude is optimized through the Orr mechanism.

5. Optimal forcing

Since boundary layers are convectively unstable, acting thereby as noise amplifiers, a preeminent role is played by the response to forcing, rather than by the detailed time-evolution of the initial condition, and the optimal forcing is therefore a relevant measure of the maximum possible growth that may be obtained in the box. While the evolution due to the optimal initial condition can be seen as a wave packet propagating, eventually leaving the computational box (or measurement section), the response from the flow to forcing will be persistent structures that at each streamwise station have a fixed amplitude, oscillating around the mean flow. In this section we are investigating the structure of the optimal forcing and the response at different frequencies. Figure 10 shows the resolvent norm as defined in (11), where a large value indicates a

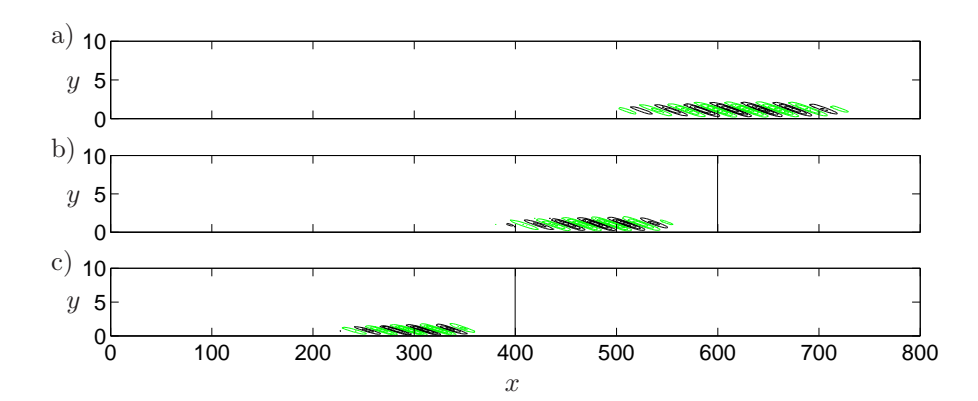


FIGURE 8. Initial conditions corresponding to the pure Orr mechanism for different domain lengths. a) $L_x=800$, b) $L_x=600$ and c) $L_x=400$. The vertical lines indicates the end of the computational domain. The optimal initial condition is always located close to the outflow boundary, consistent with the prediction made in local analysis; namely that the Orr mechanism has increasing growth potential for increasing Reynolds number.

large response to the given real frequency Ω . Note that the magnitude of the resolvent norm is both influenced by the distance $\operatorname{dist}(\mathbf{\Lambda} + i\Omega \mathbf{I})$ in the complex plane to the eigenvalues and the condition number $\operatorname{cond}(\mathbf{F}) = ||\mathbf{F}||_2 ||\mathbf{F}^{-1}||_2$ of the Cholesky factor of the energy measure. For normal operators the condition number is unity, hence the distance from an eigenvalue and the resolvent norm coincide. However, in our case the discretized dynamical matrix A is highly non-normal, so the condition number is considerably larger than unity. The dash-dotted line in figure 10 shows the gain due to the resonance effects associated with forcing close to an eigenvalue, whereas the thin solid line shows the gain obtained by including only TS type of modes in the optimization. When using a sufficient number of modes (corresponding to a radius R = 0.12 in the complex plane) we again observe a considerable increase in growth potential. The peak of the response for all cases is at the frequency $\Omega = 0.055$ and the streamwise component of the corresponding forcing structure is shown in the inset in figure 10. Analogous to the optimal initial condition case, when using a sufficient number of modes in the optimization procedure Orr type of structures are produced, efficiently initializing TS waves. The optimal forcing structure is however more elongated in the streamwise direction than the optimal initial condition. The Orr mechanism provides a factor of five in gain compared to forcing only TS type of structures and a factor of 25 compared to exploiting pure resonant effects. The neutral point for this frequency (branch I) predicted

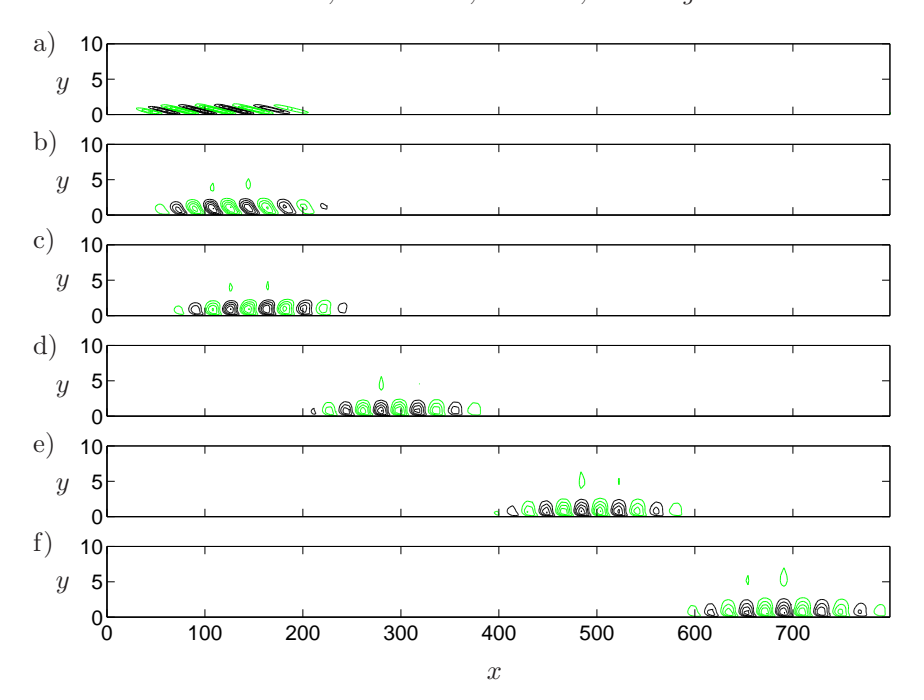


FIGURE 9. Time evolution for streamwise velocity with the combined Orr and TS mechanism. Note that the amplitude is growing from frame to frame. a) t=0, maximum amplitude A=0.2 b) t=50, A=0.38 c) t=100, A=0.52 d) t=480, A=1.0 e) t=960, A=2.78 and f) t=1440, A=5.8.

by local theory is located at x=0. We would expect the optimal forcing to be located in the vicinity of this neutral point, and indeed the forcing is located close to branch I. For lower frequencies we observe that the optimal forcing structures move further downstream and consist of longer wave lengths.

5.1. Direct Numerical Simulation results

A verification of the ability of the eigenmode system to capture the relevant dynamics of the flow is performed by applying the optimal forcing in DNS. For this purpose the real part of the optimal forcing device $\mathbf{q}_f \exp(-i\Omega t)$ has been interpolated on the DNS grid and added as a forcing function to the Navier-Stokes system. The time evolution in the eigenmode system is given explicitly in terms of the expansion coefficients

$$\mathbf{k}(t) = -(\mathbf{\Lambda} + i\Omega \mathbf{I})^{-1} \mathbf{k}_f \left(\exp\left(-i\Omega t\right) - \exp(\mathbf{\Lambda}t) \right). \tag{13}$$

Note that equation (10) describes the asymptotic response of the system. Figure 11 shows the pointwise energy integrated in the wall-normal direction,

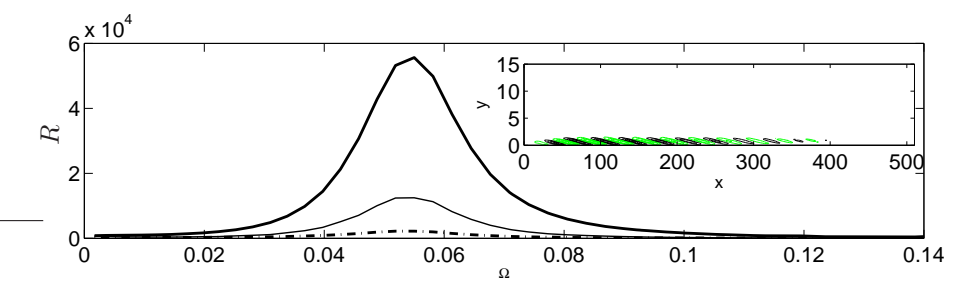


FIGURE 10. Response to forcing at different frequencies. The thick line solid line shows the resolvent using a set of modes satisfying $|\omega-0.08|<0.12$. The thin solid lines shows the resolvent including only TS type of modes and the dash-dotted line shows the gain due to resonance. It is clear that one through non-normal effects have gained a factor of ≈ 25 (compare thick solid with dash-dotted line), whereas one through the Orr mechanism has gained a factor of ≈ 5 compared to using only TS type of modes. The peak response of all systems is at $\Omega=0.055$. The inset shows the streamwise velocity component of the corresponding optimal forcing structure using all modes.

comparing the evolution in the DNS (solid lines) and the eigenmode system (dash-dotted lines). Snapshots are taken at times 80,720,1360 and 2000 with the amplitude growing as time increases. The response from the optimal forcing is the Orr mechanism followed by a TS wave. At time 2000 the disturbance has filled the box and the energy reaches a threshold where TS waves occupy most of the domain. The simple evaluation of 919 expansion coefficients yields an evolution in close agreement with the DNS, which for comparison has 1.5×10^6 degrees of freedom. At time 2000, even though the two systems are in phase an amplitude difference appears, most likely due to nonlinear effects as well as to some possible weak reflections in the eigenmode system.

6. Conclusions

For highly non-parallel flows the validity of the local approach is questionable rendering the global eigenmodes the natural tool for stability analysis. If the flow under consideration is only slightly non-parallel local analysis may still provide correct results, but it is nevertheless interesting to establish the stability characteristics of the flow in terms of the global eigenmodes of the operator. The global eigenmodes provides the "full" description of the dynamics within the computational box. The Arnoldi method together with the shift and invert strategy locates the eigenmodes closest to the shift value within a radius in the complex plane given by the size of the Krylov subspace. The computed

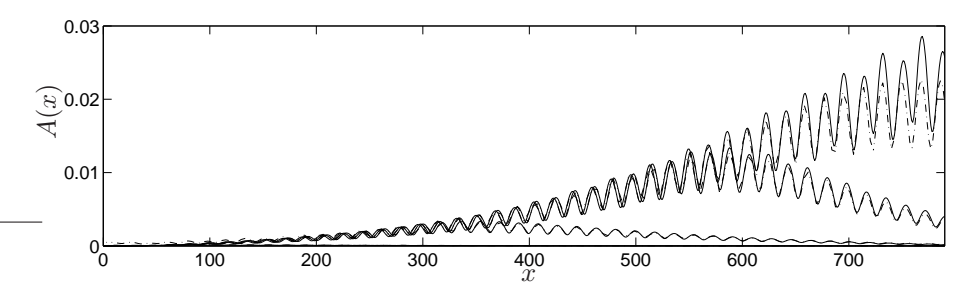


FIGURE 11. Evolution of pointwise energy integrated in wall-normal direction at times 80, 720, 1360 and 2000. Solid lines shows DNS whereas dash-dotted shows eigenmode system. The amplitude is growing with increasing times. Note that at time 2000 the disturbance has filled the box and the energy reaches a threshold where TS waves occupy most of the domain. Note that the lines showing the integrated energy at time t=80 are not visible due to their small amplitudes.

eigenmodes serve as a reduced basis in view of stability investigations, for which the basic procedure is to study features related to the pseudospectra, such as optimal initial conditions and optimal forcing. For the slightly non-parallel flow case studied here, many eigenmodes are needed in order to obtain converged results in terms of these measures. Both the optimal growth and optimal forcing analysis show that a combined effect of the Orr and TS-wave mechanism yields a large potential for downstream amplification in this convectively unstable regime. It is the description of the upstream located tilted Orr structures that requires a large number of modes; the description of the TS waves only requires about 20 eigenmodes. Optimal forcing structures are applied both in the eigenmode system and in the DNS, and the subsequent time-evolutions in the two systems match very well. This confirms the robustness of optimally summing eigenmodes in order to bring out the important dynamics of the flow.

Acknowledgement

The authors would like to thank Matthieu Marquillie for providing the DNS code and Jérôme Hœpffner for fruitful discussions. Anatoli Tumin is acknowledged for suggestions on global/local spectrum comparisons.

References

- ÅKERVIK, E., HŒPFFNER, J., EHRENSTEIN, U. & HENNINGSON, D. S. 2007 Optimal growth, model reduction and control in a separated boundary-layer flow using global eigenmodes. *J. Fluid Mech.* **579**, 305–314.
- Andersson, P., Berggren, M. & Henningson, D. S. 1999 Optimal disturbances and bypass transition in boundary layers. *Phys. Fluids* **11**, 134–150.
- Butler, K. M. & Farrell, B. F. 1992 Three-dimensional optimal perturbations in viscous shear flow. *Phys. Fluids A* 4, 1637–1650.
- Chomaz, J. M. 2005 Global instabilities in spatially developing flows: non-normality and nonlinearity. *Annu. Rev. Fluid Mech.* **37**, 357–392.
- Cossu, C. & Chomaz, J. 1997 Global measures of local convective instability. *Phys. Rev. Lett.* **77**, 4387–90.
- EHRENSTEIN, U. & GALLAIRE, F. 2005 On two-dimensional temporal modes in spatially evolving open flows: the flat-plate boundary layer. *J. Fluid Mech.* **536**, 209–218.
- Ellingsen, T. & Palm, E. 1975 Stability of linear flow. Phys. Fluids 18, 487–488.
- Gustavsson, L. H. 1979 Initial value problem for boundary layer flows. *Phys. Fluids* **22**, 1602–1605.
- HERBERT, T. 1988 Secondary instability of boundary layers. *Annu. Rev. Fluid Mech.* **20**, 487–526.
- HUERRE, P. & MONKEWITZ, P. 1990 Local and global instabilities in spatially developing flows. Annu. Rev. Fluid Mech. 22, 473–537.
- Landahl, M. T. 1980 A note on an algebraic instability of inviscid parallel shear flows. J. Fluid Mech. 98, 1–34.
- Luchini, P. 2000 Reynolds-number-independent instability of the boundary layer over a flat surface: Optimal perturbations. *J. Fluid Mech.* **404**, 289–309.
- NAYAR, M. & ORTEGA, U. 1993 Computation of selected eigenvalues of generalized eigenvalue problems. *J. Comput. Phys.* **108**, 8–14.
- Reddy, S. C. & Henningson, D. S. 1993 Energy growth in viscous channel flows. $J.\ Fluid\ Mech.\ 252,\ 209-238.$
- Schmid, P. J. & Henningson, D. S. 2001 Stability and transition in shear flows. Springer, New York.

- Schmid, P. J. & Henningson, D. S. 2002 On the stability of a falling liquid curtain. $J.\ Fluid\ Mech.\ 463,\ 163-171.$
- Trefethen, L. N., Trefethen, A. E., Reddy, S. C. & Driscill, T. A. 1993 Hydrodynamic stability without eigenvalues. *Science* **261**, 578–584.
- Trefethen, N. & Embree, M. 2005 Spectra and Pseudospectra; The Behaviour of nonnormal matrices and operators. Princeton University Press.

Paper 2

Steady solutions of the Navier-Stokes equations by selective frequency damping

By Espen Åkervik, Luca Brandt, Dan S. Henningson, Jérôme Hæpffner, Olaf Marxen & Philipp Schlatter

Linné Flow Centre, KTH Mechanics, SE-100 44 Stockholm, Sweden.

Phys. Fluids 18, 068102 (2006)

A new method, enabling the computation of steady solutions of the Navier-Stokes equations in globally unstable configurations, is presented. We show that it is possible to reach a steady state by damping the unstable (temporal) frequencies. This is achieved by adding a dissipative relaxation term proportional to the high-frequency content of the velocity fluctuations. Results are presented for cavity-driven boundary-layer separation and a separation bubble induced by an external pressure gradient.

1. Introduction

The knowledge of a steady base-flow solution of the governing Navier-Stokes equations is fundamental to instability studies and flow control. In the former case it allows for both linear modal and non-modal analyses and weakly nonlinear approaches, whereas in the latter case the stabilization of such a base flow can be adopted as a design target. Recent developments, for example as reviewed in Theofilis (2003), have allowed the research community to examine the stability of flows in increasingly complex configurations and to compute two- and three-dimensional eigenmodes, the so-called global modes (Chomaz 2005). Unfortunately, when the flow under consideration is globally unstable, it is virtually impossible to numerically compute a steady-state solution of the Navier-Stokes equations by time-marching methods, in particular for highorder schemes with inherently low numerical dissipation. In some limited cases solutions can be obtained by, e.g., artificially setting the velocity component in certain directions to zero or enforcing symmetries in the system, the most studied example for the latter case being the two-dimensional flow around a circular cylinder. For other cases, the only remaining possibility is the class of Newton iteration methods, which require heavy computational resources for large systems. In this article, we propose a simple numerical approach to compute steady solutions of the Navier-Stokes equations in unstable configurations. We show that it is possible to reach a steady state by damping the most dangerous frequencies and thus quenching the corresponding instability. The method is adapted from large-eddy simulation (LES) techniques, in particular considering the work of Pruett $et\ al.\ (2003,\ 2006)$.

2. Problem formulation

Consider the nonlinear system $\dot{q}=f(q)$, with appropriate initial and boundary conditions for the vector quantity q under the operator f(q). (A dot is used here to denote the derivative with respect to time). For a flow problem, the above system is the Navier-Stokes equations. A steady state q_s is then given by $\dot{q}_s=f(q_s)=0$. If f is unstable, any $q\neq q_s$ will quickly depart from q_s . In order to stabilize the above system we propose to apply regularization techniques common in control theory, in this case in the form of proportional (P) feedback control. This amounts to adding to the right-hand side a linear term forcing towards a target solution w,

$$-\chi(q-w) , \qquad (1)$$

where χ is the control coefficient. The theoretical target solution for the control is of course the steady-state solution q_s , which is however not available a priori. Therefore, the actual target solution is a modification of q with reduced temporal fluctuations, i.e. a temporally low-pass filtered solution w = T * q, defined as the convolution of q with the temporal filter kernel T. For the method to converge asymptotically in time to an exact solution of the steady equation, the filter cut-off frequency should be lower than that of the flow instabilities. Therefore, in the following, the unstable frequency will be referred to as high frequency. With these definitions, the modified system is written as

$$\dot{q} = f(q) - \chi(I - T) * q , \qquad (2)$$

where I is the identity operator. As q is approaching q_s , the filtered solution w=T*q will in turn approach q, therefore reducing the control influence. If q is the actual steady solution, the time-filtered value w will be identical to $q=q_s$, yielding a vanishing forcing. Hence the steady solution q_s of the controlled system (2) is also a steady solution of the original problem. Note that there is no generation of new artificial steady states.

A related technique is also used in large-eddy simulation (LES) for the temporal approximate deconvolution model (TADM) (see Pruett et al. 2006). Working with spatial filters, a similar relaxation term has been successfully applied in the spectrally-vanishing viscosity (SVV) concept introduced by Tadmor (1989) and in the (spatially filtered) approximate deconvolution model (ADM) of Stolz et al. (2001) and the ADM-RT model of Schlatter et al. (2004). Following these modeling ideas, a different interpretation of the method can be given as follows. To attenuate unstable high-frequency temporal oscillations and thus reach a steady state we include in the momentum equations an additional linear

regularization term, expression (1). This term is effectively damping the high-frequency content of q. Two parameters have to be chosen in the stabilization procedure, the filter shape T and the control gain χ . Time-domain filters are discussed first.

3. Time-domain filter

For a continuous function q(t), a causal low-pass time filter is defined

$$\overline{q}(t) = \int_{-\infty}^{t} T(\tau - t; \Delta) \ q(\tau) d\tau \ , \tag{3}$$

where \overline{q} is the temporally filtered quantity, T is the parameterized filter kernel and Δ its associated filter width (Pruett *et al.* 2003). To be admissible, the kernel T must be positive and properly normalized. Additionally, in the limit of vanishing filter width the filter (3) must approach the Dirac delta function. Probably the simplest example of such a filter is the exponential kernel,

$$T(\tau - t; \Delta) = \frac{1}{\Lambda} \exp(\frac{\tau - t}{\Lambda}) , \qquad (4)$$

with the corresponding transfer function in Fourier/Laplace space

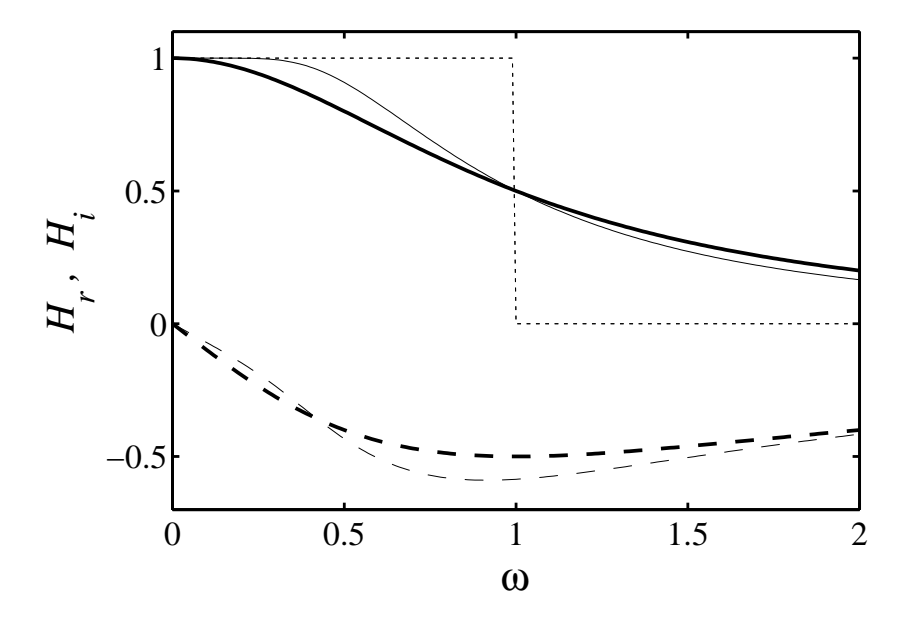
$$H(\omega; \Delta) = \int_{-\infty}^{0} T(\tau; \Delta) \exp(i\omega\tau) d\tau = \frac{1}{1 + i\omega\Delta} , \qquad (5)$$

where ω is the circular frequency and $\mathbf{i} = \sqrt{-1}$. The cutoff frequency of the filter is defined as $\Re(H(\omega_c; \Delta)) = 1/2$ and is given by $\omega_c = 1/\Delta$. The transfer function of the filter is represented in figure 1 for a fixed filter width Δ . Note that the transfer function has a considerable imaginary part, which leads to a phase lag in the filtered signal relative to the original signal. For real applications, the integral formulation of the filter (3) is impractical, since it requires the storage of the complete time history of the signal q. Therefore, the equivalent differential form is adopted,

$$\dot{\overline{q}} = \frac{q - \overline{q}}{\Delta} \ , \tag{6}$$

which can be readily advanced in time using any integration scheme.

The order of the filter is defined as the index of the first non-vanishing derivative of $\Re(H(\omega))$ with respect to ω at $\omega=0$, i.e. the filter (5) is of second order. Based on the exponential filter, also higher-order low-pass filters can be constructed by repeated application of the primary low-pass filter H (Pruett et al. 2006). The use of higher-order filters allows a better control over the separation between damped and undamped frequencies. For specific cases, i.e. if the separation between instability mode and relevant flow phenomena is small, such a filter can be beneficial, e.g. in terms of convergence rate. Figure 1 displays the transfer function of $10^{\rm th}$ -order filter (degree N=4, i.e. four applications of the exponential filter) with adapted filter width. This is one



particular case of the general formulation where the shape of the filter transfer function can be tailored for specific demands (Kailath 1980).

4. Stabilization of unstable steady solution

Analysis of the dynamics of the augmented system is presented in order to elucidate the stabilization procedure and quantify the effect of the control parameters. Considering system (2) with the exponential temporal filter (6), i.e. $w = \overline{q}$, the new system becomes

$$\begin{aligned}
\dot{q} &= f(q) - \chi(q - \overline{q}) \\
\dot{\overline{q}} &= (q - \overline{q})/\Delta
\end{aligned}$$
(7)

The effect of the regularization can be illustrated by considering the eigenvalues of system (7) linearized about the steady state. Introducing the Jacobian A of f at the steady state q_s , the linearized system is

$$\begin{pmatrix} \dot{q} \\ \dot{\overline{q}} \end{pmatrix} = \begin{pmatrix} A - \chi I & \chi I \\ I/\Delta & -I/\Delta \end{pmatrix} \begin{pmatrix} q \\ \overline{q} \end{pmatrix}. \tag{8}$$

Assume $\mu = \mu_T + i\mu_i$ is a complex eigenvalue of A (i.e. $-i\mu\phi = A\phi$) with corresponding eigenvector ϕ . Observation of the structure of system (8) suggests that the eigenvectors of the new system will be $[\phi, \alpha\phi]^T$ where α is a complex number to be determined, and the corresponding eigenvalue will be $\lambda = \lambda(\mu, \alpha, \chi)$. Introducing this ansatz in (8), α and λ are obtained as

$$\alpha^{\pm} = \frac{-F \pm \sqrt{F^2 + 4\Delta \chi}}{2\Delta \chi}, \text{ with } F := \Delta(-i\mu - \chi) + 1,$$

$$\lambda^{\pm} = \mu - i\chi(1 - \alpha^{\pm}). \tag{9}$$

The two solutions α^+ and α^- give two eigenvalues λ^+ and λ^- for the modified system, originating from the same eigenvalue μ of the original system. The eigenvalue λ^+ can be seen as the damped original eigenmode, whereas λ^- is roughly associated to the filtering and corresponds to the $1/\Delta$ term in (8). The mapping $\mu \to \lambda^{\pm}$ in the complex plane is illustrated in figure 2 for parameters $\chi = 0.02$ and $\Delta = 15$. Two lines are represented (indicating possible eigenvalues μ of the original system), with imaginary parts 0.01 and -0.03, respectively. (These regions approximately correspond to the eigenvalues we are interested to damp in the cavity flow presented below). Each line is mapped into two curves, the dashed one corresponding to λ^+ , and dash-dotted line to λ^- . The arrows indicate how two points of the original solid lines are mapped into the new eigenvalues. It can be seen that points with large real part (corresponding to large circular frequency) are simply damped, i.e. shifted downwards, by a constant value χ , with virtually no shift along the real axis. Points of small real part are moved towards the origin exhibiting both a decrease in frequency and change in growth rate (imaginary part). The width of the hump forming at low frequencies is related to the filter cutoff frequency, i.e. $1/\Delta$. It should be noted that a stable eigenvalue μ with low frequency will never be mapped into the unstable region.

In summary, the filter cutoff ω_c is related to the frequency of the relevant instabilities and should be smaller than those frequencies at which perturbation growth is expected. The gain χ is related to the growth rates of the instabilities and should be large enough to move the instability modes to the lower half plane. However, choosing a large χ will render the system evolution slow, since the low-frequency eigenvalues associated with the filter, λ^- , move towards the origin of the complex plane. The system will eventually converge to a steady state, but very slowly owing to the low damping rates. In order to have λ^+ as the least damped eigenvalue, χ needs to satisfy $\mu_i < \chi < \mu_i + 1/\Delta$. Similarly, when choosing Δ large, the additional eigenvalues, whose imaginary parts cluster around $\omega_c = 1/\Delta$, will make the subsystem for \bar{q} very slow. A balance has to be found for each system at hand to obtain quick convergence of all the time scales of the system. Testing several parameter pairs on the linear system (8) can be helpful. In cases where the Jacobian A cannot be approximated, like for the separation bubble presented below, the frequency of

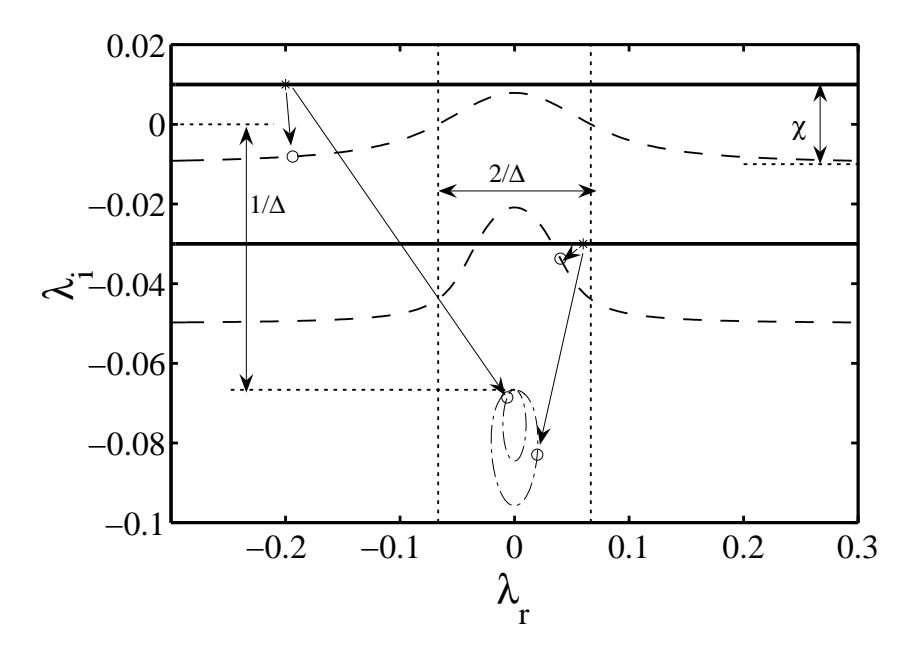


FIGURE 2. Mapping of two lines ($\mu_i = 0.01$ and $\mu_i = -0.03$, —) in the complex plane due to the modified (linear) system (8). Two points originate from each complex eigenvalue μ , one point corresponding to λ^+ (----) and one corresponding to λ^- (---). $\chi = 0.02$, $\omega_c = 1/\Delta = 1/15$.

the instability can be estimated by considering the resulting unstable flow. As a guideline, the regularization parameter χ is chosen to be twice the growth rate of the dominant disturbance. The cutoff frequency, $\omega_c = 1/\Delta$ is chosen in such a way that the unstable disturbances are well within the damped region, e.g. $\omega_c \approx 1/2\,\omega_{\rm dist}$. If the growth rate is unknown, one can estimate χ to be slightly smaller than $\mu_i + 1/\Delta \approx 1/\Delta$ assuming small μ_i .

5. Results

The selective frequency damping (SFD) method is applied to compute the steady state of the two-dimensional flow over a long cavity, and of the separation bubble induced by an external pressure distribution. Implementation of the present method into an existing code amounts to increasing the memory to store the filtered variable \overline{q} , adding the forcing term in the original time-marching scheme and advance the linear equation (6).

The streamfunction pertaining to the steady state of the cavity-driven separated flow is displayed in figure 3, where the streamwise and wall-normal

coordinates are made non-dimensional with the inflow boundary-layer displacement thickness δ^* . The inflow profile is the Blasius profile at Reynolds number $Re_{\delta^*} = 350$. This value has been chosen by gradually increasing it until a global unstable flow is obtained. The streamwise extent of the computational domain is $L_x = 409$, with the cavity being confined to an area of $x \in [30, 150]$, whereas the wall-normal height is $L_y = 80$. The numerical code uses fourthorder central finite differences and Chebyshev collocation in the streamwise and wall-normal direction, respectively. The time integration is carried out by a semi-implicit second-order backward Euler/Adams-Bashforth scheme as described in Marquillie & Ehrenstein (2003). Time history of the streamwise velocity measured just above the cavity is shown in figure 4 for two different simulations. In the first simulation, the SFD is active from the beginning of the computation where a zero initial condition is used, whereas in the second simulation SFD is switched on at time t = 3000. Both simulations eventually converge to the exact same steady state, in one case smoothly and in the other by damping the existing oscillations, the saturated unstable global mode.

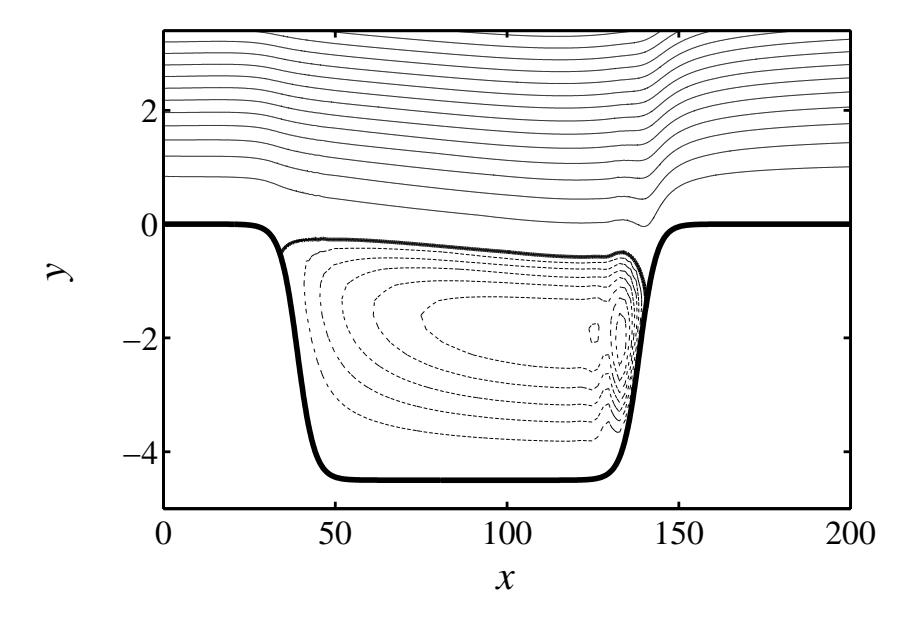


FIGURE 3. Contour lines of the steady-state streamfunction for the cavity case. Zero streamfunction is indicated by the thick line, solid lines indicate positive values with spacing 0.2, dotted lines negative values (spacing 0.025). The recirculation zone inside the cavity and the upward flow motion at the point of reattachment of the shear layer are clearly visible.

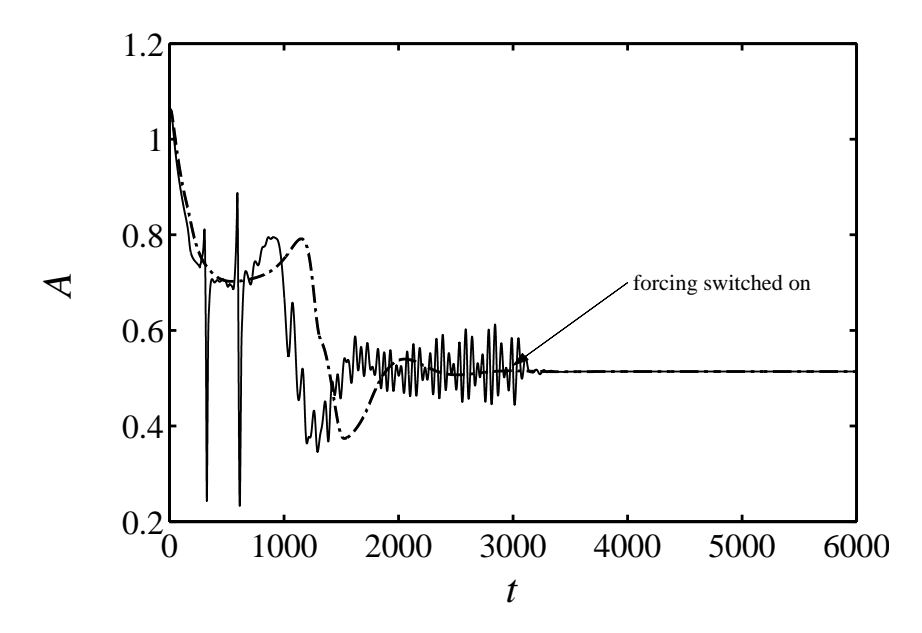


FIGURE 4. Time history of streamwise velocity measured just above the cavity at x = 153.4, y = 0.8485. (---): Simulation started with zero initial condition. (----): SFD turned on at t = 3000. Both cases are converging to identical steady states.

In the case of the separation bubble, a flow field subject to a pressure gradient prescribed via the streamwise velocity at the upper boundary is computed. The equations are solved in vorticity-velocity formulation, with the relaxation term $-\chi (\vartheta_z - \overline{\vartheta}_z)$ being added to the right-hand side of the transport equation for the spanwise vorticity ϑ_z . The code uses fourth/sixth-order finite differences on a Cartesian grid for the streamwise and wall-normal discretization together with an explicit fourth-order Runge-Kutta time integration (Kloker 1998). For the present case, a Blasius profile is prescribed at the inflow ($Re_{\delta^*}=1000$) while at the upper boundary, the streamwise velocity is quickly decreasing to about 10% of the free-stream velocity and then increasing again. The box size is $L_x \times L_y = 562 \times 64$, and $\chi = 0.4$, $\Delta = 0.75$. Two different resolutions (801 × 193) and 1601×385) were used, with the time step adapted accordingly. The resulting steady state is shown in figure 5. To check convergence towards an exact solution of the steady equations, the absolute difference between the filtered and the unfiltered vorticity $\vartheta_z - \overline{\vartheta}_z$ was sampled over time and its maximum in the domain is plotted in figure 6. Without the SFD, no steady state could be reached. The damped oscillatory behavior visible in figure 6 is not related to the frequency of the vortex shedding. It is conjectured that this is an indication of a stable oscillatory movement of the bubble itself, i.e. so-called flapping of the separation bubble. Note that the quantity $\vartheta_z - \overline{\vartheta}_z$ displayed in figure 6 is in fact proportional to both the amplitude of the relaxation term and the time derivative of the evolution equation of the filtered solution, $\bar{\vartheta}_z$. The simultaneous vanishing (to order 10^{-6} , which is sufficiently accurate for most applications) of $\partial \overline{\vartheta}_z/\partial t$ and the relaxation term as t becomes large implies that ϑ_z and $\overline{\vartheta}_z$ each essentially attain time independence; that is, a steady state has been achieved. Additionally, both grid resolutions showed the exact same convergence behavior which further stresses the point that an actual physical solution has been found. We also checked that no drifting of the steady solution is present by considering the evolution of $\vartheta_z(t+T) - \vartheta_z(t)$ over time t with T being large compared to the dominant shedding frequency. A similar behavior as in figure 6 was found and the diagram is therefore not shown here. In the case of the laminar separation bubble, the flow parameters are not incremented to follow a bifurcation but the pressure distribution is chosen arbitrarily to have an unstable flow. We thus show that the method allows attainment of a steady state without any initial guess. Of course, the initial condition becomes relevant in cases where multiple steady states coexist.

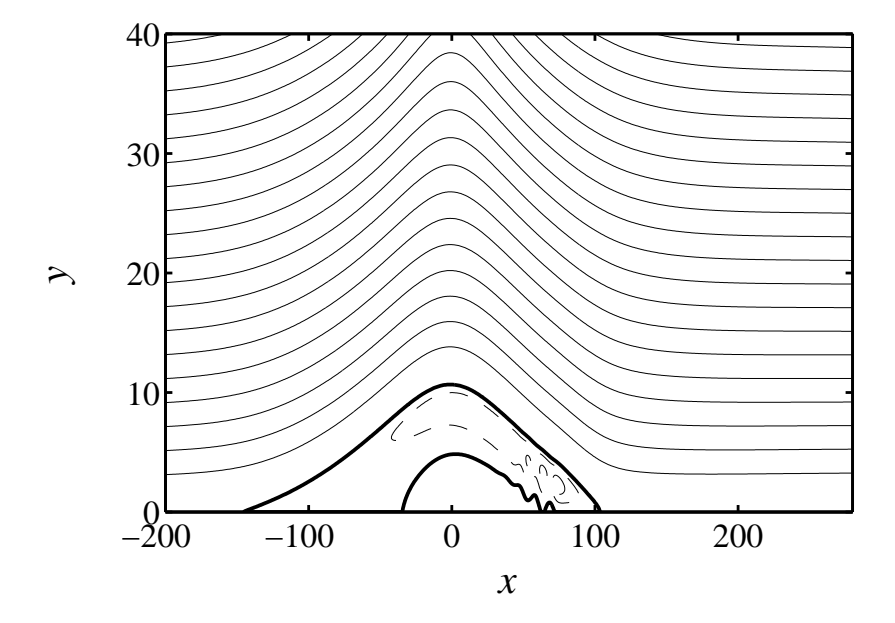


FIGURE 5. Contour lines of the streamfunction for the separation bubble. Zero streamfunction is indicated by the thick line, solid lines indicate positive values with spacing 0.1, dashed lines negative values (spacing 0.005).

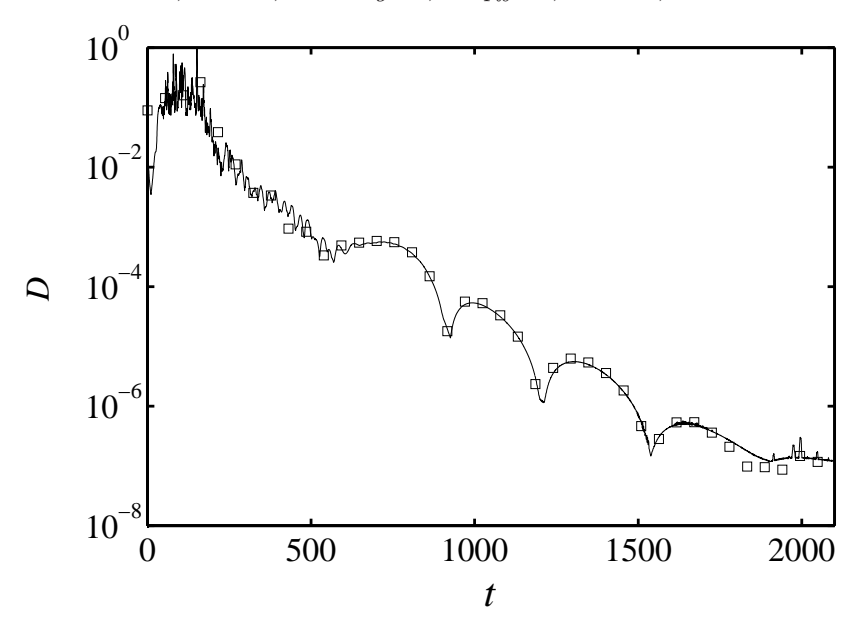


FIGURE 6. Convergence towards steady state for the separation-bubble case, showing the maximum difference between the filtered and unfiltered vorticity field, $D = \max_{x,y} |\vartheta_z - \overline{\vartheta}_z|$. ——lower resolution, \square higher resolution.

6. Conclusions

A simple numerical approach to compute steady solutions of the Navier-Stokes equations is presented. The most attractive advantages of such a strategy can be summarized as follows. It is easy to implement into an existing numerical code; it does not require a good initial guess of the solution; steady states can be computed without specific knowledge of the critical bifurcation parameters. To our experience, the SFD method appears to be very robust, and therefore this procedure provides a viable alternative to the classic Newton method.

Acknowledgements

The authors wish to acknowledge a fruitful discussion with Arne Nordmark (KTH Mechanics). P.S. thanks financial support by the Göran Gustafsson Stiftelse. O.M. acknowledges the Deutsche Forschungsgemeinschaft DFG under grant Ma 3916/1–1. Ulrich Rist and Markus Kloker (IAG, University of Stuttgart) and Uwe Ehrenstein (University of Nice-Sophia Antipolis) are thanked for providing the DNS codes.

References

- Chomaz, J.-M. 2005 Global instabilities in spatially developing flows: non-normality and nonlinearity. *Annu. Rev. Fluid Mech.* **37**, 357–392.
- Kailath, T. 1980 Linear systems. Prentice Hall.
- KLOKER, M. J. 1998 A robust high-resolution split-type compact fd scheme for spatial direct numerical simulation of boundary-layer transition. Appl. Sci. Res. 58, 353–377.
- MARQUILLIE, M. & EHRENSTEIN, U. 2003 On the onset of nonlinear oscillations in a separating boundary-layer flow. *J. Fluid Mech.* **490**, 169–188.
- PRUETT, C. D., GATSKI, T. B., GROSCH, C. E. & THACKER, W. 2003 The temporally filtered Navier–Stokes equations: Properties of the residual stress. *Phys. Fluids* $\bf 15$ (8), 2127–2140.
- PRUETT, C. D., THOMAS, B. C., GROSCH, C. E. & GATSKI, T. B. 2006 A temporal approximate deconvolution model for LES. In *Phys. Fluids*, **18** (028104),1–4.
- Schlatter, P., Stolz, S. & Kleiser, L. 2004 LES of transitional flows using the approximate deconvolution model. *Int. J. Heat Fluid Flow* **25** (3), 549–558.
- Stolz, S., Adams, N. A. & Kleiser, L. 2001 An approximate deconvolution model for large-eddy simulation with application to incompressible wall-bounded flows. *Phys. Fluids* **13** (4), 997–1015.
- Tadmor, E. 1989 Convergence of spectral methods for nonlinear conservation laws. SIAM J. Numer. Anal. 26 (1), 30–44.
- Theofilis, V. 2003 Advances in global linear instability analysis of non-parallel and three-dimensional flows. *Prog. Aerosp. Sci.* **39** (4), 249–315.

3

Paper 3

Optimal growth, model reduction and control in a separated boundary-layer flow using global eigenmodes

By Espen Åkervik 1 , Jérôme Hæpffner 2 , Uwe Ehrenstein 2 and Dan S. Henningson 1

 $^{\rm 1}$ Linné Flow Centre, KTH Mechanics, SE-100 44 Stockholm, Sweden

J. Fluid Mech., 579 (2007), pages 305-314

Two-dimensional global eigenmodes are used as a projection basis both for analysing the dynamics and building a reduced model for control in a prototype separated boundary-layer flow. In the present configuration, a high aspect ratio smooth cavity-like geometry confines the separation bubble. Optimal growth analysis using the reduced basis shows that the sum of the highly non-normal global eigenmodes are able to describe a localized disturbance. Subject to this worst-case initial condition, a large transient growth associated with the development of a wavepacket along the shear layer followed by a global cycle related to the two unstable global eigenmodes is found. The flow simulation procedure is coupled to a measurement feedback controller, which senses the wall shear stress at the downstream lip of the cavity and actuates at the upstream lip. A reduced model for the control optimization is obtained by a projection on the least stable global eigenmodes, and the resulting linear-quadratic-gaussian controller is applied to the Navier-Stokes time integration. It is shown that the controller is able to damp out the global oscillations.

1. Introduction

Open flows, such as boundary layers, wakes and mixing layers are subject to convective instabilities, where the flow acts as an amplifier of disturbances as they are transported downstream. For some of the flow cases and in particular parameter ranges, self-sustained oscillations may occur. This self-sustaining mechanism can be captured by the unstable global eigenmodes of the linearized Navier–Stokes operator. However, a combination of damped global modes is also capable of representing convective instabilities in non-parallel flows (Cossu & Chomaz 1997; Schmid & Henningson 2002; Ehrenstein & Gallaire 2005). Numerical investigations performed by Marquillie & Ehrenstein (2003) addressed separated boundary-layer flow produced by two-dimensional bump geometries.

² IRPHÉ, Université de Provence, F-13384 Marseille Cedex 13, France

They showed that elongated separation bubbles are likely to undergo bursting leading to unsteadiness. By confining the recirculation bubble between two successive bumps on the plate, Marquillie & Ehrenstein (2003) interpreted the flow oscillations in terms of the existence of a global saturated mode oscillating at a well-defined period. Building on their findings we introduce a smooth high aspect-ratio (length to depth ratio $L/D \approx 25$) cavity-like geometry, which induces a geometrically confined separation bubble in the boundary-layer flow as seen in figure 1. Note that this flow case differs from the sharp-edged small aspect-ratio (typically L/D = 2) high Reynolds number compressible cavity flow arising in aerospace applications (see e.g. Rowley & Williams 2006). We view this flow case as a prototype separated flow, where both streamwise nonnormality and global instability play a central role. In this non-parallel configuration global eigenmodes of the linearized Navier-Stokes operator becomes a natural tool for stability analysis. In this paper we first show that a sum of the non-normal global modes well describes the development of a wavepacket and the onset of a global oscillating cycle associated with the two unstable eigenmodes. Given this ability to reproduce the flow dynamics, the eigenmodes are used as a basis for a Petrov/Galerkin projection, enabling us to build a reduced-order model for control.

During the last decade modern control theory has increasingly been applied to fluid flow problems, given the available computer capacities and sensor/actuator developments. Linear optimal control theory has been introduced to flow systems governed by linear instability mechanisms (Bewley & Liu 1998), as for instance spatially developing boundary layers (Högberg & Henningson 2002) and it may also be relevant for nonlinear flows, such as turbulent boundary-layers (Kim 2003). Optimal control of fluid flow based on full state-space representation of the flow field necessitates manipulation of very high-dimensional dynamical systems. In weakly non-parallel flow configurations the problem may become tractable by determining control and estimation kernels for individual wavenumbers in the approximately homogeneous space directions (Högberg & Henningson 2002). In practical flow situations full state information is not available, hence the flow state must be estimated based on sensor measurements. The estimation process can be seen as an optimal filtering problem using a Kalman filter, based on the linearized Navier-Stokes equations. Appropriate stochastic models for the relevant statistics of sensor noise and external disturbances are essential in order to extract the relevant information from the system (Hoepffner et al. 2005). In the present work we use the linear quadratic gaussian (LQG) control synthesis, where the two subproblems of full information control and estimation are solved separately in an optimal manner. Combining the two leads to an optimal measurement feedback control, where the estimated flow is used for control feedback (see e.g. Lewis & Syrmos 1995).

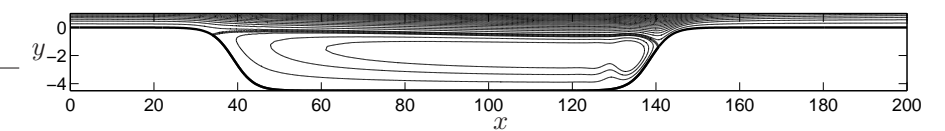


FIGURE 1. Streamlines of steady state base flow solution used for stability analysis at Re=350. The thick line represents the zero level contour. Note the large aspect ratio of $L/D\approx25$ and the smooth lips.

The design of the controller is intimately related to model reduction and the usual procedure is that of projecting the equations onto a subspace. One possible approach is to use the proper orthogonal decomposition modes of the excited flow, thereby capturing the high-energy content of the flow. Balanced truncation provides a more attractive basis by selecting vectors that are equally controllable and observable. When the system becomes large (e.g. 1000 states or more) the standard approach of directly solving Lyapunov equations needed for balanced truncation becomes intractable. Rowley (2005) discussed a computationally tractable approach to obtaining the balancing vectors, based on time-marching algorithms. In globally unstable flow configurations, the global eigenmodes of the linearized Navier–Stokes system form a natural projection basis due to their immediate physical interpretation. For instance one can judge the best placement of the sensors and actuators for observability and controllability, intimately connected to the localization of the least stable direct and adjoint modes respectively (Chomaz 2005).

2. Flow configuration and numerical methods

The Navier–Stokes equations are solved in the domain $0 \le x \le 400$, $\eta(x) \le y < 80$, large enough to recover freestream uniform flow. All variables are made non-dimensional with the displacement thickness δ^* and the free-stream velocity U_{∞} at the inflow x=0, where a blasius profile is prescribed. The Reynolds number is defined as $Re=U_{\infty}\delta^*/\nu$, where ν is the kinematic viscosity. The function $\eta(x)$ is the graph of the wall. The smooth cavity is symmetric with respect to its centre at $x_c=89$, and its upstream part is given by $\eta(x)=-2.25 \left(\tanh(a(x-b)) + 1 \right), 0 \le x \le x_c$ with a=0.2 and b=39 matching smoothly the flat plate upstream and downstream.

The streamlines in a subset of the computational domain for the steady state at Re=350 are depicted in figure 1. Note that the main effect of the smooth cavity is the generation of a recirculation zone and a shear layer. The Direct Numerical Simulation (DNS) procedure has previously been used in Marquillie & Ehrenstein (2003). Accounting for wall curvature a mapping transforms the physical coordinates into the computational ones, which are discretized using fourth-order finite differences in streamwise direction (with

2048 grid points) and Chebyshev-collocation in the vertical direction (with 97 collocation points).

2.1. Steady state

We found that above Re=325 the flow became subject to self-sustained oscillations. For a general geometry of this type it is the Reynolds number combined with the length to depth ratio L/D and the non-dimensional depth D/δ^* that constitutes the relevant non-dimensional quantities, however when fixing the length and depth of the smooth cavity the Reynolds number is the only relevant bifurcation parameter. In a globally unstable regime any noise present in the high order numerical discretization will grow exponentially, making it impossible to numerically compute a steady-state solution by standard time-marching methods. Therefore the technique proposed in Åkervik $et\ al.\ (2006)$ is used to recover the steady state at the current Reynolds number of Re=350. The Navier–Stokes equations are forced by adding a term proportional to the difference between the flow state and a filtered solution. If $\dot{q}=\mathrm{NS}(q)$ represents the nonlinear Navier–Stokes system, the modified system reads

$$\dot{q} = NS(q) - \chi(q - \bar{q}), \quad \dot{\bar{q}} = (q - \bar{q})/\Delta,$$
 (1)

where the rightmost equation represents the differential form of a causal low-pass temporal filter. The steady state of (1) is also a steady state of the Navier–Stokes system. A filter width of $\Delta=15$ has been chosen such that the frequencies of the instability are targeted and a damping coefficient $\chi=0.02$ was found to be appropriate (see Åkervik *et al.* 2006).

2.2. Eigenmodes

The global eigenmodes are computed linearizing the Navier–Stokes system about the steady state $\boldsymbol{U}(x,y)=(U(x,y),V(x,y))$. The disturbance flow field $\boldsymbol{u}(x,y,t)=\hat{\boldsymbol{u}}(x,y)~e^{-i\omega t}$ and pressure $p(x,y,t)=\hat{p}(x,y)~e^{-i\omega t}$ satisfy the partial differential system

$$-i\omega\hat{\mathbf{u}} = -(\mathbf{U}\cdot\nabla)\hat{\mathbf{u}} - (\hat{\mathbf{u}}\cdot\nabla)\mathbf{U} - \nabla\hat{p} + \frac{1}{Re}\nabla^2\hat{\mathbf{u}}, \qquad (2)$$

$$0 = \nabla \cdot \hat{\mathbf{u}}. \tag{3}$$

After discretization this is written

$$-i\omega_l \mathbf{B} \mathbf{q}_l = \mathbf{A} \mathbf{q}_l \quad \text{with adjoint} \quad i\omega_l \mathbf{B}^H \mathbf{q}_l^+ = \mathbf{A}^H \mathbf{q}_l^+$$
 (4)

for the eigenfunction \mathbf{q}_l with corresponding adjoint eigenfunction \mathbf{q}_l^+ , \mathbf{B} is the projection of the total disturbance field on the velocity components; \mathbf{A}^H is the adjoint discretized operator (conjugate transpose) and the bi-orthogonality condition $\langle \mathbf{q}_k, \mathbf{B} \mathbf{q}_l^+ \rangle = \delta_{kl}$ with respect to the finite-dimensional inner product applies. The operators of the eigenvalue problem have been discretized on a domain of extent $0 \le x \le 300$, $\eta(x) \le y \le 75$, sufficiently large to produce converged eigenmodes. Homogeneous Dirichlet boundary conditions are used at

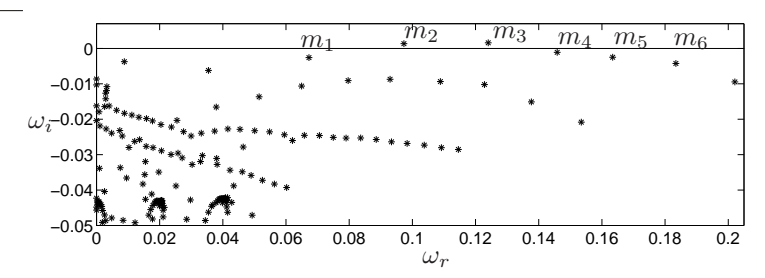


FIGURE 2. Eigenvalues of the direct problem (4). There are two unstable modes. The modes labelled $m_1 - m_6$ is depicted in figure 3.

all boundaries except at the outflow, where homogeneous Neumann condition is imposed. The domain is mapped into $[-1,1] \times [-1,1]$ and a Chebyshev-Chebyshev collocation discretization is used. The basic steady flow is then interpolated on the new grid. A similar procedure has been used in Ehrenstein & Gallaire (2005) for the computation of global modes in the flat plate boundary layer. A collocation grid with 350×65 collocation points yielded converged stability results. The resulting eigenvalue problem is far too large to be solved by standard QZ algorithms. However Krylov subspace projections with dimension m = 800 together with the Arnoldi algorithm (see Nayar & Ortega 1993) proved suitable to recover the part of the spectrum relevant for our analysis. here the eigenfunction figure For the steady state shown in figure 1 the spectrum is depicted in figure 2. For the present parameters there are 2 unstable eigenvalues labelled m_2 and m_3 (only half of the spectrum with $\omega_r > 0$ is shown). Figure 3a)-f) show the vertical velocity components of the direct eigenfunctions associated with the eigenvalues labelled $m_1 - m_6$ in figure 2, respectively. As can be seen, there are many similar eigenfunctions, a typical feature of non-normal operators, and in the following section we will describe the implications of this when it comes to optimal growth. The vertical velocity component of the adjoint eigenfunction corresponding to the least stable eigenvalue m_3 is depicted in figure 3g). We observe a clear separation in space between the direct (see figure 3c)) and adjoint eigenfunctions, indicating a strong streamwise non-normality (see Chomaz 2005).

3. Optimal growth

here the envelope

For sufficiently low-amplitude flow perturbations $\mathbf{q}(t)$, an eigenmode expansion

$$\mathbf{q}(t) = \sum_{l=1}^{N} \kappa_l(t) \mathbf{q}_l, \tag{5}$$

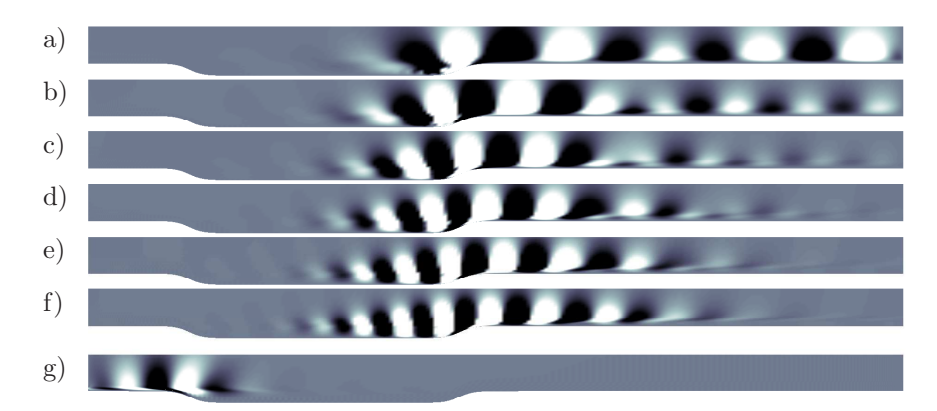
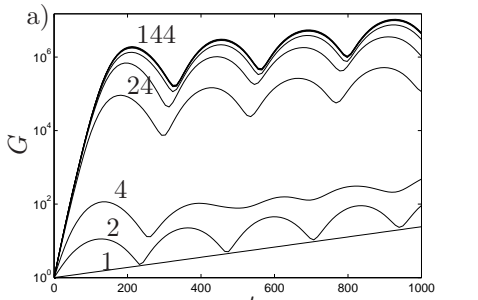


FIGURE 3. a)-f) Vertical velocity components of direct eigenfunctions corresponding to the eigenvalues labelled $m_1 - m_6$ in figure 2, respectively. g) Adjoint eigenfunction corresponding to m_3 , the most unstable eigenvalue. Black indicates large negative values and white indicates large positive values, with the grey tones adjusting accordingly. The domain is truncated at y = 14.

can be used to describe the flow dynamics. The flow evolution is initiated by superimposing the optimal initial condition \mathbf{q}_0 on the steady state, leading to the maximum energy growth $||\mathbf{q}(t)||_E$ at a given time t:

$$G(t) = \max_{\mathbf{q}_0 \neq 0} \frac{||\mathbf{q}(t)||_E}{||\mathbf{q}_0||_E}.$$

The procedure to compute the optimal initial condition is outlined in Schmid & Henningson (2001) and the subsequent energy envelope for the present flow case is depicted in figure 4a). Using one mode we observe the exponential growth of the most unstable mode. All of the direct eigenfunctions shown in figure 3 are similar; they are oscillatory and exponentially growing along the shear layer. By optimally summing the non-normal eigenmodes, cancellation results in an upstream-located initial wavepacket. This leads to a fast transient growth up to t=200, followed by a global cycle with a period of approximately 300 time units. This cycle is associated with the least stable eigenvalues in figure 2. Since the real parts of these modes are a distance of $\delta \approx 0.02$ apart, and the corresponding eigenfunctions have a very similar structure, they have the ability to cancel each other, giving rise to a "beating" with a period of $2\pi/\delta$. Schmid & Henningson (2002) observed the same phenomena studying a model equation for a falling liquid curtain. Figure 4b) shows the actual energy evolution when integrating the eigenmode system (thick line) and DNS system



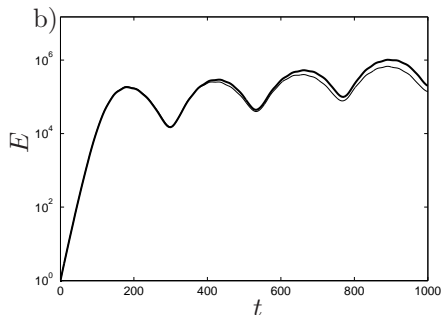


FIGURE 4. a) Envelope of maximum energy growth from initial conditions. The different lines correspond to increasing number of eigenmodes included in the optimization, 1, 2, 4, 24, ..., 124, 144 from bottom to top. b) One realization using initial condition based on 100 modes: Thick line shows eigenmode system integrated in time and thin line shows DNS evolution.

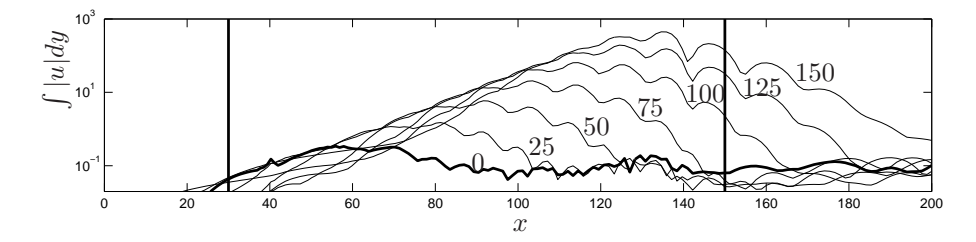


FIGURE 5. Snapshots of y-integrated streamwise velocity at times $0, 25, \ldots, 150$, showing propagation of wavepacket in the eigenmode system. The thick line shows the initial disturbance. The vertical lines indicates the approximate start and end of the recirculation region.

(thin line) in time using the optimal initial condition based on 100 modes, confirming the ability of the eigenmode system to describe the relevant flow dynamics. Note that in the DNS system the initial condition is superimposed to the steady state.

xt diagram

The initial evolution of the wavepacket in the eigenmode system is shown in figure 5. We observe the spatial exponential growth in disturbance amplitude as the wavepacket propagates along the shear layer. The spatio-temporal diagram of the dynamics in the DNS system is depicted in figure 6, where one sees the convection and growth of the wavepacket along the shear layer, and regeneration at the upstream cavity lip. A global pressure change, visible in the form

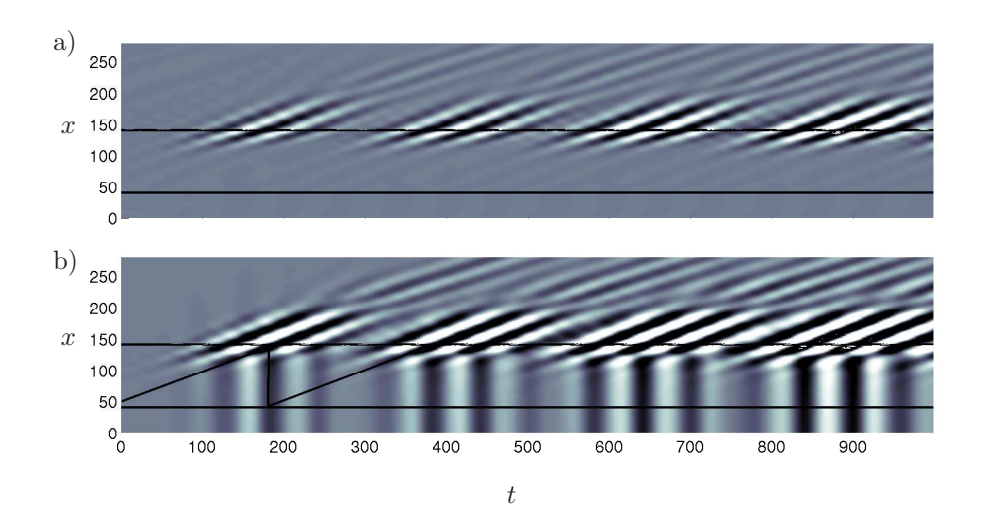


FIGURE 6. x/t diagram for a) the vertical flow velocity at y=2 and b) the pressure at y=10, tracing the quantities in the streamwise direction and in time at their respective vertical position. Black indicates large negative values whereas white indicates large positive values. The flow initial condition is the optimal initial condition. The horizontal lines show the location of the cavity lips. The oblique lines trace the path of the wavepacket back to its origin and the triggering position at the upstream lip of the cavity at the first reflection.

of vertical rays, occurs when the wavepacket reaches the downstream cavity lip; the subsequent propagation of the regenerated wavepacket is emphasized by the oblique line. This instability mechanism may be seen as a destabilization of the global mode by the pressure field, where the pressure yields an immediate feedback mechanism and the strong streamwise non-normality causes a large growth of the disturbances along the shear layer.

4. Control

To control the cavity flow, we introduce one sensor and one actuator as sketched in figure 7. The actuator is located at the upstream limit of the cavity, where the least stable adjoint eigenfunctions have their maximum, so as to trigger the most efficient response. The least stable adjoint eigenfunction is shown in figure 3g). The sensor is placed in the vicinity of the downstream cavity lip where the eigenfunctions have large amplitude. The sensor measures the wall shear stress $\int \mathcal{C}(x)(\partial u/\partial y)\mathrm{d}x$, where $\mathcal{C}(x)$ is a Gaussian function with a width of ≈ 20 . This operation may formally be written as $r = C^{DNS}q$ for the flow

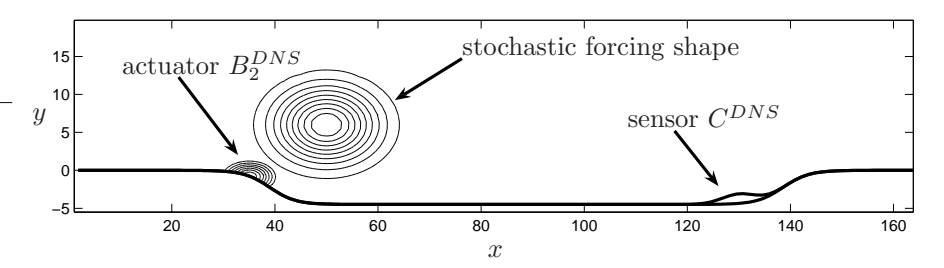


FIGURE 7. Sketch of the control setting, with a volume forcing actuator, and a wall skin friction sensor.

state q. The actuator is a volume forcing of Gaussian shape on the vertical velocity component located close to the wall at the upstream cavity lip, with a width of ≈ 20 and a height of ≈ 2 .

A dynamic model for the cavity flow is built using the eigenmode expansion (5). Based on this model a LQG control procedure gives rise to the system

$$\begin{cases} \dot{k} = Ak + B_1 w + B_2 \phi, & r = Ck + g, \\ \dot{k}_e = Ak_e + B_2 \phi - L(r - r_e), & r_e = Ck_e, \\ \phi = Kk_e. \end{cases}$$
(6)

The vector $k(t) = [\kappa_1(t), \dots, \kappa_N(t)]^T$ of the expansion coefficients of the flow obeys the model dynamics, where A is now the diagonal matrix of the eigenvalues. The external disturbances are modelled as white noise stochastic input w(t) with variance W, and B_1 is the projection on the eigenmodes of the Gaussian-shaped spatial forcing function centered at x=50. The projected actuator is denoted B_2 , and $\phi(t)$ is the actuation signal. These projections are achieved by performing the inner product with the adjoint modes. The measurement is denoted r, and C is the measurement matrix. The measurement is corrupted by a stochastic sensor noise g(t) with variance G^2 . An estimator is built, with estimated state k_e , obeying the model dynamics, and with an estimation feedback forcing $L(r-r_e)$. The estimation gain L will be designed such that the estimated state k_e converges to the flow state k, i.e. minimizes the mean kinetic energy of the estimation error $k - k_e$. The control actuation ϕ is a feedback of the estimated flow state, with control feedback gain K that will be designed such as to minimize a weighted sum of the flow mean kinetic energy and the actuation effort.

A central issue is the controllability and observability of the flow for the chosen actuator and sensor pair. Since, as observed in $\S 3$ the eigenmodes capture the relevant dynamics, the magnitude of the projections B_2 and C of the actuator and sensor indicate the controllability and observability for each eigenmode. In this manner one can choose the shape and location of the actuator and sensor based on the magnitude of these coefficients on the relevant

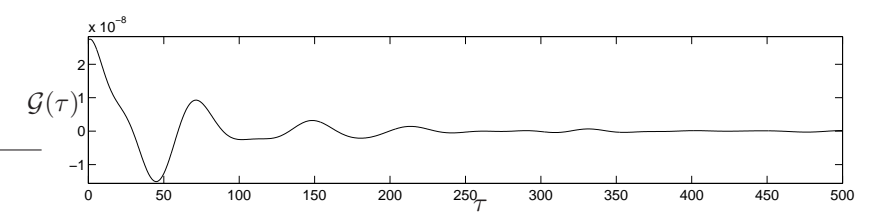


FIGURE 8. Impulse response $\mathcal{G}(\tau)$ from measurement signal to control signal. The controller uses information from about 350 time units in the past.

modes as a measure of the quality of the representation of the actuator and sensor in the reduced system. We have checked that the response from an impulsive input from the actuator in the DNS and in the eigenmode system give the same measurement signal in the two systems.

The optimal feedback gains K and L that minimize the flow and estimation error mean kinetic energy are found by the solution of two algebraic Riccati equations (see Skelton 1988)

$$0 = A^{H}X_{c} + X_{c}A - X_{c}B_{2}\ell^{-2}B_{2}^{H}X_{c} + Q,$$

$$0 = AX_{e} + X_{e}A^{H} - X_{e}C^{H}G^{-2}CX_{e} + B_{1}WB_{1}^{H},$$

for the matrix unknowns X_c and X_e , and the feedback gains can be obtained as $K = -\ell^{-2}B_2X_c$ and $L = -X_eC^HG^{-2}$. In our computations, we have assumed an external disturbance w with unit variance (W = 1). The control penalization and sensor noise variance were chosen $\ell = 5 \cdot 10^5$ and $G = 7 \cdot 10^5$ in order to enforce low amplitude feedback gains. The matrix Q is defined such that k^HQk measures the kinetic energy of the disturbances.

Once the two Riccati equations are solved and the feedback gains are obtained, we can couple the flow and the controller in the following manner

$$\dot{q} = NS(q) + B_2^{DNS}\phi, \qquad r = C^{DNS}q$$
 (7)

$$\dot{k}_e = (A + B_2 K + LC)k_e - Lr, \quad \phi = Kk_e \tag{8}$$

where B_2^{DNS} and C^{DNS} are the actuator and sensor expressed in the DNS. The measurement r is driving the estimated state k_e , which in turn is updated online by a Crank-Nicholson time-integration procedure, feeding back at every time step the control signal ϕ to the DNS.

To emphasize the linear relation between the measurement signal and the control signal through the controller system, we can write

$$\phi(t) = \int_0^\infty \underbrace{Ke^{(A+B_2K+LC)\tau}}_{\mathcal{G}(\tau)} r(t-\tau)d\tau, \quad r(t) = 0, t < 0, \tag{9}$$

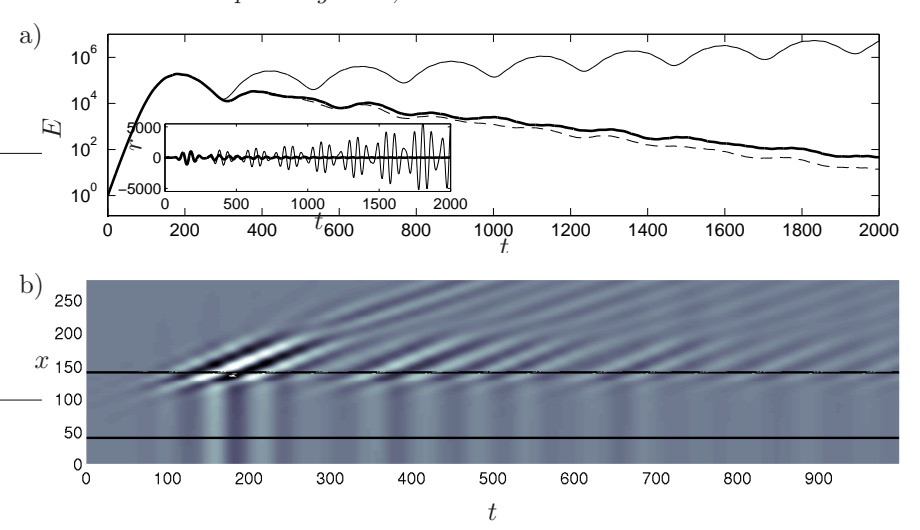


FIGURE 9. a) Energy of the uncontrolled flow (thin solid line), controlled flow using model with 4 modes (thick solid) and 25 modes (dashed). Inserted frame shows the sensorsignal in the uncontrolled case as thin solid line and controlled using 4 modes as thick solid line. b) x/t diagram for the pressure when the control is applied. This is to be compared to figure 6b).

where $\mathcal{G}(\tau)$ is the impulse response from r to ϕ , and illustrates how the actuation $\phi(t)$ depends on past measurements $r(t-\tau)$. The impulse response is shown in figure 8. Note that this formulation could provide an alternative hardware implementation of the controller. In order to assess the performance of the computed control and estimation gains the controller is applied to the same configuration that led to the evolution shown in figure 6. Reduced models consisting of the 25 and the 4 least stable eigenmodes are considered. Figure 9a) shows that when control is applied, the exponential energy growth is turned into exponential decay after the first peak. There is an almost equivalent performance for both controller dimensions. The sensor signals for the controlled and uncontrolled case are shown in the inserted frame in figure 9a). The sensor signal from the controlled case decays after the first reflections of the wavepacket at $t \approx 125$. It is not possible to control the initial energy growth, before the wavepacket has reached the sensor located at the downstream cavity lip. The x/t diagram for the controlled flow in figure 9b) is to be compared with figure 6b). When the control is applied one still observes the vertical rays of the global pressure changes but the wavepacket regeneration is reduced, leading to a decrease in the levels of fluctuations at each cycle, i.e. flow stabilization.

5. Conclusions

The cavity flow considered here may be seen as a prototype of non-parallel flow with self-sustained global instability behaviour. Due to the non-normallity of the underlying operator, computed eigenmodes are sensitive to numerical errors and require high resolution even when using spectral collocation. This sensitivity is however mostly seen in loss of accuracy for the location of eigenvalues in the complex plane; the mechanism of wavepacket propagation followed by pressure reflections obtained through optimally summing the non-normal modes proved robust and in close agreement with DNS, even at lower resolution. Despite the fact that about 100 modes are required for converged results of optimal growth, much fewer modes are needed for a stabilizing controller. There is only a negligible loss of control performance when using as few as 4 modes in the reduced model. The small controller is run in parallel to the DNS at a low computational cost, and provides the feedback control signal based on the measurement signal taken from the full DNS. The satisfactory performance of the controller, combined with the low online computational effort provides promising perspectives of using reduced order models for fluid flows, built by projection on global eigenmodes in the LQG framework.

References

- ÅKERVIK, E., BRANDT, L., HENNINGSON, D. S., HŒPFFNER, J., MARXEN, O. & SCHLATTER, P. 2006 Steady solutions of the Navier–Stokes equations by selective frequency damping. *Phys. Fluids* **18**, 068102.
- Bewley, T. R. & Liu, S. 1998 Optimal and robust control and estimation of linear paths to transition. *J. Fluid Mech.* **365**, 305–349.
- Chomaz, J. M. 2005 Global instabilities in spatially developing flows: non-normality and nonlinearity. *Annu. Rev. Fluid Mech.* **37**, 357–392.
- Cossu, C. & Chomaz, J.M. 1997 Global measures of lacal convective instability. *Phys. Rev. Lett.* **77**, 4387–90.
- EHRENSTEIN, U. & GALLAIRE, F. 2005 On two-dimensional temporal modes in spatially evolving open flows: the flat-plate boundary layer. *J. Fluid Mech.* **536**, 209–218.
- Hœpffner, J., Chevalier, M., Bewley, T. R. & Henningson, D. S. 2005 State estimation in wall-bounded flow systems. part I: Laminar flows. *J. Fluid Mech.* **543**, 263–294.
- HÖGBERG, M. & HENNINGSON, D. S. 2002 Linear optimal control applied to instabilities in spatially developing boundary layers. *J. Fluid Mech.* 470, 151–179.
- Kim, J. 2003 Control of turbulent boundary layers. Phys. Fluids 15, 1093.
- LEWIS, F. & SYRMOS, V. 1995 Optimal control. John Wiley and Sons, New York.
- MARQUILLIE, M. & EHRENSTEIN, U. 2003 On the onset of nonlinear oscillations in a separating boundary-layer flow. *J. Fluid Mech.* **490**, 169–188.
- NAYAR, M. & ORTEGA, U. 1993 Computation of selected eigenvalues of generalized eigenvalue problems. J. Comput. Phys. 108, 8–14.
- ROWLEY, C. R. 2005 Model reduction for fluids, using balanced proper orthogonal decomposition. *Int. J. Bifurcation and Chaos* **15**, 997–1013.
- ROWLEY, C. R. & WILLIAMS, D. R. 2006 Dynamics and control of high-reynoldsnumber flow over open cavities. *Annu. Rev. Fluid Mech.* **38**, 251–276.
- Schmid, P. J. & Henningson, D. S. 2001 Stability and Transition in Shear Flows. Springer, New York.
- Schmid, P. J. & Henningson, D. S. 2002 On the stability of a falling liquid curtain. J. Fluid Mech. 463, 163–171.
- Skelton, R. E. 1988 $Dynamics\ System\ Control.$ John Wiley and Sons, New York.

4

Matrix-free methods for the stability and control of boundary layers

By Shervin Bagheri, Espen Åkervik, Luca Brandt, Dan S. Henningson

Linné Flow Centre, KTH Mechanics, SE-100 44 Stockholm, Sweden

AIAA Journal, submitted

This paper presents matrix-free methods for the stability analysis and control design of high-dimensional systems arising from the discretized linearized Navier-Stokes equations. The methods are applied to the two-dimensional spatially developing Blasius boundary-layer. A critical step in the process of systematically investigating stability properties and designing feedback controllers is solving very large eigenvalue problems by storing only velocity fields at different times instead of large matrices. For stability analysis, where the entire dynamics of perturbations in space and time is of interest, iterative and adjointbased optimization techniques are employed to compute the global eigenmodes and the optimal initial conditions. The latter are the initial conditions yielding the largest possible energy growth over a finite time interval. The leading global eigenmodes take the shape of Tollmien-Schlichting wavepackets located far downstream in streamwise direction, whereas the leading optimal disturbances are tilted structures located far upstream in the boundary layer. For control design on the other hand, the input-output behavior of the system is of interest and the snapshot-method is employed to compute balanced modes that correctly capture this behavior. The inputs are external disturbances and wall actuation and the outputs are sensors that extract wall shear stress. A low-dimensional model that capture the input-output behavior is constructed by projection onto balanced modes. The reduced-order model is then used to design a feedback control strategy such that the growth of disturbances are damped as they propagate downstream.

1. Introduction

Control of wall-bounded transitional and turbulent flows has been the subject of several research efforts owing to the high potential benefits. In these fluid-mechanics systems, due to the large flow sensitivity, dramatic effects on global flow parameters may be achieved by minute local perturbations using devices sensing and acting on only small parts of the flow with a small amount of energy.

Such control devices can be used to obtain reduction of the skin-friction drag, for example, implying relevant savings of the operational cost of commercial aircrafts and cargo ships.

In this paper we perform stability analysis and control design for the Blasius flow. The work is motivated by the need to provide efficient numerical tools to analyze complex flows and design efficient control strategies. Although we present results for the Blasius flow the methodology is applicable to any complex flow described by the direct and adjoint linearized Navier–Stokes equations. The techniques in this paper share a common methodology: very large eigenvalue problems are solved based only on snapshots of the velocity field at different points in time. No large matrices are stored. Therefore the main tool is a code that time integrates the forward and adjoint linearized Navier-Stokes equations. This so called timestepper technique has become increasingly popular in both stability analysis (Blackburn et al. 2008; Barkley et al. 2002) and for control design (Bagheri et al. 2008a).

It is now well understood that wall-bounded flows are very sensitive to specific perturbations (Schmid & Henningson 2001). In particular, boundary layer flows support convective instabilities and behave as noise amplifiers (Huerre & Monkewitz 1990). Convectively unstable shear flows are stable from a global point of view (Huerre & Monkewitz 1990; Chomaz 2005); wave packets generated locally, grow in amplitude as they travel downstream and finally decay or leave the observation window. This behavior can be captured by a non-modal analysis (see e.g. Schmid 2007). It is therefore meaningful to analyze the spatial structure of the initial conditions and forcing yielding largest possible energy growth over a finite time interval. This optimization problem can be solved efficiently for complex flows by solving the direct and adjoint Navier-Stokes equation for the linear evolution of perturbation about a steady state (c.f. Barkley et al. 2002, 2008).

Two aspects in flow control have been identified as crucial in order to apply feedback control in more complex flows and to move towards an implementation in wind-tunnel tests. They are; i) model reduction to significantly decrease the cost of both constructing the controller and running it online, thus allow the fast computation of the control signal directly from the sensor output; ii) the need to naturally consider localized sensors and actuators. Both these aspects are addressed in Bagheri $et\ al.\ (2008a)$. In this paper, the results of Bagheri $et\ al.\ (2008a)$ are extended by introducing wall actuation and wall shear stress measurements instead of idealized volume forcing actuation and velocity measurements inside the flow. The incorporation of actuators and sensors at the physical boundaries in our design, brings us one step closer to using the controller in actual experiments.

Model reduction becomes essential in order to apply modern control theoretical tools to fluid flow systems. For linear control, the aim is to build a model

of low dimension that captures the input-output behavior of the Navier-Stokes system and use this model for optimal feedback control design. Balanced truncation (Moore 1981) is a method for model reduction that takes into account both the flow structures most easily influenced by the input and the flow structures to which the outputs are most sensitive. The method provides a set of bi-orthogonal modes, called the balanced modes, that serve as a projection basis for model reduction. The method employed to compute the balanced modes is the snapshot-based balanced truncation introduced by Rowley (2005). This method has been recently applied to the channel flow (Ilak & Rowley 2008), the flow around a pitching airfoil (Ahuja et al. 2007) and the Blasius flow (Bagheri et al. 2008a).

Recently, several groups have suggested and pursued the combination of computational fluid dynamics and control theory, thus going past early attempts of flow control based on physical intuition or on a trial-and-error basis (see the review in Kim & Bewley 2007). The reader is also referred to Bagheri et al. (2008b) for a thorough review of the many tools used in flow control. In early work from our group (Högberg & Henningson 2002; Högberg et al. 2003), a linear model-based feedback control approach, that minimizes an objective function which measures the perturbation energy, is formulated where the Orr-Sommerfeld/ Squire equations model the flow dynamics. The latter equations describe the linear evolution of perturbations evolving in a parallel base flow. The control problem is combined with a state estimator: The so called Kalman and extended Kalman filter have been implemented in order to reconstruct the flow in an optimal manner by only considering distributed wall measurements. These studies have also shown the importance of physically relevant stochastic models for the estimation problem (Hoepffner et al. 2005; Chevalier et al. 2006), where stochastic noise needs to describe accurately enough the unmodeled dynamics, like uncertainties and nonlinearities. Based on these models the estimator is shown to work for both infinitesimal as well as finite amplitude perturbations in direct numerical simulations of transitional flows (Chevalier et al. 2007a; Monokrousos et al. 2008). These studies however assumed a parallel base flow and distributed sensing and actuation at the wall.

The paper is organized as follows: The modal and nonmodal stability analysis is presented in section 2. We start with describing the flow setup and formulating two eigenvalue problems. We continue with showing how the eigenvalue problems can be solved iteratively and finally present results for the Blasius flow. Section 3 deals with the control design. We introduce inputs, outputs and write the system in the state-space formulation. A brief summary of the LQG framework is provided before model reduction based on balanced modes is introduced. The snapshot method used for model reduction is explained and results on the performance of the reduced-order and controller are shown. Section 4 provides concluding remarks.



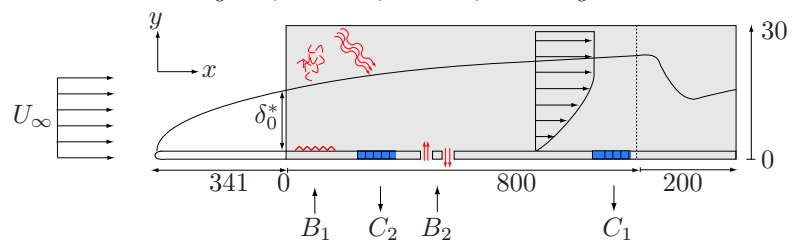


FIGURE 1. The configuration used for the control of perturbations in a two-dimensional flat-plate geometry. The computational domain $\Omega=(0,L_x)\times(0,L_y)$, shown by the gray region, extends from x=0 to x=1000 with the fringe region starting at x=800. The first input \mathcal{B}_1 , located at $(x_w,y_w)=(35,1)$, models the initial receptivity phase, where disturbances are induced by free-stream turbulence, acoustic waves or wall roughness. The actuator, \mathcal{B}_2 , provides a mechanism to manipulate the flow, in this case by a wall blowing and suction centered at $x_u=400$. Two sensors \mathcal{C}_1 and \mathcal{C}_2 , measuring the skin friction at the wall, are located at $x_y=300$ and $x_z=750$ respectively. The upstream measurements are used to estimate the incoming perturbations, while the downstream sensor quantifies the effect of the control.

2. Stability Analysis

2.1. Flow Configuration and the Initial Value Problem

We consider the two-dimensional incompressible flow over a flat plate with constant free-stream velocity U_{∞} as shown in figure 1. Starting from the leading edge a viscous boundary layer evolves downstream. The evolution of the streamwise velocity u, the wall-normal velocity v and the pressure p in time t and space (x,y) is governed by the incompressible non-linear Navier–Stokes equation (see e.g. White 1991). Our analysis deals with the evolution of infinitesimal perturbations on this laminar boundary layer solution and is limited to the computational domain shown by the gray area in figure 1: The inflow boundary is set to the downstream position corresponding to a Reynolds number $Re_{\delta_0^*} = U_{\infty} \delta_0^* / \nu = 1000$, where δ_0^* is the local displacement thickness of the boundary layer and ν is the kinematic viscosity. Throughout the paper all variables are non-dimensionalized by U_{∞} and δ_0^* . The length and height of the domain are $L_x = 1000$ and $L_y = 30$ in the streamwise direction x and wall-normal direction y, respectively.

The steady state, about which a linearization is performed, is obtained by marching the nonlinear governing equations in time. The linearized Navier-Stokes equations with boundary conditions can be cast (c.f. Bagheri *et al.*

2008a; Kreiss et al. 1993; Bewley et al. 2000)) as an initial-value problem

$$\dot{\mathbf{u}} = \mathcal{A}\mathbf{u} \tag{1}$$

$$\mathbf{u} = \mathbf{u}_0 \quad \text{at} \quad t = 0. \tag{2}$$

with $\mathbf{u}=(u,v)^T$. However, in general, it is not always possible to have an explicit form for the operator \mathcal{A} , and once it is discretized it will have very large dimension, i.e. the number of grid points times the number of velocity components $n=2N_xN_y$. Our analysis will therefore be entirely based on the solution of the linearized Navier–Stokes equations that can be represented by an evolution operator

$$\mathbf{u}(\mathbf{x},t) = \mathcal{T}(t)\mathbf{u}(\mathbf{x},0) = e^{At}\mathbf{u}_0. \tag{3}$$

The evaluation of the evolution operator $\mathcal{T}(t)$ is the key to both stability analysis and control design, all of which will be discussed in the subsequent sections. However, this operator also poses the greatest computational challenge due its dimension. The dimension, n, of the discretized operator depends on the number of non-homogeneous spatial directions of the base flow. Except for onedimensional base flows the operator must be approximated. As an example, the storage of the one dimensional Orr-Sommerfeld matrix for the evolution of disturbances in parallel flows requires approximately 1MB of memory, the system matrix for the present spatially inhomogeneous flow with the numerical scheme introduced above requires approximately 200GB, while the memory usage for a full three-dimensional system would be of the order of 200TB. However, the action of $\mathcal{T}(t)$ on any flow field simply represents integrating the Navier-Stokes equations in time and therefore the evolution operator can be approximated by numerical simulation of the governing equations. In what follows the reader should equate $\mathcal{T}(t)\mathbf{u}(s)$ with a Direct Numerical Simulation (DNS) starting with an initial condition $\mathbf{u}(x,s)$ and providing $\mathbf{u}(x,t+s)$ at a later time. In this so called "timestepper approach", system matrices are never stored and storage demands in memory are of the same order as a small number of flow fields. Numerically, the equations are solved with the pseudo-spectral DNS code described in Chevalier et al. (2007b), where the spatial operators are approximated by Fourier expansion in the streamwise direction with $N_x = 768$ equally distributed points and Chebyshev expansion in the wall-normal direction on $N_y = 101$ Gauss-Lobatto collocation points. A fringe region enforces periodicity in the streamwise direction (Chevalier et al. 2007b).

2.2. Modal Stability

The first step in the understanding of the fluid problem at hand is examining the hydrodynamic stability of the flow, i.e. the behavior of infinitesimal disturbances to a base flow. In particular, modal stability deals with the response behavior of the baseflow to disturbances as time tends to infinity. This

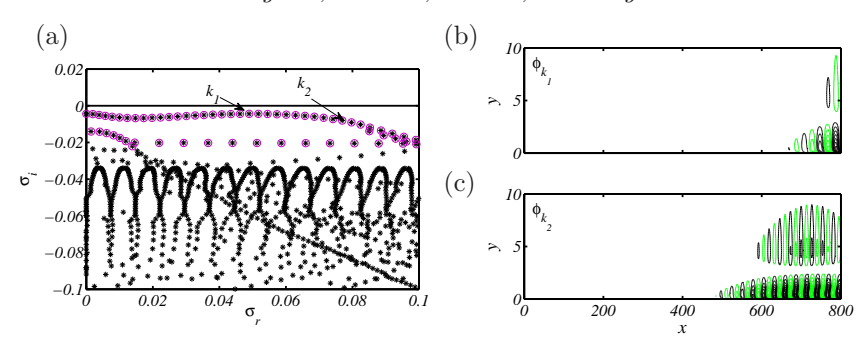


FIGURE 2. (a) Eigenvalues of \mathcal{A} as computed by the shift and invert Arnoldi method (shown as stars) and eigenvalues computed by time-stepping using the evolution operator $\mathcal{T}(t_f)$ (shown as circles). The slightly damped eigenvalues, corresponding to Tollmien-Schlichting (TS) modes, and the free-stream propagating modes are found by both methods. (b) Streamwise velocity component of the least stable TS eigenvectors, marked k_1 in (a). (c) Streamwise velocity component of a high frequency but more damped TS mode, marked k_2 in (a).

asymptotic response is governed by the eigenmodes of the evolution operator

$$\sigma_j \phi_j = \mathcal{T}(t_f) \phi_j, \qquad |\sigma_1| > |\sigma_2| > \dots$$
 (4)

for a fixed time t_f large enough. The stability of disturbances as $t_f \to \infty$ is determined by the eigenvalue with the largest magnitude. If $|\sigma_1| > 1$, the system is linearly globally unstable. Note that the evolution operator $\mathcal T$ has the same eigenfunctions as $\mathcal A$ and the eigenvalues λ_j of $\mathcal A$ can be related to those of $\mathcal T$ through $\lambda_j = \ln(\sigma_j)/t_f$.

2.3. Nonmodal stability

The amount of information obtained from the eigenvalue problem (4) is limited to the asymptotic flow response and does not reveal the short time behavior of disturbances inherent to many flow systems. Relevant transient growth (Schmid & Henningson 2001) of perturbations is indeed observed for many fluid dynamical systems due to the non-normality of the operator \mathcal{A} (an operator which does not commute with its adjoint) and nonmodal analysis is concerned with finding instabilities that are amplified in a finite time interval. Furthermore, a competition between nonmodal and modal growth is observed in many systems, for example for three-dimensional perturbations in the Blasius boundary layer (Levin & Henningson 2003). For such flows, different transition scenarios can be observed depending on the external ambient noise. Therefore, in order to examine the largest possible disturbance growth due to all possible

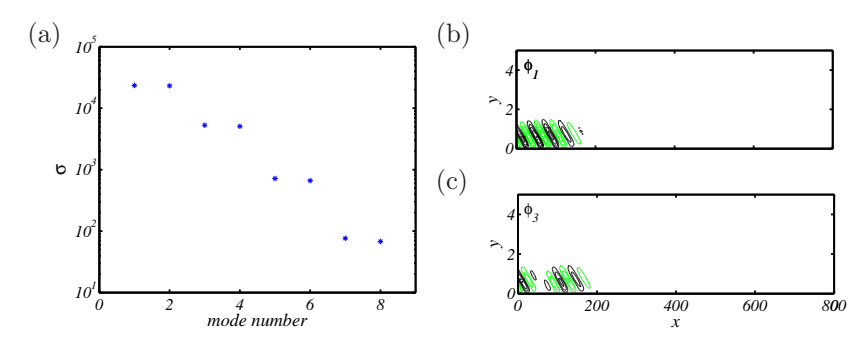


FIGURE 3. (a) Eigenvalues of T^*T computed using the forward and adjoint timestepper with $t_m = 1800$. (b) Streamwise velocity component of the optimal disturbance corresponding the largest eigenvalue in (a). (c) Streamwise velocity component of a suboptimal, corresponding to the third largest eigenvalue in (a).

unit-norm initial conditions \mathbf{u}_0 we will consider the energy associated to the disturbance at any time t_m

$$\|\mathbf{u}(t_m)\|^2 = (\mathcal{T}(t_m)\mathbf{u}_0, \mathcal{T}(t_m)\mathbf{u}_0) = (\mathbf{u}_0, \mathcal{T}^*(t_m)\mathcal{T}(t_m)\mathbf{u}_0).$$
 (5)

In the expression above the perturbation kinetic energy is the relevant norm and the adjoint evolution operator $\mathcal{T}^*(t_m)$ is introduced. Applying this operator corresponds to the integration of an adjoint state from time t_m to time 0. One can show (Bagheri et al. 2008a) that an initial-value problem for the adjoint linearized Navier-Stokes equations governed by \mathcal{A}^* but with negative time derivative can be associated to the adjoint evolution operator \mathcal{T}^* . For a derivation of the adjoint operators in general we refer to Giles & Pierce (2001) and for this particular setup to Bagheri et al. (2008a).

Initial conditions experiencing the largest nonmodal growth correspond to the leading eigenvalues of the operator $\mathcal{T}^*(t_m)\mathcal{T}(t_m)$, i.e.

$$\sigma_i \phi_i = \mathcal{T}^*(t_m) \mathcal{T}(t_m) \phi_i, \qquad \sigma_1 > \sigma_2 > \dots > 0.$$
 (6)

In particular, the first unit-norm eigenvector ϕ_1 is the optimal initial condition, resulting in the largest energy growth at time t_m . If its corresponding eigenvalue is larger than one, $\sigma_1 > 1$, the system can support nonmodal growth. The corresponding flow state at time t_m can be found by the evaluation of $\mathcal{T}(t_m)\phi_1$. In order to obtain a full map of the potential for transient growth the computations are repeated for different times t_m . Note that when the system is discretized, we are again faced with a very large eigenvalue problem.

2.4. Iterative Timestepping technique

The eigenvalue problems defined in (4) and (6) provide information about the modal and non-modal flow behavior of the system, respectively. The dimension of the matrices obtained by discretizing the operators appearing in (4) and (6) is too large to be solved by direct methods, such as the standard QR method. Therefore one has to resort to iterative methods, such as the Arnoldi method (Lehoucq et al. 1998), which is based on the projection of the large matrix onto a lower-dimensional subspace. This results in a significantly smaller system that can be solved with direct methods. In addition, as mentioned above, in many cases only instantenous velocity fields at different times are available. A particular subspace is the Krylov subspace $\mathcal K$ spanned by snapshots taken from flow fields separated by a constant time interval Δt ,

$$\mathcal{K} = \operatorname{span}\{\mathbf{u}_0, \mathcal{F}(\Delta t)\mathbf{u}_0, \mathcal{F}(2\Delta t)\mathbf{u}_0, \dots, \mathcal{F}((m-1)\Delta t)\mathbf{u}_0\}$$
 (7)

with $\mathcal{F}(t) = \mathcal{T}(t)$ (modal stability) or $\mathcal{F}(t) = \mathcal{T}^*(t)\mathcal{T}(t)$ (nonmodal stability) and \mathbf{u}_0 is the initial guess that should contain nonzero components of the eigenmodes. By orthonormalizing \mathcal{K} with an m-step Arnoldi factorization we obtain a unitary basis \mathbf{V} on the which \mathcal{F} can projected on; $\mathcal{F}(\Delta t) \approx \mathbf{V} \mathbf{H} \mathbf{V}^T$. This leads to small eigenvalue problem of the form $\mathbf{H} \mathbf{S} = \mathbf{\Sigma} \mathbf{S}$ which can easily be solved to recover the eigenmodes by $\Phi = \mathbf{V} \mathbf{S}$.

2.5. Results

Results on modal and non-modal stability of the two-dimensional perturbations of the Blasius boundary layer are presented in this section. As mentioned above, the flow under investigation here is locally unstable but globally stable. Locally unstable perturbations, the Tollmien-Schlichting waves, grow while travelling downstream eventually leaving our control domain. From a global point of view the flow is then stable since disturbances have to be continuously fed upstream to avoid that the flow returns to its undisturbed state at each streamwise position. However, a significant transient growth of the disturbance energy in the domain is associated to the propagation of the unstable wave-packet (Ehrenstein & Gallaire 2005; Åkervik et al. 2007a). This is also referred to as streamwise non-normality (Cossu & Chomaz 1997; Chomaz 2005).

2.5a. Modal stability. For two-dimensional perturbations of the Blasius boundary layer flow the memory requirements are still small enough to enable the storage of the system matrix A (the discretized operator A) in memory; the leading eigenmodes from the matrix eigenvalue problem $\lambda_j \phi_j = A \phi_j$ can thus be obtained by means of the shift and invert Arnoldi procedure. Figure 2(a) shows the eigenvalues obtained by the shift and invert matrix method as black stars. In the spectrum, one can identify several branches which all can be related to corresponding modes in the spectrum of a parallel Blasius boundary layer, as found by solving the Orr-Sommerfeld equations, though modified

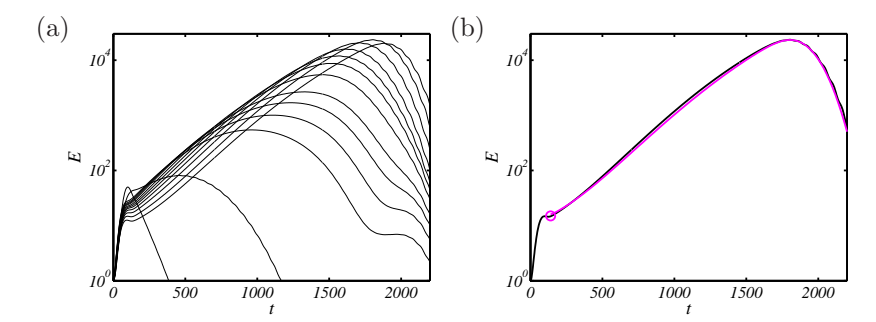


FIGURE 4. (a) Energy growth when optimizing for different times. The maximum is achieved for time $t_m=1800$ for which the maximum energy is $E=2.35\cdot 10^4$. (b) Thin line repeats the energy evolution leading to the maximum growth at $t_m=1800$, whereas thick line shows the energy evolution obtained when projecting the system onto a small number of eigenvectors related to the TS branch in Figure 2(a). The latter clearly does not account for the initial gain due to the Orr mechanism, but by rescaling and shifting in time the two curves collapse, showing that the long time evolution is governed by propagating TS waves.

by non-parallelism and boundary conditions (Åkervik et al. 2007a). The upper branch can be identified as pure Tollmien-Schlichting (TS) waves. These modes are characterized by slightly damped eigenvalues with the corresponding eigenvectors obtaining their maximum values inside the boundary layer while decaying exponentially in the free stream. More stable modes can be associated to modes of the continuous spectrum, that is modes oscillating in the free stream and decaying inside the boundary layer.

Figure 2(b) and figure 2(c) show two examples of TS eigenvectors associated with eigenvalues marked k_1 and k_2 in Figure 2(a). As a consequence of the convective nature of the instabilities arising in the Blasius flow where disturbances grow in amplitude as they are convected in the downstream direction, the global eigenmodes are located far downstream where the flow energy is the largest. The streamwise wavelength of the eigenvectors increases as we go towards lower frequencies. The wall normal structure of these modes are very similar to those obtained by local temporal analysis in the framework of the Orr–Sommerfeld equation. The amplitude of the waves is exponentially increasing downstream: this, together with the temporal decay rate given by the eigenvalue, accounts for the spatial behavior of the mode. The matrix-free method based on the timestepper introduced in section 2.4 successfully locates

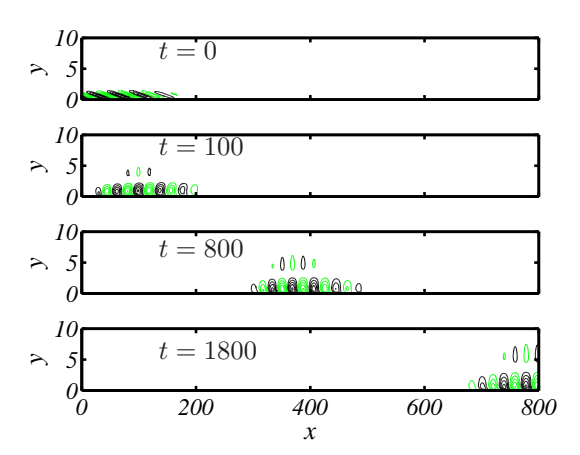


FIGURE 5. Time evolution for streamwise velocity with the combined Orr and TS mechanism, when initiated with the optimal initial condition from $t_m = 1800$. Note that the maximum amplitude is growing from frame to frame following the energy evolution given in figure 4(b).

the least damped eigenvalues by solving the eigenvalue problem (4). The eigenvalues are shown as circles in figure 2(a), and are in perfect agreement with the results obtained by the matrix method.

Note that all the eigenvalues are damped, indicating that we will never observe the evolution of single eigenmodes in the flow, but rather we should focus our attention on the non-modal behavior, in other words the transient growth scenario. It is possible to project the system (5) on a set of eigenmodes obtained from (4), thereby approximating the flow dynamics by a low-dimensional model living in the space spanned by a finite number of eigendirections (Schmid & Henningson 2001). For globally unstable flows, only one or few eigenmodes may be sufficient to capture the physical mechanism of the instability, see e.g. the shallow rounded cavity flow in Åkervik et al. (2007b), where an oscillating cycle could be captured by the sum of two unstable eigenmodes. However for a boundary layer flow like that studied here, it is shown in Åkervik et al. (2007a) that $\mathcal{O}(1000)$ eigenmodes are needed to capture the full instability mechanism. With the present discretization and boundary conditions, moreover, the sum of the 1500 eigenmodes obtained from the Arnoldi method is not able to correctly describe the Orr mechanism (Orr 1907; Åkervik et al. 2007a) as obtained by the optimization via the time-stepper defined in (6). This is most likely due to the presence of eigenmodes related to the fringe region among the least damped eigenmodes. This points to the limitations of using eigenvalues as a general tool to study stability of complex systems characterized by strong non-normality.

2.5b. Nonmodal stability. Figure 3 shows the spectrum and two eigenfunctions of the eigenvalue problem (6) computed using the timestepper with $t_m = 1800$. Since $\mathcal{T}^*\mathcal{T}$ is a self-adjoint positive-definite operator, its eigenvalues are real and positive. Moreover, the eigenvalues shown in figure 3(a) come in pairs with similar maginitudes. The corresponding velocity fields have the same wavepacket structure 90 degrees out of phase, representing traveling structures. The most unstable mode, i.e. the optimal disturbance and a suboptimal mode are shown in figure 3(b) and (c). They both have a spatial support far upstream, where the sensitivity of the flow is the largest. The modes are tilted in the upstream direction, "leaning" against the shear layer. As noticed by Butler & Farrell (1992), the upstream tilting of the optimal initial conditions can be attributed to the wall-normal non-normality of the governing operator; perturbations extract energy from the mean shear by transporting momentum down the mean velocity gradient (the so-called Orr mechanism). It is also noteworthy to remark on the separation of the spatial support of the optimal disturbance modes shown in figure 3(b)(far upstream) and global eigenmodes shown in figure 4(far downstream). This separation is associated to streamwise non-normality of the system (Chomaz 2005). Finally, note that there is nearly one order of magnitude between the energy of first pair and second pair of eigenvalues shown in figure 3(a). As a consequence, one can expect a selection of disturbances in a randomly forced flow that resembles the flow response obtained when using the optimal disturbance as initial condition.

The energy evolution when solving for the largest eigenvalues of (6) at times $t = \{100, 200, \dots, 2000\}$ is reported in figure 4(a). When optimizing for short times the optimal initial condition consists of upstream tilted structures that exploit the Orr mechanism only (Åkervik et al. 2007a) to extract energy from the flow. Increasing the optimization time, the upstream-tilted structures move upstream, towards the start of our computational domain, weighting the possibility of growth due to the local Orr mechanism with the energy gain associated to the amplification and propagation of TS waves. The maximum energy growth in this box is obtained for final time $t_m = 1800$. The corresponding optimal initial condition is shown in the top frame in figure 5. In figure 4(b) we compare the energy evolution due to this optimal initial condition with the energy evolution obtained when projecting (6) onto the space spanned by a small number of modes, all part of the TS branch in figure 2. The evolution in the reduced system clearly does not capture the initial energy gain due to the Orr mechanism; however by rescaling the energy curve and shifting it in time to account for the initial gain due to the Orr mechanism, the subsequent evolution (amplification and propagation of the TS waves) is almost perfectly matching that of the full system. These results indicate that when computing optimal perturbations in the space spanned by some of the system eigenvalues care has to be taken in checking the general validity of the results.

The detailed evolution of the streamwise velocity due to the optimal initial condition at time t=1800 is shown in figure 5. At the initial time the structures are leaning backwards against the shear. During the initial phase of the development the disturbance is raised up, gaining energy through the Orr mechanism (Orr 1907; Åkervik et al. 2007a) and forming a wavepacket consisting of TS-waves. The wavepacket then propagates downstream, grows in size and finally leaves the computational domain; the energy evolution for this flow is reported in figure 4(b).

3. Control Design

3.1. Introducing Inputs and Outputs

The next step after the analysis of the internal dynamics of our linear system is to manipulate it or in other words to control it. In particular, our objective is to minimize the perturbation energy resulting from the growth of instabilities during the transition process in order to suppress or delay turbulence. To this end, we introduce actuators and sensors, or the inputs $\mathcal{B}_1 w$, $\mathbf{u}_w \varphi$ and outputs $\mathcal{C}_1, \mathcal{C}_2$ into our system;

$$\dot{\mathbf{u}} = \mathcal{A}\mathbf{u} + \mathcal{B}_1 w,
\mathbf{u}(x, 0, t) = \mathbf{u}_w \varphi(t) = (0, v_w(x))^T \varphi(t),
z(t) = \mathcal{C}_1 \mathbf{u}
y(t) = \mathcal{C}_2 \mathbf{u}.$$
(8)

In the above expression, the wall actuation is a blowing and suction with function $v_m(x)\varphi$ on the wall normal velocity with streamwise shape given by equation (A2) in Appendix A. The linearized Navier-Stokes equations is now forced with external disturbances represented by the term $\mathcal{B}_1(x)w(t)$ on the right-hand side of equation (8a). External disturbances enter the boundary layer upstream through some receptivity mechanism such as free-stream turbulence or acoustic waves interacting with roughness as shown schematically in figure 1. In practice, the entire spatio-temporal evolution of disturbances is not available and it is therefore necessary to monitor the disturbance behavior through measurements. To accomplish this task, two sensors, C_1 and C_2 are introduced that measure the shear stress at the wall. The partial information of the incoming perturbations provided from the first sensor measurements (\mathcal{C}_2 in figure 1) is used to reconstruct the actual flow dynamics by using a Kalman filter. Based on this flow estimation we can alter the behavior of disturbances by injecting fluid through blowing/suction holes in the wall. This type of actuation corresponds to imposing an inhomogeneous boundary condition \mathbf{u}_w at the wall y=0 as given in equation (8b). Measurements provided by the second sensor \mathcal{C}_1 located far downstream is used to determine whether our controller have been successful in reducing the shear stress at the wall. It thus plays the role of an objective function.

3.2. The lifting procedure and state space formulation

Unfortunately, the formulation (8) based on wall actuation does not fit into the standard state-space formulation used in systems and control theory. Therefore, the boundary term $\mathbf{u}_w(x)\varphi(t)=(0,v_w(x))^T\varphi$ is lifted into a volume forcing (Curtain & Zwart 1995). In the same manner as Högberg *et al.* (2003), we split the solution \mathbf{u} into a homogeneous part \mathbf{u}_h and a particular part \mathbf{u}_p , so that $\mathbf{u}=\mathbf{u}_h+\mathbf{u}_p$. The particular solution fulfils the boundary conditions

$$\dot{\mathbf{u}}_p = \mathcal{A}\mathbf{u}_p
\mathbf{u}_p(x, 0, t) = (0, v_w(x))^T \varphi(t),$$
(9)

and the homogeneous part satisfies homogeneous boundary conditions. In principle we can seek any solution \mathbf{u}_p of the above system, but one suitable choice is to use the steady steady state $\mathcal{A}\mathbf{u}_p=0$. This is obtained by marching the DNS in time subject to steady $(\varphi=1)$ wall blowing $v_w(x)$ until a stationary state $\dot{\mathbf{u}}_p=0$ is obtained. In the following we denote this solution $\mathcal{Z}(x)$. The inhomogeneous boundary condition is satisfied by this solution, enabling us to write the particular solution for all times as $\mathbf{u}_p=\mathcal{Z}\varphi$, implying that the total field is given by $\mathbf{u}=\mathbf{u}_h+\mathcal{Z}\varphi(t)$. Again expressing the equation for \mathbf{u} in terms of the homogeneous and particular solution we get

$$\dot{\mathbf{u}}_h = \mathcal{A}\mathbf{u}_h + \mathcal{A}\mathcal{Z}\varphi - \mathcal{Z}\dot{\varphi} = \mathcal{A}\mathbf{u}_h + \mathcal{B}_2\dot{\varphi}. \tag{10}$$

Here we have used that $\mathcal{AZ} = 0$. Further we have defined the input operator $\mathcal{B}_2 = -\mathcal{Z}$ for the homogeneous system. The evolution of the state \mathbf{u}_h and φ can be written as an augmented system for $\hat{\mathbf{u}} = (\mathbf{u}_h, \varphi)^T$ as

$$\dot{\hat{\mathbf{u}}} = \hat{\mathcal{A}}\hat{\mathbf{u}} + \hat{\mathcal{B}}_2\phi, \quad \text{with} \quad \hat{\mathcal{A}} = \begin{pmatrix} \mathcal{A} & 0\\ 0 & 0 \end{pmatrix}, \, \hat{\mathcal{B}}_2 = \begin{pmatrix} \mathcal{B}_2\\ 1 \end{pmatrix}, \, \phi = \dot{\varphi}.$$
 (11)

Note that in the lifted system (11) the control signal is given by time derivative of the boundary control signal, $\phi = \dot{\varphi}$. Similarly the input operator \mathcal{B}_1 is extended to $\hat{\mathcal{B}}_1 = (\mathcal{B}_1, 0)^T$ and the outputs are augmented to $\hat{\mathcal{C}}_1 = (\mathcal{C}_1, \mathcal{C}_1 \mathcal{Z})$ and $\hat{\mathcal{C}}_2 = (\mathcal{C}_2, \mathcal{C}_2 \mathcal{Z})$.

The system (8) with inhomogeneous boundary condition can now be written in the standard state-space form

$$\dot{\mathbf{u}} = \mathcal{A}\mathbf{u} + \mathcal{B}\mathbf{f},\tag{12}$$

$$y = \mathcal{C}\mathbf{u} + \mathcal{D}f, \tag{13}$$

where we have omitted the superscript $\hat{}$. Furthermore, $\mathcal{B}=(\mathcal{B}_1,0,\mathcal{B}_2)$ contains the two input operators, $\mathcal{C}=(\mathcal{C}_1,\mathcal{C}_2)$ the two output operators, $\boldsymbol{f}=(w,g,\phi)$ input time signals and $\boldsymbol{y}=(y,z)$ the output time signals. We have introduced the additional feed-through term \mathcal{D} to model the effects of measurements noise (g) and to penalize the actuation effort ϕ ,

$$\mathcal{D} = \left(\begin{array}{ccc} 0 & 0 & l \\ 0 & \alpha & 0 \end{array}\right). \tag{14}$$

The outputs are now directly forced by in the inputs. The first output, or the objective function, can be written as $z(t) = C_1 \mathbf{u} + l\phi$ which results in the objective functional¹

$$||z||^2 = \int_0^\infty (||\mathcal{C}_1 \mathbf{u}|| + l^2 \phi^2) \, dt,$$
 (15)

For large values of the scalar l the control effort is considered to be expensive, whereas small values indicate cheap control. The second output $y(t) = C_2 \mathbf{u} + \alpha g$ is forced with noise g to model the uncertainty that may exist in the measurements under realistic conditions. It can be considered as a third forcing, but rather than forcing the Navier–Stokes equations it forces the measurements. Large values of the scalar α indicate high level of noise corruption in the output signal, whereas for low values of α the measurement y reflects information about the flow field with high fidelity.

3.3. The
$$LQG/\mathcal{H}_2$$
 Problem

The LQG/ \mathcal{H}_2 framework provides a controller that minimizes the cost functional (15). It is appropriate if the system operator \mathcal{A} accurately describes the flow dynamics, whereas a precise knowledge of external disturbances and the degree of noise contamination of the measurements are not available. We refer to Anderson & Moore (1990); Zhou et al. (2002); Bagheri et al. (2008b) for further details on the \mathcal{H}_2 control algorithm, as we will only outline the main steps here. The method can be extended (the so called \mathcal{H}_{∞} method) in order to guarantee certain robustness properties. The control problem from an input-output viewpoint, or the \mathcal{H}_2 problem, can be formulated as follows:

Find an optimal control signal $\phi(t)$ based on the measurements y(t) such that the in the presence of external disturbances w(t) and measurement noise g(t) the output z(t) is minimized.

The determination of the control signal ϕ is based only on the measurements from the sensor \mathcal{C}_2 . However, for linear systems — due to the separation principle (Zhou et al. 2002) — the feedback control law can be determined assuming that the complete velocity field is known. The forcing needed to reproduce the flow only from wall measurements can be computed independently. Hence, the design of the \mathcal{H}_2 -controller is performed by solving two quadratic matrix equations called Riccati equations (Zhou et al. 1999) that are independent of each other. Solving the first Riccati equation we obtain the feedback type of control signal $\phi = \mathcal{K}\mathbf{u}$. The second Riccati equation provides the estimation feedback gain $\mathcal{L} =$ so that the observer $\dot{\mathbf{u}} = (\mathcal{A} + \mathcal{LC}_2)\hat{\mathbf{u}} + \mathcal{L}y$ can estimate

 $^{^{1}}$ We assume that the cross weighting between the state and control signal is zero (Zhou *et al.* 1999).

the state $\hat{\mathbf{u}}$ from the wall stress measurements. Finally, the compensator is obtained by the combination of these two as

$$\dot{\hat{\mathbf{u}}} = (\mathcal{A} + \mathcal{B}_2 \mathcal{K} + \mathcal{L} \mathcal{C}_2) \hat{\mathbf{u}} - \mathcal{L} y,
\phi = \mathcal{K} \hat{\mathbf{u}}.$$
(16)

This compensator runs online next to the experiments. Based on wall shear stress measurements y extracted by the first sensor, it provides an optimal control signal ϕ proportional to the estimated flow $\hat{\mathbf{u}}$.

Any adequately accurate spatial discretization of the Navier-Stokes equations linearized about two or three dimensional baseflows results in a system with at least $n \geq 10^5$ degrees of freedom. Due to the high dimensional statespace we can in general not solve the Riccati equations. Moreover, it would be very expensive to run the compensator online, since it has the same dimension as the full system. Therefore, to be able to apply modern control theoretical tools, it is important to construct a much smaller model of the Navier-Stokes system.

3.4. The Model Reduction Problem and Balanced Truncation

The main features of the flow behavior which are relevant to preserve in the reduced order model is the input-output (I/O) behavior of the system, *i.e.* the relation between disturbances, wall actuation and the sensor outputs. Rather than investigating entire dynamics of flow fields at different times, the I/O behavior considers the time signals, f(t) and y(t). Fortunately, the I/O behavior has significantly simpler dynamics compared to stability analysis where the entire flow dynamics is under investigation.

The model reduction problem for the preservation of input-output dynamics can be posed as following: Find the state-space system of order $r \ll n$,

$$\dot{\kappa} = A\kappa + B\mathbf{f},
\hat{\mathbf{y}} = C\kappa + D\mathbf{f}.$$
(17)

so that for any input f the difference between the output of the original and of the reduced system is small, i.e.

$$\sup_{f} \frac{\|\boldsymbol{y} - \hat{\boldsymbol{y}}\|}{\|f\|} = \|G - G_r\|_{\infty} \le \epsilon_r \tag{18}$$

with $\epsilon_r \ll 1$. Equivalently, the model reduction error can be written in terms of the associated transfer functions $G_r = C(sI - A)^{-1}B$ and $G = C(sI - A)^{-1}B$ in the frequency domain $s \in C$ instead of the time-domain.

One way to compute the reduced-order model (17) with a nearly minimal model reduction error (18) is called balanced truncation (Moore 1981). The method can be introduced in many different ways. In this section we will outline the method in manner that is reminiscent of the optimization problems that arise in the stability analysis. The presentation follows closely Bagheri

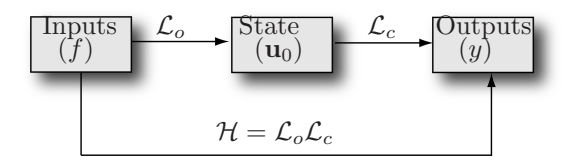


FIGURE 6. The operators used to examine the system inputoutput behavior. The controllability operator \mathcal{L}_c relates past inputs to the present state, while the observability mapping \mathcal{L}_o relates the present state to the future outputs. Their combined action is expressed by the Hankel operator \mathcal{H} .

et al. (2008a), where also definitions of appropriate Hilbert spaces and adjoint operators are provided. Whereas, in stability analysis we were concerned with the properties of the evolution operator $\mathcal{T}(t)$, here our focus will lie on the so called Hankel operator (Glover 1999) that maps input signals to output signals. In particular, it is defined as the mapping from past inputs $\mathbf{f}(t): t \in (-\infty, 0]$ to future outputs $\mathbf{y}(t): t \in [0, \infty)$,

$$\mathbf{y}(t) = \mathcal{H}\mathbf{f}(t) = \mathcal{C} \int_{-\infty}^{0} \mathcal{T}(t-\tau)\mathcal{B}\mathbf{f}(\tau) d\tau.$$
 (19)

The amplification of the output signal at time t is given by

$$\|\mathbf{y}(t)\|^2 = (\mathcal{H}\mathbf{f}, \mathcal{H}\mathbf{f}) = (\mathbf{f}, \mathcal{H}^*\mathcal{H}\mathbf{f}). \tag{20}$$

In particular, the unit-norm input signals that result in the largest output response are the eigenmodes of $\mathcal{H}^*\mathcal{H}$, *i.e.*

$$\mathcal{H}^* \mathcal{H} \boldsymbol{f}_j = \sigma_j^2 \boldsymbol{f}_j, \qquad \sigma_1 > \sigma_2 > \dots$$
 (21)

where the square root of the eigenvalues σ_j^2 are called the Hankel singular values (HSV). If $\sigma_1 > 1$, then the unit-norm input signal f_1 active in the past $t \in (-\infty, 0]$ will generate an amplified output signal in the future $t \in [0, \infty)$.

Upper and lower bounds of the model reduction error for balanced reduced-order model of order r is given by the HSV as

$$\sigma_{r+1} < \|G - G_r\|_{\infty} \le 2 \sum_{j=r+1}^{n} \sigma_j.$$
 (22)

To obtain the balanced reduced-order model (17) and its associated transfer function G_r we project Navier-Stokes equations including inputs and outputs onto a set of bi-orthogonal modes, referred to as the balanced modes. These modes can be derived by decomposing the Hankel operator into $\mathcal{H} = \mathcal{L}_o \mathcal{L}_c$ (shown schematically in Figure 6) which is possible since the operator (19)

characterizes the I/O behavior via a reference state \mathbf{u}_0 . In one part, the controllability operator \mathcal{L}_c , generates the reference state from past input signals, i.e.

$$\mathbf{u}_0 = \int_{-\infty}^0 \mathcal{T}(-\tau) \mathcal{B} \mathbf{f}(\tau) \, d\tau = \mathcal{L}_c \mathbf{f}(t).$$
 (23)

The range of \mathcal{L}_c , i.e. the restriction of the state-space to all possible initial states that we are able to reach with f(t) is called the controllable subspace. In particular the initial conditions that require the smallest input effort to reach are called controllable states and are the leading eigenmodes of the controllability Gramian

$$\mathcal{P} = \mathcal{L}_c \mathcal{L}_c^* = \int_0^\infty \mathcal{T}(\tau) \mathcal{B} \mathcal{B}^* \mathcal{T}^*(\tau) \, d\tau.$$
 (24)

The other part of the Hankel operator is the observability operator \mathcal{L}_o operator which generates future outputs from the reference state,

$$y(t) = \mathcal{C}\mathcal{T}(t)\mathbf{u}_0 = \mathcal{L}_o\mathbf{u}_0. \tag{25}$$

If $\mathcal{L}_o \mathbf{u}_0 = 0$ for an initial condition \mathbf{u}_0 , then \mathbf{u}_0 is unobservable, since it cannot be detected by the sensors. The observable states on the other hand are the initial conditions that are responsible for the largest output signals. These states the leading eigenmodes of the observability Gramian,

$$Q = \mathcal{L}_o^* \mathcal{L}_o = \int_0^\infty \mathcal{T}^*(\tau) \mathcal{C}^* \mathcal{C} \mathcal{T}(\tau) \, d\tau.$$
 (26)

Using the mapping \mathcal{L}_c and \mathcal{L}_o we can now obtain the balanced modes $\{\phi_j\}_{j=1}^m$ by mapping the most dangerous inputs signals f_j , i.e. right eigenvectors of $\mathcal{H}^*\mathcal{H}$ onto the state-space; $\phi_j = \mathcal{L}_c f_j$. A set of modes that are bi-orthogonal to ϕ_j ($(\phi_i, \psi_j) = \delta_{i,j}$) can be found from $\psi_j = \mathcal{L}_o^* g_j$, where g_j are the left eigenvectors of the Hankel operator (see Bagheri *et al.* 2008*a*, for further details). The projection of the full Navier-Stokes equations on the balanced modes; $A_{i,j} = (\psi_j, \mathcal{A}\phi_i)$, $B_1 = (\psi_i, \mathcal{B}_1)$ and $C_1 = \mathcal{C}_1\phi_i$ results in the balanced reducer-order model (17).

Traditionally, the balanced modes are defined as the eigenvectors of the product of the controllability and observability Gramian. This formulation is easily obtained by noting that

$$\mathcal{L}_c \mathcal{H}^* \mathcal{H} f_j = \mathcal{L}_c \mathcal{L}_c^* \mathcal{L}_o^* \mathcal{L}_o \mathcal{L}_c f_j = \sigma_j^2 \mathcal{L}_c f_j \tag{27}$$

which results in the following eigenvalue problem for the balanced modes

$$\mathcal{P}\mathcal{Q}\phi_i = \sigma_i^2 \phi_i. \tag{28}$$

Similar to the modal and nonmodal analysis we end up with a very large eigenvalue problem when the state-space system is discretized.

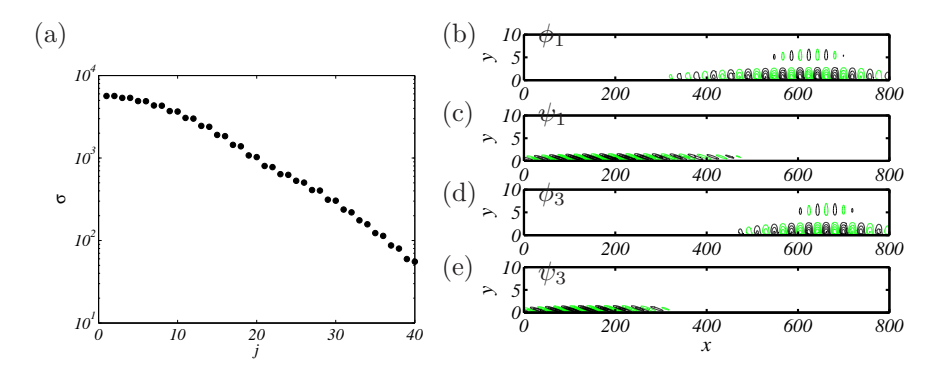


FIGURE 7. (a) Singular values of Hankel operator. The streamwise velocity component of first and third direct are shown in (b) and (d) respectively. Their associated adjoint modes are shown in (c) and (e).

3.5. The Snapshot Method

In this section a brief summary of the snapshot method (Sirovich 1987) for solving the eigenvalue problem (28) is presented. It is based on the recognition that the controllability and observability Gramians are the state correlation matrices generated from the impulse response of the forward and adjoint states respectively. The method for the computation of the balanced modes based on snapshots was introduced by Rowley (2005) where it is also described in more detail.

The method has similarities to the Krylov-method presented earlier to compute global eigenmodes and optimal disturbances. This time, we will build two Krylov subspaces but avoid iterative techniques by exploiting the fact that the input and output spaces are much smaller than the state-space. In our case we have two inputs and two outputs (i.e. r=p=2) whereas the dimension of the state-space is approximately $n=10^5$. The controllability and observability subspaces are, respectively,

$$X = \operatorname{span}\{\mathcal{B}, \mathcal{T}(\Delta t)\mathcal{B}, \mathcal{T}(2\Delta t)\mathcal{B}, \dots, \mathcal{T}((m-1)\Delta t)\mathcal{B}\}$$
 (29)

$$Y = \operatorname{span}\{\mathcal{C}^*, \mathcal{T}^*(\Delta t)\mathcal{C}^*, \mathcal{T}^*(2\Delta t)\mathcal{C}^*, \dots, \mathcal{T}^*((m-1)\Delta t)\mathcal{C}^*\}.$$
(30)

Each element of X contains snapshots from DNS simulations of the impulse response of each input \mathcal{B}_i . Similarly, each element of Y contains snapshots from adjoint DNS simulations of the impulse response of each output \mathcal{C}_i .

In a discretized setting, X is a $n \times (rm)$ matrix and Y a $n \times (pm)$ matrix. The Gramians can be approximated with $\mathcal{P} \approx XX^T\Delta t$ and $\mathcal{Q} \approx YY^T\Delta t$. Thus the eigenvalue problem (27) can then be approximated as

$$\mathcal{PQ}\phi_{j} \approx (\Delta t)^{2} X X^{H} Y Y^{H} \phi_{j} = \sigma^{2} \phi_{j}. \tag{31}$$

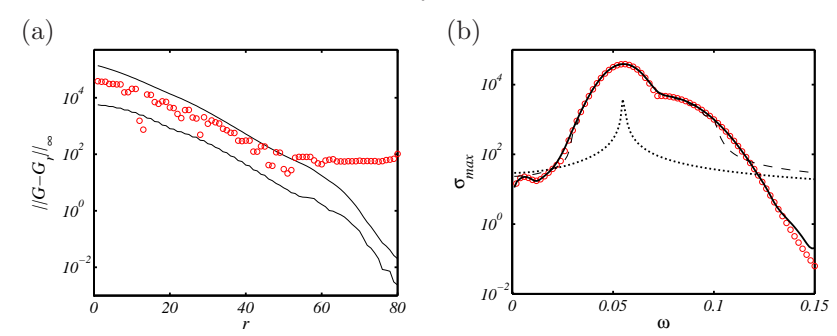


FIGURE 8. (a) The error at capturing the peak frequency is shown with circles. The upper and lower theoretical bounds are depicted with solid lines. (b) The largest singular values σ of the transfer function $|G(i\omega)|$ from all input to all outputs computed using the time-stepper is shown with circles. The largest response is for $\omega=0.055$ with a peak value of $3.86 \cdot 10^4$. The frequency response of the reduced model with rank 2 (dotted), 40 (dash-dotted) and 74 (thick solid). Note that already the small model with rank 2 locates the frequency where the original system is most amplified.

This eigenvalue problem is of size $n \times n$ and prohibitively expensive to solve for Navier-Stokes system. One can again resort to Arnoldi method and iterative techniques to solve the above eigenvalue problem as suggested in Willcox & Peraire (2002). However, this can be avoided by expanding the sought-after balanced modes in snapshots, i.e. $\phi_j = XH_j$. The column vector H_j contains the expansion coefficients. This leads to small eigenvalue problem of size $pm \times rm$ for H,

$$(XYY^{H}X)H_{j} = \sigma_{i}^{2}H_{j}. \tag{32}$$

Usually the number of snapshots m times the number inputs (r) or outputs (p) is significantly smaller than the number of states n, which makes this method computationally tractable for systems of very large dimensions.

3.6. Results

3.6a. Performance of Reduced-Order Model. Figure 7 shows the spectrum and two eigenfunctions obtained by solving the eigenvalue problem (28) using the snapshot method. The first and third balanced modes and their associated adjoint modes are shown in figure 7(b). The singular values come in pairs (2j-1,j), resolving the n-th harmonics (Ilak & Rowley 2008; Ahuja et al. 2007; Bagheri et al. 2008a). Therefore the second and fourth balanced mode looks like first and third mode respectively, but shifted in the streamwise direction. We observe that the leading balanced modes (figure 7(a) and (c)) appear as

wavepackets located at the downstream end of the domain, whereas the adjoint balanced modes (figure 7(b) and (d)) are upstream tilted structures located at the upstream end of the domain. The adjoint modes are similar to the linear optimal disturbances shown in figure 5(a) and the balanced modes are similar to global eigenmodes shown in figure 2(b). The adjoint balanced modes thus account for the output sensitivity and the direct balanced modes for the most energetic structures.

The projection of the full Navier-Stokes equations on the balanced modes; $A_{i,j} = (\psi_j, \mathcal{A}\phi_i), B_1 = (\psi_i, \mathcal{B}_1)$ and $C_1 = \mathcal{C}_1\phi_i$ results in the reducer-order model (17). The model reduction error (18) is shown in figure 8(a) together with the theoretical bounds given by the Hankel singular values in (22). The infinity norm of the transfer function equals the peak value of the frequency response. Estimating the model reduction error amounts to the calculation of the difference of the peak values of the reduced-order and the Navier–Stokes system. We observe the error norm remains approximately withing the bounds given by the Hankel singular values for the first 50 modes. Higher modes become increasingly ill-conditioned and as a consequence the numerical round-off errors increase, the bi-orthogonality condition is gradually lost and the reduced system is no longer balanced. However, the singular values shown figure 7(a) decrease rapidly, indicating that the I/O behavior of the chosen setup can be captured by a low-dimensional model.

To investigate this further, the amplitudes of the transfer functions with $s=i\omega,\ i.e.$ the frequency response, are displayed in figure 8(b) for reduced-order models of order r=2,40 and 70 and for the full DNS model of order 10^5 . All frequencies in the interval [0,0.13] are amplified and the most dangerous frequency, i.e. the peak response, is approximately $\omega=0.055$. From figure 8(b) we observe that the reduced-order model of order 2 captures the most important aspect of the input-output behavior, which is the response of the most dangerous frequency. The model with 40 modes is able to estimate the gains of all the amplified frequencies, but fails to capture the damped low and high frequencies. Adding 30 additional modes results in a model that preserves the input-output behavior correctly for nearly all frequencies.

Finally, the impulse responses from all inputs to all outputs of the reduced-order model (17) are compared to the full Navier–Stokes system (12). In figure (9) three signals $\mathcal{B}_1 \to \mathcal{C}_1$, $\mathcal{B}_1 \to \mathcal{C}_2$ and $\mathcal{B}_2 \to \mathcal{C}_1$ are shown with lines. The response of \mathcal{C}_2 to forcing in \mathcal{B}_2 is zero, since disturbances traveling upstream are quickly damped. These impulse responses were obtained by using the time-stepper with $\sim 10^5$ degrees of freedom. The impulse responses of the reduced-order model (17) with r=70 given by $y(t)=Ce^{At}B$ are shown with dashed lines. We observe that reduced-model registers the same signal as the full model from all inputs to all outputs. The wavepacket triggered by the impulse of \mathcal{B}_1 reaches the first sensor \mathcal{C}_2 after 600 time units and the second

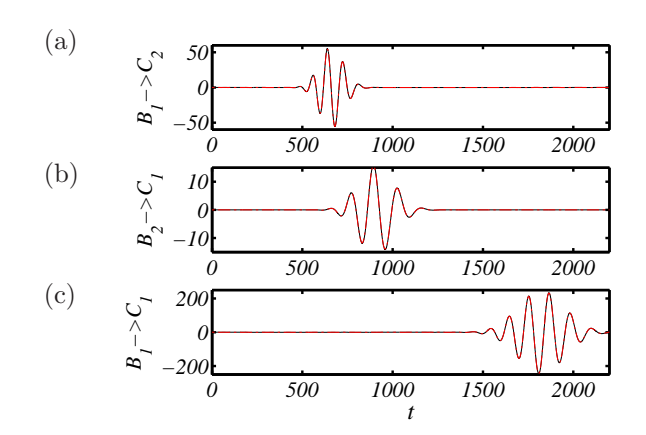


FIGURE 9. The impulse response from $\mathcal{B}_1 \to \mathcal{C}_2$ (a), $\mathcal{B}_2 \to \mathcal{C}_1$ (b) and $B_1 \to \mathcal{C}_1$ (c). The solid line represents direct numerical simulations with 10^5 degrees of freedom and the dashed line the balanced reduced-model with 50 degrees of freedom.

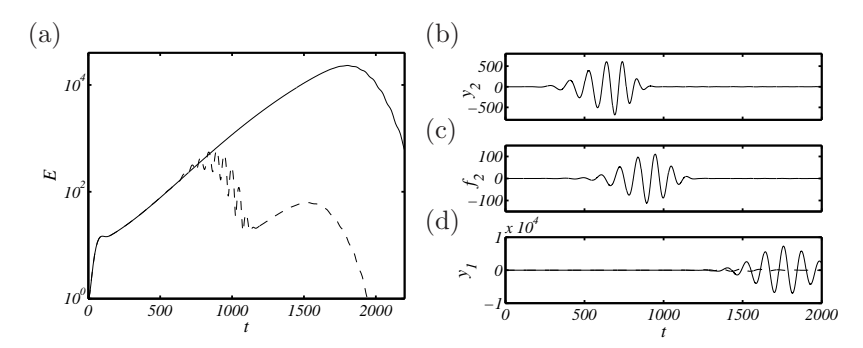


FIGURE 10. Control of the wavepacket due to the worst case initial condition. (a) Solid line shows uncontrolled energy evolution (as in figure 4 (b)) and dashed line shows the energy for the cheap controller. (b) Output signal as measured by the sensor \mathcal{C}_2 driving the controller. (c) Control signal fed into the wall actuator. (d) Signals from the sensor \mathcal{C}_1 measuring the objective function. Solid line shows uncontrolled case whereas dashed line shows the controlled case.

sensor C_1 after 1500 time units. The wavepacket triggered from the actuator B_2 reaches the second sensor after 600 time units.

3.6b. Performance of Controller. In this section a reduced-order feedback controller, with the same dimension as the reduced-order model (r = 70) of the

previous section, is developed. The closed-loop behavior of the system and the objective function will be investigated and compared to the uncontrolled case for the flat-plate boundary layer flow. In particular, the output z of the closed-loop, i.e. the compensator (16) connected to the full Navier–Stokes model (8) is compared to the linearized Navier–Stokes equations without control when the system is forced with stochastic excitation or initiated with an optimal disturbance.

Three controllers are investigated; (i) cheap control/low noise contamination with control penalty l=1 and noise parameter $\alpha=10^2$, (ii) expensive control/high noise contamination with $l=10^2$ and $\alpha=10^7$ and (iii) an intermediate case with l=10 and $\alpha=10^5$.

The performance of the cheap controller in case (i) for the control of the optimal initial condition discussed in Section 2 is examined first. This case is interesting because the controller is not designed specifically for this configuration and it only has a limited window in time to counteract the disturbances that are propagating through the domain in the form of a localized wavepacket. In figure 10(a) the full domain kinetic energy as a function of time is shown as a solid black line for the uncontrolled evolution and as a dashed line for the controlled case. The effect of the controller is evident. The measurement signal detected by the sensor C_2 is shown in figure 10(b) revealing that the sensor picks up the front of the wavepacket arriving at $t \approx 350$. A time lag of ≈ 300 consistent with the speed of the propagating wavepacket $(0.3 U_{\infty})$ is observed until the controller starts acting on the information (see figure 10(c)). The downstream measurement, i.e. the objective function to be minimized, is shown in figure 10(d) as a black solid line for the uncontrolled case and as a dashed black line for the controlled case. It can be seen that also this measure shows a satisfactory performance of the controller.

The three different controllers are tested on a flow case which is forced by the upstream disturbance input \mathcal{B}_1 with a random time signal. The wall-normal maximum of the rms-values of the streamwise velocity component in cases with and without control are shown in figure 11. The rms-value grows exponentially downstream in the uncontrolled case until the fringe region at x = 800. The rms of the controlled perturbation grows only until it reaches the actuator position where it immediately begins to decay. At the location of the objective function \mathcal{C}_1 (x = 750), the amplitude of the perturbations is one order of magnitude smaller than in the uncontrolled case for the cheapest controller.

The rms values in the case of the expensive (case ii) and intermediate control (case iii) are shown with dashed and dashed-dotted lines respectively. The expensive control is very conservative as the measurement signals are highly corrupted and the control effort limited; it results only in a small damping of the disturbances. The intermediate controller (case iii) is more cautious in

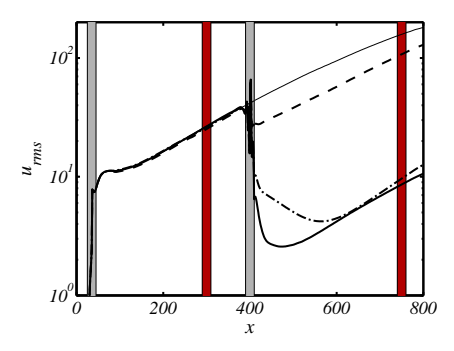


FIGURE 11. The rms-values of the uncontrolled system (thin solid line), cheap controller (thick solid line), intermediate controller (dash-dotted line) and expensive controller (dashed line). The gray bar represent the size (defined as 99% of the spatial support) and location of the two inputs, whereas the darker bars correspond to the two outputs.

Modes	EVP	Snapshots	Method
Global modes	$\mathcal{T}\phi = \sigma\phi$	$\mathcal{T}(j\Delta t)\mathbf{u}_0$	Arnoldi
Optimal disturbances	$T^*T\phi = \sigma\phi$	$\mathcal{T}^*(j\Delta t)\mathcal{T}(j\Delta t)\mathbf{u}_0$	Arnoldi
Balanced modes	$PQ\phi = \sigma\phi$	$\mathcal{CT}^*(j\Delta t)\mathcal{T}(j\Delta t)\mathcal{B}$	Snapshot

Table 1. Eigenvalue problems to solve and the corresponding subspace method used in order to obtain measures for stability and control.

reducing the perturbation energy just downstream of the actuator when compared to the cheap controller. It is interesting to note, however, that at the location where the objective function is measured, the disturbance amplitude has decreased nearly as much as with the cheap controller, although the total perturbation energy is larger over the entire domain.

4. Conclusion

Two prerequisites for successful control design are stability analysis and model reduction. The former provides a sound understanding of the instabilities, sensitivities and growth mechanisms in the flow, whereas the latter provides a simple and small model that is able to capture the essential dynamics. This preparatory work for control design amounts to solving various large eigenvalue problems as listed in table 1. The short-time and asymptotic behavior of disturbances can be completely characterized by the solution of two large eigenvalue

problems involving the evolution operator of the linearized Navier-Stokes equations \mathcal{T} . The global spectrum of \mathcal{T} , determine the asymptotic growth/decay, dominant temporal frequencies and the dominant spatial location of instabilities. The global spectrum of $\mathcal{T}^*\mathcal{T}$, determine the short-time growth/decay of disturbances and the spatial structure of the most dangerous disturbances. This knowledge is indispensable for actuator and sensor placements. Sensors are placed where the flow energy is large, whereas actuators are placed where the flow sensitivity is large in order to minimize the input effort. Since the relation between a few inputs and outputs has much simpler dynamics than the instability physics a reduced-order model can be constructed by solving a third eigenvalue problem involving the inputs, outputs and the evolution operator. This results in the balanced modes. The computation of the three sets, global eigenmodes, optimal disturbances and balanced modes is performed with a time-stepper thereby avoiding to store large matrices. When the entire flow dynamics is of interest the high dimensions of the state require iterative techniques. When the I/O behavior is of interest, on the other hand, computational tractability depends on the number of inputs and outputs. Therefore the snapshot method can be employed in the case of few inputs and outputs. The results of this paper also enhance our previous work (Bagheri et al. 2008a) by incorporating actuation and sensing at the wall. The next step towards applying the controller in experiments, is to design a similar control strategy for three-dimensional disturbances in the Blasius flow. Rows of localized actuators and sensors at the wall in the spanwise direction and more realistic disturbance environments, such as free-stream turbulence will be modeled.

Appendix A. Inputs and outputs

The expression of inputs \mathcal{B}_1 , \mathbf{u}_w and outputs \mathcal{C}_1 and \mathcal{C}_2 are given in this section. The input \mathcal{B}_1 is modelled by Gaussian type of volume forcing

$$\begin{bmatrix} \sigma_{w,x}\gamma_{w,y} \\ -\sigma_{w,y}\gamma_{w,x} \end{bmatrix} \exp(-\gamma_{w,x}^2 - \gamma_{w,y}^2), \qquad \gamma_{w,x} = \frac{x - x_w}{\sigma_{w,x}}, \qquad \gamma_{w,y} = \frac{y - y_w}{\sigma_{w,y}}, \tag{A1}$$

with $(\sigma_{w,x} = 4, \sigma_{w,y} = 0.25)$ determining the width and height of the function of the function centered around $(x_w = 35, y_w = 1)$. The actuator is in this case a localized zero mass-flux actuation on the wall-normal velocity, $\mathbf{u}_w = (0, v_w)^T$ at the lower wall given by

$$v_w(x) = \left(1 - \left(\frac{x - x_u}{\sigma_{u,x}}\right)^2\right) \exp\left(\frac{(x - x_u)^2}{2\sigma_{u,x}^2}\right),\tag{A2}$$

with the width $\sigma_{u,x} = 2.5$ and centered at $x_u = 400$. Finally, both measurements extract approximately the wall normal derivative of the streamwise

velocity component (wall shear stress) in limited regions at the wall

$$\int_{\Omega} \left(\gamma_{s,x} \gamma_{s,y} \mathcal{D}_y \quad 0 \right) \begin{pmatrix} u \\ v \end{pmatrix} d\Omega, \tag{A3}$$

where

$$\gamma_{s,x} = \exp\left(-\frac{(x-x_s)^2}{\sigma_{s,x}^2}\right), \quad \gamma_{s,y} = \frac{1}{\sigma_{s,y}} \exp\left(\frac{y^2}{\sigma_{s,y}^2}\right).$$
(A4)

The center of the function is $x_e = 300$ for the output C_2 and $x_e = 750$ for C_1 , and the width of the regions are determined by $\sigma_{s,x} = 5$ for both sensors. The operator \mathcal{D}_y denotes the y-derivative. The y-dependent weighting relies on a width parameter $\sigma_{s,y} = 0.05$. Note that in the limit $\sigma_{s,y} \to 0$ the function approaches the delta function so that (A3) defines the exact wall wall shear stress at the wall. The reason for using an approximation to the wall shear stress is the need for an adjoint sensor C^* (see Section 3.4), which is derived with the respect to the signal to state inner product (as explained in Bagheri et al. 2008a)

$$(r, \mathcal{C}\mathbf{u})_s = (\mathcal{C}^*r, \mathbf{u})_{\Omega}. \tag{A5}$$

These inner products are defined as

$$(r,s)_s = r^T s$$
 and, $(\mathbf{p}, \mathbf{q})_{\Omega} = \int_{\Omega} \mathbf{p}^T \mathbf{q} \, d\Omega$. (A6)

for the scalars r and s, and the states ${\bf q}$ and ${\bf p}$. The adjoint sensor obtained from this definition is in other words

$$(r, \mathcal{C}\mathbf{u})_{s} = \int_{\Omega} r^{T} (\gamma_{s,x} \gamma_{s,y} \mathcal{D}_{y} \quad 0) \mathbf{u} d\Omega = \int_{\Omega} r^{T} (2y \gamma_{s,x} \gamma_{s,y} / \sigma_{s,y}^{2} \quad 0) \mathbf{u} d\Omega$$
$$= (\mathcal{C}^{*}r, \mathbf{u})_{\hat{\Omega}}, \tag{A7}$$

where we have used integration by parts and the boundary conditions in y. This leads to the recognition of the adjoint sensor in the definition of the observability Gramian (26) as

$$C^* = \begin{pmatrix} 2y\gamma_{s,x}\gamma_{s,y}/\sigma_{s,y}^2 \\ 0 \end{pmatrix}. \tag{A8}$$

Acknowledgements

The authors would like to thank Antonios Monokrousos for assisting in the implementations and acknowledge the financial support from the Swedish Research Council (VR).

References

- Ahuja, S., Rowley, C. W., Kevrekidis, I. G. & Wei, M. 2007 Low-dimensional models for control of leading-edge vortices: Equilibria and linearized models. AIAA Paper 2007-709, 45th AIAA Aerospace Sciences Meeting and Exhibit.
- ÅKERVIK, E., EHRENSTEIN, U., GALLAIRE, F. & HENNINGSON, D. S. 2007a Global two-dimensional stability measures of the flat plate boundary-layer flow. Eur. J. Mech. B/Fluids 27, 501–513.
- ÄKERVIK, E., HŒPFFNER, J., EHRENSTEIN, U. & HENNINGSON, D. S. 2007b Optimal growth, model reduction and control in a separated boundary-layer flow using global eigenmodes. J. Fluid. Mech. 579, 305–314.
- Anderson, B. & Moore, J. 1990 Optimal control: Linear Quadratic Methods. New York: Prentice Hall.
- Bagheri, S., Brandt, L. & Henningson, D. S. 2008a Input-output analysis, model reduction and control design of the flat-plate boundary layer. J. Fluid Mech. In press.
- Bagheri, S., Hœpffner, J., Schmid, P. & Henningson, D. 2008b Input-output analysis and control design applied to a linear model of spatially developing flows. *Appl. Mech. Rev.* In press.
- Barkley, D., Blackburn, H. & Sherwin, S. J. 2008 Direct optimal growth analysis for timesteppers. *Int. J. Numer. Meth. Fluids* **57**, 1435–1458.
- Barkley, D., Gomes, M. G. & Henderson, R. D. 2002 Three-dimensional instability in flow over a backward-facing step. *J. Fluid Mech.* 473, 167–190.
- Bewley, T., Temam, R. & Ziane, M. 2000 A general framework for robust control in fluid mechanics. *Physica D: Nonlinear Phenomena* 138, 360–392.
- Blackburn, A. M., Barkley, D. & Sherwin, S. 2008 Teonvective instability and transient growth in flow over a backward-facing step. *J. Fluid Mech.* **603**, 271–304.
- Butler, K. & Farrell, B. F. 1992 Three-dimensional optimal perturbations in viscous shear flow. *Phys. Fluids A* 4, 1637–1650.
- Chevalier, M., Hoepffner, J., Åkervik, E. & Henningson, D. S. 2007a Linear feedback control and estimation applied to instabilities in spatially developing boundary layers. *J. Fluid Mech.* 588, 163–187.
- Chevalier, M., Hoepffner, J., Bewley, T. R. & Henningson, D. S. 2006 State

- estimation in wall-bounded flow systems. Part 2. Turbulent flows. J. Fluid Mech. **552**, 167-187.
- Chevalier, M., Schlatter, P., Lundbladh, A. & D.S., H. 2007b A pseudo spectral solver for incompressible boundary layer flows. *Technical Report, Trita-Mek* 7.
- Chomaz, J. M. 2005 Global instabilities in spatially developing flows: Non-normality and nonlinearity. *Ann. Rev. Fluid Mech.* **37**, 357–392.
- Cossu, C. & Chomaz, J. 1997 Global measures of local convective instability. *Phys. Rev. Lett.* **77**, 4387–90.
- Curtain, R. & Zwart, H. 1995 An introduction to infinite-dimensional linear systems theory. New York: Springer Verlag.
- EHRENSTEIN, U. & GALLAIRE, F. 2005 On two-dimensional temporal modes in spatially evolving open flows: the flat-plate boundary layer. *J. Fluid Mech.* **536**, 209–218.
- GILES, M. B. & PIERCE, N. A. 2001 Analytic adjoint solutions for the quasi-onedimensional Euler equations. J. Fluid Mech. 426, 327–345.
- GLOVER, K. 1999 All optimal Hankel-norm approximations of linear multivariable systems and the l^{∞} -error bounds. Int. J. Control **39**, 1115–1193.
- Hoepffner, J., Chevalier, M., Bewley, T. R. & Henningson, D. S. 2005 State estimation in wall-bounded flow systems. Part 1. Perturbed laminar flows. *J. Fluid Mech.* **534**, 263–294.
- HÖGBERG, M., BEWLEY, T. R. & HENNINGSON, D. S. 2003 Linear feedback control and estimation of transition in plane channel flow. J. Fluid Mech. 481, 149–175.
- HÖGBERG, M., BEWLEY, T. R. & HENNINGSON, D. S. 2003 Relaminarization of $re_{\tau}=100$ turbulence using gain scheduling and linear state-feedback control. *Phys. Fluids* **15**, 3572–3575.
- HÖGBERG, M. & HENNINGSON, D. S. 2002 Linear optimal control applied to instabilities in spatially developing boundary layers. *J. Fluid Mech.* 470, 151–179.
- Huerre, P. & Monkewitz, P. A. 1990 Local and global instabilities in spatially developing flows. *Annu. Rev. Fluid Mech.* **22**, 473–537.
- ILAK, M. & ROWLEY, C. W. 2008 Modeling of transitional channel flow using balanced proper orthogonal decomposition. *Phys. Fluids* **20**, 034103.
- Kim, J. & Bewley, T. R. 2007 A linear systems approach to flow control. Annu. Rev. Fluid Mech. 39, 383–417.
- KREISS, G., LUNDBLADH, A. & HENNINGSON, D. 1993 Bounds for threshold amplitudes in subcritical shear flows. *J. Fluid Mech.* 1994, 175–198.
- Lehoucq, R. B., Sorensen, D. & Yang, C. 1998 ARPACK Users' Guide: Solution of Large-Scale Eigenvalue Problems with Implicitly Restarted Arnoldi Methods. SIAM, Philadelphia.
- Levin, O. & Henningson, D. S. 2003 Exponential vs algebraic growth and transition prediction in buondary layer flow. Flow, Turbulence and combustion 70, 183–210.
- Monokrousos, A., Brandt, L., Schlatter, P. & Henningson, D. S. 2008 DNS and LES of estimation and control of transition in boundary layers subject to free-stream turbulence. *Int. J. Heat Fluid Flow* **29** (3), 841–855.

- MOORE, B. 1981 Principal component analysis in linear systems: Controllability, observability, and model reduction. *Automatic Control, IEEE Transactions* **26** (1), 17–32.
- ORR, W. M. F. 1907 The stability or instability of the steady motions of a perfect liquid and of a viscous liquid. Part I: A perfect liquid. Part II: A viscous liquid. *Proc. R. Irish Acad. A* 27, 9–138.
- ROWLEY, C. W. 2005 Model reduction for fluids using balanced proper orthogonal decomposition. *Int. J. Bifurc. Chaos* **15** (3), 997–1013.
- SCHMID, P. J. 2007 Nonmodal stability theory. Ann. Rev. Fluid Mech. 39, 129-62.
- Schmid, P. J. & Henningson, D. S. 2001 Stability and transition in shear flows. New York: Springer.
- SIROVICH, L. 1987 Turbulence and the dynamics of coherent structures i-iii. *Quart. Appl. Math.* **45**, 561–590.
- White, F. M. 1991 Viscous Fluid Flow, second edition edn. McGraw-Hill, Inc.
- WILLCOX, K. & PERAIRE, J. 2002 Balanced model reduction via the proper orthogonal decomposition. AIAA J. 40 (11), 2323–2330.
- Zhou, K., Doyle, J. & Glover, K. 2002 Robust and Optimal Control. New Jersey: Prentice Hall.
- Zhou, K., Salomon, G. & Wu, E. 1999 Balanced realization and model reduction for unstable systems. *Int. J. Robust Nonlinear Control* **9**, 183–198.

5

Linear feedback control and estimation applied to instabilities in spatially developing boundary layers

By Mattias Chevalier^{1,2}, Jérôme Hæpffner³, Espen Åkervik² and Dan S. Henningson²

¹The Swedish Defence Research Agency (FOI), SE-164 90, Stockholm, Sweden
 ²Linné Flow Centre, KTH Mechanics, SE-100 44, Stockholm, Sweden
 ³ IRPHÉ, Université de Provence, F-13384 Marseille Cedex 13, France

J. Fluid Mech., 588 (2007), pages 163-187

This paper presents the application of feedback control to spatially developing boundary layers. It is the natural follow-up of Högberg & Henningson (2002), where exact knowledge of the entire flow state was assumed for the control. We apply recent developments of stochastic models for the external sources of disturbances that allow the efficient use of several wall measurement for estimation of the flow evolution: the two components of the skin-friction and the pressure fluctuation at the wall. Perturbations to base flow profiles of the family of Falkner-Skan-Cooke boundary layers are estimated by use of wall measurements. The estimated state is in turn fed back for control in order to reduce the kinetic energy of the perturbations. The control actuation is achieved by means of unsteady blowing and suction at the wall. Flow perturbations are generated at the upstream region in the computational box and are propagating in the boundary layer. Measurements are extracted downstream over a thin strip, followed by a second thin strip where the actuation is performed. It is shown that flow disturbances can be efficiently estimated and controlled in spatially evolving boundary layers for a wide range of base flows and disturbances.

1. Introduction

There is much to be gained in the application of control to fluid mechanical systems, the most widely recognized and targeted aim being the reduction of skin friction drag on airplane wings. Flow control is a growing field and much research effort is spent in both fundamental understanding and direct application of control methods. For a review see e.g. Bewley (2001) and Högberg & Henningson (2002).

Linear control theory gives powerful model-based tools for application of control to fluid systems provided the system at hand can be well described by a linear dynamic model. The theory of Linear—Quadratic—Gaussian control (LQG) is one of the major achievements in the field of control theory. It gives a methodology to compute the optimal, measurement based, control when the dynamic model is linear, the objective is quadratic, and the external sources of excitations are stochastic. This theory is applied to boundary layer control in the present work.

Feedback control design can be conceptually and technically decomposed into two subproblems. The first subproblem is to estimate the flow state from noisy wall measurements. In our case, the state is the flow perturbation about the known base flow profile. The estimator is a simulation of the dynamic system that is run in parallel to the flow. Its state is forced by a feedback of the measurements in order to converge to the real flow state. The estimated state is in turn used for feedback control of the flow which constitutes the second subproblem. The closed loop system with estimation and control is commonly referred to as measurement feedback control or compensator.

This paper is the necessary follow-up of Högberg & Henningson (2002) in which full information control was applied to spatially developing flows. The use of stochastic models for external sources of excitation was introduced in Hopffner et al. (2005) and Chevalier et al. (2006), which allows computation of well-behaved estimation feedback kernels for three wall measurements: the two components of the skin-friction and the wall pressure. Each of these three measurements provide the estimator with additional information on the instantaneous flow state. This variety of measurements is instrumental when complex flows are targeted. This improvement of the estimation thus makes it possible to apply the full theory of feedback control to complex flow cases such as the transitional scenarios presented in this paper. For this reason, we have systematically reconsidered the flow cases of Högberg & Henningson (2002), where exact knowledge of the entire flow state was assumed, and applied measurement-feedback control, where the estimated flow state is used for control. We compared the performance between the full information control of Högberg & Henningson (2002) and the present estimation based control, and found satisfactory performance.

One of the major limitations to the application of control to spatially distributed systems (system in space and time, usually described by partial differential equations) is the realization of the sensing and actuation that would handle relatively fast events as well as small scales of fluid motion. In addition, control over physical surfaces typically requires dense arrays of sensors and actuators. Recent development in MEMS technology and related research may lead to solutions of this problem. For application of MEMS technology to flow control see e.g. Yoshino et al. (2003).

Several recent investigations have pursued the application of LQG-type feedback control to wall-bounded flow systems. A recent overview of this progress is given in Kim (2003). Högberg $et\ al.\ (2003a)$ demonstrated the localization of the feedback kernels. This property allows a local application of the control, i.e. only the local properties of the system (dynamics, disturbance sources and measurement information) are necessary for control. The efficiency of the control scheme we use here was illustrated in Högberg $et\ al.\ (2003b)$, where relaminarization of a fully developed turbulent flow was achieved. In Hoepffner $et\ al.\ (2005)$ and Chevalier $et\ al.\ (2006)$, the focus was on the estimation performance. By introducing a relevant model for the external source of disturbance, it was possible to improve the estimation performance on both transitional and turbulent flows.

The procedures of control design are based on the manipulations of a linear dynamic model for the flow system, which is typically of large order. In the case of spatially invariant systems, i.e. system for which the dynamics is independent of some spatial coordinates, the problem can be decoupled in a parameterized family of smaller systems. In our case, we assume spatial homogeneity over the two horizontal directions. After Fourier transforming, this allows to design and tune the controller and estimator for individual wavenumber pairs.

In a spatially developing flow like the boundary layer, this procedure can still be used, even though the spatial invariance in the streamwise direction is lost. Indeed, the localization of the control and estimation kernels ensures that the feedback is local, so that the flow can be assumed to be locally parallel. In Högberg & Henningson (2002), the actuation was successfully applied over a strip parallel to the leading edge in Falkner–Skan–Cooke (FSC) boundary layers, and the control feedback law was computed based upon the local Reynolds number. In Högberg $et\ al.\ (2003c)$, a measurement strip was added, and the subsequent state estimate was used for control. The present paper aims at the application of the recent development and improvement on the estimation of the complex flow cases where the full information control was shown to be successful in Högberg & Henningson (2002).

The structure of this paper is as follow. In $\S 2$, the flow system is described: dynamics, input and output. In $\S 3$, we outline the main issues for the feedback control and estimation. The numerical method is described in $\S 4$. The performance of the control in several flow cases is shown in $\S 5$, and concluding remarks are given in $\S 6$.

2. System description

2.1. Flow dynamics

The Navier–Stokes equations are linearized about solutions of the FSC boundary layer. Favourable and adverse pressure gradients can be accounted for as well as the effect of a sweep. To obtain the family of FSC similarity solutions we assume that the chordwise outer-streamline velocity obeys the power law $U_{\infty}^* = U_0^* (x^*/x_0^*)^m$ and that the spanwise free-stream velocity W_{∞}^* is constant. In the expression above, U_0^* is the free-stream velocity at a fixed position x_0^* , the physical distance from the leading edge, and the asterisks (*) denote dimensional quantities. Note that the Blasius profile is a special case of the FSC boundary layer with zero cross-flow component and no pressure gradient. If we choose the similarity variable ξ as A

$$\xi(y^*) = y^* \sqrt{\frac{m+1}{2} \frac{U_{\infty}^*}{2\nu x^*}}$$

one can derive the following self-similar boundary layer profiles,

$$f''' + ff'' + \beta_h (1 - f'^2) = 0,$$

 $g'' + fg' = 0,$

where the Hartree parameter β_h relates to the power law exponent m as $\beta_h = 2m/(m+1)$. The accompanying boundary conditions are

$$f = f' = g = 0$$
, for $\xi = 0$,
 $f' \to 1$, $g \to 1$, as $\xi \to \infty$.

The complete derivation can be found in e.g. Schlichting (1979) and Cooke (1950). From the FSC similarity solutions f and g, we construct the nondimensional velocity profiles

$$U(y) = f'(\xi(y)), \tag{1a}$$

$$W(y) = \frac{W_{\infty}^*}{U_{\infty}^*} \mathbf{g}(\xi(y)), \tag{1b}$$

for a fixed $x=(x^*-x_0^*)/\delta_0^*$ and where $y=y^*/\delta_0^*$. The symbol δ_0^* denotes the displacement thickness at position $x^*=x_0^*$. The velocity profiles (1a) and (1b) are then used as base flow when constructing the linear dynamic model for the flow disturbance and the initial conditions for the direct numerical simulations (DNS).

Once linearized, the system can be transformed to Fourier space by assuming local spatial invariance. This implies that the non-parallel effects are small, i.e. the base flow is slowly developing in the streamwise direction. After transformation to the velocity–vorticity $(v - \eta)$ formulation, we obtain the Orr–Sommerfeld/Squire equations (see e.g. Schmid & Henningson 2001)

$$\begin{pmatrix} \dot{v} \\ \dot{\eta} \end{pmatrix} = \begin{pmatrix} \mathcal{L}_{OS} & 0 \\ \mathcal{L}_{C} & \mathcal{L}_{SQ} \end{pmatrix} \begin{pmatrix} v \\ \eta \end{pmatrix}, \tag{2}$$

where

$$\mathcal{L}_{OS} = \Delta^{-1}[-i(k_xU + k_zW)\Delta + ik_xU'' + ik_zW'' + \Delta^2/Re],$$

$$\mathcal{L}_{SQ} = -i(k_xU + k_zW) + \Delta/Re,$$

$$\mathcal{L}_{C} = i(k_xW' - k_zU'),$$
(3)

and where the Laplacian operator is denoted $\Delta=D^2-k^2$ and D is the wall-normal derivative and $k^2=k_x^2+k_z^2$. The boundary conditions are defined as

$$v(0,t) = \varphi, \quad Dv(0,t) = 0, \quad \eta(0,t) = 0,$$

 $v(y,t) = 0, \quad Dv(y,t) = 0, \quad \eta(y,t) = 0, \quad \text{as} \quad y \to \infty.$ (4)

The control actuation affects the system through a non-homogeneous boundary condition on the wall-normal velocity $\varphi(t)$ (time varying wall blowing and suction). The Reynolds number Re is based on the free-stream velocity and displacement thickness.

In order to apply tools from control theory, see for example Lewis & Syrmos (1995), it is convenient to write the linearized fluid system in the general state-space form

$$\dot{q} = Aq + B_2 u_c + B_1 f, \quad q(0) = q_0,$$

 $y = Cq + g,$ (5)

where q is the state, A is the linear operator representing the dynamics of the system. The external disturbances, denoted by f, force the state through the input operator B_1 , and q_0 is the initial condition. The operator B_1 transforms a forcing on (u, v, w) to a forcing on (v, η) , since the flow state is expressed in this formulation. The control signal u_c affects the system through the input operator B_2 . Operator C extracts the measurements from the state variable, and g adds a stochastic measurement noise with given statistical properties. The noisy measurement is then denoted by g.

The controlled Orr–Sommerfeld/Squire system can be cast into the formalism of (5) by means of a lifting procedure (see e.g. Högberg *et al.* 2003a) where the control at the wall now enters the flow through a volume forcing term instead of as an inhomogeneous boundary condition at the wall. This is done by decomposing the flow state into a time varying homogeneous component (subscript h) and a steady particular (subscript p) component

$$\begin{pmatrix} v(t) \\ \eta(t) \end{pmatrix} = \begin{pmatrix} v_h(t) \\ \eta_h(t) \end{pmatrix} + \begin{pmatrix} v_p \\ \eta_p \end{pmatrix} \varphi(t). \tag{6}$$

The augmented state q, incorporating the actuation variable, thus reads

$$q = \begin{pmatrix} v_h(y,t) \\ \eta_h(y,t) \\ \varphi(t) \end{pmatrix}, \tag{7}$$

and augmented operator A and operator B (see §3) can be written

$$A = \begin{pmatrix} \mathcal{L}_{OSS} & \mathcal{L}_{OSS}q_p \\ 0 & 0 \end{pmatrix}, \quad B = \begin{pmatrix} -q_p \\ 1 \end{pmatrix}, \tag{8}$$

with

$$\mathcal{L}_{OSS} = \begin{pmatrix} \mathcal{L}_{OS} & 0\\ \mathcal{L}_{C} & \mathcal{L}_{SQ} \end{pmatrix}, \tag{9}$$

and where the particular solution q_p is chosen to satisfy the numerically convenient equation $\mathcal{L}_{OSS} q_p = 0$ with a unity boundary condition on the wall-normal velocity at the wall. With this formulation the control signal becomes $u_c = \dot{\varphi}$.

2.2. Stochastic disturbances

2.2a. Modeling of the external disturbances. The description of a dynamical system can also include a description of its input (external sources of excitations) and its output (measurements, possibly corrupted by noise). The performance of the state estimation relies on the construction of a proper model for the flow disturbances. Indeed, if the external sources of perturbations in the flow are well identified, it becomes an easy task to estimate the flow evolution using a dynamic model of the system.

The external sources of perturbations in typical aeronautical applications can be wall roughness, acoustic waves, and free-stream turbulence. In the case where the sensors are distributed over a strip in the boundary layer, upstream instabilities can generate waves that are to be considered as disturbances to the estimator.

We will assume the external disturbance forcing $f = (f_1, f_2, f_3)^T$ in (5) to be a zero-mean stationary white Gaussian process with auto-correlation

$$E[f_j(x, y, z, t)f_k(x + r_x, y', z + r_z, t')] = \underbrace{\delta(t - t')}_{\text{Temporal}} \underbrace{Q_{f_j f_k}(y, y', r_x, r_z)}_{\text{Spatial}},$$

where $\delta(\cdot)$ denotes the Dirac δ -function.

The remaining property to be described is the spatial extent of the two-point, one-time, auto-correlation of f over the whole domain

$$Q_{f_i f_k}(y, y', r_x, r_z) = E[f_i(x, y, z, t) f_k(x + r_x, y', z + r_z, t)].$$

The corresponding quantity in Fourier space is a covariance operator, obtained for any wavenumber pair $\{k_x, k_z\}$ via the following integration over the homogeneous directions

$$R_{f_j f_k}(y, y', k_x, k_z) = \int \int Q_{f_j f_k}(y, y', r_x, r_z) e^{-i(k_x r_x + k_z r_z)} dr_x dr_z.$$

Our model for the covariance of f assumes that the disturbance has a localized structure in space (i.e., the two-point correlation of the disturbance decays exponentially with distance) and that the correlations between forcing terms on different velocity components are zero. We assume a model for the covariance of the external forcing f of the form

$$R_{f_i f_k}(y, y', k_x, k_z) = d(k_x, k_z) \, \delta_{jk} \mathcal{M}^y(y, y'),$$
 (10)

where

$$d(k_x, k_z) = \exp\left[-\left(\frac{k_x - k_x^0}{d_x}\right)^2 - \left(\frac{k_z - k_z^0}{d_z}\right)^2\right]. \tag{11}$$

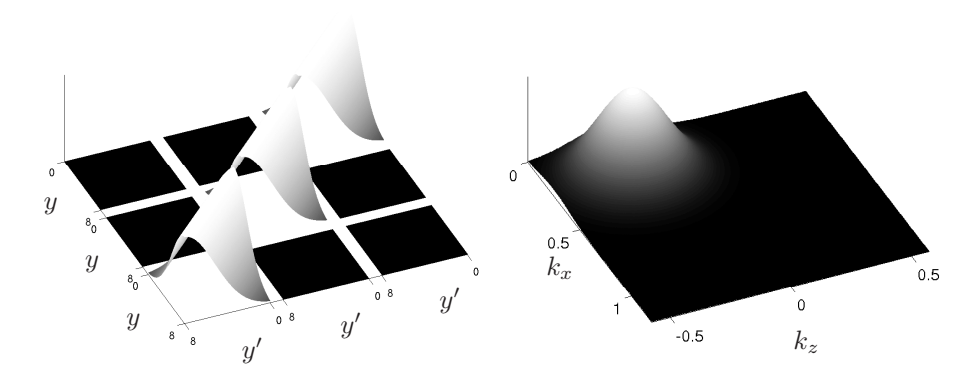


FIGURE 1. The covariance of f, for the FSC problem (cases 12–13 in table 1), is depicted in (a). From top to bottom and right to left each square represent the covariance for f_1 , f_2 , and f_3 . The wavenumber space amplitude function is shown in (b). The peak is set at $\{0.25, -0.25\}$, about the mode that is triggered in the FSC simulations.

The model parameters k_x^0 and k_z^0 can be used to locate the peak energy of the disturbances in Fourier space, and d_x and d_z to tune the width of this peak. These parameters are specific for each flow case, e.g. for a typical TS-wave the peak energy will be at $k_x^0 = 0.3$ and $k_z^0 = 0$, or for a typical streamwise streak, the choice will be $k_x^0 = 0$ and $k_z^0 = 0.49$.

The y-variation of $R_{f_if_k}$ is given by the function

$$\mathcal{M}^{y}(y, y') = \exp\left[-\frac{(y - y')^2}{2d_y}\right],\tag{12}$$

where the design parameter d_y governs the width of the two-point correlation of the disturbance in the wall-normal direction. A common choice of the sto-chastic model has been to consider an uncorrelated model in the wall-normal direction. However, in Hoepffner et al. (2005) it was shown that better estimator performance could be achieved by using a physically motivated stochastic model similar to the model described in this section. The model specific parameters for all flow cases presented are given in table 2.

Other forms for $d(k_x, k_z)$ are also possible, and may be experimented with in future work. Note that we will denote $R = R_{ff} = \text{diag}(R_{f_1f_1}, R_{f_2f_2}, R_{f_3f_3})$ in the sections that follow.

2.2b. Sensors and sensor noise. The measurements used in this study are the streamwise and spanwise shear stresses and the wall pressure fluctuations defined as

$$\begin{cases} \tau_x = \tau_{xy}|_{\text{wall}} = \frac{1}{Re} \left. \frac{\partial u}{\partial y} \right|_{\text{wall}} = \frac{1}{Re} \frac{i}{k^2} (k_x D^2 v - k_z D \eta)|_{\text{wall}}, \\ \tau_z = \tau_{zy}|_{\text{wall}} = \frac{1}{Re} \left. \frac{\partial w}{\partial y} \right|_{\text{wall}} = \frac{1}{Re} \frac{i}{k^2} (k_z D^2 v + k_x D \eta)|_{\text{wall}}, \\ p = p|_{\text{wall}} = \frac{1}{Re} \frac{1}{k^2} D^3 v|_{\text{wall}}. \end{cases}$$

which yields the following measurement matrix C

$$C = \frac{1}{Re} \frac{1}{k^2} \begin{pmatrix} ik_x D^2|_{\text{wall}} & -ik_z D|_{\text{wall}} \\ ik_z D^2|_{\text{wall}} & ik_x D|_{\text{wall}} \\ D^3|_{\text{wall}} & 0 \end{pmatrix}.$$

In Hoepffner $et\ al.\ (2005)$ it was discussed how the estimator performance degrades when different measurements are left out.

Each of the three measurements is assumed to be corrupted by random sensor noise processes, the amplitude of which is determined by the assumed quality of the sensors. The covariance of the sensor noise vector g can thus be described in Fourier space by a 3×3 matrix G where the diagonal elements α_t^2 are the variances of the sensor noise assumed to be associated with each individual sensor. The covariance for each sensor can be written on the following form

$$R_{g_{\iota}(t),g_{\kappa}(t')} = \delta_{\iota\kappa}\delta(t - t')\alpha_{\iota}^{2}, \tag{13}$$

where $\delta_{\iota\kappa}$ denotes the Kronecker delta. Thus, in the present work, we assume that the sensor noise is uncorrelated in both space and time.

When the signal-to-noise ratio is low, the measured signal must be fed back only gently into the estimator, lest the sensor noise disrupt the estimator. When the signal-to-noise ratio is high, the measured signal may be fed back more aggressively into the estimator, as the fidelity of the measurements can be better trusted. For a given covariance of the external disturbances, the tuning of the assumed overall magnitude of the sensor noise in the Kalman filter design thus provides a natural "knob" to regulate the magnitude of the feedback into the estimator.

3. Compensation

The system is now described: its dynamics is governed by (2), it is excited by external sources of disturbance as in (11) and the sensor information is corrupted by noise as in (13). We can now apply the procedure of LQG control and estimation governed by system 5.

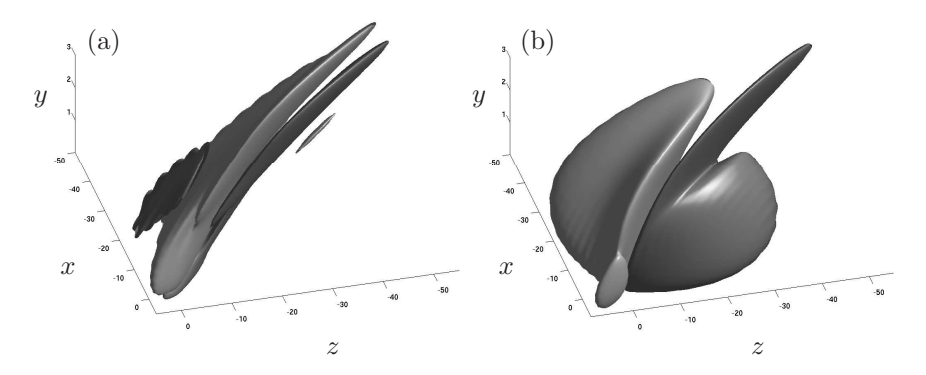


FIGURE 2. Steady-state control convolution kernels relating the flow state \hat{v} (a) and $\hat{\eta}$ (b) to the control at $\{x=0,\ y=0,\ z=0\}$ on the wall. Positive (dark) and negative (light) isosurfaces with isovalues of $\pm 20\%$ of the maximum amplitude for each kernel are illustrated. The kernels correspond to cases 12–13 in table 1 and 3.

3.1. Controller

To construct an optimization problem we need to define an objective function. The performance measure for optimality is chosen as a weighted sum of the flow kinetic energy and the control effort. We thus aim at preventing small disturbances from growing, and achieve this goal with the minimum possible actuation energy. The objective functional thus reads

$$J = \int_0^\infty (q^* \mathcal{Q}q + l^2 u_c^* u_c) \,\mathrm{d}t \tag{14}$$

where l^2 is included to penalize the time derivative of the control $u_c = \dot{\varphi}$, and

$$Q = \begin{pmatrix} Q & Qq_p \\ q_p^* Q & (1+r^2)q_p^* Qq_p \end{pmatrix}$$
 (15)

where the term r^2 is an extra penalty on the control signal itself. The operator Q represents the energy inner-product in the (v, η) space

$$(v^* \quad \eta^*) Q \begin{pmatrix} v \\ \eta \end{pmatrix} = \frac{1}{8k^2} \int_0^\infty \left(k^2 |v|^2 + \left| \frac{\partial v}{\partial y} \right|^2 + |\eta|^2 \right) dy,$$
 (16)

with $k^2 = k_x^2 + k_z^2$.

We now want to find the optimal K that feeds back the state to update the control $u_c = Kq$. It can be found as the solution of an algebraic Riccati equation (ARE)

$$A^*X + XA - \frac{1}{l^2}XB_2B_2^*X + Q = 0 (17)$$

154

where X is the unique non-negative self-adjoint solution. Note that the linear feedback law does not depend on the disturbances present in the flow and is thus computed once and for all for a given objective function and base flow. The optimal control gain K is

$$K = -\frac{1}{l^2} B_2^* X. (18)$$

A sufficient range of wavenumber pairs are computed and after Fourier transformation in both horizontal directions, we obtain physical space control convolution kernels. Examples of such control kernels are depicted in figure 2.

3.2. Estimator

We build an estimator analogous to the dynamical system (5) as

$$\dot{\hat{q}} = A\hat{q} + B_2 u_c - L(y - \hat{y}), \quad \hat{q}(0) = \hat{q}_0,
\hat{y} = C\hat{a}.$$
(19)

where \hat{q} is the estimated state and \hat{y} represents the measurements in the estimated flow.

Kalman filter theory, combined with the models outlined in §2.2a and §2.2b for the statistics of the unknown external forcing f and the unknown sensor noise g respectively, provides a convenient and mathematically-rigorous tool for computing the feedback operator L in the estimator described above such that $\hat{q}(t)$ converges to an accurate approximation of q(t) (see e.g. Lewis & Syrmos 1995, p. 463–470). Note that the volume forcing $v_e = L(y - \hat{y})$ used to apply corrections to the estimator trajectory is proportional to the measurement difference in the flow and in the estimator $\tilde{y} = y - \hat{y}$.

The problem reduces to solving an algebraic Riccati equation similar to equation (17)

$$0 = AP + PA^* - PC^*G^{-1}CP + B_1RB_1^*, (20)$$

where P is the unique non-negative self-adjoint solution. The optimal gain L that minimizes the expected energy of the state estimation error at steady state is

$$L = -PC^*G^{-1}. (21)$$

Estimation convolution kernels are exemplified in figure 3.

3.3. Extension to spatially developing flows

When solving the linear control problem and computing optimal control and estimation gains we have linearized about a base flow profile at a specific streamwise position, hence assuming a parallel base flow. However, due to the non-parallel base flows in the DNS, errors will be introduced when the control signal and estimation forcing are computed. Based on findings in Högberg & Henningson (2002), Högberg $et\ al.\ (2003b)$, Högberg $et\ al.\ (2003c)$, and Chevalier

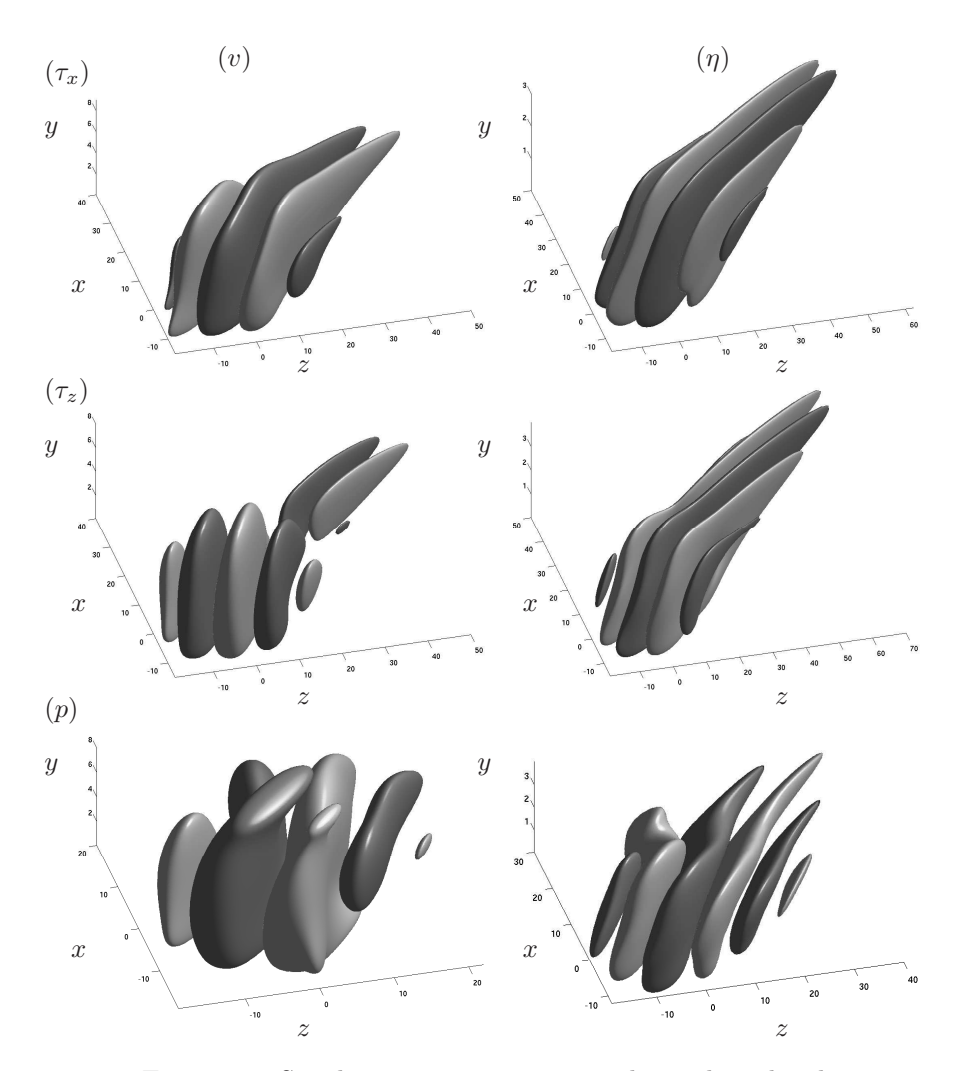


FIGURE 3. Steady-state estimation convolution kernels relating the measurements τ_x , τ_z , and p at the point $\{x=0,\ y=0,\ z=0\}$ on the wall to the estimator forcing on the interior of the domain for the evolution equation for the estimate of (left) \hat{v} and (right) $\hat{\eta}$. Positive (dark) and negative (light) isosurfaces with isovalues of $\pm 10\%$ of the maximum amplitude for all kernels illustrated. The kernels correspond to case 13 in tables 1 and 3.

et al. (2006) it was expected that the controller and the estimator had some robustness properties with respect to changes in the base flow profile. Due to the fact that the convolution kernels themselves, for proper choices of parameters, are localized indicates that only local information is needed which relaxes the requirement of constant base flow profile. For almost all control and estimation gains, the base flow profile in the centre of the control and measurement regions have been used. For the longer control interval in the optimal perturbation flow case, the same gains were used as for the shorter interval.

The control and estimation convolution kernels for the Falkner–Skan–Cooke boundary layer flow, corresponding to cases 12–13 in table 1, are depicted in figures 2 and 3. Both the control and estimation kernels were computed with a physical box size of $100 \times 10 \times 125.7$ with $192 \times 65 \times 125.7$ Fourier, Chebyshev, Fourier modes. Furthermore, the kernels were based on the mean-flow at x = 95 and x = 200 for the estimation and control respectively. For all cases studied the general behaviour of the control kernels are the same in the sense that they all reach upstream in order to get information about the perturbations present in the flow. Correspondingly the estimation kernels reach downstream from the point of sensoring yielding information on how each measurement should force the estimator. However, due to the differing base flows and their inherent instabilities the kernels will differ in shape and extent. The streamwise length of the sensing/actuation strip is limited above due to the non-parallel base flow, and below by the physical extent of the convolution kernels. The control and estimation region lengths used in this paper for the spatial flow cases were chosen in this range. Note that the performance of the controller/estimator degrades with "out of limit" parameters but will generally still produce reasonable results.

4. Numerical issues

4.1. Direct numerical simulations

All direct numerical simulations have been performed with the code reported in Lundbladh $et\ al.\ (1992)$ and Lundbladh $et\ al.\ (1999)$, which solves the incompressible Navier–Stokes equations

$$\frac{\partial \mathbf{u}}{\partial t} = NS(\mathbf{u}) + \lambda(x)(\mathbf{u} - \mathbf{u}_{\lambda}) + \mathbf{F},$$

$$\nabla \cdot \mathbf{u} = 0,$$
(22)

by a pseudo-spectral approach. The velocity vector \mathbf{u} is defined as $\mathbf{u} = (u, v, w)^T$. In the subsequent we will divide the velocity field into a base flow $\mathbf{U} = (U, V, W)$ and a disturbance part $\mathbf{u}' = (u', v', w')$ so that $\mathbf{u} = \mathbf{U} + \mathbf{u}'$. In order to allow spatially developing flows, a fringe region technique as described in e.g. Nordström *et al.* (1999) has been applied. This forcing is implemented in the term $\lambda(x)(\mathbf{u} - \mathbf{u}_{\lambda})$, where $\lambda(x)$ is a non-negative function which is nonzero only in the fringe region located in the downstream end of the computational

box. The outflow and inflow conditions are determined by the desired velocity distribution \mathbf{u}_{λ} . The other additional forcing term $\mathbf{F} = [F_1, F_2, F_3]^T$ is used e.g. to enforce a parallel base flow in temporal simulations, or to introduce perturbations in the spatial simulations.

At the lower wall a no-slip boundary condition is applied where it is also possible to apply zero mass-flux blowing and suction. An asymptotic free-stream boundary condition is used to limit the computational box in the wall-normal direction, at a constant height from the lower wall (see e.g. Malik *et al.* 1985).

The computational domain is discretized in space by Fourier series in both horizontal directions and with Chebyshev polynomials in the wall-normal direction. The time integration uses a four-step low-storage third-order Runge–Kutta method for the advective and forcing terms whereas the viscous terms are treated by a Crank-Nicolson method. The incompressibility condition is enforced implicitly by expressing the flow state in the wall-normal velocity and wall-normal vorticity state space.

4.2. Temporal simulations

When needed, we add a volume forcing vector $\mathbf{F} = [F_1, F_2, F_3]^T$ to enforce a parallel base flow, defined as

$$F_{1} = -\frac{\partial U(y,t)}{\partial t} - \frac{1}{Re} \frac{\partial^{2} U(y,t)}{\partial y^{2}},$$

$$F_{2} = 0,$$

$$F_{3} = -\frac{1}{Re} \frac{\partial^{2} W(y,t)}{\partial y^{2}}.$$
(23)

The velocity profiles U(y,t) and W(y,t) are given for a spatial position x_r . To further allow for a moving frame we make the following variable transformation $x_r = x_0 + ct$ where c is the reference frame speed and let $U(x_r, y) = U(x_0 + ct, y) = U(t, y)$.

4.3. Spatial simulations

4.3a. Fringe region. By adding the fringe forcing mentioned in §4.1 we can enforce flow periodicity and thus apply spectral methods allowing us to solve spatially developing flows. The fringe function is defined as

$$\lambda(x) = \lambda_{\text{max}} \left[S\left(\frac{x - x_{\text{start}}}{\Delta_{\text{rise}}}\right) - S\left(\frac{x - x_{\text{end}}}{\Delta_{\text{fall}}}\right) \right]$$
 (24)

where the ramping function S is defined as

$$S(x) = \begin{cases} 0, & x \le 0, \\ 1/\left[1 + \exp\left(\frac{1}{x-1} + \frac{1}{x}\right)\right], & 0 < x < 1, \\ 1, & x \ge 0. \end{cases}$$
 (25)

Case	Flow	Perturbat	ion	ion Estimation			Control	
					$x_m \in$	r^2	l	$x_c \in$
0	A	Eigenmoo	le					
1	A	Eigenmoo	le			0	10^{2}	[0, 25.14]
2	A	Eigenmoo	le	[(0, 25.14	0	10^{2}	[0, 25.14]
3	В	TS-wave						
4	В	TS-wave				0	10^{2}	[100, 250]
5	В	TS-wave			[0, 100]	0	10^{2}	[100, 250]
6	$^{\mathrm{C}}$	Optimal						
7	$^{\mathrm{C}}$	Optimal				0	10^{2}	[300, 450]
8	\mathbf{C}	Optimal			[0, 300]	0	10^{2}	[300, 450]
9	$^{\mathrm{C}}$	Optimal				0	10^{2}	[300, 750]
10	$^{\mathrm{C}}$	Optimal			[0, 300]	0	10^{2}	[300, 750]
11	D	Random						
12	D	Random				0	10^{2}	[175, 325]
13	D	Random		[,	40, 150	0	10^{2}	[175, 325]
14	\mathbf{E}	Stationar	V		, ,			. , ,
15	\mathbf{E}	Stationar	~			0	10^{2}	[150, 300]
16	E	Stationar		[40, 150	0	10^{2}	[150, 300]
	Flow		Re	esolı	ution		Box	
A	Temp	oral FSC	4 >	< 12	9×4	25.14	× 20 :	× 25.14
В	_	al Blasius	576	\times (65×4	1128	× 20 >	< 12.83
С	Spatia	al Blasius	576	\times (65×4	1128	× 20 >	< 12.83
D	Spatia	al FSC	192	$\times 4$	9×48	500	× 8 ×	251.4
_E	_	al FSC	768	\times 6	5×24	500	× 8 ×	25.14
	Flow				I	Fringe		
			$x_{\rm st}$	art	x_{mix}	Δ_{mix}	$\Delta_{\rm rise}$	Δ_{fall}
В	_	al Blasius	92		928	50	30	15
$^{\rm C}$		al Blasius	10:		1028	40	100	20
D	Spati	ial FSC	35	0	400	40	100	20
$_{\rm E}$	Spati	ial FSC	35	0	400	40	100	20

Table 1. The tables contain detailed information about the simulations performed in this study. Both the control and estimation kernels are computed based on a velocity profile from the centre of each domain except for cases 9–10 where the same control kernels were used as for cases 7–8. The rise and fall distance of the control region and the measurement regions are always $\Delta x=5$. The domain x_m denotes the measurement region used in the estimator and the domain x_c denotes the region where blowing and suction is applied in the control part of the simulations. The estimator model parameters for the different cases are given in table 3.

Parameter	Cases		Parameter	Cases	
	3–5	6–10		11–13	14-16
x_f	-201.06	-158.16	x_0	20.95	20.95
ω	0.06875	0	a_t	0.001	
k_z	0	0.4897	a_s		0.0036
a_s	10^{-5}		x_{scale}	10	10
t_s	0		$y_{ m scale}$	1	1
t_r	20		$z_{ m scale}$		-25.14
			$z_{ m center}$	0	0
			$l_{ m skew}$		1
			n_{modes}	21	
			t_{dt}	1	

Table 2. Volume forcing parameters for the spatial simulations. Note that negative coordinates indicate positions upstream of the inflow boundary.

The parameters $x_{\rm start}$ and $x_{\rm end}$ define the start and end location of the fringe domain, whereas the parameters $\Delta_{\rm rise}$ and $\Delta_{\rm fall}$ define the rise and fall distance of the fringe function.

In order to enforce the inflow boundary condition at the downstream end of the domain we construct the following blending function which gives a smooth interpolation between two velocity profiles. Let the velocity components be defined as

$$u_{\lambda} = U(x,y) + [U(x - l_{x}, y) - U(x,y)] S\left(\frac{x - x_{\text{mix}}}{\Delta_{\text{mix}}}\right) + u'_{f}(x - l_{x}, y, z, t),$$

$$w_{\lambda} = W(x,y) + [W(x - l_{x}, y) - W(x,y)] S\left(\frac{x - x_{\text{mix}}}{\Delta_{\text{mix}}}\right) + w'_{f}(x - l_{x}, y, z, t),$$
(26)

where l_x is the box length in the streamwise direction. The parameters $x_{\rm mix}$ and $\Delta_{\rm mix}$ are both blending parameters. The former is the start of the blending region and the latter is the rise distance of the blending. Additional forcing to add streaks or different wave forms can be added through the velocity components (u'_f, v'_f, w'_f) directly in the fringe.

4.3b. Perturbations. To introduce perturbations into the spatially evolving flow an external volume force can be applied locally in the computational domain. This forcing can either be applied in the fringe region, as for the optimal disturbance and the TS-wave case, or in the physical flow domain.

In order to introduce unsteady perturbations in the physical computational domain, we use a random forcing, acting only on the wall-normal component of the momentum equations

$$F_2^{\text{rand}} = a_t \exp[-((x - x_{\text{center}})/x_{\text{scale}})^2 - (y/y_{\text{scale}})^2]f(z, t),$$
 (27)

where

$$f(z,t) = [(1 - b(t))h^{k}(z) + b(t)h^{k+1}(z)]$$
(28)

and

$$k = \text{floor}(t/t_{dt}),$$

$$b(t) = 3p^2 - 2p^3,$$

$$p = t/t_{dt} - k,$$
(29)

where floor denote rounding to the next smaller integer, and $h^k(z)$ is a Fourier series of unit amplitude functions with random phase generated at every time interval k. Within each time interval $t_{\rm dt}$, the function b(t) ramps the forcing smoothly in time. The maximum amplitude is determined by a_t and the forcing is exponentially decaying in both the streamwise and wall-normal directions centred at $x_{\rm center}$. The number of modes with non-zero amplitude is determined by the parameter $n_{\rm modes}$. This forcing has been used to generate the travelling cross-flow vortices described as cases 11–13 in table 1 with the corresponding parameters given in table 2.

Generating disturbances in the fringe region is done through prescribing the components (u_f', v_f', w_f') in equation (26). Since we are looking at the evolution of linear disturbances, these components can be taken as the eigenfunctions of the parabolized stability equations, known as the PSE (Bertolotti *et al.* 1992; Herbert 1997). Input to the eigenvalue problem is a given real frequency ω , an appropriate Reynolds number Re and a real spanwise wavenumber k_z^f . A set of equations valid for both algebraically and exponentially growing disturbances was derived in Levin (2003), capturing the different scales associated with the two growth scenarios. Having obtained the complex eigenvalues $k_x^f(x)$ and the eigenfunctions $\hat{q} = (\hat{u}(x,y), \hat{v}(x,y), \hat{w}(x,y))^T$ from the solution of the PSE, one can readily formulate the forcing applied in the fringe as the real part of

$$q_f' = a_s \,\hat{q}(x, y) \exp\left(iRe \int_{x_f}^x k_x^f(\xi) d\xi + ik_z^f z - i\omega t\right) S\left(\frac{t - t_s}{t_r}\right)$$
(30)

where x_f is typically the start of the fringe region and a_s is the amplitude of the disturbance. The ramping function S is given by equation (25) and t_s and t_r are used as time ramping parameters.

4.3c. Zero mass-flux actuation. The numerical model in the DNS does not allow for net inflow or outflow, we thus have to enforce a zero-mass flux through the actuation strip by the transformation

$$\hat{\varphi}(x,z) = (\varphi(x,z) + c)H(x), \tag{31}$$

where

$$c = -\frac{\int_{z} \int_{x} \varphi(x, z) H(x) \, dx \, dz}{z_{l} \int_{x} H(x) \, dx}$$
(32)

and

$$H(x) = S\left(\frac{x - (x_c - l_x^c)}{\Delta x}\right) - S\left(\frac{x - (x_c - l_x^c)}{\Delta x}\right).$$
 (33)

The parameter S(x) is defined as in equation (25) and x_c denotes the centre of the control interval. Parameters l_x^c and l_z^c are respectively the length and width of the control domain and Δx is the rise and fall distance of the actuation.

4.4. Compensator algorithm

The compensator algorithm is depicted in figure 4. The "real" flow could be an experimental setup where only wall information is extracted. In our studies the "real" flow is represented by a DNS. The estimator is another DNS, which is used to recover the state from sensor information. The compensation algorithm can be sketched in the following steps

- 1. Take wall measurements in both real and estimated flows
- 2. Compute the estimator volume forcing based on precomputed estimation gains and the difference of the wall measurements from the real and estimated flows
- 3. Apply the volume forcing to the estimator flow to make it converge to the real flow
- 4. Compute the control signal as a feedback of the reconstructed state in the estimator
- 5. Apply the control signal in both the real and estimated flows

5. Flow cases

In order to evaluate the compensator performance in transitional flows we test a range of different flow cases. To ease the comparison with the full information controller results reported in Högberg & Henningson (2002) we study partly the same flow cases and the same control parameter $l^2=100$ has been used. However, some control regions have been moved further downstream to fit also a measurement region into the computational domain. Note that in principle we could have overlapping control and measurement regions. The computational parameters for each flow type are listed in table 1, 2 and 3.

5.1. Single eigenmode

To validate the numerical implementation of the control and the estimator forcing we studied a temporal FSC boundary layer flow where the Reynolds number

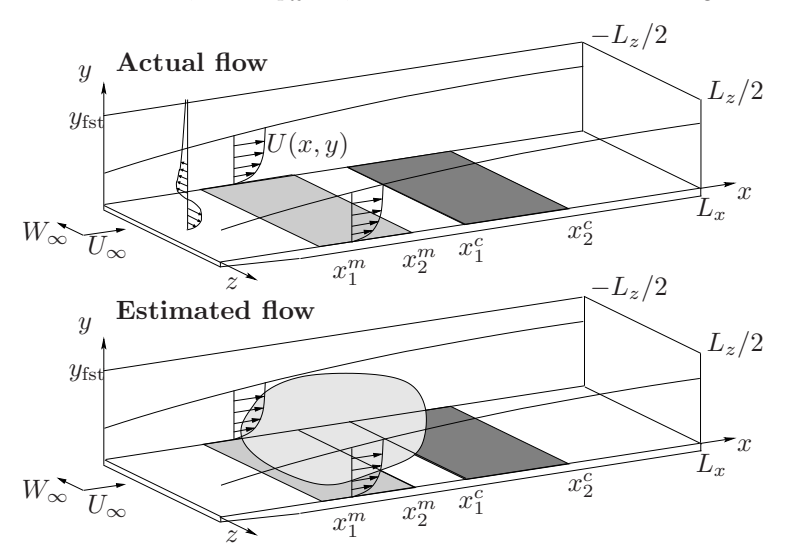


FIGURE 4. Compensator configuration. The upper box represents the "real" flow where the light grey rectangle along the wall is the measurement region $(x \in [x_1^m, x_2^m])$ and the corresponding dark grey rectangle is the control area $(x \in [x_1^c, x_2^c])$. In the beginning of the box a perturbation is indicated as a function of the wall-normal direction. This perturbation will evolve as we integrate the system in time. The estimated flow system is depicted in the lower box. Here the volume force that is based on the wall measurements and the estimation gains is shown as a grey cloud in the computational domain.

at the beginning of the simulation box was Re=337.9 with a free-stream cross-flow velocity component $W_{\infty}=1.44232\,U_{\infty}(x=0)$ and a favourable pressure gradient m=0.34207 as defined in §2.1. The same flow setup is also studied in a spatial setting in §5.4. In the case of temporal flow the measurement and control regions overlap since they both extend over the complete wall.

The initial disturbance is the unstable eigenfunction associated with the eigenvalue c=-0.15246+i0.0382 that appears at $k_x=0.25$ and $k_z=-0.25$. The exponential energy growth of the uncontrolled eigenmode is depicted in figure 5 as a thick solid line. In the same figure the full information controller is plotted as a thick dashed line and the disturbance energy decays rapidly in time and levels out. All thin lines are related to the compensator simulation. The thin solid line represents the disturbance energy in the estimator and it increases initially to quickly align with the energy growth of the actual state. This can also be viewed through the estimation error plotted as a thin dash-dotted line which decays exponentially in time. The compensator control is

Parameter			Cases		
	3	5	8 & 10	13	16
k_x^0	0.25	0.28	0.0	0.25	0.25
k_z^0	-0.25	0.0	0.49	-0.25	-0.25
d_x	0.10	0.25	0.15	0.20	0.20
d_y	0.50	0.10	0.50	0.50	0.50
d_z	0.10	0.25	0.15	0.20	0.20
$\alpha_{ au_x}$	29.56	4.0	0.20	0.20	0.20
$\alpha_{ au_z}$	2.21	0.30	0.20	0.20	0.20
α_p	14783	2000	300	30000	30000

Table 3. Estimator model parameters. The parameters k_x^0 , k_z^0 , d_x , d_y , and d_z all relate to the covariance model of the external disturbances and the parameters α_{τ_x} , α_{τ_z} , and α_p relate to the modeling of the sensor noise. See §2.2 for definitions of the parameters.

shown as the thin dashed line. Initially when the estimated state is poor the controller is not very efficient. However as the estimated state improves the compensator control is also improving.

5.2. TS-wave

The TS-wave perturbation is applied in a spatially developing Blasius boundary layer with an inflow Reynolds number of Re=1150. This base flow can be obtained as a similarity solution described in §2.1 with m=0. The perturbations are introduced by means of forcing in the fringe region as described in §4.3b. Since the TS-wave is a pure two-dimensional instability, the spanwise wavenumber in (30) is $k_z^f=0$. These waves are forced at the dimensionless oscillating frequency F=59, relating to the physical frequency ω as $F=10^62\pi\omega\nu/U_\infty^2$. This value is chosen according to Levin (2003) where it was found to be the most unstable. The unstable area for this wave extends from Branch I at x=-124 ($Re\approx949$) to branch II at x=621 ($Re\approx1854$). The measurement region is $x\in[0,100]$ and the control region is $x\in[100,250]$ so that they are both located in the exponential growth region. The simulation parameters correspond to cases 3–5 in table 1 and the parameters defining the fringe forcing are given in table 2.

Figure 6 shows the uncontrolled energy growth and decay as the solid thick line. Full information control, displayed as the thick dash-dotted line, performs perfectly, lowering the amplitude of the energy by approximately five decades. The estimator builds up energy levels throughout the whole estimation region, reaching almost the amplitude of the original flow. This is visualized as the thin solid line.

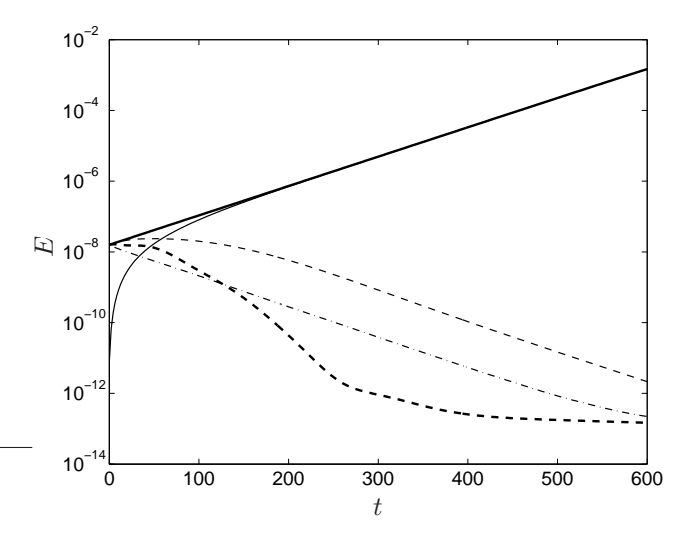


FIGURE 5. Time evolution of the perturbation energy of the uncontrolled unstable eigenmode at $k_x=0.25, k_z=-0.25$ in a FSC boundary layer and the corresponding controlled system. Solid: uncontrolled energy growth (case 0). Dashed: full information control applied (case 1). Solid-thin: energy growth in the estimator when no control is applied. Dash-dotted-thin: the estimation error when no control is applied. Dashed-thin: compensator control is applied (case 2). The simulations correspond to cases 0–2 in table 1.

Note that the difference between the compensator control and full information control in Figure 6 is exaggerated due to the logarithmic scale. In fact this difference is of the same order of magnitude as the energy difference between the real and estimated flow. Indeed by extending the estimation region (and moving the control region further downstream) one can get a closer agreement between the compensator and the full information controller. Note however that there is an interest in controlling the TS-wave evolution as far upstream as possible. Choosing the moderate estimation region length of 100, the compensator still manages to lower the energy levels by almost three decades.

Figure 7(a) shows a snapshot of an x-y plane of the wall-normal uncontrolled velocity field. The forcing has been turned on long enough to let the waves propagate throughout the whole computational box. In figure 7(b) the compensator control has been active for 926 time units, corresponding to approximately fifteen periods of the forcing. At this instance of time there are still large amplitude disturbances present far downstream, but as can be seen from figure 7(c), 30 periods later the contour-levels of the disturbances are small throughout the whole domain. It is evident that the unsteady blowing

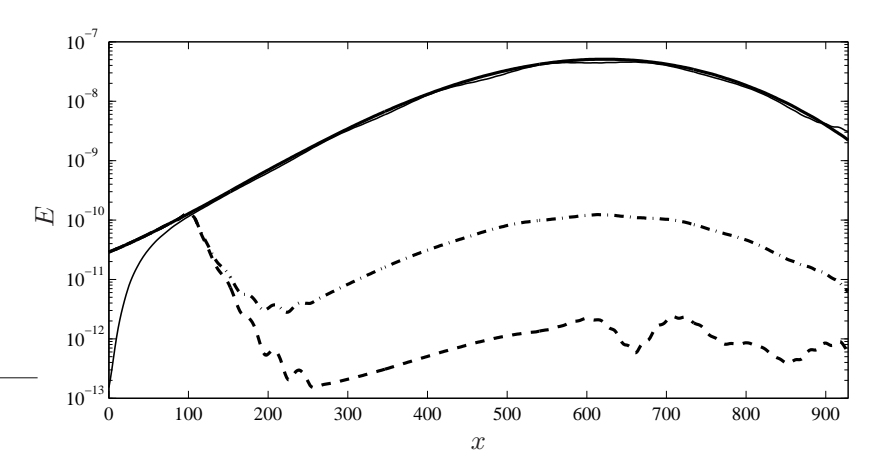


FIGURE 6. Spatial evolution of the perturbation energy of a TS-wave in a spatially growing boundary layer. Solid: uncontrolled energy growth. Solid-thin: estimated flow energy. Dashed: full information control applied. Dash-dotted: compensator control applied.

and suction has effectively diminished the disturbances, leaving the remaining TS-wave to be advected out of the domain by the base flow.

Instantaneous control signals for the full information control and the compensator control are shown in figure 8. The control signals mimic waves with decaying amplitude in the streamwise direction. The large amplitude at the beginning of the control interval is due to the fact that the controller manages to do the job within only a few wavelengths of the TS-wave, hence leaving large amplitude control further downstream unnecessary.

5.3. Optimal perturbation

The compensator performance is also studied for transiently growing perturbations, also known as optimal perturbations after Butler & Farrell (1992). The spatial optimal perturbations in a Blasius boundary layer have been computed by Andersson et al. (1999) and Luchini (2000). The optimal perturbation is introduced at x = -158.16 and then marched forward to x = 0 with the technique developed in Andersson et al. (1999). The perturbation is introduced in the fringe region to give the proper inflow condition, as described in §4.3 and with the choice of parameters displayed in table 2. The perturbation is optimized to peak at x = 237.24.

The base flow is essentially the same as the one described in §5.2, with the same box-size but with a smaller fringe region and a lower Reynolds number. Here the local Reynolds number at the inflow is Re = 468.34 (Andersson *et al.* (2000)). The simulation parameters are given in table 1 as cases 6–10.



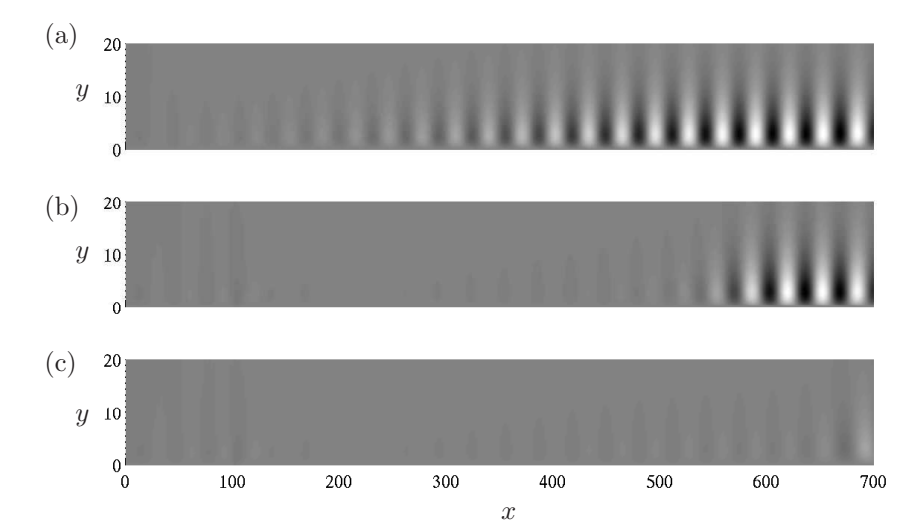


FIGURE 7. Snapshots of the wall-normal perturbation velocity for controlled and uncontrolled TS-waves. (a) The TS-wave with no control. (b) Compensator control applied during 15 TS-wave periods which corresponds to 926 time units. (c) Compensator control applied during 45 TS-wave periods. The unsteady wall blowing and suction effectively eliminates disturbances, with the result that the original TS-wave disturbances are advected out of the domain. The black to white scales lie within the interval $v \in [-9.87 \cdot 10^{-5}, 8.18 \cdot 10^{-5}]$

Figure 9 shows the energy of the uncontrolled flow, estimated flow, full information control and compensator control once steady state has been reached. The compensator control manages to reduce the disturbance energy to almost the same level as the full information control does. Here the energy is defined as

$$E = \int_0^{2\pi/k_z^0} \int_0^\infty (u^2 + v^2 + w^2) \, \mathrm{d}y \, \mathrm{d}z, \tag{34}$$

where the spanwise wave number is $k_z^0 = 0.4897$. Two different lengths of the control regions have been implemented. Both types of controllers for both control intervals work well at reducing the perturbation energy. In the case with a narrow control strip the perturbation energy starts to grow again since a stronger component of the growing disturbance remains.

The control signal for the full information and compensator control cases, applied in the interval $x \in [300, 750]$, are depicted in figure 10. The actuation presents a peak at the beginning of the control region and then a fast decay

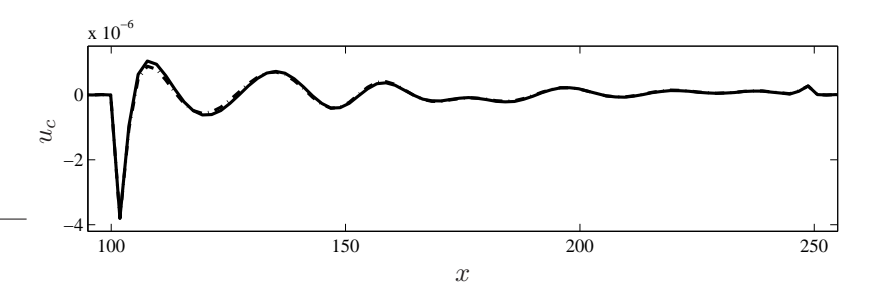


FIGURE 8. Control signal when the control has been turned on for 926 time units. Solid: Full information control. Dashdotted: Compensator control.

which levels out progressively. A similar feature is reported in Cathalifaud & Luchini (2000) where control is applied over the whole domain.

5.4. Travelling cross-flow vortices

The FSC boundary layer flow studied in this paper is subject to several other studies, for example Högberg & Henningson (1998) and Högberg & Henningson (2002). Originally it was an attempt to reproduce experimental results where travelling cross-flow modes have been observed (see e.g. Müller & Bippes 1988). A random perturbation in space and time that generates cross-flow vortices downstream is applied, as described in §4.3b. The specific numerical details can be found under cases 11–13 in tables 1 and 2.

In case 11 we compute the time evolution of the forcing as it develops downstream and forms the cross-flow vortices. When the simulations have reached a statistically steady state the disturbance energy is sampled and averaged in time and the spanwise direction as shown in figure 13. The energy growth of the perturbation is shown as a black solid line. In case 12 we apply full information control. Exponential decay then replaces the uncontrolled exponential growth, as shown by the dashed line in figure 11. However almost adjacent to the downstream end of the control region the disturbances start to grow exponentially. Indeed, this wave is unstable over the whole box, and resumes growth behind the control strip. In the same figure the perturbation energy for the compensator is plotted as a dash-dotted line.

In figure 12 the evolution in time of the perturbation energy, integrated throughout the computational box in space, is shown. The energy in the estimator is shown as a thin-solid line which is zero at time t=0 but as time evolves reaches the same level as the perturbation energy in the real flow. From figure 12 it is also evident that the estimator is able to adapt to the time variations of the perturbation energy.

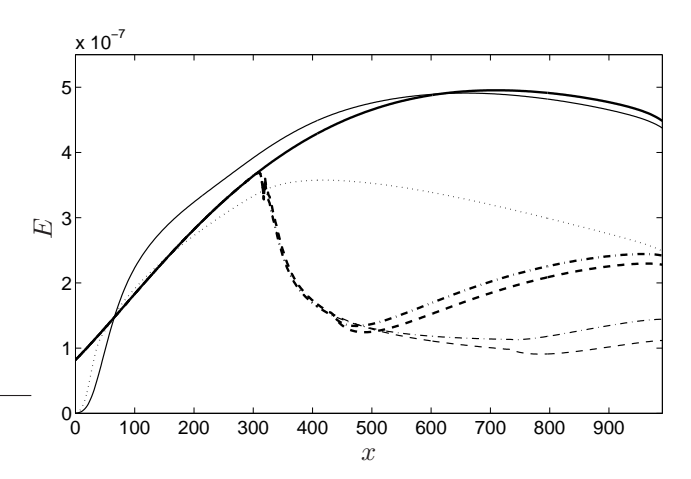


FIGURE 9. Spatial energy evolution of the optimal perturbation. Solid: no control. Thin-solid: estimated flow energy employing stochastic forcing according to parameters given in table 3 but with $d_y=2.0$. Thin-dotted: estimated flow energy with spatially uncorrelated stochastic forcing. Dashed: full information control applied in region $x \in [300, 450]$. Dash-dotted: compensator control with measurement region $x_m \in [0,300]$ and the control region $x_c \in [300,450]$. Thin-dashed: full information control applied in region $x \in [300,725]$. Thin dash-dotted: compensator control with the measurement region $x_m \in [0,300]$ and the control region $x_c \in [300,725]$. The flow cases correspond to cases 6–10 in table 1.

The control gains are computed for the base flow at position x = 250 which is the centre of the control domain $x \in [175, 325]$. The estimator gains are centred at x = 95 and the measurements are taken in $x \in [40, 150]$. In figure 13(a) the uncontrolled flow for the wall-normal perturbation velocity is plotted at y = 1.0. The corresponding plot for the compensated flow is depicted in figure 13(b).

5.5. Stationary cross-flow vortices

Stationary perturbations introduced at the beginning of the computational domain, with large enough amplitudes, will generate stationary nonlinearly saturated cross-flow vortices that develop downstream.

The control is acting in the interval $x \in [150, 300]$ and the control kernels are computed based on the mean flow at x = 225 with $l = 10^2$. The measurement region is in the interval $x \in [40, 150]$ and the estimation kernels are

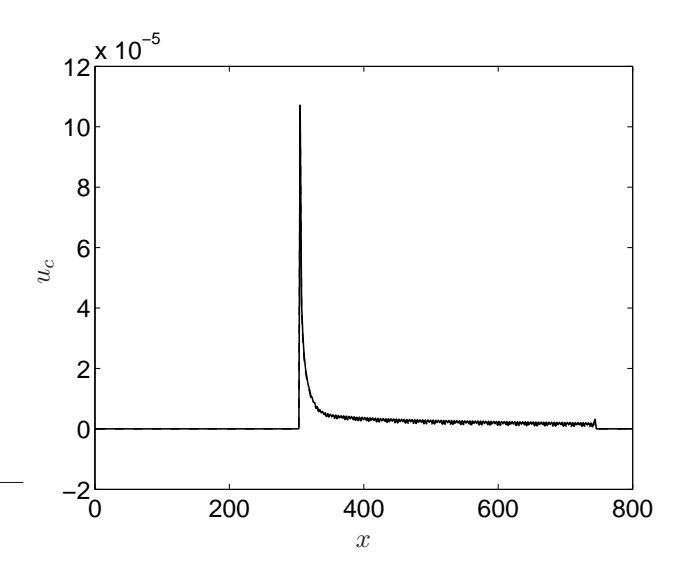


FIGURE 10. The control signal for the optimal disturbance case after the initial transient. Solid: full information control. Dashed: compensator control in domain. The simulations correspond to case 9 and 10 in table 1.

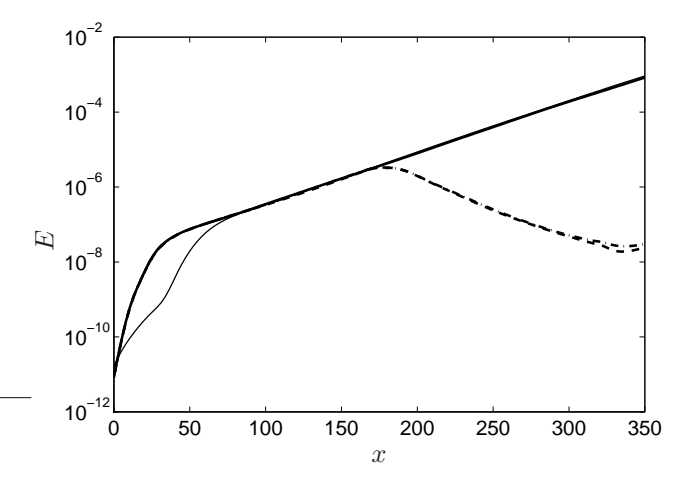


FIGURE 11. Time averaged perturbation energy for cross-flow vortices in a Falkner–Skan–Cooke boundary layer. Solid: uncontrolled. Dashed: full information control. Dash-dotted: compensator control. Thin-solid: estimator energy. The simulations correspond to cases 11–13 in table 1.

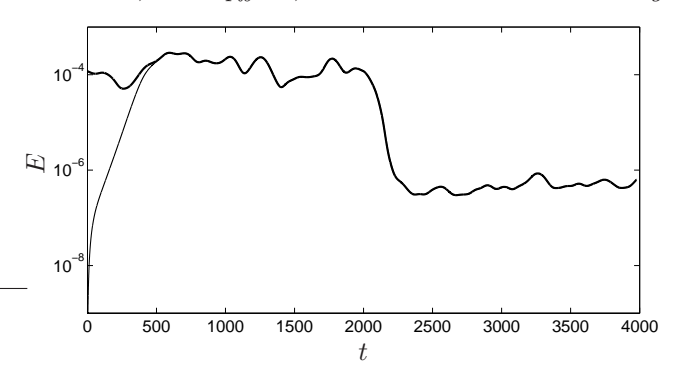


FIGURE 12. Time evolution of the disturbance energy integrated throughout the computational box. During the first 2000 time units the flow is uncontrolled. At time t=2000 the compensator is turned on. Solid: energy in the flow. Thinsolid: energy in the estimator.

computed based on the base flow centred in that interval. The complete set of parameters for these simulations is given as cases 14–16 in table 1.

The full information control has been applied to both a flow with fully developed cross-flow vortices throughout the computational domain as well as a flow where the control is turned on at the same time as the perturbation is first introduced in the upstream region. Both approaches give the same result after the initial transients, due to the control. However the transition phase in the former case requires smaller time steps due to stronger transients. There could also be a problem in the former case if too strong wall-normal velocities are generated due to technical limitations in the spectral code that are being used.

For estimation-based control, two approaches regarding the initial state of the estimator have been attempted. First the control is applied after a well converged estimated state is obtained. This leads to full actuation strength immediately. To avoid a strong initial actuation, we turn on estimator and control at the same time. The results shown here have been produced with the latter method.

The simulation is run until a stationary state has been reached and the corresponding energy is shown in figure 14. The solid line shows the perturbation energy and the thin line shows the corresponding estimator state energy. The dashed and dash-dotted lines show the full information and compensated control cases respectively. In both cases, oscillations in the upstream part of the control region indicate that there are nonlinear interactions taking place. As reported in Högberg & Henningson (2002), the full information control turns

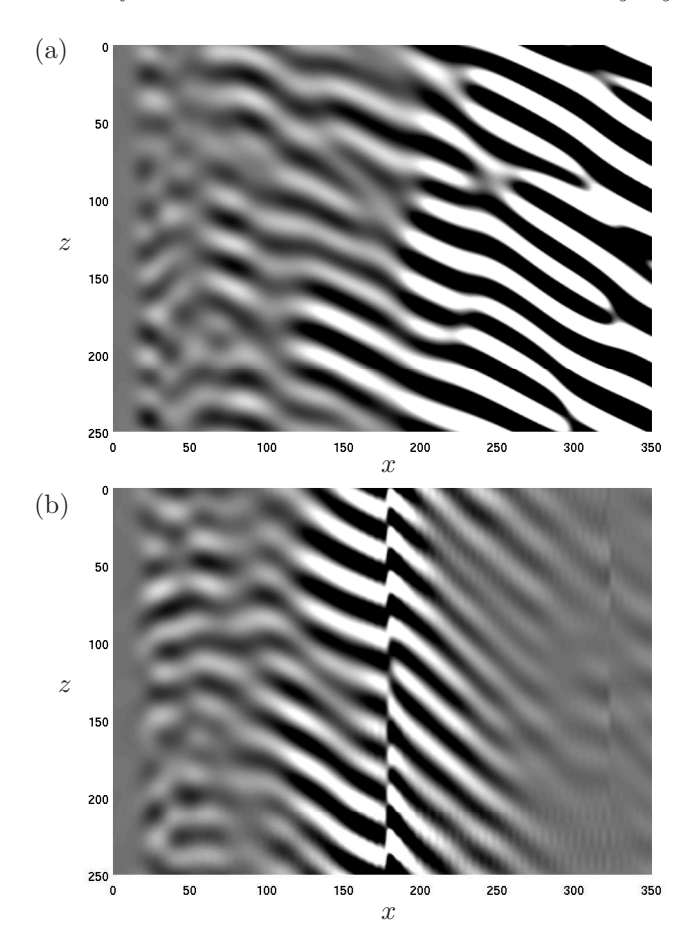


FIGURE 13. Snapshots of the wall-normal velocity component at y=1.0. The flow state is depicted in part (a). In (b) the effect of the compensator control is shown. In the controlled flow the actuation was applied in 2000 time units. The black to white scales lie within the interval $v \in [-0.00045, 0.00055]$.

exponential growth into exponential decay, and downstream of the control region, new cross-flow vortices appear due to the inflectional instability. The compensator control never reaches exponential decay but rather maintains a more or less constant perturbation energy throughout the control interval.

5.6. Impact of stochastic modelling on estimation

We have seen that the performance of the estimator can be improved if the external excitation sources are well described by the stochastic model of §2.2.

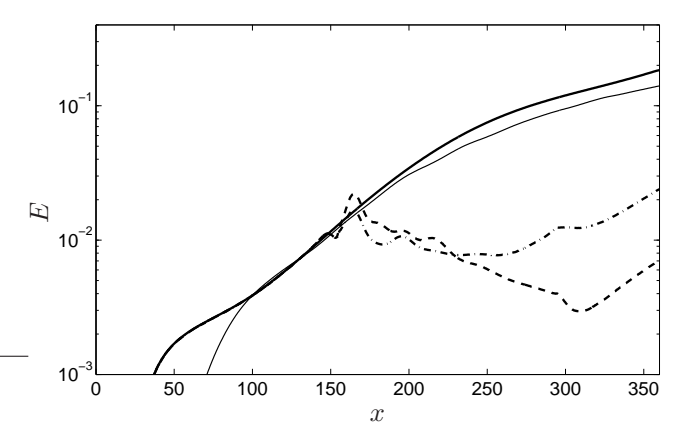


FIGURE 14. Perturbation energy growth for cross-flow vortices in a Falkner–Skan–Cooke boundary layer. Solid: uncontrolled. Dashed: full information control. Dash-dotted: compensator control. Thin-solid: estimator energy. The simulations correspond to cases 14–16 in table 1.

The parameters given in table 3 are chosen to fairly well fit each specific perturbation for the different flow cases we have considered. In this section we perform a quantitative comparison of the estimator performance applied to the streaky flow case of §5.3 for three sets of model parameters; the uncorrelated model, and the correlated model with two different correlation lengths in the wall-normal direction.

A first comparison of the estimation performance for different models was shown in figure 9. Using the correlated model with $d_y=2.0$, the upstream part of the streak energy was over predicted while the downstream part was slightly under predicted, however yielding the lowest overall energy of the estimation error when compared to other choices of wall-normal correlation length parameter d_y . On the other hand the estimator built from the uncorrelated stochastic model has correct energy levels in the first half of the measurement region, but is simply not able of converging to good estimate of the flow downstream, where the flow response has largest energy. Note that $d_y=0.5$ gives the best compensator performance due to its slightly better energy level match in the upstream region of the flow.

When changing the stochastic properties of the external forcing the strength of the resulting gains changes. In order to keep the strength of the gains on the same level, keeping in mind that they act directly as forcing terms in the

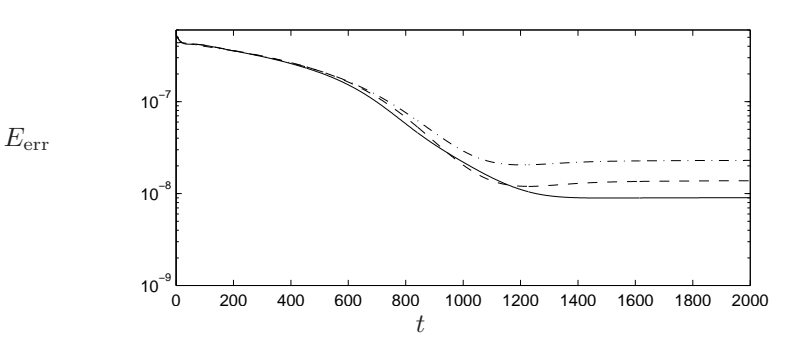


FIGURE 15. Comparison of the energy of the estimation error $E_{\rm err}$ for the streaky flow case for three different stochastic models. Solid: Correlated model with $d_y=2.0$. Dashed: Correlated model with $d_y=0.5$. Dash-dotted: uncorrelated.

$\overline{d_y}$	d_x	d_z	k_x^0	k_z^0	α_{τ_x}	α_{τ_z}	α_p	$J_{ au_x}$	$J_{ au_z}$	$\overline{J_p}$
0.10	0.15	0.15	0.0	0.49	0.20	0.20	300	18.3619	21.5604	0.0562

Table 4. Reference values, according to integral (35), of the estimation gains for the streak instability. All gains in the comparison study are scaled to match these values for J_{τ_x} , J_{τ_z} and J_p respectively.

estimator, we scale them to maintain a reference value of the integrated quantities

$$J_{\chi} = \int_{0}^{L_{z}} \int_{0}^{L_{x}} \int_{0}^{y_{\infty}} L_{\chi}^{2} \, \mathrm{d}y \, \mathrm{d}x \, \mathrm{d}z, \tag{35}$$

where χ represents the different measurements τ_x , τ_z and p. The integrated quantities of (35) for the reference stochastic model is given in table 4.

In figure 15 the time history of the difference in energy of the estimation error between the three stochastic models is shown. The solid and the dashed line show the estimator results based on correlated stochastic forcing with the parameters $d_y=2.0$ and $d_y=0.5$ respectively, see equation (12). The dash-dotted line represents the uncorrelated stochastic forcing. All three estimators converge to reasonable energy levels, however the best performance is obtained with the parameter $d_y=2.0$. For larger values of d_y the estimation error starts to increase again. Similar behaviour is observed for the other flow perturbation scenarios.

6. Conclusions

Based on findings on how to improve the performance state estimation performance, reported in Hœpffner et al. (2005), combined with the state-feedback control used in, for instance, Bewley & Liu (1998) and Högberg & Henningson (2002), viscous instabilities, non-modal transient energy growth and inflectional instabilities in spatially developing boundary layer flows are controlled based on wall measurement.

The key to the improved performance of the estimator is the design of a relevant stochastic model for the external sources of disturbances. For this purpose we choose a correlation length. We also choose an amplitude distribution in wavenumber space such that it represents the most dominant wavenumbers in the specific flow being studied. This procedure leads to resolution independent well resolved estimation gains for the three measurements: streamwise and spanwise skin frictions and wall pressure. Both the sensor noise and the external disturbances are assumed to be white noise processes. As the estimator is switched on, there is an initial transient that propagates with the group velocity of the dominating disturbances through the computational domain. Upstream of this transient the estimate is converged. This feature makes the compensator control efficient since little extra time is needed to have a good state estimate where it is needed for control, i.e. above the actuation region.

Acknowledgement

This work has been partially financed by the Innovation fund at the Swedish Defence Research Agency (FOI) and from the EOARD grant FA8655-04-1-3032 which is greatfully acknowledged.

References

- Andersson, P., Berggren, M. & Henningson, D. S. 1999 Optimal disturbances and bypass transition in boundary layers. *Phys. Fluids* 11, 134–150.
- Andersson, P., Brandt, L., Bottaro, A. & Henningson, D. S. 2000 On the breakdown of boundary layer streaks. *J. Fluid Mech.* 428, 29–60.
- Bertolotti, F. P., Herbert, T. & Spalart, P. R. 1992 Linear and nonlinear stability of the Blasius boundary layer. *J. Fluid Mech.* 242, 441–474.
- Bewley, T. R. 2001 Flow control: new challenges for a new Renaissance. *Progress in Aerospace Sciences* 37, 21–58.
- Bewley, T. R. & Liu, S. 1998 Optimal and robust control and estimation of linear paths to transition. *J. Fluid Mech.* **365**, 305–349.
- Butler, K. M. & Farrell, B. F. 1992 Three-dimensional optimal perturbations in viscous shear flow. *Phys. Fluids A* 4, 1637–1650.
- CATHALIFAUD, P. & LUCHINI, P. 2000 Algebraic Growth in Boundary Layers: Optimal Control by Blowing and Suction at the Wall. Eur. J. Mech. B Fluids 19, 469–490
- Chevalier, M., Hæpffner, J., Bewley, T. R. & Henningson, D. S. 2006 State estimation of wall bounded flow systems. Part 2. Turbulent flows. *J. Fluid Mech.* **552**, 167–187.
- COOKE, J. C. 1950 The boundary layer of a class of infinite yawed cylinders. *Proc. Camb. Phil. Soc.* 46, 645–648.
- HERBERT, T. 1997 Parabolized stability equations. Annu. Rev. Fluid Mech. 29, 245–283.
- Hœpffner, J., Chevalier, M., Bewley, T. R. & Henningson, D. S. 2005 State estimation in wall-bounded flow systems, Part 1. Laminar flows. *J. Fluid Mech.* 534, 263–294.
- HÖGBERG, M., BEWLEY, T. R. & HENNINGSON, D. S. 2003a Linear feedback control and estimation of transition in plane channel flow. J. Fluid Mech. 481, 149–175.
- HÖGBERG, M., BEWLEY, T. R. & HENNINGSON, D. S. 2003b Relaminarization of Re $_{\tau}$ =100 turbulence using gain scheduling and linear state-feedback control. *Phys. Fluids* **15**, 3572–3575.
- HÖGBERG, M., CHEVALIER, M. & HENNINGSON, D. S. 2003c Linear compensator

- control of a pointsource induced perturbation in a Falkner–Skan–Cooke boundary layer. *Phys. Fluids* **15** (8), 2449–2452.
- HÖGBERG, M. & HENNINGSON, D. S. 1998 Secondary instability of cross-flow vortices in Falkner–Skan–Cooke boundary layers. J. Fluid Mech. 368, 339–357.
- HÖGBERG, M. & HENNINGSON, D. S. 2002 Linear optimal control applied to instabilities in spatially developing boundary layers. *J. Fluid Mech.* 470, 151–179.
- Kim, J. 2003 Control of turbulent boundary layers. Phys. Fluids 15 (5), 1093–1105.
- Levin, O. 2003 Stability analysis and transition prediction of wall-bounded flows. Licentiate thesis, Royal Institute of Technology, Stockholm.
- Lewis, F. L. & Syrmos, V. L. 1995 Optimal control. Wiley-Interscience.
- Luchini, P. 2000 Reynolds-number-independent instability of the boundary layer over a flat surface: optimal perturbations. *J. Fluid Mech.* **404**, 289–309.
- Lundbladh, A., Berlin, S., Skote, M., Hildings, C., Choi, J., Kim, J. & Henningson, D. S. 1999 An Efficient Spectral Method for Simulations of Incompressible Flow over a Flat Plate. Technical Report TRITA-MEK 1999:11. Department of Mechanics, Royal Institute of Technology, KTH.
- Lundbladh, A., Henningson, D. S. & Johansson, A. 1992 An Efficient Spectral Integration Method for the Solution of the Navier–Stokes Equations. Technical Report FFA TN 1992-28. FFA, the Aeronautical Research Institute of Sweden, FFA
- Malik, M. R., Zang, T. A. & Hussaini, M. Y. 1985 A spectral collocation method for the Navier–Stokes equations. *J. Comp. Phys.* **61**, 64–88.
- MÜLLER, B. & BIPPES, H. 1988 Experimental study of instability modes in a three-dimensional boundary layer. AGARD-CP 438 18.
- NORDSTRÖM, J., NORDIN, N. & HENNINGSON, D. S. 1999 The fringe region technique and the Fourier method used in the direct numerical simulation of spatially evolving viscous flows. SIAM J. Sci. Comp. 20 (4), 1365–1393.
- SCHLICHTING, H. 1979 Boundary-Layer Theory, seventh edn. Springer.
- Schmid, P. J. & Henningson, D. S. 2001 Stability and transition in shear flows, Applied Mathematical Sciences, vol. 142. Springer-Verlag.
- Yoshino, T., Suzuki, Y. & Kasagi, N. 2003 Evaluation of GA-based feedback control system for drag reduction in wall turbulence. In *Proc. 3rd Int. Symp. on Turbulence and Shear Flow Phenomena*, pp. 179–184.

Paper 6

6

Global optimal disturbances in the Blasius flow using time-steppers

By Antonios Monokrousos, Espen Åkervik, Luca Brandt, and Dan S. Henningson

Linné Flow Centre, KTH Mechanics, SE-100 44 Stockholm, Sweden

Technical Report

The stability of the Blasius flat-plate boundary-layer flow to three-dimensional disturbances is studied by means of optimisation methods at relatively high Reynolds numbers. We consider both the optimal initial condition leading to the largest growth at finite times and the optimal time-periodic forcing leading to the largest asymptotic response. Both optimisation problems are solved using a Lagrange multiplier technique, where the objective function is the kinetic energy of the flow perturbations and the constraints involve the linearised Navier-Stokes equations. In both cases the evolution equations for the Lagrange multiplier are the adjoint Navier-Stokes equations. The approach proposed here is particularly suited to examine convectively unstable flows, where single global eigenmodes of the system do not capture the downstream growth of the dusturbances. The optimal initial condition for spanwise wavelengths of the order of the boundary layer thickness are streamwise vortices exploiting the lift-up mechanism to create streaks. For long spanwise wavelengths it is the Orr mechanism combined with oblique wave packet propagation that dominates. It is found that the latter mechanism is dominant for the relatively high Reynolds number and the long computational domain considered here. The spatial structure of the optimal forcing is similar to the that of the optimal initial condition, and the response to forcing is also dominated by the Orr/oblique wave mechanism, however less so than in the former case. The lift-up mechanism is, as in the local approach using the Orr-Sommerfeld squire equations, most efficient at zero frequency and degrades slowly for increasing frequencies.

1. Introduction

The flat-plate boundary layer is a classic example of convectively unstable flows; these behave as a broadband amplifier of incoming disturbances. As a consequence, a global stability analysis based on the asymptotic behavior of single eigenmodes of the system will not capture the relevant dynamics. From

180

this global perspective all the eigenmodes are damped, and one has to resort to an input/output formulation in order to obtain the initial conditions yielding the largest possible disturbance growth at any given time and the optimal forcing via an optimization procedure. The aim of this work is to investigate the global stability of the flow over a flat plate subject to external perturbations and forcing and to examine the relative importance of the different instability mechanisms at work, see discussion below. The approach adopted here can be extended to any complex flow provided a numerical solver for the direct and adjoint linearized Navier-Stokes equations is available.

Recently the stability of the spatially-evolving Blasius flow subject to twodimensional disturbances have been studied within an optimisation framework projecting the system onto a low-dimensional subspace consisting of damped Tollmien-Schlichting (TS) eigenmodes (Ehrenstein & Gallaire 2005). These results were extended by Åkervik et al. (2008), who found that by not restricting the spanned space to include only TS modes, the optimally growing structures could exploit both the Orr and TS wave packet mechanism to yield a substantially higher energy growth. The Orr mechanism was studied in the context of shear flows in the Orr-Sommerfeld/Squire equations framework by Butler & Farrell (1992), who termed it the Reynolds stress mechanism. This instability extracts energy from the mean shear by transporting momentum down the mean momentum gradient through the action of the perturbation Reynolds stress. In other words disturbances that are tilted against the shear can borrow momentum from the mean flow while rotating due to the shear until aligned with it. This mechanism is also referred to as wall-normal non-normality. From the local point of view the TS waves appear as unstable eigenvalues of the Orr-Sommerfeld equation. In the global framework however the global eigenmodes belonging to the TS branch are damped (Ehrenstein & Gallaire 2005), and the evolution of TS waves consist of cooperating global modes that produce wave packets. Considering the model problem provided by the Ginzburg-Landau equation with spatially varying coefficients, Cossu & Chomaz (1997) demonstrated that the non-normality of the streamwise eigenmodes leads to substantial transient growth. This non-normality is considered to be associated with the streamwise separation of the direct and adjoint global modes due to the basic advection and it is also termed as streamwise non-normality (Chomaz 2005).

It is now well established that when incoming disturbances exceed a certain amplitude threshold the flat-plate boundary layer is likely to undergo transition due to three-dimensional instabilities arising via the lift-up effect (Ellingsen & Palm 1975; Landahl 1980). This transient growth scenario, where streamwise vortices induce streamwise streaks by the transport of the streamwise momentum of the mean flow, was studied for a variety of shear flows in the locally parallel assumption (c.f. Butler & Farrell 1992; Reddy & Henningson 1993; Trefethen et al. 1993). The extension to the non-parallel flat plate boundary

layer was performed at the same time by Andersson $et\ al.$ (1999) and Luchini (2000) by considering the steady linear boundary-layer equations parabolic in the streamwise direction. In both of these papers the optimal forcing structures were located at the leading edge and a Reynolds number independent growth was found for the evolution of streaks at large downstream distances. Levin & Henningson (2003) examined variations of the position at which disturbances are introduced and found an optimal forcing position downstream of the leading edge. In the global framework an interpretation of the lift-up mechanism is presented e.g. in Marquet $et\ al.$ (2008): Whereas the TS mechanism is governed by a transport of the disturbances by the base flow, the lift-up mechanism is governed by a transport of the base flow by the disturbances. Inherent to the lift up mechanism is the component-wise transfer of momentum to the streamwise velocity component from the two others (component-wise non-normality).

The standard way of solving the optimisation problems involved in the determination of optimal initial condition (or forcing) is to directly calculate the matrix norm of the discretized evolution operator (or resolvent) of the system. In the local approach, where the evolution is governed by the Orr-Sommerfeld/Squire equations it is clearly feasible to directly evaluate the matrix exponential. In the global approach it is in general difficult and in some cases impossible to build the discretized system matrix. One possible remedy is to compute a set of global eigenmodes and project the flow system onto the subspace spanned by the eigenvectors to obtain a low dimensional model of the flow (Schmid & Henningson 2001; Åkervik et al. 2007, 2008). The direct approach of introducing the adjoint evolution operator and solve the eigenvalue problem of the composite operator only using Direct Numerical Simulations is preferable. This approach is commonly referred to as a time-stepper technique (Tuckerman & Barkley 2000), and has been applied to several generic flow cases such as backward facing step flow (Blackburn et al. 2008), separation bubbles (Marquet et al. 2008) and the flat-plate boundary-layer flow subject to two-dimensional disturbances (Bagheri et al. 2008).

In this paper we study the stability of the flat-plate boundary-layer flow subject to three-dimensional disturbances from a global perspective using a time-stepper technique. The base flow only has two inhomogeneous directions, namely the wall normal and streamwise, thereby allowing a decoupling of Fourier modes in the spanwise direction only. Both optimal initial condition and optimal forcing are considered for a range of spanwise wavenumbers, seeking to find the optimal wavenumber. In the case of optimal initial conditions, we optimize over a range of final times, while time-periodic optimal forcing are computed for a range of frequencies. Whereas the computation of optimal initial condition is well known in the global time-stepper context (see references above), the formulation of the optimal forcing problem in this framework is novel. The analysis proposed can have direct implications for flow control

as well: The optimization procedure allows us to determine the location and frequency of the forcing to which the flow under consideration is most sensitive.

The paper is organised as follows. Section 2 is devoted to the description of the base flow and the governing linearised equations. Section 3 and 4 describe the Lagrange approach to solving the optimization problems defined by the optimal initial conditions and optimal forcing, respectively. The main results are presented in section 5; the paper ends with a summary of the main conclusions.

2. Basic steady flow, governing equations and norms

We investigate the stability of the classical spatially-evolving two-dimensional flat-plate boundary-layer flow subject to spanwise harmonic disturbances. The computational domain starts at a distance from the leading edge given by the Reynolds number $Re_x = U_{\infty}x/\nu = 3.38 \cdot 10^5$ or $Re_{\delta^*} = 1.72\sqrt{Re_x} = U_{\infty}\delta_0^*/\nu = 1.72\sqrt{Re_x}$ 10^3 . Here U_{∞} is the uniform free stream velocity, δ^* is the local displacement thickness and ν is the kinematic viscosity. We denote the displacement thickness at the inflow position δ_0^* . All variables are non-dimensionalized by U_{∞} and δ_0^* . The corresponding non-dimensional inflow position is $x_0 = 337.7$. The non-dimensional height of the computational box is $L_y = 30$ and the length is $L_x = 1000$, while the spanwise width L_z is defined in each simulation by the Fourier mode under investigation. We solve the linearized Navier-Stokes equations using a spectral DNS code described in Chevalier et al. (2007) on a domain $\Omega = [0, L_x] \times [0, L_y] \times [0, L_z]$. In the wall normal y direction a Chebyshev-tau technique with $n_y = 101$ polynomials is used; the no-slip condition is enforced at the wall, whereas the Blasius solution is recovered at $y = L_y$. In the streamwise and spanwise directions we assume periodic behaviour, hence allowing for a Fourier transformation of all variables. In the streamwise direction the continuous variables are approximated by $n_x = 768$ Fourier polynomials, whereas in the spanwise direction we solve for each wavenumber separately, a decoupling justified by the spanwise homogeneity of the base flow. Since the boundary layer flow is spatially evolving a fringe region technique is used to ensure that the flow is forced back to the laminar inflow profile at x=0 (Nordström et al. 1999). The fringe forcing is quenching the incoming perturbations and is active at the downstream end of the computational domain, $x \in [800, 1000]$, so that x = 800 can be considered as the effective outflow location, corresponding to $Re_x = 1.138 \cdot 10^6$. The steady state used in the linearization is obtained by marching the nonlinear Navier-Stokes equations in time until the norm of the time derivative of the solution is numerically zero. Thus the two-dimensional steady state with velocities $\mathbf{U} = (U(x,y),V(x,y),0)^T$ and pressure $\Pi(x,y)$ differs slightly from the well-known Blasius similarity solution.

2.1. The linearised Navier-Stokes equations

We are investigating the growth of small amplitude three-dimensional disturbances on a two-dimensional base flow. The stability characteristics of the base

flow **U** to small perturbations $\mathbf{u} = (u(\mathbf{x},t),v(\mathbf{x},t),w(\mathbf{x},t))^T$ are determined by the linearized Navier–Stokes equations

$$\partial_t \mathbf{u} + \mathbf{U} \cdot \nabla \mathbf{u} + \mathbf{u} \cdot \nabla \mathbf{U} = -\nabla \pi + Re^{-1} \Delta \mathbf{u} + \mathbf{g},$$
 (1)

$$\nabla \cdot \mathbf{u} = 0, \tag{2}$$

subject to initial condition $\mathbf{u}(\mathbf{x},t=0) = \mathbf{u}_0(\mathbf{x})$. The boundary conditions for the perturbations are periodicity in x and z and homogeneous Dirichlet conditions in y. Note that we have included a divergence-free forcing term $\mathbf{g} = \mathbf{g}(\mathbf{x},t)$ to enable us to also study the response to forcing as well as to initial condition. In the expression above, the fringe forcing term is omitted for simplicity.

When performing systematic analysis of the linearized Navier–Stokes equations we are interested in the initial condition $\mathbf{u}(0)$ and in the features of the flow states $\mathbf{u}(t)$ that are reached at times t>0. We will also consider the spatial structure of the time-periodic forcing \mathbf{g} that creates the largest response at large times, that is when all transients effects have died out. Our analysis will therefore consider flow states induced by forcing or initial conditions, where a flow state is defined by the three-dimensional velocity vector field throughout the computational domain Ω at time t. To this end, it is preferable to re-write the equations in a more compact form. In order to do so we define the velocities as our state variable, i.e. $\mathbf{u} = (u, v, w)^T$, discarding the pressure π . An important observation can be made from equations (1) and (2); for incompressible flows the pressure only acts as a Lagrange multiplier to maintain divergence free velocity fields. We follow the notation of Kreiss $et\ al.\ (1994)$ and let the forced linearized Navier–Stokes equations be written as

$$\partial_t \mathbf{u} = -(\mathbf{U} \cdot \nabla)\mathbf{u} - (\nabla \mathbf{U})\mathbf{u} + Re^{-1}\Delta \mathbf{u} + \nabla \pi + \mathbf{g}, \tag{3}$$

where the pressure is a known function of the divergence free velocity field ${\bf u}$ and base flow ${\bf U}$

$$\Delta \pi = \nabla \cdot (-(\mathbf{U} \cdot \nabla)\mathbf{u} - (\nabla \mathbf{U})\mathbf{u}). \tag{4}$$

Inversion of the Laplacian requires boundary conditions, and formally we may obtain these by projecting (3) on the outwards pointing normal of the domain \mathbf{n} . If we let the solution of (4) be denoted as $\pi = \mathcal{K}\mathbf{u}$ we end up with with the following expression for the system operator

$$\mathcal{A} = -(\mathbf{U} \cdot \nabla) - (\nabla \mathbf{U}) + Re^{-1}\Delta + \nabla \mathcal{K}. \tag{5}$$

The resulting state space formulation of equation (3) can then be written

$$(\partial_t - \mathcal{A})\mathbf{u} - \mathbf{g} = 0, \quad \mathbf{u}(0) = \mathbf{u}_0, \tag{6}$$

with solution

$$\mathbf{u}(t) = \underbrace{\exp(\mathcal{A}t)\mathbf{u}_{0}}_{\text{initial value problem}} + \underbrace{\int_{0}^{t} \exp(\mathcal{A}\tau)\mathbf{g}(\mathbf{x}, t - \tau) \,d\tau}_{\text{forced problem}}.$$
 (7)

The operator $\exp(\mathcal{A}t)$ is referred to as the evolution operator (or propagator) and maps a solution from time t_0 to time $t_0 + t$. In what follows we will utilise the above evolution expression to study both the response to initial condition, excluding the forcing terms, and the response to forcing by excluding the initial value part, *i.e.* we set the initial condition to zero. If we were to explicitly discretized the operator \mathcal{A} it becomes a matrix of size $n \times n$, with $n = 3n_x n_y n_z$ for general three-dimensional disturbances. When considering spanwise periodic disturbances focusing on one wave number at the time, the dimension of the system matrix becomes $n = 3n_x n_y$. Even in this case the evaluation of the discretized evolution operator $\exp(\mathcal{A}t)$ is not computationally feasible. However the complete stability analysis, including the optimisation, can be performed only by considering solutions to (7), which is readily obtained by time marching using a linearised DNS. This so called time stepper technique has indeed become increasingly popular in stability analysis (Tuckerman & Barkley 2000; Blackburn *et al.* 2008).

2.2. Choice of norm and the adjoint equations

In order to measure the departure from the base flow we introduce the norm based on the kinetic energy of the flow

$$\|\mathbf{u}(t)\|^2 = (\mathbf{u}(t), \mathbf{u}(t)) = \int_{\Omega} \mathbf{u}^H \mathbf{u} \, d\Omega,$$
 (8)

where the superscript H denotes the complex conjugate transpose that reduces to the ordinary transpose T for real valued quantities. The above norm will be used extensively throughout this paper to in order to systematically determine the optimal initial condition and optimal forcing. Associated with the inner product (8) we may define the adjoint evolution operator. The adjoint evolution operator associated with the adjoint linearized Navier–Stokes equations is central to the optimisation framework when investigating the flow non-modal stability. Using the above inner product we may define the action of adjoint evolution operator as

$$(\mathbf{p}, \exp(\mathcal{A}t)\mathbf{u}) = (\exp(\mathcal{A}^{\dagger}t)\mathbf{p}, \mathbf{u}), \tag{9}$$

where \mathcal{A}^{\dagger} is defined by the initial value problem

$$-\partial_t \mathbf{p} = \mathcal{A}^{\dagger} \mathbf{p} = (\mathbf{U} \cdot \nabla) \mathbf{p} - (\nabla \mathbf{U})^T \mathbf{p} + Re^{-1} \Delta \mathbf{p} + \nabla \mathcal{K}^{\dagger} \mathbf{p}, \quad \mathbf{p}(T) = \mathbf{p}_T, \quad (10)$$

for the adjoint pressure $\mathcal{K}^{\dagger}\mathbf{p}$. The adjoint system (10) is derived using the inner product in time space domain $\Sigma = [0, T] \times \Omega$ as shown in Appendix A. This initial value problem has stable integration direction backwards in time so we may define the adjoint solution at time T-t for the forward running time t as

$$\mathbf{p}(T-t) = \exp(\mathcal{A}^{\dagger}t)\mathbf{p}_{T}, \quad t \in [0, T]. \tag{11}$$

It is important to note that the addition of the forcing term \mathbf{g} in (3) has no effect on the derivation of the adjoint equations.

3. Optimal initial condition

In this section, the derivation of the optimality system to be solved in order to find the initial conditions that optimally excites flow disturbances is reported. When seeking the optimal initial condition we assume that the forcing term \mathbf{g} in (6) is zero, so that only the initial value part of (7) is of interest. We wish to determine the unit norm initial condition \mathbf{u}_0 yielding the maximum possible energy $(\mathbf{u}(T), \mathbf{u}(T))$ at a prescribed time T. A common way of obtaining the optimal initial condition is to recognise that the condition

$$G(t) = \max_{\|\mathbf{u}_0\| \neq 0} \frac{\|\mathbf{u}(T)\|^2}{\|\mathbf{u}_0\|^2} = \max_{\|\mathbf{u}_0\| \neq 0} \frac{\|\exp(\mathcal{A}T)\mathbf{u}_0\|^2}{\|\mathbf{u}_0\|^2}$$
$$= \max_{\|\mathbf{u}_0\| \neq 0} \frac{(\mathbf{u}_0, \exp(\mathcal{A}^{\dagger}T)\exp(\mathcal{A}T)\mathbf{u}_0)}{(\mathbf{u}_0, \mathbf{u}_0)}$$
(12)

defines the Rayleigh quotient of the composite operator $\exp(A^{\dagger}T)\exp(AT)$. The optimization problem to be solved is hence the eigenvalue problem

$$\gamma \mathbf{u}_0 = \exp(\mathcal{A}^{\dagger} T) \exp(\mathcal{A} T) \mathbf{u}_0. \tag{13}$$

In the case of large system matrices, as is inherent to fluid-flow systems in more than one space dimension, this eigenvalue problem can not be solved by directly manipulating the matrices. Instead the eigenvalue problem is solved efficiently by matrix-free methods such as power-iterations or the more advanced Arnoldi method; both methods only need a random initial guess for \mathbf{u}_0 and a numerical solver to determine the action of $\exp(\mathcal{A}T)$ and $\exp(\mathcal{A}^{\dagger}T)$. An alternative approach to our optimization problem relies on the use of the Lagrange multiplier technique. As we will show below, this yields the same results for the problem considered here. However, within this framework, it is more straightforward to implement modifications in e.g. the function to maximize. When defining the problem, we need to define the objective function, in our case the kinetic energy of the perturbations at time T

$$\mathcal{J} = (\mathbf{u}(T), \mathbf{u}(T)). \tag{14}$$

Formally, the task is to maximize the above quadratic measure subject to two constraints: the flow needs to satisfy the governing linearized Navier–Stokes equations (6) (without forcing) and initial condition must have unit norm $(\mathbf{u}_0,\mathbf{u}_0)=1$. Note that the second normalization condition selects a unique solution of the eigenvalue problem (13) and thus enable the numerical procedure to converge. By introducing Lagrange multipliers (or costate variables) we may formulate an unconstrained optimization problem for the functional

$$\mathcal{L}(\mathbf{u}, \mathbf{u}_0, \mathbf{u}_T, \mathbf{p}, \gamma) = (\mathbf{u}_T, \mathbf{u}_T) - \int_0^T (\mathbf{p}, (\partial_t - \mathcal{A}) \mathbf{u}) d\tau - \gamma ((\mathbf{u}_0, \mathbf{u}_0) - 1).$$
(15)

We thus need to determine $\mathbf{u}, \mathbf{u}_0, \mathbf{u}_T, \mathbf{p}$ and γ such that \mathcal{L} is stationary, necessary condition for first order optimality. This can be achieved by requiring

that the variation of \mathcal{L} is zero.

$$\delta \mathcal{L} = \left(\frac{\partial \mathcal{L}}{\partial \mathbf{u}}\right) \delta \mathbf{u} + \left(\frac{\partial \mathcal{L}}{\partial \mathbf{p}}\right) \delta \mathbf{p} + \left(\frac{\partial \mathcal{L}}{\partial \mathbf{u}_0}\right) \delta \mathbf{u}_0 + \left(\frac{\partial \mathcal{L}}{\partial \mathbf{u}_T}\right) \delta \mathbf{u}_T + \left(\frac{\partial \mathcal{L}}{\partial \gamma}\right) \delta \gamma = 0.$$
 (16)

This is only fulfilled when all terms are zero simultaneously. The variation with respect to the costate variable (or adjoint state variable) yields directly the state equation

$$\left(\frac{\partial \mathcal{L}}{\partial \mathbf{p}}\right) \Rightarrow (\partial_t - \mathcal{A})\mathbf{u} = 0,$$
 (17)

and similarly the variation with respect to the multiplier γ yields a normalisation criterion

$$\left(\frac{\partial \mathcal{L}}{\partial \gamma}\right) \Rightarrow (\mathbf{u}_0, \mathbf{u}_0) = 1.$$
 (18)

In order to take the variations with respect to the other variables we perform integration by parts on the second term of \mathcal{L} in (15) to obtain

$$\mathcal{L} = (\mathbf{u}_T, \mathbf{u}_T) - \int_0^T (\mathbf{u}, (-\partial_t - \mathcal{A}^{\dagger}) \mathbf{p}) d\tau - (\mathbf{p}_T, \mathbf{u}_T) + (\mathbf{p}_0, \mathbf{u}_0) - \gamma ((\mathbf{u}_0, \mathbf{u}_0) - 1).$$
(19)

Note that the inner product between the direct and adjoint variables \mathbf{p} at the initial and end time is obtained in the integration, see derivation in Appendix A. The variation of this expression with respect to the state variable \mathbf{u} yields an equation for the adjoint variable

$$\left(\frac{\partial \mathcal{L}}{\partial \mathbf{u}}\right) \Rightarrow (-\partial_t - \mathcal{A}^{\dagger})\mathbf{p} = 0. \tag{20}$$

The variations with respect to \mathbf{u}_0 and \mathbf{u}_T give

$$\left(\frac{\partial \mathcal{L}}{\partial \mathbf{u}_0}\right) \Rightarrow \mathbf{u}_0 = \gamma^{-1} \mathbf{p}_0,
\left(\frac{\partial \mathcal{L}}{\partial \mathbf{u}_T}\right) \Rightarrow \mathbf{p}_T = \mathbf{u}_T.$$
(21)

The optimality system to be solved is hence composed of equations (17),(18),(20) and (21). From (18) and the first relation in (21), it can readily be seen that $\gamma = (\mathbf{p}_0, \mathbf{p}_0)$. The remaining equations are solved iteratively as follows. Starting with an initial guess \mathbf{u}_0^n

- (i) we integrate (17) forward in time and obtain \mathbf{u}_T
- (ii) $\mathbf{p}_T = \mathbf{u}_T$ is used as an initial condition at t = T for the adjoint system
- (20), which integrated backward in time gives \mathbf{p}_0
- (iii) determine a new initial guess by normalizing $\mathbf{u}_0^{n+1} = \mathbf{p}_0/\gamma$
- (iv) if $|\mathbf{u}_0^{n+1} \mathbf{u}_0^n|$ is larger than a given tolerance, the procedure is repeated.

Before convergence is obtained \mathbf{u}_0 and \mathbf{p}_0 are not aligned. At convergence however, \mathbf{u}_0 is an eigenvalue of (13). This can be seen from the initial and end

time conditions in equation (19) that according to the above conditions and the definitions of the evolution operators satisfy

$$(\mathbf{p}_T, \mathbf{u}_T) = (\mathbf{u}_T, \mathbf{u}_t) = (\exp(\mathcal{A}T)\mathbf{u}(0), \exp(\mathcal{A}T)\mathbf{u}(0)) = (\mathbf{u}(0), \exp(\mathcal{A}^{\dagger}T)\exp(\mathcal{A}T)\mathbf{u}(0)) = \gamma(\mathbf{u}(0), \mathbf{u}(0)).$$
(22)

The iteration scheme above might, in other words, be seen as a power iteration scheme for finding the largest eigenvalue of (13). Since the composite operator is symmetric its eigenvalue are real and its eigenvectors form an orthogonal basis. The eigenvalues of the system rank the set of optimal initial conditions according to the output energy at time T. If several optimals are sought, e.g. to build a reduced order model of the flow, the sequence of \mathbf{u}_0^n produced in the iteration can be used to build a Krylov subspace suitable for the Arnoldi method.

4. Optimal forcing

Whereas in the previous section the initial value problem defined in (7) was considered, this section will focus on the regime response of the system to time-periodic forcing. Thus we assume zero initial conditions, $\mathbf{u}_0 = 0$, and periodic behavior of the forcing function, *i.e.*

$$\mathbf{g} = \Re \left(\mathbf{f}(\mathbf{x}) \exp(i\omega t) \right), \quad \mathbf{f} \in \mathbb{C}, \quad \omega \in \mathbb{R},$$
 (23)

where ${\bf f}$ is the spatial structure of the forcing, ω is its circular frequency and \Re denotes extracting the real part. With these assumptions, the governing equations become

$$(\partial_t - \mathcal{A})\mathbf{u} - \Re\left(\mathbf{f}\exp(i\omega t)\right) = 0, \quad \mathbf{u}(0) = 0. \tag{24}$$

In this case, we wish to determine the spatial structure of the forcing \mathbf{f} that maximise the response of the flow at the frequency ω in the limit of large times, *i.e.* the regime response of the flow. The measure of the optimum is also here based on the energy norm.

In order to formulate the optimization problem we go to the frequency domain, thereby removing the time dependence. By assuming time periodic behaviour for the quantities involved, \mathbf{u} and \mathbf{p} are replaced by the complex fields $\tilde{\mathbf{u}}$ and $\tilde{\mathbf{p}}$

$$\mathbf{u} = \Re \left(\tilde{\mathbf{u}} \exp(i\omega t) \right), \tag{25a}$$

$$\mathbf{p} = \Re \left(\tilde{\mathbf{p}} \exp(i\omega t) \right). \tag{25b}$$

The resulting governing equations can then be written

$$(i\omega \mathcal{I} - \mathcal{A})\tilde{\mathbf{u}} - \mathbf{f} = 0. \tag{26}$$

The objective function is the disturbance kinetic energy of the regime response,

$$\mathcal{J} = (\tilde{\mathbf{u}}, \tilde{\mathbf{u}}) = \int_{\Omega} \tilde{\mathbf{u}}^H \tilde{\mathbf{u}} \, d\Omega, \tag{27a}$$

where the complex variable $\tilde{\mathbf{u}}$ requires the use of the Hermitian transpose. The Lagrange function for the present optimisation problem is similar in structure to that used to determine the optimal initial condition and is formulated as follows

$$\mathcal{L}(\tilde{\mathbf{u}}, \tilde{\mathbf{p}}, \gamma, \mathbf{f}) = (\tilde{\mathbf{u}}, \tilde{\mathbf{u}}) - (\tilde{\mathbf{p}}, (i\omega\mathcal{I} - \mathcal{A})\tilde{\mathbf{u}} - \mathbf{f}) - \gamma((\mathbf{f}, \mathbf{f}) - 1). \tag{28}$$

Notice that in the definition of the costate there is no time integral involved. In this case, we need to take variations with respect to $\tilde{\mathbf{u}}$, $\tilde{\mathbf{p}}$, \mathbf{f} and γ

$$\delta \mathcal{L} = \left(\frac{\partial \mathcal{L}}{\partial \tilde{\mathbf{u}}}\right) \delta \tilde{\mathbf{u}} + \left(\frac{\partial \mathcal{L}}{\partial \tilde{\mathbf{p}}}\right) \delta \tilde{\mathbf{p}} + \left(\frac{\partial \mathcal{L}}{\partial \mathbf{f}}\right) \delta \mathbf{f} + \left(\frac{\partial \mathcal{L}}{\partial \gamma}\right) \delta \gamma. \tag{29}$$

The first order optimality condition requires all of the terms to be simultaneously zero. By taking variations with respect to the costate variable (or adjoint variable) we again obtain the state equation

$$\left(\frac{\partial \mathcal{L}}{\partial \tilde{\mathbf{p}}}\right) \Rightarrow -(i\omega \mathcal{I} - \mathcal{A})\tilde{\mathbf{u}} + \mathbf{f} = 0, \tag{30}$$

and similarly the variation with respect to the multiplier γ yields a normalisation criterion

$$\left(\frac{\partial \mathcal{L}}{\partial \gamma}\right) \Rightarrow (\mathbf{f}, \mathbf{f}) - 1 = 0. \tag{31}$$

In order to take the variations with respect to the other variables we perform integration by parts on the second term of \mathcal{L} in (28) to obtain

$$\mathcal{L}(\tilde{\mathbf{u}}, \tilde{\mathbf{p}}, \gamma, \mathbf{f}) = (\tilde{\mathbf{u}}, \tilde{\mathbf{u}}) - (\tilde{\mathbf{u}}, (i\omega\mathcal{I} - \mathcal{A}^{\dagger})\tilde{\mathbf{p}}) + (\mathbf{f}, \tilde{\mathbf{p}}) - \gamma((\mathbf{f}, \mathbf{f}) - 1). \tag{32}$$

No initial-final condition terms appear during this integration by parts since here the inner product is only in space (in contrast to the optimal initial condition). The spatial boundary terms cancel owing to the chosen boundary conditions as seen in Appendix A. Variations with respect to the state variable $\tilde{\mathbf{u}}$ and to the forcing function \mathbf{f} yield

$$\left(\frac{\partial \mathcal{L}}{\partial \tilde{\mathbf{u}}}\right) \Rightarrow \tilde{\mathbf{u}} - (i\omega \mathcal{I} - \mathcal{A}^{\dagger})\tilde{\mathbf{p}} = 0, \tag{33}$$

$$\left(\frac{\partial \mathcal{L}}{\partial \mathbf{f}}\right) \Rightarrow \mathbf{f} = \gamma^{-1}\tilde{\mathbf{p}}.\tag{34}$$

Equations (30) and (33) provide the two equations we have to solve, equation (31) gives the normalisation condition and (34) provides the optimality condition that is used to calculate the new forcing field after each iteration of the optimisation loop.

Next, we show the equivalence between this method and the corresponding standard matrix method. The formal solution of equation (24) can be written

$$\tilde{\mathbf{u}} = (i\omega I - \mathcal{A})^{-1}\mathbf{f}.$$
 (35)

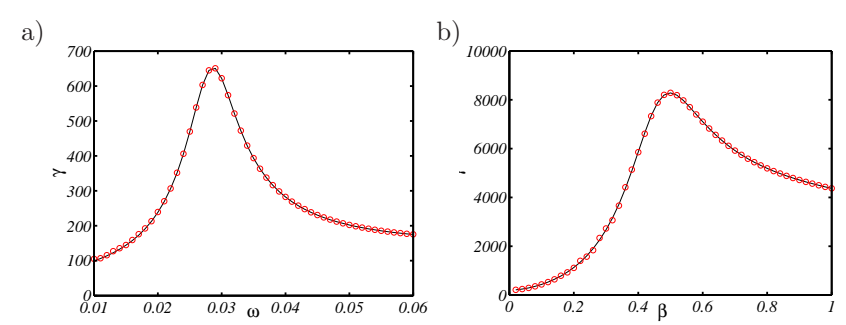


FIGURE 1. Comparison of adjoint iteration scheme for optimal forcing (shown as circles) and direct solution in terms of SVD of the OSS resolvent (shown as solid lines). a) Wavenumber $(\alpha, \beta) = (0.1, 0)$ for different frequencies ω at Reynolds number Re = 1000. b) Zero streamwise wavenumber $(\alpha = 0.1)$ for different spanwise wavenumbers β subject to zero frequency forcing at Reynolds number Re = 500. Both plots shows excellent agreement between the two methods.

The corresponding solution for the adjoint system

$$\tilde{\mathbf{p}} = (i\omega I - \mathcal{A}^{\dagger})^{-1}\tilde{\mathbf{u}}. \tag{36}$$

Combining the two equations above with (34)

$$\mathbf{f} = \frac{1}{\gamma} (i\omega I - \mathcal{A}^{\dagger})^{-1} (i\omega I - \mathcal{A})^{-1} \mathbf{f}.$$
 (37)

This is a new eigenvalue problem defining the spatial structure of the optimal forcing at frequency ω that is solved iteratively; the largest eigenvalue corresponds to the square of the resolvant norm.

$$\gamma = \|(i\omega I - A)^{-1}\|^2. \tag{38}$$

Note that the actual implementation is using a slightly different formulation, since the available time-stepper does not solve directly (30) and (33). In practice, the governing equations are integrated in time long enough that the transient behaviour of the system operator $\mathcal A$ has died out. The regime response for the direct and adjoint system is extracted by performing a Fourier transform of the velocity field during one period of the forcing.

The iteration steps are:

- (i) Integrate (24) forward in time and obtain the Fourier transform response $\tilde{\mathbf{u}}$ at the frequency of the forcing.
- (ii) $\tilde{\mathbf{u}}$ is used as a forcing for the adjoint system which in time domain is written

$$(-\partial_t - \mathcal{A}^{\dagger})\mathbf{p} - \Re\left(\tilde{\mathbf{u}}\exp(i\omega t)\right) = 0. \tag{39}$$

- (iii) A new forcing function is determined by normalizing $\mathbf{f}^{n+1} = \tilde{\mathbf{p}}/\gamma$.
- (iv) If $|\mathbf{f}^{n+1} \mathbf{f}^n|$ is larger than a given tolerance, the procedure is repeated.

A validation of the method is presented in figure 1, where the present adjoint iteration scheme is compared to the standard method of performing a singular value decomposition (SVD) on the resolvent of the Orr–Sommerfeld/Squire equations (c.f. Schmid & Henningson 2001). In figure 1a) the response to forcing for different frequencies at the wavenumber pair $(\alpha, \beta) = (0.1, 0)$ is shown at Re = 1000. Figure 1b) shows the response to steady forcing and streamwise wavenumber $\alpha = 0$ for different spanwise wavenumbers β at Re = 500. Both cases shows excellent agreement between the two methods.

5. Results

The flat plate boundary layer flow is globally stable, i.e. there are no eigenvalues of A located in the unstable half plane. Hence we do not expect to observe the evolution of single eigenmodes. In Åkervik et al. (2008) the non-modal stability of this flow subject to two-dimensional disturbances was studied by considering optimal superposition of eigenmodes. These authors found that the optimal initial condition exploits the well known Orr mechanism to efficiently trigger the propagating Tollmien-Schlichting wave packet. In Bagheri et al. (2008), the stability of the same flow was studied using forward and adjoint iteration scheme together with the Arnoldi method to reproduce the same mechanism. By allowing for three-dimensional disturbances, it is expected that in addition to the instability mechanisms mentioned above (convective Tollmien-Schlichting instability and the Reynolds stress mechanism of Orr) the lift-up mechanism will be relevant in the system. This has been well understood both using the Orr-Sommerfeld/Squire equations (Butler & Farrell 1992) and in the Parabolized Stability framework (Andersson et al. 1999; Luchini 2000; Levin & Henningson 2003). In the former formulation, the base flow is assumed to be parallel. At the Reynolds number Re = 1000, the inflow Reynolds number of the present investigation, it is found that for spanwise wavenumbers β larger than ≈ 0.3 there is no exponential instability of TS/oblique waves. The largest non-modal growth due to the lift-up mechanism is observed at the wavenumber pair $(\alpha, \beta) = (0, 0.7)$. In the present work we do not restrict ourselves to zero streamwise wavenumber $\alpha = 0$, but instead we take into account the developing base flow. Indeed the spatially developing base flow allows for transfer of energy between different wavenumbers through the convective terms.

5.1. Optimal initial condition

We investigate the potential for growth of initial conditions with different spanwise wavenumbers β by solving the eigenvalue problem (13) for a range of instances of time T. This amounts to performing a series of direct and adjoint numerical simulations until convergence towards the largest eigenvalues of (13)

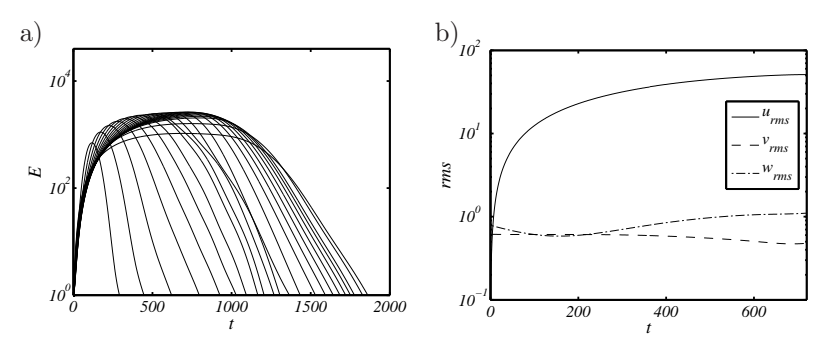


FIGURE 2. a) Energy when optimising for different time T at the wavenumber $\beta=0.55$, where the optimal streak growth is obtained. Each curve is obtained from an adjoint iteration scheme. The maximum growth is obtained at time T=720. b) Component-wise rms-values when optimising for time T=720. There is a transfer of energy from the wall normal and spanwise component to the streamwise velocity in time, clearly showing that the lift-up mechanism is present. The maximum at each time in this figure defines the envelope of growth.

at time T is obtained. If only the largest eigenvalue of (13) is desired it suffices to use a power iteration scheme, whereas if several of the leading eigenvalues are needed, one has to resort to a Krylov/Arnoldi procedure (c.f. Nayar & Ortega 1993; Lehoucq et al. 1997). Both of these approaches rely on the repeated action of $\exp(\mathcal{A}^{\dagger}T)\exp(\mathcal{A}T)$ on an initial velocity field $\mathbf{u}(0)$. In other words, it is not necessary to store matrices in order to obtain the eigenvalues.

Figure 2a) shows the energy evolution when optimising for different times at the spanwise wavenumber $\beta=0.55$. It is at this wave number that the maximum growth due to the lift-up mechanism is found for the computational box under consideration. From figure 2b) it is evident that the disturbance leading to the maximum streak growth at time T=720 exploits the component-wise transfer between velocity components, inherent to the lift-up mechanism. The initial condition is in fact characterized by strong wall-normal v and spanwise v perturbation velocity while the flow at later times is perturbed in its streamwise velocity component.

Four different optimal initial conditions for $\beta=0.55$ and T=720 are shown in figure 3. The wall-normal velocity component of the eigenvector leading to the maximum growth is reported in 3a). Since the base flow is uniform in the spanwise direction, the second eigenvector has the exact same shape as the first, only shifted half a wavelength in z as shown in figure 3b). These eigenvectors correspond to the same eigenvalue $\gamma_{1,2}=2.6\cdot 10^3$, and they may be combined linearly to obtain a disturbance located at any spanwise position.



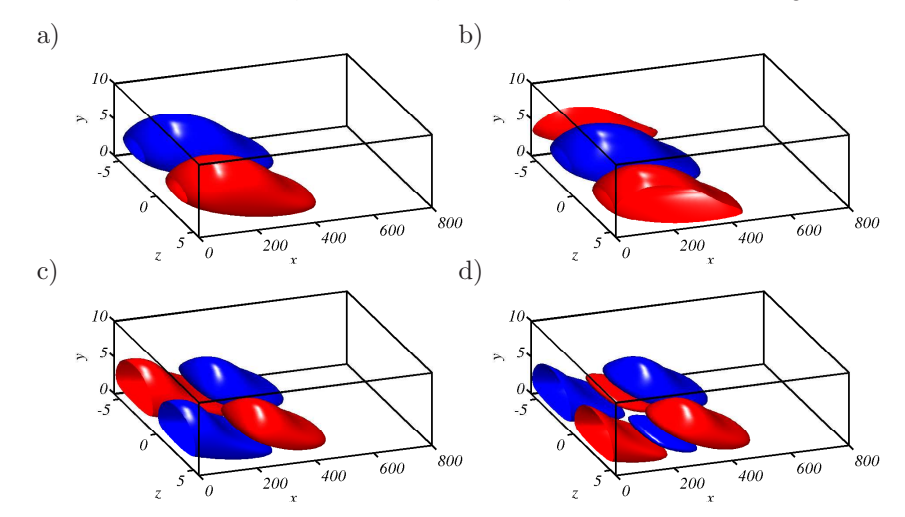


FIGURE 3. Wall-normal component of the leading four eigenvectors for the optimisation problem at $\beta=0.55,\,t=720,\,\mathrm{plot}$ ted over one wavelength in the spanwise direction. Red/blue colour signifies isosurfaces corresponding to positive/negative veloicities at 10 percent of the maximum. a) The first eigenvector. b) The second eigenvector which is similar to the first eigenvector, only shifted in the spanwise direction. c) The third eigenvector, which is similar to the fourth eigenvector (thus not shown), only shifted in the spanwise direction. d) The fifth eigenvector. Note that the axes are not at the actual aspect ratio, the structures are elongated.

In figure 3c)-d) the third eigenvector associated with $\gamma_3=2.2\cdot 10^3$ and the fifth associated with $\gamma_5=1.7\cdot 10^3$ are shown respectively. Also these eigenvectors come in pairs with matching eigenvalues. It is thus possible with the Arnoldi method to obtain several optimals for a single parameter combination. This has not been done previously for the Blasius flow, while Blackburn *et al.* (2008) computed several optimals for the flow past a backward-facing step.

An important feature of this high Reynolds number flat plate boundary layer flow with length $L_x=800$ is that the combined Orr/Tollmien-Schlichting mechanism is very strong with a growth potential of $\gamma_1=2.35\cdot 10^4$ (Bagheri et al. 2008) obtained at time T=1800. Indeed, also using the Orr–Sommerfeld/Squire equations one may confirm that the slow exponential downstream growth of TS waves will dominate the long time behaviour of the linear system. If however the streaks formed by the lift-up mechanism have reached sufficiently large amplitudes to trigger non-linear effects, the TS wave transition scenario will be by-passed. In figure 4 a contour map of the maximum

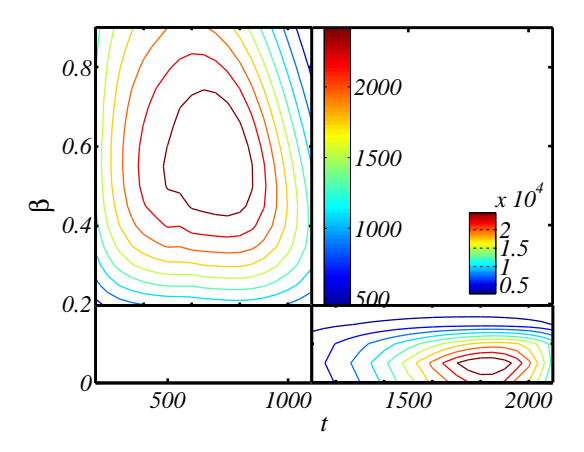


FIGURE 4. Contour map of optimal growth due to initial condition in the time spanwise wavenumber domain. The maximum streak growth is obtained for $\beta=0.55$ at time T=720. The global maximum is obtained for $\beta=0.05$, with the streamwise exponential amplification of oblique waves combined with the Orr mechanism.

growth and time of maximum for different spanwise wavenumbers β is shown. Note that the growth is divided into two regimes; a low spanwise wavenumber regime dominated by the TS/oblique waves, where the growth is slow. For high spanwise wavenumber it is the fast lift-up mechanism that is dominating. The contour levels are different in the two regimes, and the TS/oblique mechanism can be seen to yield one order of magnitude larger growth than the lift-up instability. The global maximum growth is obtained at the wavenumber $\beta=0.05$. Figure 5 shows the streamwise velocity component of the optimal initial condition leading to the maximum growth at time T=1820 and the flow structure at that time. The initial disturbance is as in the two-dimensional case leaning against the shear (see figure 5a). The resulting instability exploits the Orr-mechanism to efficiently initialize the wave packet propagation finally giving the disturbance shown in figure 5b).

5.2. Optimal forcing

Since boundary layers are convectively unstable, thereby acting as noise amplifiers, a prominent role is played by the response to forcing, rather than by the detailed time-evolution of the initial condition; The optimal forcing is therefore a relevant measure of the maximum possible growth that may be observed in the computational domain. Analysis of the frequency response can



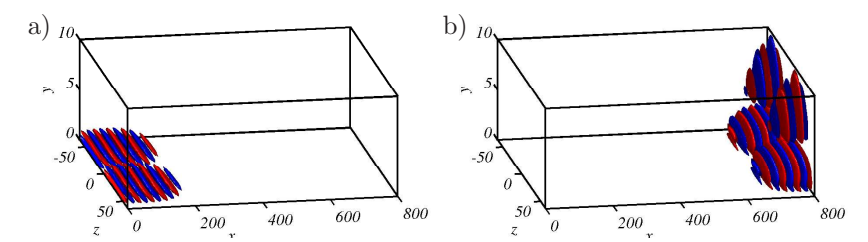
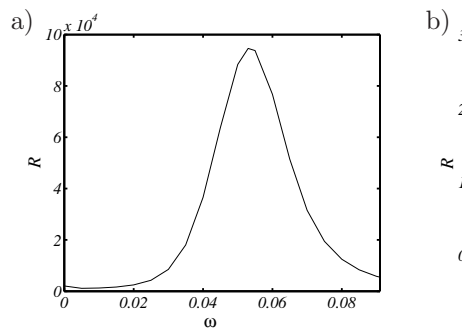


FIGURE 5. Isosurfaces of streamwise component of disturbances at the spanwise wavenumber $\beta=0.05$. Red/blue colour signifies isosurfaces corresponding to positive/negative veloicities at 10 percent of the maximum. a) Streamwise component of optimal initial condition leading to the global optimal growth at time T=1820. b) Corresponding flow response at time T=1820

also have implications for control revealing the forcing location and frequencies the flow is most sensitive to. While the evolution of the optimal initial condition consists of the propagation and amplification of a wave packet, eventually leaving the computational box (or measurement section), the response of the flow to periodic forcing will consist of structures with a fixed amplitude at each streamwise station, oscillating around the mean flow. We investigate the structure of the optimal forcing and the corresponding response for a range of spanwise wavenumbers and frequencies. Thus, for each wave number we examine a number of temporal frequencies. Ideally we would like to solve the linearized Navier-Stokes equations for very large times, ensuring that we are only considering the regime (long-time) response at the specific frequency under investigation. In practice however we are restricted to a finite final time by the computational cost of solving the direct and adjoint equations involved in the iteration scheme. Using power iterations to find the largest eigenpair typically requires approximately 15 iterations, or in other words integrating the equations 30 times. As can be seen from the results in the previous section transiently growing perturbations of small spanwise scale leave our domain at time $t \approx 2000$, while locally unstable TS-waves propagates at a speed of about $0.3~U_{\infty}$. This observation along with several convergence tests using different final times to extract the flow regime response lead to the conclusion that the integration T = 5000 is long enough to observe the pure frequency response.

Figure 6 shows the square of the resolvent norm, *i.e.* the response to forcing for the two limiting cases $\beta=0$ and $\omega=0$. In figure 6a) the response to two-dimensional forcing, inducing perturbations with $\beta=0$, is displayed. The maximum response is observed for the frequency $\omega=0.055$. This maximum is obtained at the frequency where the least stable TS eigenvalue is located (see Bagheri *et al.* 2008). Indeed it is known that by projecting the dynamics of the



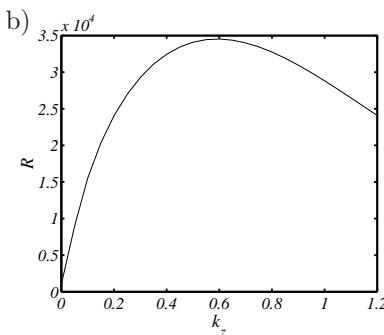


FIGURE 6. a) Frequency response for zero spanwise wavenumber *i.e.* two-dimensional disturbances. The optimal response is obtained for the frequency $\omega=0.055$. b) Response to zero frequency forcing $\omega=0$ for different spanwise wavenumbers. The maximum response is obtained at $\beta=0.6$

flow onto the basis of eigenmodes, the response to forcing is given by the combination of resonant effects (distance in the complex plane from forcing frequency to eigenvalue) and non-modal effects, i.e. the cooperating non-orthogonal eigenvectors (Schmid & Henningson 2001). In Åkervik et al. (2008) it was shown for a similar flow that non-normal eigenvectors could induce a response about a factor twenty larger than that induced only by resonant effects.

The response to zero temporal frequency for different spanwise wavenumbers β is shown in figure 6b), where according to local theory the maximum response is expected for spanwise periodic excitations. The maximum growth may be observed for the wavenumber $\beta=0.6$, a slightly larger value than for the optimal initial condition case. Notice that in the case of optimal forcing, there is a smaller difference in the maximum gain due to the two different dominating mechanisms (TS-waves vs. streaks).

A full parameter study has been carried on in the frequency ω versus spanwise wavenumber β plane. A contour map showing the regime response to optimal forcing is displayed in figure 7. As in the case of the optimal initial condition, the global maximum response to forcing is observed for $\beta=0.05$. It reaches this maximum for the frequency $\omega=0.055$. A second region of strong amplification is found for low frequencies and high spanwise wavenumbers. Here the most amplified structures consist of streamwise vortices that form streamwise elongated streaks. At the largest spanwise wavenumbers, we also observe that the decay of the amplification when increasing the forcing frequencies is rather slow. Conversely, the peak corresponding to excitation of the TS-waves is more narrow.

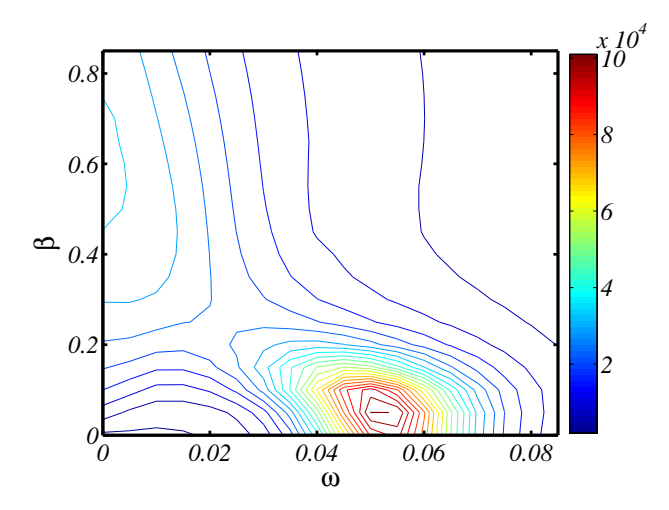


FIGURE 7. Contour map of response to forcing with frequency ω versus spanwise wavenumber β . The maximum response to forcing is observed for $\beta=0.05$. It reaches this maximum for the frequency $\omega=0.055$. The maximum growth due to the streak mechanism is found for the spanwise wavenumber $\beta=0.6$ at $\omega=0$

The overall maximum amplification, found for the spanwise wavenumber of $\beta=0.05$ and at the same frequency as the optimal two-dimensional forcing, is presented next. The forcing term in the streamwise momentum equation and the streamwise velocity component of the optimal response are shown in figure 8. The optimal forcing structures are leaning against the shear (see 8a) to optimally trigger the Orr mechanism; the regime long-time response of the flow, shown in figure 8b), reveals the appearance of amplified TS-waves at the downstream end of the computational domain.

The optimal forcing structure at $\beta=0.6$ and the zero frequency has almost all its energy in the spanwise and wall normal components, that is the flow is forced optimally in the wall-normal and spanwise direction as shown among other by Jovanovic & Bamieh (2005) for channel flows. The wall-normal and spanwise velocity of the forcing structures are displayed in figure 9a) and b). The rms values of the streamwise component of the forcing is only two percent of that pertaining to its spanwise and wall-normal counterparts. The lift-up effect transfers momentum into the streamwise component (shown in figure 9c), which contains 99.99 percent of the energy of the flow response. The streak amplitude increases in the streamwise direction untill the fringe region is encountered.

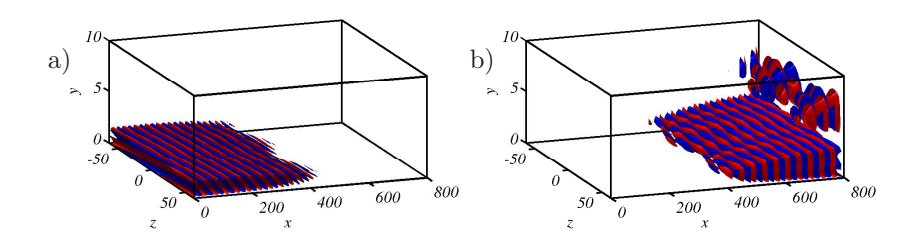


FIGURE 8. Isosurfaces of optimal forcing and response for the streamwise wavenumber $\beta=0.05$ subject to forcing at the frequency $\omega=0.055$. Red/blue colour signifies isosurfaces corresponding to positive/negative velocities at 10 percent of the maximum. a) Streamwise component of optimal forcing structure. b) Streamwise velocity component of response.

Conclusions

We have used a Lagrange multiplier technique in conjunction with direct and adjoint linearized Navier—Stokes equations in order to quantify the growth potential in the spatially developing flat-plate boundary-layer flow at moderately high Reynolds subject to three-dimensional spanwise periodic disturbances. We consider both the initial conditions leading to the largest possible energy amplification at time T and the optimal spatial structure of time-periodic forcing. To the best of our knowledge, the latter is computed for the first time for this type of spatially inhomogeneous flows. The optimisation framework adopted does not restrict us to assume slow variation of the base flow in the streamwise direction, common to both the first order approximation of the OSS formulation and the more advanced PSE approximation. Specifically we do not, as in the PSE framework, need different equations to describe the lift-up instability and the wavepacket propagation.

For the optimal initial condition we find that the largest potential for growth is found at small spanwise wavenumbers and consists of upstream tilted structures, enabling the subsequent disturbances to exploit the Orr mechanism and convective instability of the oblique wavepacket. The lift-up instability mechanism inherent to moderately high spanwise wavenumbers is faster than the Orr/oblique instability; we show that for the present configuration the latter instability needs approximately 300 time units more to extract as much energy as the lift-up instability. As concerns the optimal response to periodic forcing, the difference in the two instabilities is less pronounced. In this case, the Orr/oblique wave instability only manages to gain a factor of two in energy more than the streak mechanism. These results, the largest amplification of the local convective instability over the non-modal streak generation, can be explained by the long computational box examined and the relatively high



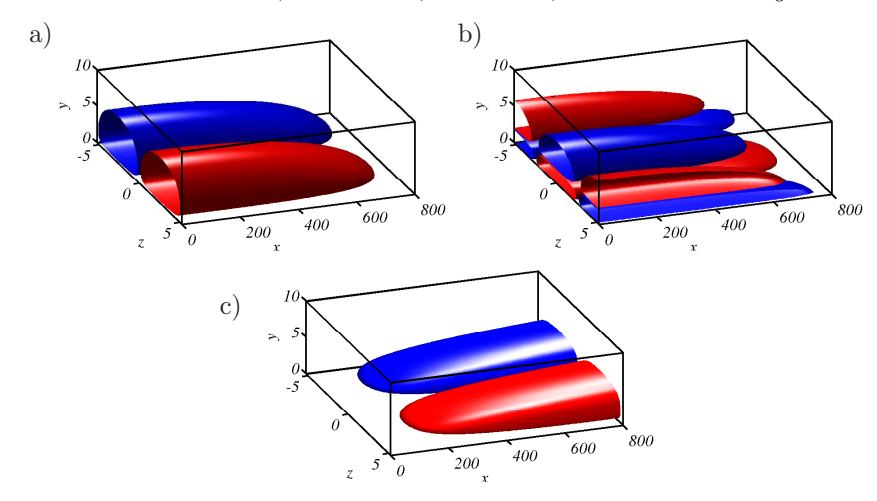


FIGURE 9. Isosurfaces of optimal forcing and response for the streamwise wavenumber $\beta=0.6$ subject to steady forcing. Red/blue colour indicates isosurfaces corresponding to positive/negative veloicities at 10 percent of the maximum. a) Wall-normal component of optimal forcing structure. b) Spanwise component of optimal forcing. c) Streamwise velocity component of the flow response. Both the forcing structures and the response are elongated in the streamwise direction.

inflow Reynolds number. Starting closer to the leading edge, one can expect streaks to dominate the transition scenario.

Three different destabilising mechanisms are considered in this study, all at work in the boundary layer flow. Although these could be explained using the OSS equations, they are in this paper analysed without any simplifying assumptions, rendering the present work of a more general character. By choosing an objective function and using the full linearized Navier–Stokes equations as constraints we are not limiting ourselves to simple geometries. Whenever a DNS code is available to accurately describe a flow, all that is needed in order to investigate the stability characteristics is a linearized version of the code and the implementation of the corresponding adjoint equations along with a wrapper built around these two simulations ensuring the correct optimisation scheme. The method used here is therefore applicable to any geometrical configuration.

Appendix A. Derivation of the adjoint equations

In this section we show the derivation of the adjoint linearized Navier–Stokes equations, needed to perform directional derivatives on the augmented cost functions (15) and (28). Associated with the inner product $(\mathbf{u}, \mathbf{u}) = \int_{\Omega} \mathbf{u}^T \mathbf{u} \, d\Omega$

we may define the adjoint evolution operator. Using the above inner product we may define the action of adjoint evolution operator as

$$(\mathbf{p}, \exp(\mathcal{A}t)\mathbf{u}) = (\exp(\mathcal{A}^{\dagger}t)\mathbf{p}, \mathbf{u}), \tag{A1}$$

derived using the inner product in time-space domain $\Sigma = [0, T] \times \Omega$

$$(\mathbf{u}, \mathbf{u})_{\Sigma} = \int_{0}^{T} (\mathbf{u}, \mathbf{u}) dt = \int_{0}^{T} \int_{\Omega} \mathbf{u}^{T} \mathbf{u} d\Omega dt.$$
 (A2)

By noting that the linearized Navier–Stokes equations can be written as $(\partial_t - \mathcal{A})\mathbf{u} = 0$ we will recognise that the adjoint should satisfy the following property

$$(\mathbf{p}, (\partial_t - \mathcal{A})\mathbf{u})_{\Sigma} = ((-\partial_t - \mathcal{A}^{\dagger})\mathbf{p}, \mathbf{u})_{\Sigma} = 0.$$
 (A3)

In order to move the action of the operators ∂_t and \mathcal{A} from \mathbf{u} to \mathbf{p} we will need to perform integration by parts on the left most part of the above expression

$$0 = (\mathbf{p}, (\partial_{t} - \mathcal{A})\mathbf{u})_{\Sigma}$$

$$= \int_{0}^{T} \int_{\Omega} (\mathbf{p})^{T} \left(\partial_{t}\mathbf{u} - (\mathbf{U} \cdot \nabla)\mathbf{u} - (\nabla\mathbf{U})\mathbf{u} + Re^{-1}\Delta\mathbf{u} + \nabla\pi \right) d\Omega dt$$

$$= \int_{0}^{T} \int_{\Omega} \mathbf{u}^{T} \left(-\partial_{t}\mathbf{p} + (\mathbf{U} \cdot \nabla)\mathbf{p} - (\nabla\mathbf{U})^{T}\mathbf{p} + Re^{-1}\Delta\mathbf{p} + \nabla\sigma \right) d\Omega dt$$

$$+ \int_{0}^{T} B.C. dt + \int_{\Omega} (\mathbf{p}(T))^{T}\mathbf{u}(T) d\Omega - \int_{\Omega} (\mathbf{p}(0))^{T}\mathbf{u}(0) d\Omega$$

$$= ((-\partial_{t} - \mathcal{A}^{\dagger})\mathbf{p}, \mathbf{u})_{\Sigma} + \int_{0}^{T} B.C. dt + (\mathbf{p}(T), \mathbf{u}(T)) - (\mathbf{p}(0), \mathbf{u}(0)),$$

where σ is the pressure for the adjoint equations which can also be obtained through a Poisson equation to satisfy $\sigma = \mathcal{K}^{\dagger}\mathbf{p}$. The above expression defines the adjoint linearized Navier–Stokes equations

$$-\partial_t \mathbf{p} = \mathcal{A}^{\dagger} \mathbf{p} = (\mathbf{U} \cdot \nabla) \mathbf{p} - (\nabla \mathbf{U})^T \mathbf{p} + Re^{-1} \Delta \mathbf{p} + \nabla \mathcal{K}^{\dagger} \mathbf{p}, \quad \mathbf{p}(T) = \mathbf{p}_T \quad (A5)$$

if the boundary conditions of the adjoint system is set so that the integral containing boundary conditions vanishes. The chosen boundary conditions are periodic along the boundaries the two wall parallel directions and Dirichlet on the wall and the free stream.

The initial and end time inner products equals, i.e.

$$(\mathbf{p}(T), \mathbf{u}(T)) = (\mathbf{p}(T), \exp(\mathcal{A}T)\mathbf{u}(0)) = (\exp(\mathcal{A}^{\dagger}T)\mathbf{p}(T), \mathbf{u}(0)) = (\mathbf{p}(0), \mathbf{u}(0)).$$
(A6)

Hence it is seen that the adjoint evolution operator

$$\mathbf{p}(T-t) = \exp(\mathcal{A}^{\dagger}t)\mathbf{p}(T), \tag{A7}$$

solves the adjoint linearized Navier–Stokes equations backwards in time to fulfil the inner product relation (A3).

References

- ÅKERVIK, E., EHRENSTEIN, U., GALLAIRE, F. & HENNINGSON, D. S. 2008 Global two-dimensional stability measures of the flat plate boundary-layer flow. *Eur. J. Mech. B/Fluids* **27**, 501–513.
- ÅKERVIK, E., HŒPFFNER, J., EHRENSTEIN, U. & HENNINGSON, D. S. 2007 Optimal growth, model reduction and control in a separated boundary-layer flow using global eigenmodes. *J. Fluid Mech.* **579**, 305–314.
- Andersson, P., Berggren, M. & Henningson, D. S. 1999 Optimal disturbances and bypass transition in boundary layers. *Phys. Fluids* 11, 134–150.
- Bagheri, S., Åkervik, E., Brandt, L. & Henningson, D. S. 2008 Matrix-free methods for the stability and control of boundary layers. *AIAA J.* Submitted.
- Blackburn, H. M., Barkley, D. & Sherwin, S. J. 2008 Convective instability and transient growth in flow over a backward-facing step. *J. Fluid Mech.* **608**, 271–304.
- Butler, K. M. & Farrell, B. F. 1992 Three-dimensional optimal perturbations in viscous shear flow. *Phys. Fluids A* 4, 1637–1650.
- Chevalier, M., Schlatter, P., Lundbladh, A. & S., H. D. 2007 A pseudo spectral solver for incompressible boundary layer flows. *Technical Report, Trita-Mek* 7.
- Chomaz, J. M. 2005 Global instabilities in spatially developing flows: non-normality and nonlinearity. *Annu. Rev. Fluid Mech.* **37**, 357–392.
- Cossu, C. & Chomaz, J. 1997 Global measures of local convective instability. *Phys. Rev. Lett.* **77**, 4387–90.
- EHRENSTEIN, U. & GALLAIRE, F. 2005 On two-dimensional temporal modes in spatially evolving open flows: the flat-plate boundary layer. *J. Fluid Mech.* **536**, 209–218.
- Ellingsen, T. & Palm, E. 1975 Stability of linear flow. Phys. Fluids 18, 487–488.
- JOVANOVIC, M. R. & BAMIEH, B. 2005 Componentwise energy amplification in channel flows. *J. Fluid Mech.* **534**, 145–183.
- Kreiss, G., Lundbladh, A. & Henningson, D. S. 1994 Bounds for treshold amplitudes in subcritical shear flows. *J. Fluid Mech.* 270, 175–198.
- Landahl, M. T. 1980 A note on an algebraic instability of inviscid parallel shear flows. J. Fluid Mech. 98, 1–34.

- Lehoucq, R. B., Sorensen, D. & Yang, C. 1997 Arpack users' guide: Solution of large scale eigenvalue problems with implicitly restarted arnoldi methods.
- Levin, O. & Henningson, D. S. 2003 Exponential vs algebraic growth and transition prediction in boundary layer flow. *Flow, Turbulence and Combustion* **70**, 183–210.
- Luchini, P. 2000 Reynolds-number-independent instability of the boundary layer over a flat surface: Optimal perturbations. *J. Fluid Mech.* **404**, 289–309.
- MARQUET, O., SIPP, D., CHOMAZ, J. M. & JACQUIN, L. 2008 Amplifier and resonator dynamics of a low-reynolds-number recirculation bubble in a global framework. *J. Fluid Mech.* **605**, 429–443.
- NAYAR, M. & ORTEGA, U. 1993 Computation of selected eigenvalues of generalized eigenvalue problems. *J. Comput. Phys.* **108**, 8–14.
- NORDSTRÖM, J., NORDIN, N. & HENNINGSON, D. S. 1999 The fringe region technique and the fourier method used in the direct numerical simulation of spatially evolving viscous flows. *SIAM J. Sci. Comp.* **20** (4), 1365–1393.
- REDDY, S. C. & HENNINGSON, D. S. 1993 Energy growth in viscous channel flows. J. Fluid Mech. 252, 209–238.
- Schmid, P. J. & Henningson, D. S. 2001 Stability and transition in shear flows. Springer.
- Trefethen, L. N., Trefethen, A. E., Reddy, S. C. & Driscill, T. A. 1993 Hydrodynamic stability without eigenvalues. *Science* **261**, 578–584.
- Tuckerman, L. & Barkley, D. 2000 Bifurcation Analysis For Timesteppers, pp. 453–566. Numerical Methods for Bifurcation Problems and Large-Scale Dynamical Systems . Springer, New York.